



New electrochemical cells for energy conversion and storage

Thesis submitted by
Laura Navarrete Algaba
To apply for the Degree of Doctor

Supervisor:
Prof. José Manuel Serra Alfaro

Valencia, January 2017



UNIVERSITAT
POLITÈCNICA
DE VALÈNCIA



INSTITUTO DE
TECNOLOGÍA
QUÍMICA



CSIC
Consejo Superior de Investigaciones Científicas

A mis padres

A mi hermana y Javi

A mis abuelos, Manolo y Lucía

*"Failure is simply the opportunity to begin again, this time more
intelligently."*

*"Coming together is a beginning. Keeping together is progress.
Working together is success."*

-Henry Ford-

Outline

1. Context and scope of the thesis	11
1.1. References	15
2. Resumen/Summary/Resum	19
2.1. Resumen	19
2.2. Summary	21
2.3. Resum	23
3. Introduction	27
3.1. Technologies	27
3.1.1. Power-to-Power: fuel cells.....	27
3.1.1.1. Types of fuel cells.....	28
3.1.1.2. Solid oxide fuel cells.....	31
3.1.1.3. Phosphate-based fuel cells	33
3.1.2. Power-to-Hydrogen: Electrolyzer	34
3.1.2.1. Solid oxide electrolyzer	35
3.1.2.2. Phosphate-based electrolyzer	36
3.1.3. Power-to-Gas	37
3.2. Conductivity	40
3.2.1. Intrinsic defects.....	42
3.2.1.1. Ionic defects	42
3.2.1.2. Electronic defects.....	44
3.2.2. Extrinsic defects: mixed conductivity.....	45
3.2.3. Diffusion mechanisms.....	51
3.3. Cell components and material	53
3.3.1. Electrolyte	53
3.3.1.1. Materials	54

3.3.1.1.1.	Ionic conductors.....	54
3.3.1.1.2.	Protonic conductors.....	56
3.3.1.1.2.1.	High temperature	56
3.3.1.1.2.2.	Low temperature	58
3.3.2.	Electrodes	59
3.3.2.1.	Materials	60
3.3.2.1.1.	High temperature	60
3.3.2.1.1.1.	Perovskites.....	60
3.3.2.1.1.2.	Ruddlesden-Popper	62
3.3.2.2.	Electrode configuration	63
3.3.2.2.1.	Electrochemical activation of oxygen	65
3.3.2.2.2.	Electrochemical activation of hydrogen	67
3.4.	Appendix: Defect chemistry and mechanisms.....	68
3.5.	References	68
4.	Methodology	75
4.1.	Material synthesis.....	75
4.1.1.	Solid state reaction (SSR)	75
4.1.2.	Pechini.....	77
4.1.3.	Co-precipitation	78
4.2.	Materials summary	79
4.3.	Structural characterization	81
4.3.1.	X-Ray Diffraction (XRD)	81
4.3.2.	Scanning Electron Microscopy (SEM)	84
4.3.3.	Transmission Electron Microscopy (TEM).....	86
4.3.4.	Thermogravimetric Analysis (TGA)	87
4.4.	Sample preparation	89
4.4.1.	Dense samples	89

4.4.2.	Electrodes preparation	91
4.5.	Electrochemical characterization.....	94
4.5.1.	DC total electrical conductivity	94
4.5.2.	Electrochemical Impedance Spectroscopy (EIS)	96
4.5.3.	Fuel cell mode	100
4.5.4.	Electrolyzer mode	102
4.5.5.	High temperature set-up	104
4.5.6.	Low temperature set-up	107
4.5.7.	Gas chromatography.....	109
4.5.8.	Mass spectrometry	110
4.6.	Summary	110
4.7.	References	111
5.	Improvement of BSCF performance by B site dopants	115
5.1.	Introduction	115
5.2.	Results and discussion	116
5.2.1.	Structural characterization	116
5.2.1.1.	X-Ray diffraction.....	116
5.2.1.2.	Thermogravimetric analysis in CO ₂ atmosphere	118
5.2.1.3.	Total DC electrical conductivity	120
5.2.2.	Symmetrical cells characterization	121
5.2.2.1.	Electrode microstructure	121
5.2.2.2.	Polarization resistance	123
5.2.2.2.1.	Operation temperature influence	123
5.2.2.2.2.	Oxygen partial pressure influence on the cell performance	131
5.2.2.2.3.	CO ₂ containing atmosphere influence on the cell performance	134

5.2.3.	Fuel cell characterization	136
5.2.3.1.	Influence of the operation temperature.....	137
5.2.3.2.	Influence of pO_2 , pH_2 and pH_2O in the fuel cell performance 139	
5.2.3.3.	Total flow influence on the fuel cell performance.....	143
5.2.3.4.	Stability on the cell performance.....	144
5.2.4.	Electrolyzer characterization	146
5.2.4.1.	Steam electrolysis	146
5.2.4.2.	Co-electrolysis	150
5.2.4.3.	Electrolysis and co-electrolysis comparison	157
5.3.	Conclusions	158
5.4.	References	159
6.	$La_{2-x}A_xNi_{1-y}B_yO_{4+\delta}$ electrodes for ionic electrolytes.....	165
6.1.	Introduction	165
6.2.	Results and discussion	166
6.2.1.	Characterization of $La_{2-x}A_xNi_{1-y}B_yO_{4+\delta}$ compounds	166
6.2.1.1.	Cell parameters and δ determination.....	166
6.2.1.2.	DC total conductivity measurement	173
6.2.1.3.	Electrochemical impedance spectroscopy measurements 176	
6.2.1.3.1.	Temperature influence on EIS results.....	176
6.2.1.3.2.	Co-doped influence on EIS results	178
6.2.1.3.3.	LPNCO temperature influence on EIS results	181
6.2.1.3.4.	LPNCO pO_2 influence on EIS results	183
6.2.2.	Fully-assembled cell	185
6.2.2.1.	SEM micrographs characterization	185
6.2.2.2.	Fuel cell mode performance	186

6.2.2.3.	Electrolysis mode	188
6.2.2.4.	Co-electrolysis mode.....	189
6.2.2.5.	Thermodynamic simulation of co-electrolysis	191
6.3.	Conclusions	192
6.4.	References	193
7.	LSM electrode improvement strategies	199
7.1.	Introduction	199
7.2.	Results and discussion	199
7.2.1.	Symmetrical cells characterization	200
7.2.1.1.	Phases compatibility	200
7.2.1.2.	XRD and FE-SEM characterization.....	201
7.2.1.3.	Polarization resistance determination.....	204
7.2.1.3.1.	LSM and LSM-GDC cathode electrochemical performance 207	
7.2.1.3.2.	Stability of the infiltrated cathodes	208
7.2.1.3.3.	Influence of oxygen partial pressure	211
7.2.2.	Fully-assembled cell performance	213
7.2.2.1.	Fuel cell mode performance	213
7.2.2.2.	Electrolysis mode performance	215
7.3.	Conclusions	217
7.4.	References	218
8.	La_{2-x}A_xNi_{1-y}B_yO_{4-δ} electrodes for protonic electrolytes.....	223
8.1.	Introduction	223
8.2.	Results and discussion	224
8.2.1.	Electrodes characterization	224
8.2.1.1.	Reactivity test.....	224
8.2.1.2.	Electrochemical characterization.....	225

8.2.1.2.1.	Influence of operation temperature.....	225
8.2.1.3.	Influence of electrode sintering temperature	233
8.2.1.3.1.	Influence of composite electrodes	235
8.2.1.3.2.	Dry conditions and isotopic effect influence	237
8.2.1.3.2.1.	$\text{La}_2\text{NiO}_{4+\delta}$	237
8.2.1.3.2.2.	$\text{La}_{1.5}\text{Pr}_{0.5}\text{Ni}_{0.8}\text{Co}_{0.2}\text{O}_{4+\delta}$	240
8.2.1.3.2.3.	$\text{La}_{1.5}\text{Pr}_{0.5}\text{NiO}_{4+\delta}$	242
8.2.1.3.2.4.	$\text{Nd}_2\text{NiO}_{4+\delta}$	243
8.2.1.3.2.5.	General remarks	244
8.3.	Conclusions	248
8.4.	References	248
9.	Cer-cer cathodes for PC-SOFC.....	253
9.1.	Introduction	253
9.2.	Results and discussion	255
9.2.1.	Compatibility test.....	255
9.2.2.	Electrochemical characterization.....	256
9.2.2.1.	Cathode sintering temperature influence	256
9.2.2.1.1.	Microstructure characterization	256
9.2.2.1.2.	Electrochemical analysis of cer-cer cathodes sintering temperature.....	259
9.2.2.2.	Influence of volume ratio on the electrode performance 263	
9.2.2.3.	LSM/LWO 60/40 % v/v electrode limiting mechanisms ..	266
9.2.2.4.	Infiltration of the electrode composite.....	269
9.2.2.4.1.	XRD and FESEM characterization.....	271
9.2.2.4.2.	Electrochemical characterization	272
9.2.2.4.3.	Stability of SDC infiltrated sample	276

9.2.2.5.	Fully-assembled fuel cell	278
9.3.	Conclusions	281
9.4.	References	282
10.	CsH₂PO₄-based electrochemical cell.....	287
10.1.	Introduction	287
10.2.	Results and discussion	289
10.2.1.	Structural characterization	289
10.2.1.1.	XRD characterization.....	289
10.2.1.2.	Conductivity characterization	290
10.2.1.2.1.	Influence of temperature	290
10.2.1.2.2.	Influence of water partial pressure	291
10.2.2.	Electrochemical characterization of symmetrical cells.....	293
10.2.2.1.	Symmetrical cell configuration	293
10.2.2.1.1.	Influence of system pressure on the cell operation ...	295
10.2.2.1.2.	Influence of steam content on the cell operation	297
10.2.2.1.3.	Influence of temperature on the cell operation	299
10.2.3.	Electrochemical characterization in asymmetrical cells	303
10.2.3.1.	Electrolyte supported cell	303
10.2.3.1.1.	Fuel cell mode	303
10.2.3.1.2.	Electrolysis mode	306
10.2.3.2.	Steel supported cell	310
10.2.3.2.1.	Fuel cell mode	311
10.2.3.2.2.	Electrolysis mode	313
10.2.3.2.3.	FIB-SEM characterization.....	316
10.2.4.	Tailoring the mechanical properties of CDP electrolyte	317
10.2.4.1.	SEM and XRD electrolyte characterization	319
10.2.4.2.	Electrochemical characterization of the electrolyte.....	320

10.2.5.	Active electrode support –Ni sponge.....	321
10.2.5.1.	SEM and XRD electrode characterization	321
10.2.5.2.	Electrochemical characterization.....	324
10.2.5.2.1.	Electrodes characterization by symmetrical cell configuration.....	324
10.2.5.2.2.	Fuel cell characterization	336
10.3.	Conclusions	338
10.4.	References	339
11.	General remarks.....	343
12.	Acronyms.....	349
13.	Figures list.....	355
14.	Tables list.....	371
15.	Scientific contribution	373

1

Context and scope of the thesis

1. Context and scope of the thesis

The energy demand has been raised during the last years in more than 50 % since 1990. As the society wants to develop and grow, the energetic economy becomes a limiting factor. Energetic economy is involved in the economy through so many sectors: industry, transport, agriculture, building heat and cooling, etc. However, the instability of the price of energy makes compulsory to reconsider which are the best energy systems in terms of cost and safety.

Now, fossil fuel accounts 87 % of the primary energy supply, being the oil demand around 33% and used predominantly in petrochemical production and transportation, whereas coal is employed for electricity production and in some industries. For instance, during many generations, coal was one of most used source of energy, with more than 40 % of global electricity demand. However, the use of coal has been eroded in last years due to the big contribution to the total greenhouse gas emission (73%) in the power sector. The use of this type of energy source during last years has had detrimental impact in the greenhouse gas generation, with the consequence of climate change and global warming. Thus, it is mandatory to redirect energy sources in order to reduce the fossil fuel power generation, taking into account the air pollution and the use of renewable energies.

The renewable energies sources supply has been growing in the last decades, particularly wind and solar power energy, becoming as important alternative of fossil fuels. These technologies have existed during years, but only hydropower was used at large scale [1]. The fast reduction of cost has enabled the renewable energies to become competitive with fossil fuels. The use of renewable energy would permit to reduce the fossil fuel dependency and the impact of their prices instability. Furthermore, apart from the biomass, the renewable energy has a negligible air pollution impact with few or no CO₂ emissions.

Nevertheless, energy production by renewables, as wind, solar, hydro or geothermal, is dependent on fluctuating environmental conditions. Consequently, when some surplus is generated, they should be combined with some energy storage device.

H₂ with a low CO₂ foot print could play an important role in the green house mitigation and allow reducing the temperature rise. H₂ is a flexible energy carrier, which can be used directly to produce energy (fuel cells) or be easily transformed in other forms of energy for different end applications (Figure 1.1). Furthermore, the hydrogen can be stored in different ways depending on its final application, for instance, it can be stored for long periods of time and integrated in power generation system from variable renewable energy. Although hydrogen is present in the nature, energy is required for pure hydrogen production.

H₂ production can be carried out from different methods, the most conventional processes coming from fossil fuels: steam reforming, coal gasification or the partial oxidation of some heavy hydrocarbons. On the other hand CO₂-neutral processes are being studied based on reforming, pyrolyzing and fermentation of biomass, but efficiencies are not good enough for decreasing the time-to-market. H₂ produced from water is an efficient, green and commercial technology, where the used techniques include solar thermochemical or photocatalytic water splitting and electrical water electrolysis.

In addition, fuel cells have grown interest in the market, due to their high efficiency, noiseless and the ability to work with H₂. Under these premises, it seems that the generation of H₂ by an efficient electrolysis system with the use of a fuel cell or sub product (fuels, chemicals, etc.) will be a green alternative for the energy production. Efforts in the present thesis were direct towards the optimization of electrochemistry devices able to produces energy and products as H₂, CO and CH₄ that could be integrated in system shown in Figure 1.1.

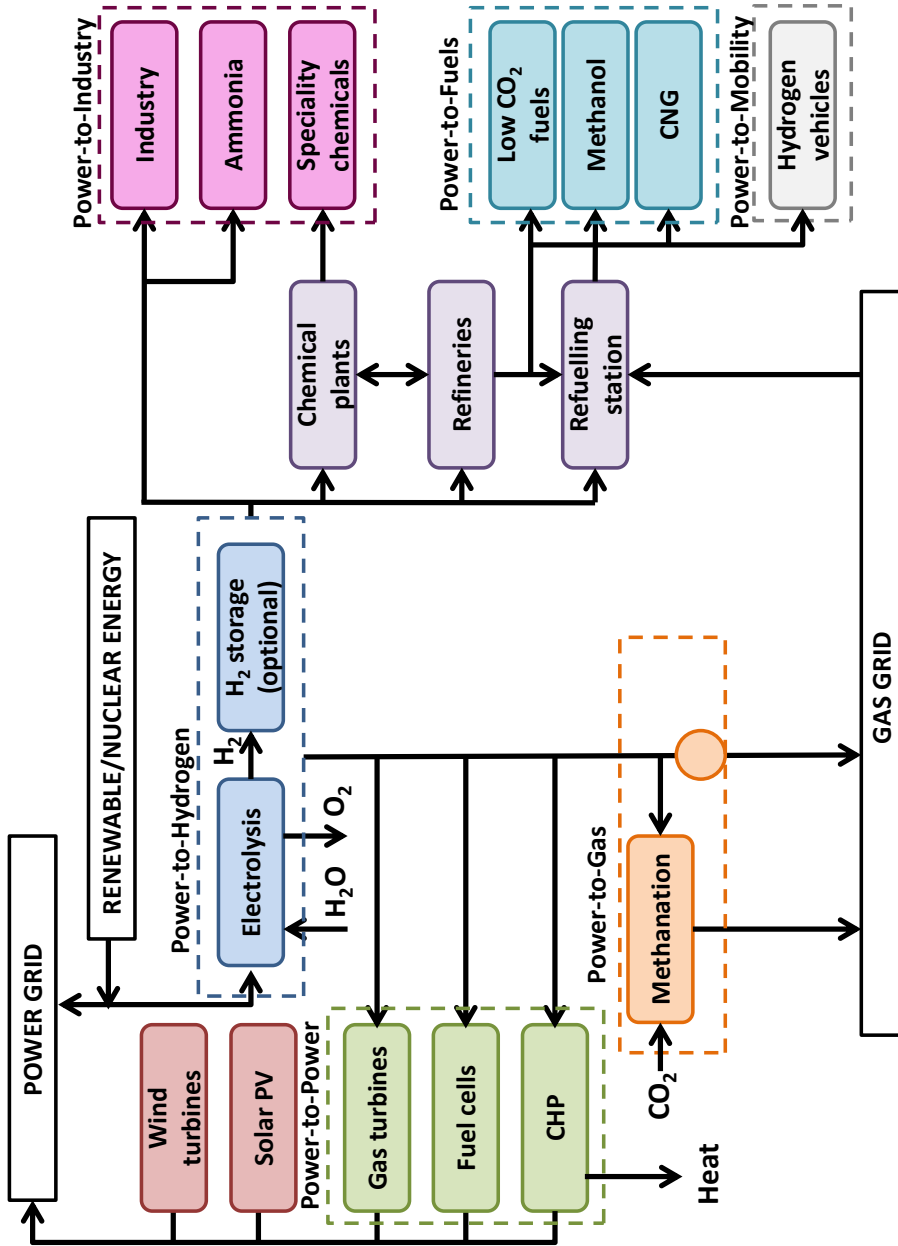


Figure 1.1: Hydrogen layout of green energy, gas, transport and industrial sector applications [2].

This thesis has been focused on the development of new materials for their application and characterization for electrochemical cells. The thesis can be divided in two main groups; cells based in proton conductors and ionic conductors. In addition, the cells based on proton conductors can be subdivided into high and low operation temperature groups. Whereas the high operation temperature materials are solid oxides, the group of low temperature materials consists on solid acids. The optimal operation temperature of the cell will depend on the properties of each material of the cell components. Those materials have been employed in different type of cells; fuel cells, electrolyzers and co-electrolyzers.

The optimization of the different components of cells has been carried out in this thesis, but the main efforts have been focused on tailoring the electrodes performance.

The main objectives of this thesis can be divided in two:

- 1- Development of fuel cells that can operate properly in the range of 200-400 °C or 400-800°C. For that purpose, it was necessary to study in fundamental and experimental level, the electrolytic materials and new electrocatalyst suitable for that range of temperature.
- 2- Development of novel proton/ion conductor devices that allow the production of fuels or other chemical, from electric power and starting compounds such water and CO₂. The operating range of these devices varies between 200 °C and temperatures up to 800°C, depending on the type of catalytic reaction and stability of the final product.

The sub-objectives of the thesis can be listed as below:

- 1- Improvement of the performance and stability of Ba_{0.5}Sr_{0.5}Co_{0.8}Fe_{0.2}O_{3-δ} perovskite by doping with a 3% in B position (ABO_{3-δ}) used as electrode in a fuel and electrolyzer cells.
- 2- Study of the influence of different dopants, by doping in La and Ni position, on the electrochemical properties of La₂NiO_{4+δ} compound, pertaining to the Ruddlesden-Popper series. Testing of the materials synthesized as fuel and electrolyzer cells.

- 3- Enhancement of the electrochemical performance of the $\text{La}_{0.8}\text{Sr}_{0.2}\text{MnO}_{3-\delta}$ -based electrodes by developing new electrodes configurations: composite electrodes and nanocatalyst infiltration. Application of the electrodes designed in real operation conditions as fuel and electrolyzer cells.
- 4- Optimization of ceramic-ceramic electrodes for proton conducting electrolytes. Study of the electrode configuration (volume ratio of phases in the electrode and nanoparticles infiltration) and sintering temperature influence.
- 5- Characterization of $\text{La}_2\text{NiO}_{4+\delta}$ -based compounds as cathodes for proton conductor fuel cells.
- 6- Development of new type of fuel cells and electrolyzers based on acid salts able to work at high pressures (up to 30 bar) and moderate temperatures (< 300 °C).

To achieve these objectives was necessary to develop different devices and certain techniques:

- 1- Adaptation of the high temperature fuel cell set-up for electrolysis and co-electrolysis mode.
- 2- Design and development of the experimental set-up for measuring electrochemical cells at moderate temperature (< 300 °C). This set up should enable to work with moderate temperatures, high pressures and high contents of water. Furthermore, the device must allow the possibility to split the set up in two independents chamber (cathode and anode) and perform electrochemical measurements (electrical contacts).
- 3- Optimization of the method for porous electrodes fabrication and the infiltration technique for the selected electrodes.

1.1. References

[1] T.g.c.o.t.e.a. climate, The New Climate Economy.

2

Resumen/Summary/Resum

2. Resumen/Summary/Resum

2.1. Resumen

En la presente tesis doctoral se han desarrollado materiales para su uso en celdas electroquímicas. Las celdas electroquímicas estudiadas, se podrían separar en dos grandes grupos: materiales de óxido sólido y sales ácidas.

En el primer grupo, se optimizaron materiales para su uso como electrodos en pilas de combustible y electrolizadores, basados en electrolitos con conducción puramente iónica. Dentro de este grupo, se comprobó la influencia de dopar la perovskita $\text{Ba}_{0.5}\text{Sr}_{0.5}\text{Co}_{0.8}\text{Fe}_{0.2}\text{O}_{3-\delta}$, con un 3% de Y, Zr y Sc en la posición B ($\text{ABO}_{3-\delta}$). Esta optimización llevó a la reducción de la resistencia de polarización así como a una mejora de la estabilidad con el tiempo. Así mismo, se determinaron los mecanismos limitantes en la reacción de reducción de oxígeno, y se comprobó la influencia de la presencia de CO_2 en condiciones de operación.

El $\text{La}_2\text{NiO}_{4+\delta}$ perteneciente a la serie de Ruddlesden-Popper, es un conductor mixto de iones oxígeno y electrones. Éste, fue dopado tanto en la posición del La (con Nd y Pr) como en la posición del Ni (con Co). Los dopantes introducidos además de producir cambios estructurales, provocaron mejoras en el rendimiento de la celda, reduciendo para alguno de ellos, como el $\text{La}_{1.5}\text{Pr}_{0.5}\text{Ni}_{0.8}\text{Co}_{0.2}\text{O}_{4+\delta}$, en casi un orden de magnitud la resistencia de polarización del electrodo de referencia ($\text{La}_2\text{NiO}_{4+\delta}$).

De la misma manera, se optimizaron las propiedades del electrodo basado en el conductor electrónico puro $\text{La}_{0.8}\text{Sr}_{0.2}\text{MnO}_{3-\delta}$ (LSM). La adición de una segunda fase, con conductividad iónica, permitió aumentar los puntos triples (TPB) en los que la reacción de reducción de oxígeno tiene lugar y reducir la resistencia de polarización. Con el fin de mejorar la reacción de reducción de oxígeno, se estudió la adición de nanocatalizadores mediante la técnica de infiltración. Los diferentes óxidos infiltrados produjeron el cambio de las propiedades electroquímicas del electrodo, siendo el óxido de praseodimio el catalizador que consiguió disminuir en dos órdenes de magnitud la resistencia de polarización del composite no infiltrado. De la misma manera, la mejora de la eficiencia del electrodo infiltrado con Pr, mejoró los resultados de la celda

electroquímica trabajando como pila (mayores densidades de potencia) y como electrolizador (menores voltajes).

En lo que respecta a los materiales seleccionados para su uso como electrodos en electrolitos con conductividad protónica, se optimizó la eficiencia del cátodo basado en LSM, mediante el uso de una segunda fase conductora protónica ($\text{La}_{5.5}\text{WO}_{12.6}$) y variando la temperatura de sinterización del electrodo. Finalmente, se mejoró la actividad catalítica mediante la infiltración de nanopartículas de ceria dopada con samario, produciendo mayores densidades de corriente de la pila de combustible.

Los materiales pertenecientes a la serie de Ruddlesden-Popper y usados para cátodos en pilas iónicas, fueron empleados también para cátodos en pilas protónicas. Después de comprobar que el material electrolítico (LWO) era compatible con los compuestos de la serie de Ruddlesden-Popper, se estudió la influencia de la temperatura de sinterización de los electrodos en el rendimiento, así como de la composición de la atmosfera de aire (seca, H_2O y D_2O).

Finalmente, se diseñó y optimizó las celdas electroquímicas basadas en sales ácidas (CsH_2PO_4). En este sentido, se estudiaron diferentes configuraciones de celda, que permitieran obtener un electrolito denso con el menor espesor posible y unos electrodos activos a la reacción de reducción/oxidación de hidrógeno. Se consiguió reducir el espesor del electrolito soportando la celda en discos de acero y níquel porosos. Se añadió una resina tipo epoxi al material electrolítico para aumentar sus propiedades mecánicas. De la misma manera, se cambió la configuración de los electrodos pasando por conductores electrónicos puros a electrodos compuestos por conductores protónicos y electrónicos. Así mismo, se demostró el uso de cobre como catalizador en la celda electroquímica, en lugar del platino, para presiones de operación elevadas. Las celdas desarrolladas fueron capaces de trabajar con altas presiones en modo pila de combustible y electrolizador con altos contenidos de vapor de agua.

2.2. Summary

In this thesis different materials have been developed to use them in electrochemical cells. The electrochemical cells studied can be divided into two material big groups: solids oxides and acid salts materials.

In the first group, materials to use them in electrodes for fuel cells an electrolyzer based on oxygen ion conductor electrolytes were optimized. Pertaining to this group, the influence of doping the $\text{Ba}_{0.5}\text{Sr}_{0.5}\text{Co}_{0.8}\text{Fe}_{0.2}\text{O}_{3-\delta}$ perovskite with 3% of Y, Zr and Sc in B position ($\text{ABO}_{3-\delta}$) was checked. That optimization could reduce the polarization resistance of electrodes and improve the stability with time. Additionally, the limiting mechanisms in the oxygen reduction reaction were determined, and the influence of CO_2 containing atmospheres was checked.

$\text{La}_2\text{NiO}_{4+\delta}$, pertaining to the Ruddlesden-Popper serie, is a mixed conductor of electron and oxygen ions. This compound was doped in La position (with Nd and Pr) and in Ni position (with Co). The dopants introduced were able to produce structural change and improve the cell performance, reducing in more than one order of magnitude the $\text{La}_{1.5}\text{Pr}_{0.5}\text{Ni}_{0.8}\text{Co}_{0.2}\text{O}_{4+\delta}$ polarization resistance respect to the reference material ($\text{La}_2\text{NiO}_{4+\delta}$).

In addition, the properties of an electrode based on the pure electronic conductor, $\text{La}_{0.8}\text{Sr}_{0.2}\text{MnO}_{3-\delta}$ (LSM), were optimized. The triple phase boundary was enlarged by the addition of a second phase with ionic conductivity. That strategy made possible to reduce the electrode polarization resistance. In order to improve the oxygen reduction reaction, the addition of different catalysts by infiltration was studied. The different infiltrated oxides changed the electrochemistry properties, being the praseodymium oxide the catalyst which made possible a reduction in two orders of magnitude the electrode polarization resistance respects to the composite without infiltration. Furthermore, the efficiency of the cell working in fuel cell and electrolyzer mode was improved.

Concerning the materials selected to use as electrodes on proton conductor electrolytes, the efficiency of electrodes based on LSM was optimized by using a second phase with protonic conductivity ($\text{La}_{5.5}\text{WO}_{12-\delta}$) and varying the sintering temperature of the electrode. Finally, the catalytic activity of the cell

was boosted by infiltrating samaria doped ceria nanoparticles, achieving higher power densities for the fuel cell.

The materials pertaining to the Ruddlesden-Popper series and studied for ionic conductor electrolytes were also used for cathodes in proton conductor fuel cells. After checking the compatibility with the electrolyte material, the influence of different electrode sintering temperatures and air containing atmospheres (dry, H_2O y D_2O) on the cathode performance was studied.

Finally, the electrochemical cells based on acid salts (CsH_2PO_4) were designed and optimized. In that way, different cell configurations were studied, enabling to obtain thin and dense electrolytes and active electrodes for the hydrogen reduction/oxidation reactions. The thickness of the electrolyte was reduced by using steel and nickel porous supports. Furthermore, an epoxy resin type was added to the electrolyte material to enhance the mechanical properties. The electrodes configuration was modified from pure electronic conductors to composite electrodes. Moreover, copper was selected as an alternative of the expensive platinum working at high operation pressures. The cells developed were able to work with high pressures and with high content of water steam in fuel cell and electrolyzer modes.

2.3. Resum

En la present tesis doctoral es van desenvolupar materials per al seu ús en cel·les electroquímiques. Les cel·les electroquímiques estudiades poden ser dividides en dos grans grups: materials d'òxid sòlid i sals àcides.

En el primer grup, es van optimitzar materials per al seu ús com a elèctrodes en piles de combustible i electrolitzadors, basats en electròlits amb conducció purament iònica. Dins d'este grup, es va comprovar la influència de dopar la perovskita $\text{Ba}_{0.5}\text{Sr}_{0.5}\text{Co}_{0.8}\text{Fe}_{0.2}\text{O}_{3-\delta}$ amb un 3% de Y, Zr i Sc en la posició B ($\text{ABO}_{3-\delta}$). Esta optimització va portar a la reducció de la resistència de polarització així com a una millora de l'estabilitat amb el temps. Així mateix, es van determinar els mecanismes limitants en la reacció de reducció d'oxigen, i es va comprovar la influència de la presència de CO_2 en condicions d'operació.

El $\text{La}_2\text{NiO}_{4+\delta}$ pertanyent a la sèrie de Ruddlesden-Popper, és un conductor mixt d'ions oxigen i electrons. Este, va ser dopat tant en la posició del La (amb Nd i Pr) com en la posició del Ni (amb Co). Els dopants introduïts a més de produir canvis estructurals, van provocar millores en el rendiment de la cel·la, reduint per a algun d'ells, com el $\text{La}_{1.5}\text{Pr}_{0.5}\text{Ni}_{0.8}\text{Co}_{0.2}\text{O}_{4+\delta}$, en quasi un ordre de magnitud la resistència de polarització de l'elèctrode de referència ($\text{La}_2\text{NiO}_{4+\delta}$).

De la mateixa manera, es van optimitzar les propietats de l'elèctrode basat en el conductor electrònic pur $\text{La}_{0.8}\text{Sr}_{0.2}\text{MnO}_{3-\delta}$ (LSM). L'addició d'una segona fase, amb conductivitat iònica, va permetre augmentar els punts triples (TPB), en els que la reacció de reducció d'oxigen té lloc, i reduir la resistència de polarització. A fi de millorar la reacció de reducció d'oxigen, es va estudiar l'adició de nanocatalitzadors per mitjà de la tècnica d'infiltració. Els diferents òxids infiltrats van produir el canvi de les propietats electroquímiques de l'elèctrode, sent l'òxid de praseodimi el catalitzador que va aconseguir disminuir en dos ordres de magnitud la resistència de polarització del composite no infiltrat. De la mateixa manera, la millora de l'eficiència de l'elèctrode infiltrat amb Pr, va millorar els resultats de la cel·la electroquímica treballant com a pila (majors densitats de potència) i com a electrolitzador (menors voltatges).

Pel que fa als materials seleccionats per al seu ús com a elèctrodes en electròlits amb conductivitat protònica, es va optimitzar l'eficiència del càtode basat en LSM, per mitjà de l'ús d'una segona fase conductora protònica

($\text{La}_{5.5}\text{WO}_{12.6}$) i variant la temperatura de sinterització de l'elèctrode. Finalment, es va millorar l'activitat catalítica mitjançant la infiltració de nanopartícules de ceria dopada amb samari, produint majors densitats de corrent de la pila de combustible.

Els materials pertanyents a la sèrie de Ruddlesden-Popper i usats per a càtodes en piles iòniques, van ser emprats també per a càtodes en piles protòniques. Després de comprovar que el material electrolític (LWO) era compatible amb els compostos de la sèrie de Ruddlesden-Popper, es va estudiar la influència de la temperatura de sinterització dels elèctrodes en el rendiment, així com de la composició de l'atmosfera d'aire (seca, H_2O i D_2O).

Finalment, es van dissenyar i optimitzar les cel·les electroquímiques basades en sals àcides (CsH_2PO_4). En este sentit, es van estudiar diferents configuracions de cel·la, que permeteren obtenir un electròlit dens amb el menor espessor possible i uns elèctrodes actius a la reacció de reducció/oxidació d'hidrogen.

Es va aconseguir reduir l'espessor de l'electròlit suportant la cel·la en discos d'acer i níquel porosos. Es va afegir una resina tipus epoxi al material electrolític per a augmentar les seues propietats mecàniques. De la mateixa manera, es va canviar la configuració dels elèctrodes passant per conductors electrònics purs a elèctrodes compostos per conductors protònics i electrònics. Així mateix, es va demostrar l'ús de coure com a catalitzador en la cel·la electroquímica, en lloc del platí, per a pressions d'operació elevades. Les cel·les desenvolupades arribaren a treballar a altes pressions amb alts continguts de vapor d'aigua en mode pila de combustible i electrolitzador.

3

Introduction

3. Introduction

A brief introduction will be performed in order to understand the technologies studied and the devices developed in this thesis. Furthermore, the materials used and the characteristics of those types of materials will be described in the *Introduction chapter*.

3.1. Technologies

As has been stated in the *Context and Scope of the thesis*, the selection of green technologies is an important factor to work with zero emissions and avoid the global warming. Regarding the hydrogen technologies presented in Figure 1.1, this thesis will focus on three of them: Power-to-Power, Power-to-Hydrogen and Power-to-Gas, and will be described in the following points.

Moreover, ceramics and solid acids could play an important role in the mentioned technologies and have been integrated on them as will be discussed in the next chapters.

3.1.1. Power-to-Power: fuel cells

Fuel cells are devices that convert chemical energy into electrical energy directly, for that reason the efficiency is higher than the obtained by conventional combustion systems. In most of the fuel cells, the reactants are hydrogen and oxygen and when they react, a flux of electrons, heat and steam are generated, having a low environmental impact. Unlike batteries the fuel and oxidant must to be supplied continuously in order to have a continuous operation.

The unit cell of a fuel cell consists of an electrolyte layer in contact with an anode and cathode on either side. The fuel is feed in the anode side (negative electrode), where the oxidation of the fuel is produced. Nevertheless, the oxidant is introduced in the cathode side, producing the reduction of the oxidant. The system is closed by an external circuit where there is an electron flux, since the electrolyte is an electrical insulating material and only allows the selected transport of ions.

3.1.1.1. Types of fuel cells

	PEMFC	AFC	PAFC	DMFC	MCFC	SOFC
Primary fuel	H ₂	H ₂	H ₂	CH ₃ OH	H ₂ , CO, CH ₄ ...	H ₂ , CO, CH ₄ ...
Electrolyte	Polymeric membrane	KOH	H ₃ PO ₄	Polymeric membrane	Li ₂ CO ₃ K ₂ CO ₃	Ceramics
Operation temperature	65-85 °C	65-220 °C	200 °C	80 °C	650 °C	600-1000 °C
Charge carrier	H ⁺	OH ⁻	H ⁺	H ⁺	CO ₃ ²⁻	O ²⁻
Ext. reforming	Yes	Yes	Yes	No	No	No
Anode	Pt/C	Ni Raney	Pt/C	Pt/Ru/C	Ni	Ni-ZrO ₂
Cathode	Pt/C	Ag	Pt/C	Pt/C Mo ₂ Ru ₃ S ₅	NiO	LaMnO ₃ /Sr
Power density	3.8-6.5 kW/m ³	1 kW/m ³	0.8-1.9 kW/m ³	0.6 kW/m ³	1.5-2.6 kW/m ³	0.1-1.5 kW/m ³
Efficiency	35-45 %	35-55 %	40 %	30-40 %	>50 %	>50 %
Application	Portable, Back-up, stationary, transport	Military, aerospace, stationary	Combined heat and power production	Portable	Combined heat and power production, stationary	Combined heat and power production, stationary
Advantages	Low operation temperature, quick startup and solid electrolyte.	Low component costs. Quick startup.	Low temperature. High tolerance to pollutants.	High energy density of CH ₃ OH and low operation temperature.	High efficiency, fuel flexibility and variety of catalysts.	Fuel flexibility, high tolerance fuel impurities and solid components.
Drawbacks	Expensive catalyst, poisoning of cell (CO, H ₂ S), H ₂ ultrapure is required.	Sensitivity to fuel impurities; CO, CH ₄ , CO ₂ , H ₂ S. Difficulties in the KOH management.	Expensive catalysts. Slow startup and corrosive electrolyte.	Lower power density.	Slow startup, corrosion of cell components and intolerant to sulfur.	High cost, sensitivity to S and slow startup.

Table 3.1: Comparison of different fuel cells [1-4].

The fuel cells are classified as function of the electrolyte material, fuels and operation temperature. The group of low temperature is composed from Polymer Electrolyte Membrane Fuel Cell (PEMFC), Alkaline Fuel Cell (AFC), Direct Methanol Fuel Cell (DMFC) and Phosphoric Acid Fuel Cell (PAFC). In the group of high temperature are included Molten Carbonate Fuel Cell (MCFC) and Solid Oxide Fuel Cell (SOFC). Table 3.1 summarizes the main characteristic of each type of fuel cell, as the applications, advantages and drawbacks.

A schematic diagram of the different cells operation is described below:

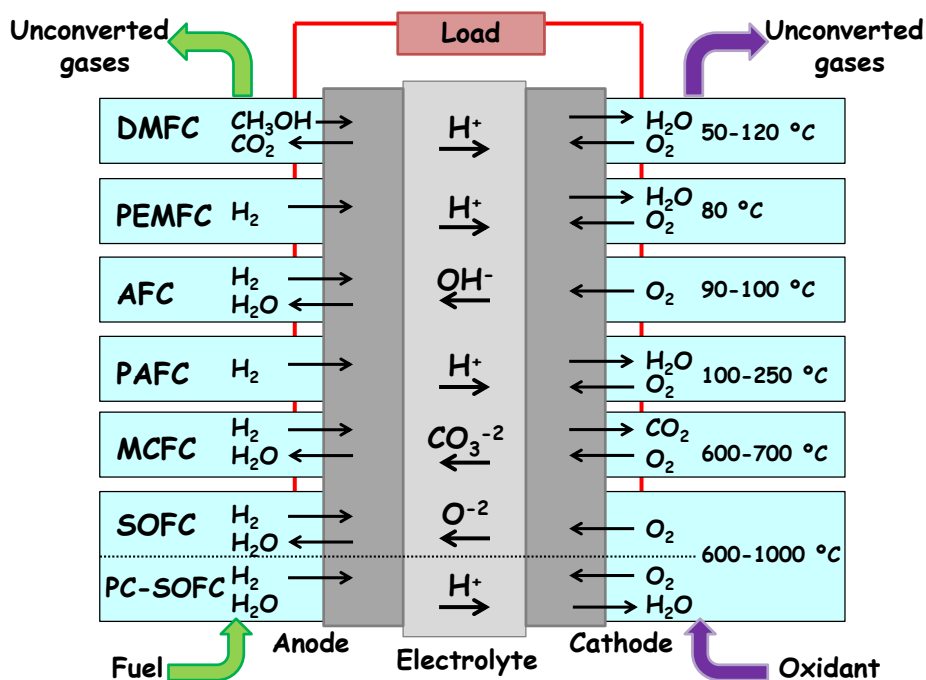


Figure 3.1: Schematic diagram of fuel cell operation.

Some of the advantages of this type of devices are the high efficiency, the low environmental impact, fuel flexibility, and modularity of the system and size flexibility.

- **High efficiency**, fuel cells have a high efficiency (35-60%) since the electric energy is generated directly from chemical energy (fuels). The

efficiency of a fuel cell can be increased if the heat generated is used in the same process, *i.e.*, cogeneration.

- **Low environmental impact**, fuel cells are able to work with common fuels as source of energy production with a low environmental impact. The emissions levels of fuel cells are several orders of magnitude lower than the common electricity production devices. The production of NO_x and SO_x compounds are negligible in this type of devices.
- **Fuel flexibility**, some types of fuel cells are able to work with different fuels. Furthermore, high temperature fuel cells can do internal reforming avoiding expensive processes.
- **Modularity**, the size of a cell can be increased or reduced, since the system efficiency is almost size independent.

The maximum electrical work in a fuel cell operating at constant pressure and temperature is given by the Gibbs free energy:

$$\Delta G = \Delta H - T\Delta S \quad (3.1)$$

$$W_{el} = \Delta G = -nFE \quad (3.2)$$

Where ΔH and ΔS are the enthalpy and entropy change, respectively. In equation (3.2), n are the electrons that participate in the reaction and F is the Faraday's constant, and E is the ideal potential of the cell.

By using the correlation (3.1) of the Gibbs free energy it can be calculated the potential of the cells in non-equilibrium conditions, that it is dependent of the temperature and electrochemistry reactions:

$$E = E^0 + \frac{RT}{nF} \sum_{react-prod} \ln(a_j) \quad (3.3)$$

The equation (3.3) is the Nernst equation and usually uses the activity of the products and reactants, by depending of reaction medium; it can be expressed as function of the partial pressure or concentration:

$$Gas \quad a_j = \gamma_j \frac{p^i}{p^0} \quad (3.4)$$

$$\text{Solute} \quad a_j = \gamma_j \frac{C_j}{C^0} \quad (3.5)$$

Where γ_j is the activity coefficient of a j substance (gas or solute).

When there is no lost in the fuel cell efficiency or when the cell is in equilibrium with not demand of current, all Gibbs free energy is transformed into electric energy. At this point, the open circuit voltage (OCV) of the cell can be calculated.

In the present thesis, fuel cells with solid components have been selected for the energy production. These types of cells present some advantages, being the most important the component management, since there are not liquid electrolytes. The two types or electrochemical devices studied are the cells working at high temperatures (600-1000 °C) made with solid oxides materials and low temperatures (250- 290 °C), with acid salts.

3.1.1.2. Solid oxide fuel cells

The solid oxide fuel cells have been selected for the energy production at high temperature. The most important advantages of this type of fuel cell are the high efficiency, being $\approx 80\%$ when the heat generated in the cells is used by a cogeneration system, and the multifuel capacity, since the high temperatures allow the internal reforming and some impurities in the inlet fuel. This type of fuel cell can be subdivided in two groups, in the first group (Solid Oxide Fuel Cell (SOFC)), the electrolyte is an ionic conductor, oxygen ions flow through the electrolyte from cathode to anode (Figure 3.2). In the second group (Proton Conductor Solid Oxide Fuel Cell (PC-SOFC)), protons flow across the electrolyte from the anode to cathode (Figure 3.3), as is represented in details below:

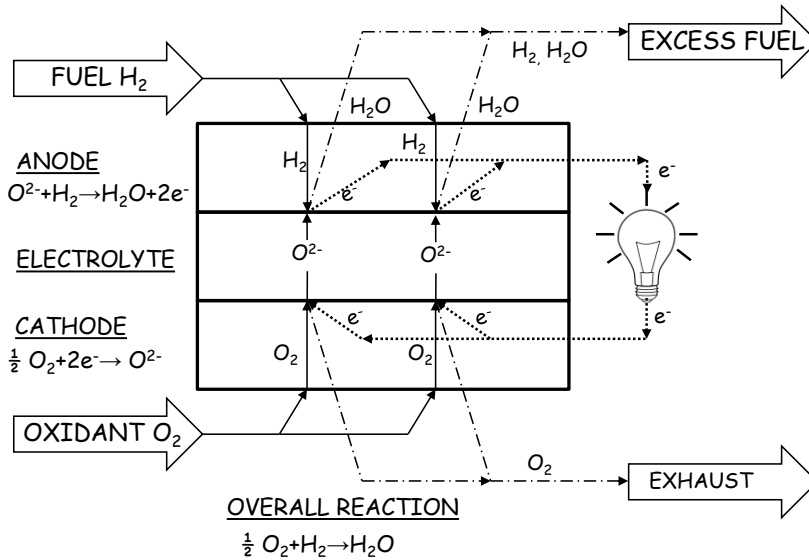


Figure 3.2: Schematic diagram of reactions in SOFCs based on oxygen ion conductors.

In the case of SOFC, oxygen is reduced in the cathode and the oxygen ions flow through the solid electrolyte and react in the anode to produce water. This reaction generates electrons that are transported in the external circuit to the cathode for the oxygen reduction. In the representation of Figure 3.2, it has been assumed that the electrodes are made of an electronic conductor, so the reactions of oxidation and reduction take place in the interface electrode and electrolyte, where electrons, gases and ions are in contact. This point is also called Triple Phase Boundary (TPB). Taking into account the overall reaction in the cell, the equation (3.3) can be written as:

$$E = E^0 + \frac{RT}{2F} \ln \frac{pO_2^{1/2} pH_2}{pH_2O} \quad (3.6)$$

On the other hand, Figure 3.3 is the schematic diagram of a solid oxide fuel cell with a proton conductor electrolyte (PC-SOFC). The hydrogen introduced in the anode is oxidized to protons generating electrons. Protons move along the electrolyte from anode to cathode, whereas electrons flow in the external circuit and react in the cathode to obtain water. Taking into account the overall reaction, the OCV of this type of fuel cell can be described with the

same equation that has been described above for ionic conductor electrolytes (Equation (3.6)).

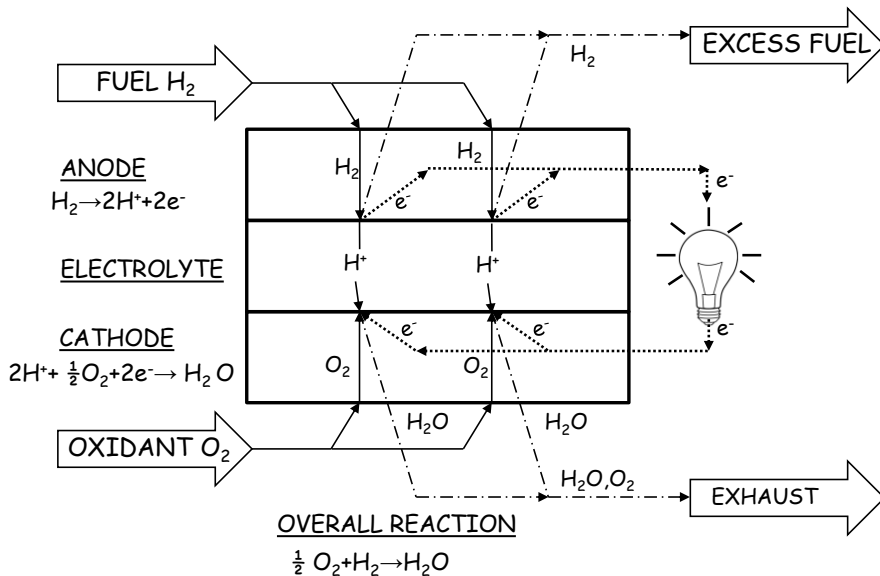


Figure 3.3: Schematic diagram of reactions in PC-SOFCs based on proton conductors.

3.1.1.3. Phosphate-based fuel cells

Regarding ionic conductors at low temperatures (200-400 °C) as electrolyte for fuel cells or electrolyzers, the most favorable materials are the proton conductor materials. In addition, the material selected should fulfil some requirements:

- High protonic conductivity.
- Negligible electronic conductivity.
- High stability.
- Good compatibility with the cell components.
- Low porosity.
- Easy to handle.
- Low cost.

In this group of low operation temperature, solid acid proton conductors, based on tetrahedral oxyanions, have been attracted interest in the last years because of their potential applications as electrolytes in fuel cells [5]. Those materials are good candidates since have a high proton transport, and include

some of the specifications mentioned above. The reactions and mechanisms that take place in this type of low temperature fuel cells coincide with the proton conductor fuel cell described before in Figure 3.3.

3.1.2. Power-to-Hydrogen: Electrolyzer

As has been explained above, H_2 can be generated by means of renewable sources, and used when this is required. One of the most efficient techniques for this H_2 generation is the electrolysis. The electrochemical reactions that take place in a steam electrolyzer are the inverse reactions to those take part in a fuel cell. Furthermore, the main components are maintain from the fuel cells, as electrolyte to separate both electrodes and external circuit to connect both electrodes, in this case to apply electric current to split water into oxygen and hydrogen.

The principal types of electrolyzers are the alkaline, acid, polymer electrolyte and solid oxide cells, the components are the same listed in Table 3.1, but the reactions in each electrode are different:

	Alkaline	Acid	Polymer Electrolyte	Solid oxide
Charge carrier	OH^-	H^+		O^{2-}
Cathode reaction	$2H_2O + 2e^- \rightarrow H_2 + 2OH^-$	$2H^+ + 2e^- \rightarrow H_2$		$H_2O + 2e^- \rightarrow H_2 + O^{2-}$ (SOEC) $2H^+ + 2e^- \rightarrow H_2$ (PC-SOEC)
Anode reaction	$2OH^- \rightarrow H_2O + \frac{1}{2}O_2 + 2e^-$	$H_2O \rightarrow \frac{1}{2}O_2 + 2H^+ + 2e^-$		$O^{2-} \rightarrow \frac{1}{2}O_2 + 2e^-$ (SOEC) $H_2O \rightarrow \frac{1}{2}O_2 + 2H^+ + 2e^-$ (PC-SOEC)

Table 3.2: Half-cell reactions of the different electrolysis cells.

The minimum energy supply required for the electrolysis process is equal to the Gibbs free energy (Equation (3.1)).

The voltage where cell power is equal to the heat generated by all internal chemical and electrochemical reactions is the thermo-neutral voltage (V_{Tn}). The thermo-neutral voltage is defined as:

$$V_{Tn} = \frac{\Delta H_f}{nF} = \frac{\Delta G_f}{nF} + \frac{T\Delta S_f}{nF} \quad (3.7)$$

Where ΔH_f is the formation enthalpy change, ΔG_f is the free energy change and ΔS_f is the formation entropy. Hence, if the cell voltage is equal to the thermo-neutral voltage all the produce Joule heat is used. Deviations from V_{Tn} , involves the external heating or cooling of the system, reducing the efficiency of the cell. If the cell operates below the thermo-neutral potential, heat must be supplied in order to maintain the operation temperature since the electric energy is lower than the enthalpy of reaction. Otherwise, when the cell is working above the thermo-neutral voltage is working in an exothermic mode. The energy consumption in the electrolysis process depends on the temperature and pressure of the cell.

3.1.2.1. Solid oxide electrolyzer

The following description of the electrolysis technology is going to be focus on the Solid Oxide Electrolyzers (SOEC), since is one of the main types of cells developed for the present thesis.

In a solid oxide electrolyzer, water acts as a reactant and is supplied in the cathode for oxygen ion conductor electrolytes and in the anode for electrolyzer working with proton conductor electrolytes (Figure 3.4 and Figure 3.5). In the first case, the hydrogen is produced in the same side that water is introduced; obtaining wet hydrogen in the cathode and dry oxygen in the anode. Nevertheless, in proton conductor solid oxide electrolyzer (PC-SOEC), the hydrogen is obtained in the opposite site where H_2O is fed, allowing a dry hydrogen flow in the cathode side. An important characteristic of electrolysis is that hydrogen and oxygen are simultaneously produced and separated.

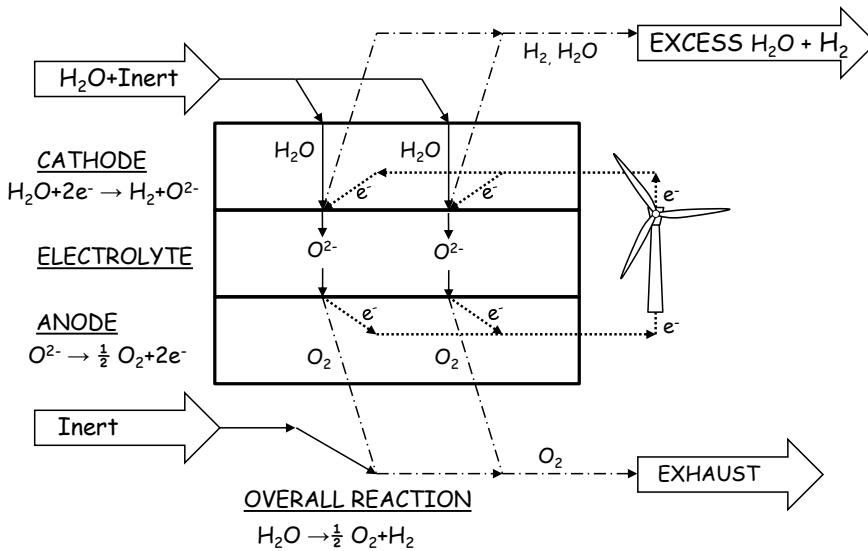


Figure 3.4: Schematic diagram of reactions in SOEC based on oxygen ion conductors.

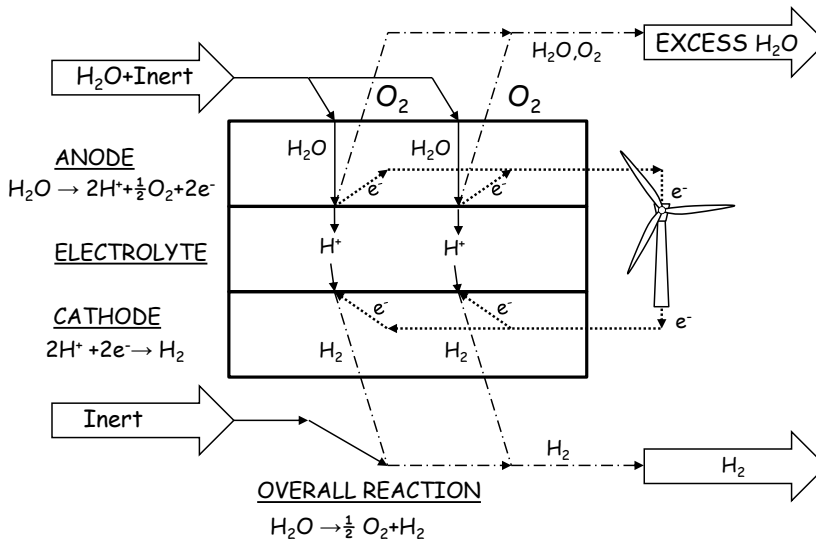


Figure 3.5: Schematic diagram of reactions in PC-SOEC based on proton conductors.

3.1.1.2. Phosphate-based electrolyzer

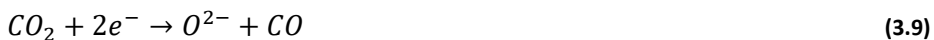
As has been explained above, the same device can be employed as fuel cell as an electrolyzer cell, but in the first case the energy is obtained by means of a fuel and in the last case, fuel (H_2) is obtained by applying current in the device.

This theory can be used for the phosphate-based fuel cells as well. In the group of solid acids, cesium dihydrogen phosphate (CsH_2PO_4) is one most common material used as electrolyte. Then, CsH_2PO_4 can be used as electrolyte in an electrolysis cell, and the reactions scheme is equal to the high temperature proton conductor electrolyzer (Figure 3.5).

3.1.3. Power-to-Gas

The catalytic conversion of CO_2 into usable fuels would positively impact the global carbon balance, reducing the greenhouse gases emissions. Hydrogen can play an important role in this process. H_2 produced by electrolysis can be used to generate fuel as methanol, methane, or other chemicals, with low greenhouse footprint (Figure 1.1). On the other hand, in the same electrolysis cell, and depending on the operation conditions, CO and CH_4 can be also generated. In this part, we are going to focus on the possible reactions and systems that can be coupled with the electrochemical production of H_2 .

Solid oxide electrolyzer cells are also capable to produce synthesis gas (CO and H_2) by means of high temperature electrolysis of H_2O and CO_2 . In the solid oxide electrolyzers (SOEC) H_2 and CO_2 flow in the fuel electrode (cathode), where the oxidant (usually air) is introduced in the anode. H_2O and CO_2 react in the electrode to form H_2 and CO , respectively:



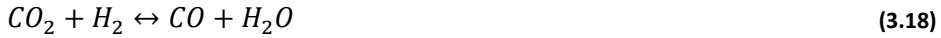
Then oxygen ions are transported across the electrolyte to the anode, to be oxidized:



Furthermore, when co-electrolysis of CO_2 and H_2 is taking place simultaneously, other reactions apart from (3.8) and (3.9) may occur in the electrodes [6], as water gas shift reaction (WGSR) (3.11) and methanation reactions (3.12), (3.13) and (3.14):



As have been explained in previous sections, the electrolyzer can work with proton conducting oxides materials as electrolyte as well. High temperature PC-SOECs offer an important advantage: only dry hydrogen is produced in the cathode (Figure 3.5) and there is no need of additional stages to separate water and hydrogen. For the syngas production, the protons produced in the TPB of the anode pass through the electrolyte and react with CO_2 , allowing the next reactions:



The thermodynamics of water electrolysis and CO_2 are given in the following figure:

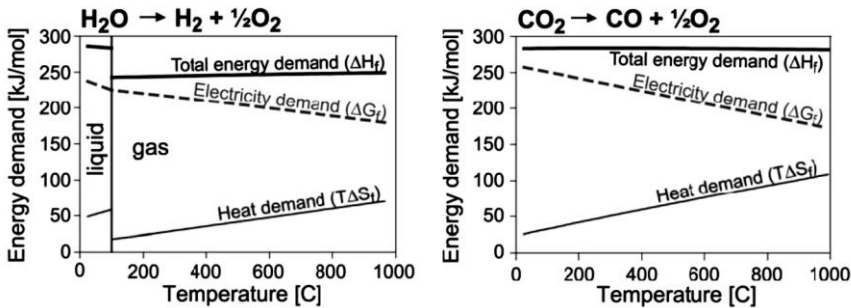
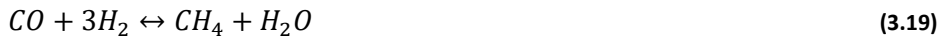


Figure 3.6: Thermodynamics of H_2O and CO_2 electrolysis at 10 bar [7].

As can be ascribed from Figure 3.6, ΔG decreases by increasing temperature, due to the endothermic reaction of H_2O and CO_2 electrolysis. Hence, at elevated temperatures the cost of H_2 and CO can be decreased, since the increasingly heat demand can be satisfied with the inevitably produced joule heat, which is produced due to the passage of electrical current through the cell, reducing the overall electricity consumption [8]. Furthermore, the kinetics of solid oxide fuel cells are improved by increasing the operation temperature [9, 10], which results in higher current densities and hydrogen production.

Hydrogen or syngas (mixture of H_2 and CO) generated from electrolysis, can be used to produce synthetic fuels as methane or used in Fisher-Tropsch reactors to produce liquid fuels [6, 11]. For instance, CH_4 can be produced from CO or CO_2 and H_2 in an external stage. The methanation is a complex mechanism where different possible reactions are involved [12, 13]:



One big advantage of obtaining syngas from co-electrolysis is the absence of high hydrocarbons (C_2H_6 , C_2H_4 and C_2H_2), which are obtained from other syngas production processes, gasification of coal and biomass. These high hydrocarbons bring a negative effect in the methanation process.

On the other hand, in the case of Fisher-Tropsch reactor the basic reaction that take place is:



At this point, it has been demonstrated the feasibility for the methane production. The methane can be generated by different ways by using electrolyzers as a source of hydrogen and carbon monoxide or dioxide:

1. Hydrogen production in an electrolyzer followed by a reactor for the catalytic hydrogenation of CO_2 .
2. Syngas production in an electrolyzer with a carbon monoxide methanation in a final stage.
3. One-stage methanation, due to the presence of H_2 and CO_2 in the electrolyzer and the optimal operation conditions and catalyst for the reaction [10]. Methane would be generated by the reactions (3.12), (3.13) and (3.14) for the solid oxide electrolyzer in oxygen ion conductors and by the reaction (3.17) in the proton conductor electrolyte cells.

3.2. Conductivity

At this stage, is very important to know the materials employed for the different cells configurations and their properties. The materials used can be divided in five groups:

- **Ceramics**, are inorganic compounds composed of metallic and non-metallic compounds bonded, forming a crystal structure. That can be ionic conductors (IC), electronic conductors (EC) or mixed electronic-ionic conductors (MIEC).
- **Metals** usually have a crystal structure and are good electronic conductors, and can be used as electronic conductors or catalyst.
- **Solid acid proton conductors** are included in the oxyanions group.
- **Composites** are mixture of two or more type of materials.
- **Solid catalysts** are generally made of a support where the actives sites are dispersed. The active sites are the place where the reactions can take place. Metals and oxides are the catalyst generally used in the present thesis.

The material selected for the cell components should have some characteristics: high conductivity, electronic or/and ionic conductivity, high electrocatalytic activity for the oxidation and reduction reaction, high compatibility with the cell components, stability in operation conditions and low cost.

Regarding the conductivity, the electrolyte must have ionic conductivity with nil or negligible electronic conductivity, whereas electrodes can show electronic or both ionic and electronic conductivity. The conductivity of the materials depends on the crystal structure, since the conductivity can be created from intrinsic defects or tailor by extrinsic defects. In the following section will be explain the main defects and the diffusion mechanisms for ions and protons.

The electrical resistance of one material is defined by the sample dimensions as is described below:

$$R \propto l/A \quad (3.28)$$

Where R is the resistance and l and A are the length and area, respectively.

Conductivity (σ) is the reciprocal of the resistivity

$$\sigma = \frac{1}{\rho} \quad (3.29)$$

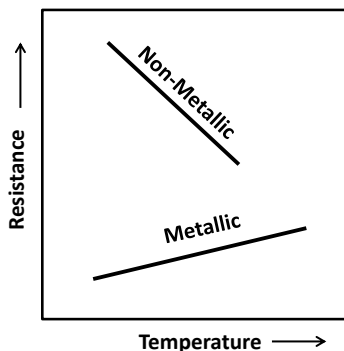


Figure 3.7: Conductivity as function of the metallic state.

The total electrical conductivity σ of a compound is the sum of the partial conductivities of the different charge carriers:

$$\sigma = \sum_i \sigma_i \quad (3.30)$$

Where σ_i is the partial conductivity of each carrier and the ratio of σ_i and the total conductivity determines the transport number (t_i) of species i :

$$t_i = \frac{\sigma_i}{\sigma} \quad (3.31)$$

The charge carriers in mixed ionic and electronic compounds are the ions and electrons. Each of these carriers have contribution from different defects and have different transport mechanisms, this will be explained in details in the next subsections. Usually, the most important contribution to the total conductivity, due to the higher mobility of electrons, is the electronic conductivity (extra electron holes in the valence band (p-type conductivity) and extra electrons in the conduction band (n-type conductivity)). Thus, the total conductivity:

$$\sigma = \sigma_i + \sigma_c = \sigma_a + \sigma_c + \sigma_n + \sigma_p \quad (3.32)$$

where σ_a , σ_c , σ_n and σ_p are anion, cation, electron and electrons holes conductivities, respectively. Often, one type of charge carrier predominates under particular conditions of oxygen partial pressure and temperature. Electronic conductor oxides are characterized by n-type conductivity, transport of electrons, or p-type conductivity, where the electron holes transport prevails. However, other materials are predominantly ionic conductors or mixed electronic and ionic conductors. Furthermore, some materials are able to transport protons in hydrogen or water vapour atmospheres.

3.2.1. Intrinsic defects

3.2.1.1. Ionic defects

Ionic conductivity or diffusion in oxides is provided by the presence of point defects, since a perfect crystal is not able to conduct ions. The ionic conductivity prevails when four premises are maintained, there is a vacant site for the ion to jump into, the potential barrier for the jump is not too high for

the ion, there is a complete path for the ions conduction and there is a driving force [14].

The possible defects can be listed as below(Figure 3.8) [15]:

- (a) **Interstitial**, ions placed at normally not occupied sites.
- (b) **Vacancies**, vacant lattice sites.
- (c) **Ions** with different charge from expected in the stoichiometric structure (acceptor or donor).
- (d) **Impurity or dopants** produced by foreign ions.

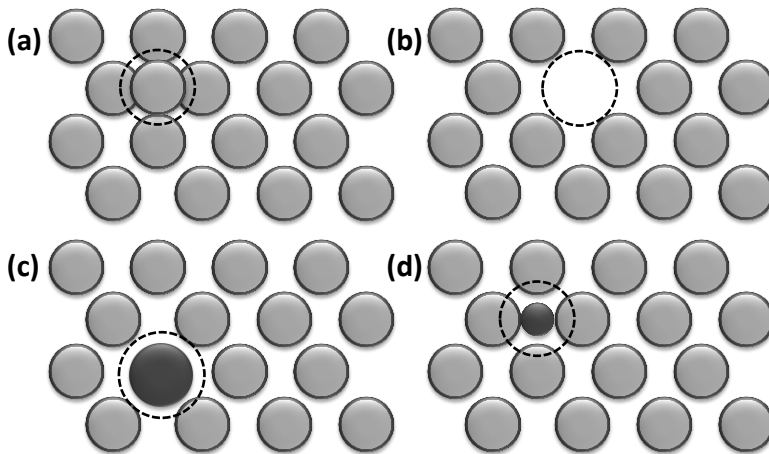


Figure 3.8: Point defects (a) self-interstitial; (b) vacancy; (c) substitutional impurity atom; and (d) interstitial impurity.

Defects cannot be treated separately, the electroneutrality condition inside the crystal has to be maintained; thermal disorder is achieved by the generation of a pair of defects (Figure 3.9). Some of these combinations are (a) Schottky disorder, (b) Frenkel disorder, (c) Anti-site disorder and (d) electron-hole pair.

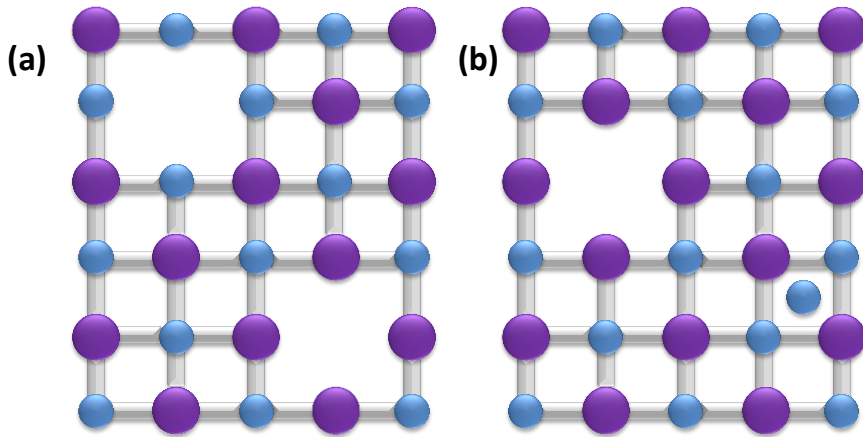


Figure 3.9: (a) Schottky and (b) Frenkel defect.

3.2.1.2. Electronic defects

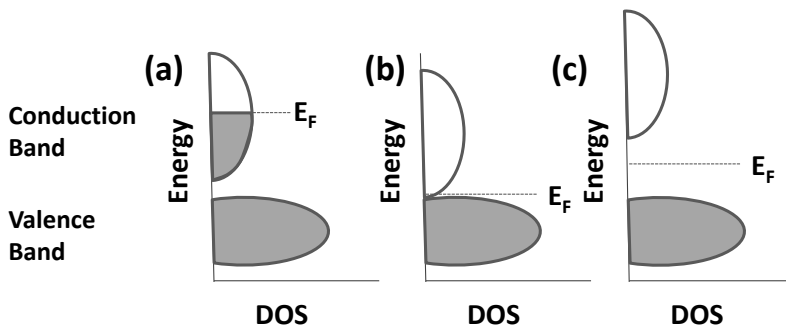


Figure 3.10: Materials conductivity: (a) metal; (b) semimetal; and (c) insulator/semiconductor.

In a metal the Fermi level (E_F) is localized in the conduction band, letting a partially filled band allowing the electrons movement (Figure 3.10a). However in the semimetal the Fermi level is in-between of the Conduction and Valence band, thus, the band gap is zero (Figure 3.10b). In the case of semiconductor or insulator there is an energy gap between both bands, as larger is the gaps as worsen is the conductivity (Figure 3.10c). Whereas in metal the electronic conductivity takes place by the electrons in the conduction band, in semiconductors the electronic conductivity is produced by the electrons in the conduction band and holes in the valence band.

Semiconductors can be intrinsic or extrinsic, intrinsic means that electrical conductivity does not depend on impurities, whereas extrinsic semiconductors are defect dependent. P-type semiconductor is generated by the incorporation of an acceptor (A), which has a lower oxidation state than the host element, there is one electron less to share with the surrounding atoms and this situation leave an electron hole in the lattice (Figure 3.11 (a)). A n-type semiconductor is produced by adding a donor (D) impurity, which has a higher valence than the host element, the valence electron that is not share is became a free electron (Figure 3.11 (b)).

The number of electrons and electrons holes generated by the introduction of donors and acceptors, respectively, are much greater than the intrinsic electronic carriers, becoming predominant in the lattice. The temperature can allow the promotion of electrons to conduction band from donor levels and electrons holes from acceptor levels.

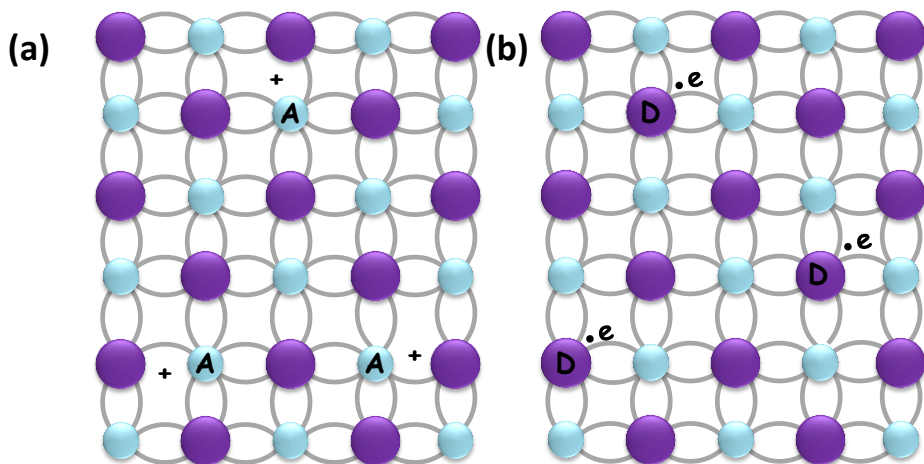


Figure 3.11: Crystal lattice of a (a) p-type and (b) n-type semiconductor.

3.2.2. Extrinsic defects: mixed conductivity

While intrinsic defects are present due to thermodynamic equilibrium of the lattice, the extrinsic defects are generated by foreign ions (impurities or dopants) in the lattice (Figure 3.8) [16]. Foreign ions can substitute a host ion or can be present on interstitial sites. If an isovalent ion replaces a host ion no substitutions compensating defects are needed to be created. However, when

an aliovalent ion substitutes a host ion, a charged impurity results. The extrinsic defects generated will interact and affect the structure around them looking for the electroneutrality condition, oppositely charged defects, either cationic, anionic or electronic, will be generated. Different types of defects will be produced for the presence of aliovalent ions depending on whether is an acceptor (A, negative charge) or donor (D, positive charge) impurity. Donor impurities, which have higher charge than the ions they replace, will generate cation vacancies or anion interstitials. However, acceptor impurity with less charge than the ions they replace, will promote cation interstitial or anion vacancies. The compensating defect and location depends on the dopant or impurity atomic radius, charge and bulk crystal structure. The defects can be generated as isolate or as defect complexes.

Semiconductors usually contain intentionally introduced dopants atoms that change the predominant charge state or introduce new extrinsic defects.

The nonstoichiometry will occur when there is an excess of one type of defect, since the ratio of anions and cations sites in a stoichiometric and nonstoichiometric is maintained, the charge equilibrium will be achieved by means of electronic defects. The extent of nonstoichiometry will be marked by the temperature and the gaseous ambient. For instance, under some conditions the doped compound can lead to an increase or reduction in the electronic conductivity.

The defect concentration of a material which is exposed to different oxygen environments can be plotted as in Figure 3.12. As can be ascribed from the figure the defect equilibrium is very sensitive to oxygen partial pressure changes. The most relevant equilibrium reactions of the defects are listed below with the mass action relations.

The defect reaction compensation of donor and acceptor as mentioned before are described as follow:

Donor



$$K_D(T)[D_M^x] = [D_M^{\cdot}] n \quad (3.34)$$

A donor impurity with a positive charge (D_M^{\cdot}), will be compensated by an electron (e').

Acceptor

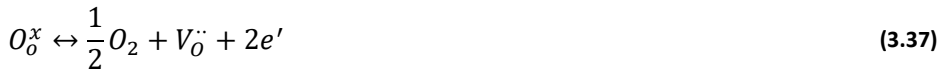
$$A_M^x \leftrightarrow A_M' + h^{\cdot} \quad (3.35)$$

$$K_A(T)[A_M^x] = [A_M'] p \quad (3.36)$$

In the case of an acceptor with a negative charge (A_M'), an electron hole (h^{\cdot}) will be generated.

Low oxygen partial pressures

When the sample is exposed to low oxygen partial pressure, there is a reduction of the sample, by the generation of oxygen vacancies [$V_O^{\cdot\cdot}$], due to the O_2 release, and expense of electrons lost:



$$K_R(T) = P_{O_2}^{1/2} [V_O^{\cdot\cdot}] n^2 \quad (3.38)$$

Frenkel equilibria on the oxygen sublattice



$$K_F(T) = [V_O^{\cdot\cdot}][O_i''] \quad (3.40)$$

Where an oxygen vacancy created in the lattice is compensated by an interstitial oxygen (O_i'').

Electronic equilibrium

If there is charge equilibrium, the electrons in the lattice will be balanced by electron holes:

$$n \leftrightarrow e' + h^{\cdot} \quad (3.41)$$

$$K_e = n \cdot p \quad (3.42)$$

Brouwer diagrams (also known as Kröger-Vink diagrams) are used to represent defect concentrations as a function of oxygen partial pressure (pO_2). In many oxides the predominant defect concentration changes as function of the oxygen activity. In the Figure 3.12 three regimes can be distinguished; low, medium and high pO_2 , in each regime a defect is become predominant.

Taking into account that the full electroneutrality condition is given by:

$$2[V_O^{\cdot\cdot}] + p \leftrightarrow 2[O_i^{\prime\prime}] + n \quad (3.43)$$

In the Range I, where there is a low oxygen partial pressure, the following approximation may be made from the equation (3.43) (Figure 3.12):

$$n = 2[V_O^{\cdot\cdot}] \quad (3.44)$$

In Range II, at or close to stoichiometry two alternative limiting conditions can be considered, the ionic Frenkel disorder (Figure 3.12(a)) and electron hole generation (Figure 3.12 (b)) [17]. If $K_e > K_f$ the intrinsic ionization of electrons predominate, thus: $n = p$. Then, the concentration of electrons and electron holes are independent of oxygen partial pressure (Figure 3.12 (b)). However, when $K_f > K_e$ the Frenkel disorder dominates and it can simplify as: $[O_i^{\prime\prime}] = [V_O^{\cdot\cdot}]$. Thus, $[O_i^{\prime\prime}]$ and $[V_O^{\cdot\cdot}]$ concentration is not dependent of pO_2 (Figure 3.12 (a)).

In the Range III (Figure 3.12), for large excess oxygen, the predominant species is the interstitial oxygen, so the equation (3.43) can be simplified as:

$$p = 2[O_i^{\prime\prime}] \quad (3.45)$$

By using the equations (3.38), (3.40) and (3.42) and the simplification in each region, the oxygen partial pressure dependence for each defect can be calculated (Table 3.3).

- Range I, for low oxygen partial pressure, the electrons and oxygen vacancies are the dominant defects, but the electrons mobility is higher than the oxygen vacancies, so the electronic conductivity prevails over the ionic conductivity. Then, the material is a n-type semiconductor and shows a $pO_2^{-1/6}$ proportionality.

- Range II, with intermediate oxygen partial pressure, two behaviors can be expected. In the first one, the oxygen defects concentration remains constant with changing oxygen partial pressure. Nevertheless, the electronic carriers have a dependence of $pO_2^{1/4}$ and $pO_2^{-1/4}$ for electrons and electrons holes, respectively. The second one, where electronic carriers are not dependent of the oxygen partial pressure, $[O_i'']$ has a $pO_2^{1/2}$ proportionality, whereas $[V_O^{\bullet\bullet}]$ has $pO_2^{-1/2}$.
- Range III, both holes and oxygen interstitial dominate, but as in Range I, the mobility of the electron holes is higher, inducing a p-type conductivity of the material. The electron holes concentration has $pO_2^{1/6}$ dependence.

	Neutrality equations	n	p	$[V_o^{\cdot\cdot}]$	$[O_i^{\cdot\cdot}]$
Range I - reduction	$n \approx 2[V_o^{\cdot\cdot}]$	$(2K_R)^{1/3} pO_2^{-1/6}$	$K_e(2K_R)^{-1/3} pO_2^{1/6}$	$\frac{(2K_R)^{1/3}}{2} pO_2^{-1/6}$	$2K_F(2K_R)^{-1/3} pO_2^{1/6}$
Range II- electronic compensation	$n \approx p$	$K_e^{1/2}$	$K_e^{1/2}$	$\frac{K_R}{K_e} pO_2^{-1/2}$	$\frac{K_F K_e}{K_R} pO_2^{1/2}$
Range II-ionic compensation	$[O_i^{\cdot\cdot}] \approx [V_o^{\cdot\cdot}]$	$K_R^{1/2} K_F^{-1/4} pO_2^{-1/4}$	$K_e \left(\frac{K_F^{1/2}}{K_R} \right)^{1/2} pO_2^{1/4}$	$K_F^{1/2}$	$K_F^{1/2}$
Range III-oxidation	$n \approx [O_i^{\cdot\cdot}]$	$\left(\frac{K_R K_e}{2K_F} \right)^{1/3} pO_2^{-1/6}$	$\left(\frac{2K_F K_e}{K_R} \right)^{1/3} pO_2^{1/6}$	$K_R^{1/3} \left(\frac{2K_F}{K_e} \right)^{2/3} pO_2^{-1/6}$	$2^{-2/3} \left(\frac{K_F K_e^2}{K_R} \right)^{1/3} pO_2^{1/6}$

Table 3-3: Region dependent equations for defect species concentration in Frenkel disorder oxides.

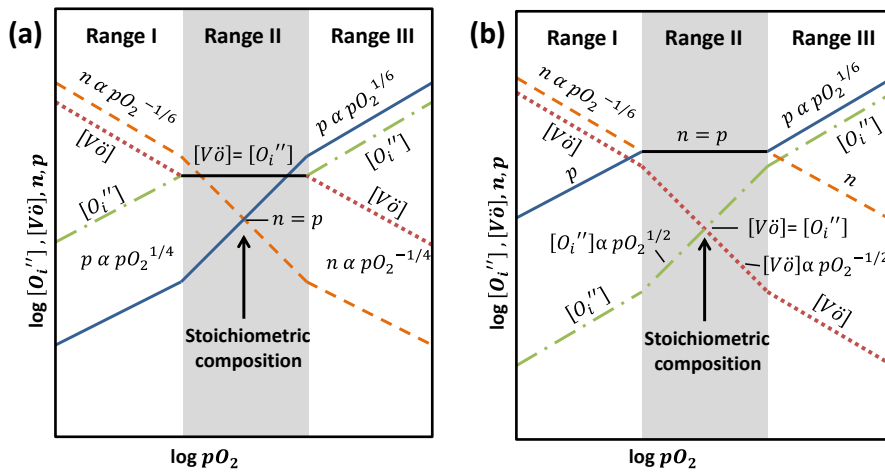


Figure 3.12: Diagrams of the oxygen and electronic defects concentration as function of the oxygen partial pressure for (a) $K_F > K_e$ and (b) $K_e > K_F$.

3.2.3. Diffusion mechanisms

The ionic diffusion takes place by the movement of the point defects (*Section 3.2.1.1*). As there are different point defects, different diffusion mechanisms can be found. The most common mechanisms of ionic diffusion are described in the Figure 3.13.

The vacancy mechanism consists of an atom hop from its normal position to a neighbor vacancy (unoccupied lattice site).

However when an atom is occupying interstitial sites, the mechanism takes place via nearby interstitial sites. Such hop of the interstitial involves a big distortion of the lattice; consequently, interstitial atoms are usually smaller than the surroundings atoms of the structure.

Finally, in the interstitialcy mechanism, an atom in interstitial position displaces another from its original site to a close interstitial site and itself occupies the lattice site of the displaced atom.

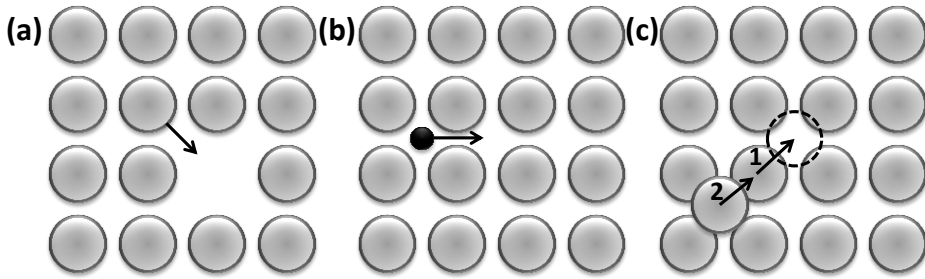
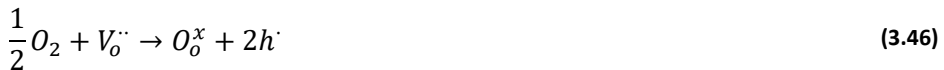


Figure 3.13: Diffusion mechanisms: (a) vacancy; (b) interstitial and (c) interstitialcy.

The oxygen mechanisms depend on the type of material, and type of defect in the structure. For instance, many perovskite with structure ABO_3 , when A site is substituted with a lower valence cation, vacancies are generated in the structure in order to compensate charges and to achieve an electroneutrality. Thus the oxygen mechanism takes place by these vacancies in the structure:



Regarding proton diffusion, as proton has no electron shell, they interact with the electrons of the lattice oxide ions. Two different mechanisms are usually studied, and are described in Figure 3.14.

The free transport mechanism or Grotthuss mechanism (Figure 3.14 (a)); which is the principal mode of transport of protons in oxides. This mechanism is characterized by the hop of the proton from one ion oxide to a close one. After each hop the proton in the OH^{\cdot} rotates with the intention to be aligned for the next hop. In this mechanism, the jump itself is the limiting step whereas the reorientation of the proton needs small activation energy.

In the vehicle mechanism (Figure 3.14 (b)) proton is transported as hydroxide ion by an oxygen vacancy mechanism ① or interstitial hydroxide ion ②.

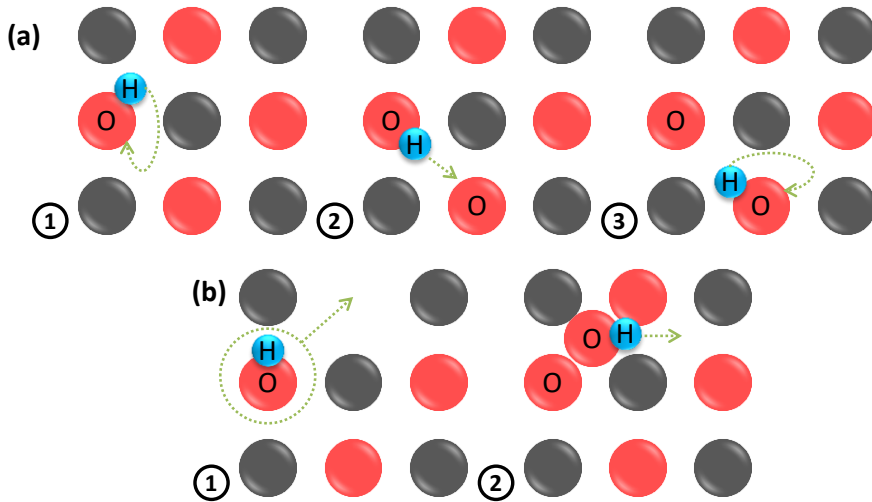


Figure 3.14: Schematic proton diffusion mechanism (a) steps of the Grotthius mechanism and (b) vehicle mechanism; 1 oxygen vacancy and 2 interstitial hydroxide ion mechanisms.

3.3. Cell components and material

After the description of the electrochemical devices and set the possible transport mechanisms of the charge carriers in these type of materials, the different components and the state-of-the-art materials will be explained in detail.

3.3.1. Electrolyte

One of most important components of electrochemical cells is the electrolyte. The type of electrolyte used will differentiate between the different fuel cells and the partial reactions in each electrode. The electrolyte is localized between both electrodes and will have the task to transport the oxygen ions or protons from one electrode to the other. All electrolytes must have some important characteristics for a good performance of the cell [18]:

- *Stability*, the electrolyte must be chemically, morphologically and dimensionally stable. Furthermore, it has to be stable in both atmosphere of the cell, oxidizing and reducing. This stability should be maintained in all range of operation conditions.
- *Conductivity*, the electrolyte should have a good ionic or protonic conductivity in the cell operation conditions. Being the ionic or

protonic as high as possible, in order to reduce the ohmic losses of the cell. In addition, the electronic conductivity should be as small as possible, as not to have current flow through the electrolyte, and the resulting reduction of the cell performance (lower Faraday's efficiency).

- *Porosity*, the electrolyte should be as dense as feasible in order to avoid gas leakage in the cell.
- *Thermal expansion coefficient (TEC)*, should match with the adjacent components of the cell, to avoid cracks, delamination, etc. Moreover TEC should be invariable with change of oxygen partial pressure in both chamber of the cell.

Furthermore, some characteristic are also desirable as the low cost, low toxicity, manufacturability and high strength.

3.3.1.1. Materials

In this section is important to divide the materials in two groups; protonic and ionic conductors.

3.3.1.1.1. Ionic conductors

Three are the most widely studied electrolyte materials with ionic conductivity; yttria stabilized zirconia (YSZ), strontium magnesium doped lanthanum gallate (LSGM) and gadolinium or samarium doped ceria (GDC or SDC).

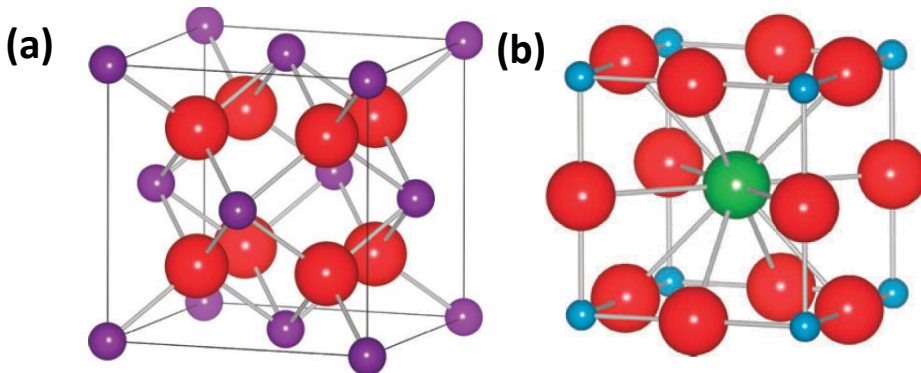


Figure 3.15: (a) Fluorite crystal structure of AO_2 , big spheres are O^{2-} and the small are Ce^{+4} in CeO_2 or Zr^{+4} in ZrO_2 . (b) Cubic perovskite structure of LaGaO_3 , La^{+3} is the sphere in the center, and the big spheres are O^{2-} and the small are Ga^{+3} .

One of the most widely studied material for SOFC electrolyte is ZrO_2 , but due to the low ionic conductivity and stability, ZrO_2 has to be doped. Trivalent or divalent cations are able to stabilize the cubic fluorite phase (Figure 3.15), increasing the oxygen vacancies and improving the ionic conductivity of the electrolyte material. Stabilized ZrO_2 has been used almost exclusively as electrolyte for fuel cells, due its good oxygen ion conductivity (above 700 °C) and stability in both atmospheres; reducing and oxidizing. Being the 8 % mol of Y_2O_3 the most common dopant for ZrO_2 (YSZ). Alternative doped ZrO_2 electrolytes have been developed with higher ionic conductivity as Scandia doped zirconia.

On the other hand, pure ceria CeO_2 , another cubic fluorite (Figure 3.15), does not need any stabilization phase. However, pure CeO_2 has low ionic conductivity, but the ionic conductivity can be improved by the introduction of different dopants. Mobile oxygen vacancies are introduced by substituting Ce^{+4} with trivalent rare earth. This material exhibits pure ionic conductivity but in some reducing atmospheres is reduced and leads to an electronic conductivity [19]. Due to the possible presence of electronic conductivity (n-type), it is important to know the electrolytic and ionic domain boundary to use it as electrolyte in solid oxide fuel cells and electrolyzers. Regarding the dopants of CeO_2 the most common are gadolinium (GDC) and samarium.

LSGM, with a cubic perovskite structure (Figure 3.15) was situated as superior oxide-ion electrolyte, with higher conductivity than YSZ (Figure 3.16) [20]. However, the low stability for long operation time due to the Ga evaporation in a reducing atmospheres and the nickel compatibility [21], limits the use of this material as electrolyte.

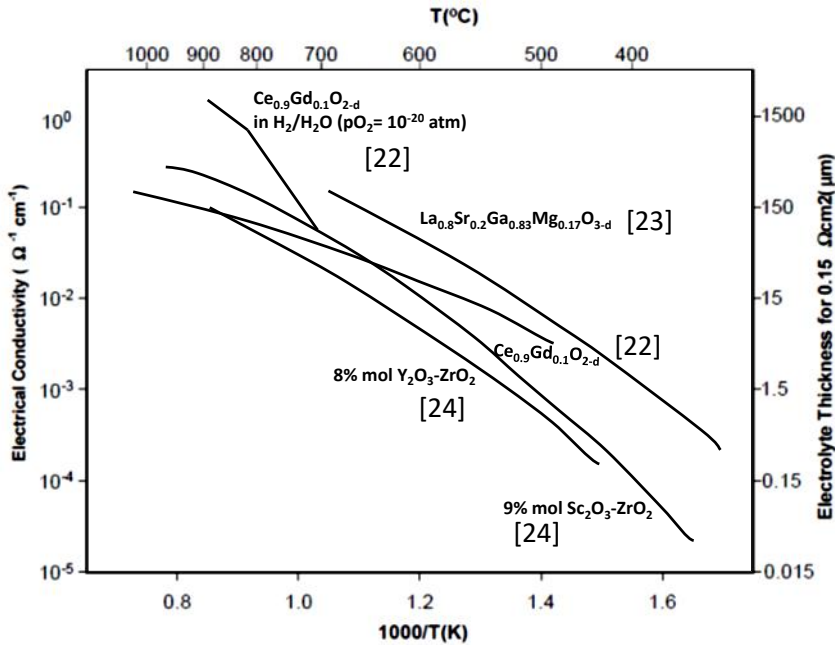


Figure 3.16: Conductivity of different electrolytes as function of the reciprocal temperature [25].

3.3.1.1.2. Protonic conductors

3.3.1.1.2.1. High temperature

The growing interest in proton conducting solid oxide fuel cells (PC-SOFC) [26-29] research is principally due to their advantages compared to conventional oxygen-ion conducting solid oxide fuel cells (SOFCs): (1) their higher efficiency and fuel utilization, since protons react with oxygen in the cathode to form water, diluting the air stream; and (2) the lower activation energy of proton transport together with the higher mobility of protons, which makes possible to reduce the operation temperature (500-700 °C) and permits the utilization of less expensive system components and increases their lifetime [30, 31].

The most widely studied proton conductors are based on BaCeO_3 , SrCeO_3 , CaZrO_3 and SrZrO_3 [18, 26, 27, 32-34], with a perovskite-type as in Figure 3.15b. These materials exhibit a p-type conductivity in absence of hydrogen or water vapor. When these materials are in contact with hydrogen or water the electronic conductivity decreases and they become protonic conductors. These pure materials exhibit only low proton conductivity, but the incorporation of

aliovalent can improve the conductivity by generating oxygen vacancies [35]. For instance, by doping BaCeO_3 with rare earth in Ce position the conductivity of the compound can be improved. Furthermore, it has been demonstrated that the water incorporation in the structure is an exothermic reaction for doped and undoped cerates and zirconates compounds. This premise explains the better proton uptake in perovskite oxides at lower temperatures.

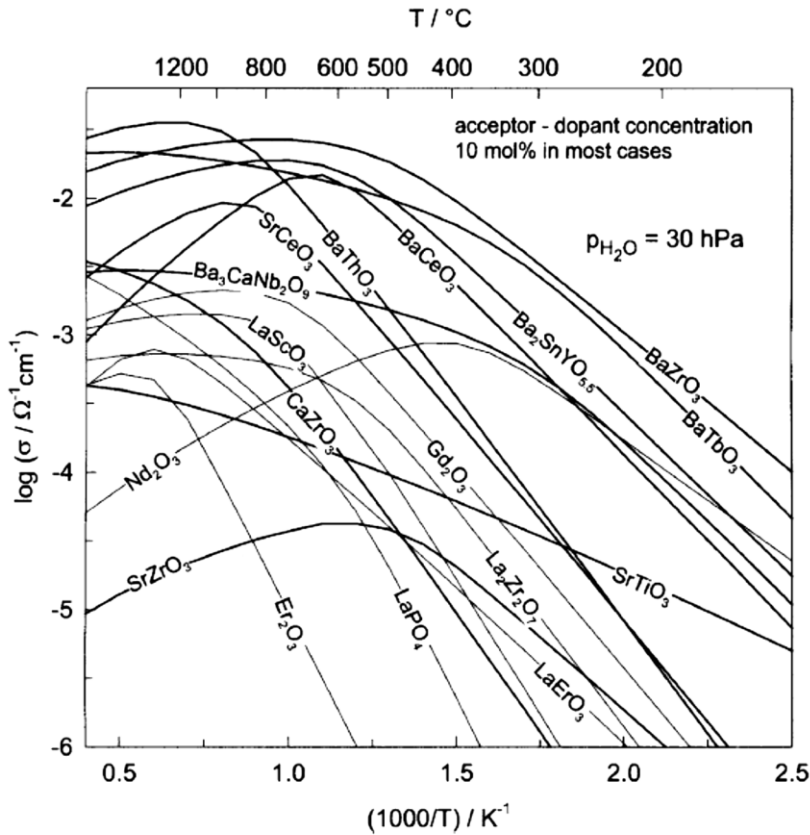


Figure 3.17: Proton conductivities of various oxides calculated from data proton concentrations and mobilities according to [36], [26].

As can be inferred from Figure 3.17 the BaCeO_3 -based compounds have higher conductivity than SrCeO_3 , SrZrO_3 and CaZrO_3 -based materials. But at high temperatures, oxygen ions transport contributes to the total conductivity, and the proton transport number decreases. However, the BaCeO_3 has poor chemical stability and electronic species are formed in reducing conditions.

Furthermore these group of compounds exhibit high grain boundary impedances limiting the conductivity [37, 38]. An oxygen deficient fluorite $\text{La}_{5.5}\text{WO}_{11.25-6}$ (LWO) [39] could be selected as alternative in this group of protonic conductors, since it exhibits reasonable high values of predominant protonic conductivity below 800 °C, low grain boundary resistance and high stability in operation conditions under CO_2 and H_2S containing atmospheres [40, 41].

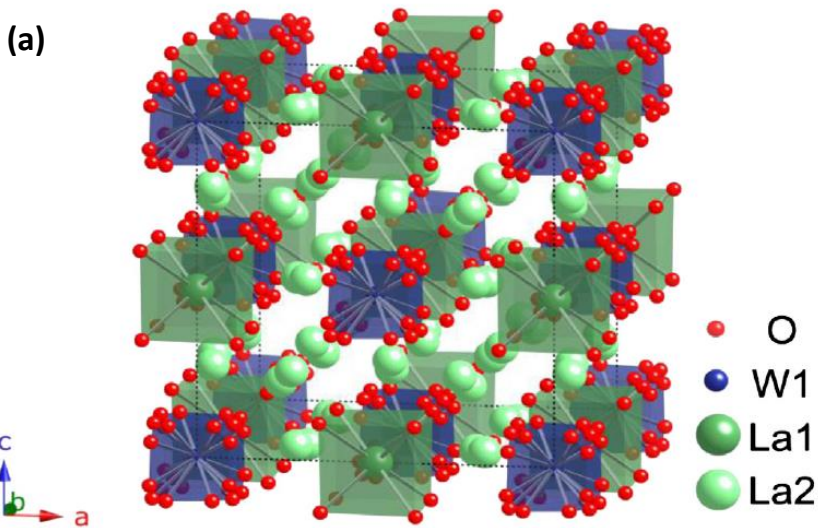


Figure 3.18: Crystal structure for $\text{La}_{5.5}\text{WO}_{11.25-6}$ with split oxygen and lanthanum sites in space group $Fm\bar{3}m$ [41].

3.3.1.1.2.2. Low temperature

Solid acid proton conductors, based on tetrahedral oxyanions, have been attracted interest in the last years because of their potential applications as electrolytes in fuel cells, hydrogen pumping or electrochemically promoted water gas shift reactions. Cesium dihydrogen phosphate, CsH_2PO_4 , is one of the compounds more studied that belongs to this group. CsH_2PO_4 is a solid acid compound, which facilitates anhydrous proton transport with high proton conductivity. CsH_2PO_4 (CDP) undergoes a phase transition from monoclinic phase at low-temperature (below 230 °C) to cubic phase at high-temperature (above 235 °C). This phase transition leads to an outstanding increase in its protonic conductivity by several orders of magnitude. Thus, CDP can be

selected as good electrolyte material for low temperature fuel cells and electrolyzers.

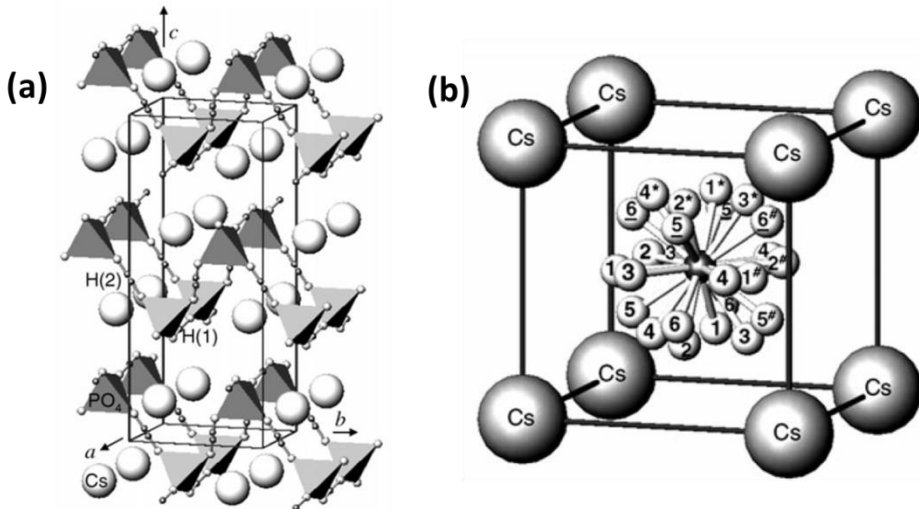


Figure 3.19: Crystal structure of CsH_2PO_4 (a) at room and (b) at high temperature.

The operation temperature of the CDP allows improving some problems obtained in PEMFC operation, as the water humidification control, or the poisoning of the Pt for the presence of CO in the fuel stream. Furthermore, the reduction of precious metal catalyst load or even the entirely substitution of precious metal can be achieved due to the CDP operation temperature.

3.3.2. Electrodes

As it has been described for the electrolytes some characteristics should be accomplished by the materials selected as electrodes in the electrochemical cells.

- *Stability*, both the oxidant and fuel electrode have to be chemically, morphologically and dimensionally stable in the working atmospheres. Furthermore, the electrode must also maintain the stability in the different operation and fabrication temperatures.
- *Conductivity*, in order to improve the cell performance the electronic conductivity has to be as large as possible at operation conditions.

Furthermore, to extend the TPB along the whole electrode surface, some oxygen ion or proton conductivity is required.

- *Porosity*, electrodes should have enough porosity to allow a fast gas transport from/to the active reaction sites. The upper limits of the electrodes porosity will be restricted by the structural characteristics and the electrical transport, whereas the lower limits will be limited by the mass transport of gasses.
- *Thermal expansion coefficient*, the TEC of electrodes should match the electrolyte and adjacent components along the operation conditions.
- *Compatibility*, in addition to the TEC, electrodes should be compatible with other components in the operation and fabrication conditions. It should be reminded that the variation of the electrodes atmospheres during operation requires a high compatibility and stability of the electrodes.
- *Catalytic activity*, electrodes must have sufficient catalytic activity (low polarization) for the different reactions that take place in the active sites, as oxygen reduction reaction, hydrogen oxidation reaction, water split reaction, etc. The reactions will be different depending on the type of cell used (proton conductor or oxygen ion conductor electrolyte) and the final application; *Power-to-Power (Section 3.1.1)*, *Power-to-Hydrogen (Section 3.1.2.)* and *Power-to-Gas (Section 3.1.3)*.

3.3.2.1. Materials

In the present thesis, several materials have been employed with different configurations (fuel cell, electrolyzer, CO₂ electrolyzer and methanation cells) and temperatures. The description of the electrodes materials will be done in general terms, speaking about material characteristics. A deep description of the materials employed will be done in each chapter depending on the operation conditions.

3.3.2.1.1. High temperature

3.3.2.1.1.1. Perovskites

One of the most commonly electrode materials used is the doped lanthanum manganite (LaMnO₃) with a high electrical conductivity in oxidizing

atmospheres, good compatibility with some electrolyte materials, as YSZ and GDC, and acceptable thermal expansion coefficient, which match adjacent components. LaMnO_3 has a cubic perovskite structure and belongs to oxides with the structure ABO_3 . Different substitutions have been performed in A and B position with cations as barium, calcium, chromium, cobalt, copper, magnesium, nickel, potassium, rubidium, sodium, strontium, titanium and yttrium. But the most common dopants are calcium and strontium which can increase the electronic conductivity in oxidizing atmospheres [42]. However, the use of doped strontium lanthanum manganite ($\text{La}_{1-x}\text{Sr}_x\text{MnO}_3$) is limited by the low oxygen ionic conductivity [43].

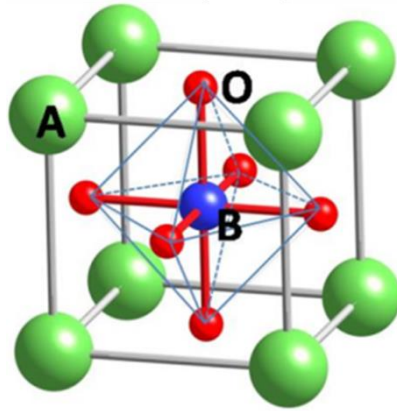


Figure 3.20: ABO_3 perovskite structure with the origin centered at the B-site ion [44].

Doped lanthanum cobaltite (LaCoO_3) is another important perovskite for solid oxide cells with higher catalytic activity than LaMnO_3 and higher oxygen ion conductivity. LaCoO_3 has a rhombohedral perovskite structure but may transform to cubic phase depending on the dopant content. When LaCoO_3 is doped with lower oxidation state cation as strontium (La^{+3} to Sr^{+2}), the compound exhibits a large oxygen deficiency at high temperature. Furthermore, the p-type conductivity is improved with the incorporation of cation in La site with a lower oxidation state. However, at low oxygen partial pressure and temperatures (below 790°C) there is a phase transition, limiting its applicability.

From the same ABO_3 (Figure 3.20) cobaltites family, $\text{SrCo}_{0.8}\text{Fe}_{0.2}\text{O}_{3-\delta}$ (SCF) was one of the first materials suggested as an oxygen transport membrane, due to

the mixed ionic and electronic conductivity. Nevertheless, SCF undergoes a phase transition, from cubic to brownmillerite, at low operation temperature and oxygen partial pressures. This new phase exhibits low oxygen conductivity due to the ordered arrangement of oxygen vacancies in the structure. However, the partial substitution of Sr by Ba in $\text{SrCo}_{0.8}\text{Fe}_{0.2}\text{O}_{3-\delta}$ avoids the formation of brownmillerite with the variation of temperature and oxygen partial pressure, giving higher stability and even improving the oxygen conductivity.

3.3.2.1.1.2. Ruddlesden-Popper

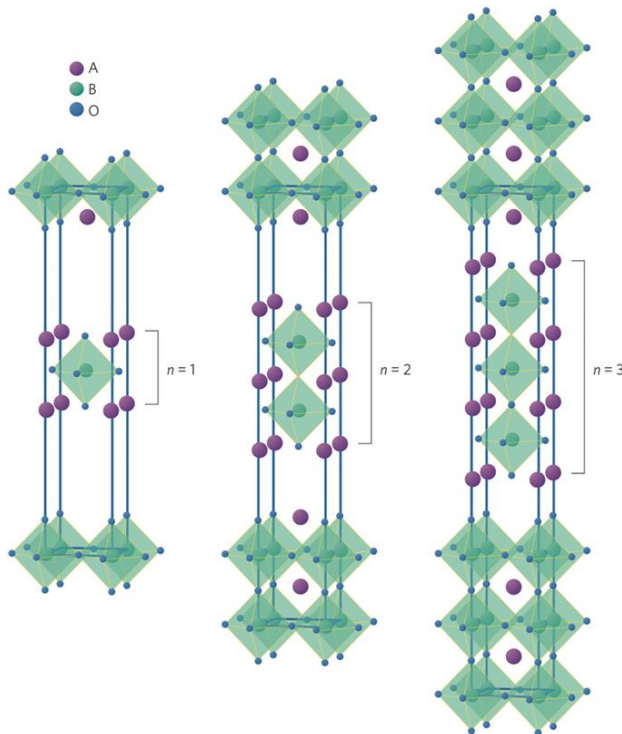


Figure 3.21: Ruddlesden–Popper phases, $\text{A}_{n+1}\text{B}_n\text{O}_{3n+1}$, where A and B are cations, and O an oxygen anion [45].

In recent years, Ruddlesden-Popper series has attracted much attention as material for electrodes at intermediate temperature (600–800 °C) due its good electrochemical properties [46, 47]. The Ruddlesden-Popper structure, with the general formula $\text{La}_{n+1}\text{Ni}_n\text{O}_{3n+1}$, is comprised of rock-salt layer and perovskite

layers interspersed [48-50]. The value of n in the general formula is related with the number of perovskite layers between two rock-salt layers (Figure 3.21). As the n value increases, the electronic conductivity increases as well, due to the presence of NiO_6 in the perovskite layers. Due to its layered structure these compounds are able to accommodate hyperstoichiometric oxygen in interstitial sites of the rock-salt layer [51], exhibiting good oxide ion conductivity at intermediate temperatures [52-55]. The highly anisotropic oxygen diffusion is produced *via* the interstitial oxygen defects in the lattice [56] and the cooperative diffusion in the vacancies in the perovskite layer [52].

3.3.2.2. Electrode configuration

Different materials can be used as electrode in the fuel cells, electrolyzers and methanation reactors systems. The selection of the most suitable electrode will depend on the operation conditions, as temperature, gas atmosphere, etc. Furthermore, depending on the final application, different material can be selected and used with different configuration in the electrode. Most of the possible microstructures and configurations are present in Figure 3.22.

In the triangle scheme, in Figure 3.22, four types of materials are represented and used in electrodes: ionic conductors (IC), mixed ionic and electronic conductors (MIEC), electronic conductors (EC) and catalyst (C). Furthermore in the triangle are included the different materials; fluorite (F), perovskite (P), double perovskite (DP), Ruddlesden-Popper (RP) and metals (M) and the possible group where each material for high operation temperature can pertain.

Furthermore, Figure 3.22 shows the different type of configuration and microstructure of an electrode in an electrochemical cell: (g) IC-EC composite, (h) single-phase MIEC electrode, (i) IC-MIEC composite structure, (j) MIEC-EC composite structure, (k) MIEC with dispersed catalyst, (l) IC coated with percolating layer of MIEC, (m) IC coated with a percolating layer of EC and MIEC and (n) EC coated with percolating layer of MIEC and dispersed catalyst.

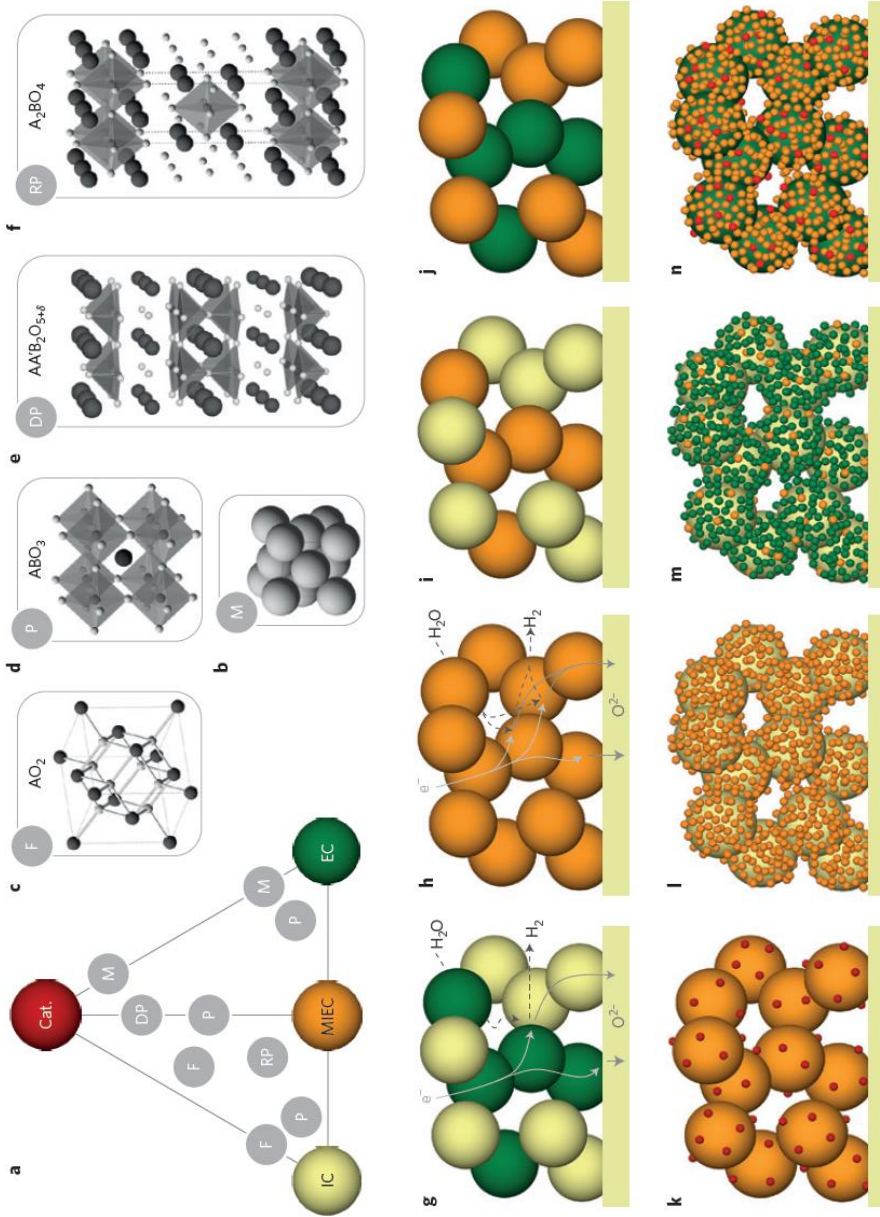


Figure 3.22: Solid oxide cells electrodes materials and microstructures [57]. Explanation of the figure is explained in the text.

3.3.2.2.1. Electrochemical activation of oxygen

In Figure 3.22 almost all the possible electrode configuration are described. To explain in more detail the mechanism of the electrochemical oxygen activation, the next part will take a closer look at only three electrodes configurations: EC, EC-IC and MIEC electrodes.

- *Electronic conductor configuration*, where the electrode is composed of a material with predominantly electronic conductivity. In this type of electrodes, the reaction takes place only in the electrode-electrolyte interface. In this point, gas, electronic phase and ionic phase are in contact (TPB) (Figure 3.23 (a)). In this type of material, the electrochemical oxygen activation includes the following steps: (i) oxygen gas diffusion, (ii) adsorption of molecular or dissociative oxygen onto the material surface, (iii) diffusion of the oxygen species adsorbed along the surface to the TPB and (iv) charge transfer reaction with the subsequent oxygen ion incorporation in the electrolyte.
- *Cer-met or cer-cer*, in this type of electrode two different phases are mixed in the electrode. The electrode can be composed of two ceramics phases (cer-cer) or by a ceramic and metallic phase (cer-met). For instance LSM-YSZ is one of the most studied cer-cer cathode for solid oxide fuel cells. Composite electrodes are able to increase the performance and enlarge the TPB along the electrode surface. Usually, one of the phases is electronic conductor whereas the other one is oxygen ion or proton conductor, enabling TPBs along the electrode surface (Figure 3.23 (c)). The stages in the electrochemical activation of oxygen in composite electrodes are: (i) oxygen gas diffusion, (ii) adsorption of molecular or dissociative oxygen onto the material surface, (iii) diffusion of the oxygen species adsorbed on the surface length to the TPB, (iv) charge transfer reaction in the TPB, (v) diffusion of the oxygen species from the ionic material of the electrode to the electrolyte material, (vi) oxygen ions incorporation from the IC material to the electrolyte.
- *MIEC materials*, this type of compounds exhibits a mixed ionic and electronic conductivity. In the last years many efforts have been focused in the search of MIEC materials. As has been explained above,

the introduction of some dopants in the structure are able to tailor the electrodes properties adding electronic conductivity or increasing the ionic conductivity. MIEC electrodes are able to enlarge the TPB along the whole electrode, making available the entire electrode surface for the oxidation/reduction reactions. In MIEC electrodes, the electrochemical oxygen activation has the next steps (i) oxygen gas diffusion, (ii) adsorption of molecular or dissociative oxygen onto the material surface, (iii) surface exchange reaction between the oxygen species in the surface and the oxygen vacancies or interstitials, (iv) diffusion of the oxygen species to the electrolyte materials and (iv) oxygen species exchange between the electrode and electrolyte material.

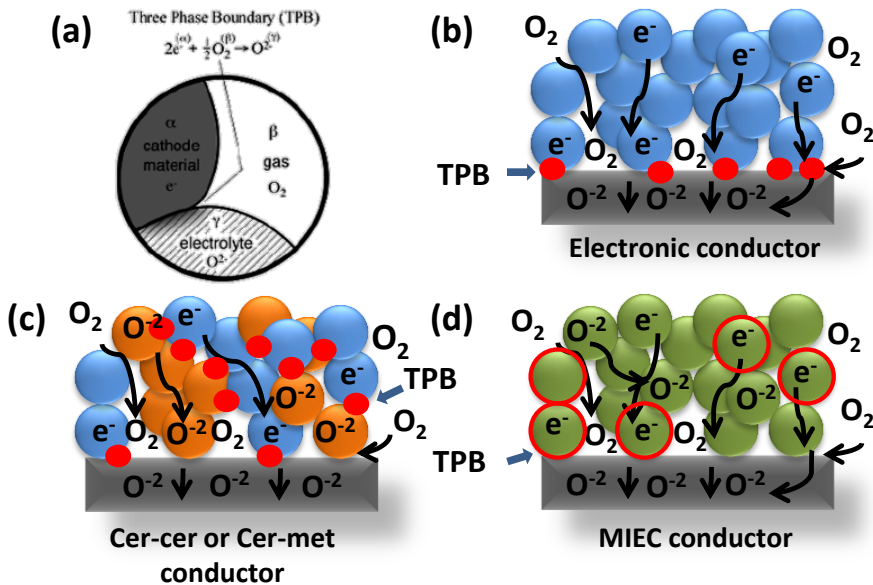


Figure 3.23: (a) Three phase boundary representation. Three phases are involved: electronic phase α , ionic phase γ and gas phase β [58]. Electrode configuration (b) electronic conductor (c) composite and (d) MIEC electrode.

3.3.2.2. Electrochemical activation of hydrogen

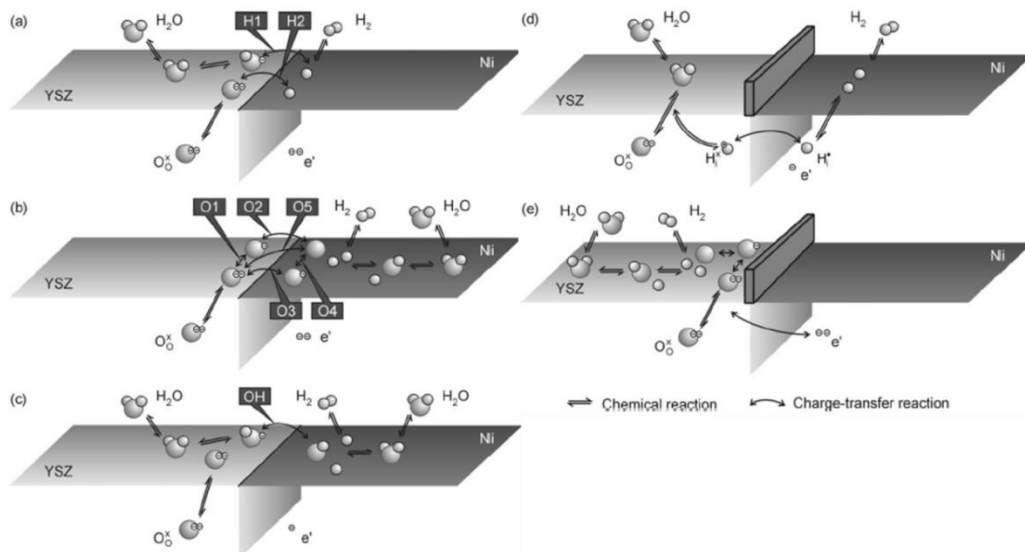


Figure 3.24: Elementary kinetic scenarios at a Ni/YSZ TPB. The different stages will be explained below [59].

Many theories have been postulated for the hydrogen oxidation in the Ni-YSZ anodes in a fuel cell mode and that theories can be extrapolated for the Ni-YSZ working as cathode in electrolysis mode. It has been difficult to reach an agreement in a simple theory, due to the complexity of the system. Different mechanism of the hydrogen oxidation in TPB of the Ni-YSZ cer-met anodes that appear in Figure 3.24 will be explained below. (a) Spillover of hydrogen adsorbed from the Ni surface onto an oxygen ion or hydroxyl ion on the YSZ surface. (b) Spillover of oxygen ions from the YSZ surface to the Ni surface by some charge transfer reactions, where the oxygen reacts with the hydrogen adsorbed on the Ni surface. (c) Hydroxyl spillover from the YSZ surface to the Ni surface. (d) Charge transfer by an interstitial proton conductivity, this process is favored by the high temperature and the water and hydrogen adsorbed are involved. (e) Charge transfer and chemical reactions on the electrolyte surface only.

3.4. Appendix: Defect chemistry and mechanisms

Kröger–Vink notation was employed for the defect chemistry and a brief summary is written below:

<i>Sites</i>	<i>Notation</i>
<i>Interstitial oxygen ion</i>	O_i''
<i>Foreign acceptor metal, A on M site</i>	A_M'
<i>Free electrons</i>	e'
<i>Occupied oxygen sites</i>	O_o^x
<i>Oxygen vacancies</i>	$V_o^{\cdot\cdot}$
<i>Foreign donor metal, D on M site</i>	D_M^{\cdot}
<i>Free positives holes</i>	h^{\cdot}
<i>Vacancy in M site</i>	V_M''

Table 3.4: Kröger–Vink notation for defect chemistry.

3.5. References

- [1] A. Kirubakaran, S. Jain, R.K. Nema, Renewable and Sustainable Energy Reviews, 13 (2009) 2430-2440.
- [2] S. Basu, Recent Trends in Fuel Cell Science and Technology, Springer New York, 2007.
- [3] B.C.H. Steele, A. Heinzl, Nature, 414 (2001) 345-352.
- [4] Fuel Cell Handbook (Sixth Edition), DIANE Publishing.
- [5] S.M. Haile, C.R.I. Chisholm, K. Sasaki, D.A. Boysen, T. Uda, Faraday Discuss., 134 (2007) 17-39.
- [6] V.N. Nguyen, L. Blum, Chemie Ingenieur Technik, 87 (2015) 354-375.
- [7] W. Dönitz, E. Erdle, Int. J. Hydrog. Energy, 10 (1985) 291-295.
- [8] S.H. Jensen, P.H. Larsen, M. Mogensen, Int. J. Hydrog. Energy, 32 (2007) 3253-3257.
- [9] N.Q. Minh, T. Takahashi, Preface, Science and Technology of Ceramic Fuel Cells, Elsevier Science Ltd, Oxford, 1995, pp. vii-viii.
- [10] X.F. Sun, M. Chen, S.H. Jensen, S.D. Ebbesen, C. Graves, M. Mogensen, Int. J. Hydrog. Energy, 37 (2012) 17101-17110.
- [11] J.G. Speight, Handbook of Industrial Hydrocarbon Processes, Elsevier Science, 2010.

- [12] D. Cheng, F.R. Negreiros, E. Aprà, A. Fortunelli, *ChemSusChem*, 6 (2013) 944-965.
- [13] J. Gao, Y. Wang, Y. Ping, D. Hu, G. Xu, F. Gu, F. Su, *RSC Advances*, 2 (2012) 2358-2368.
- [14] I. Riess, *Crystalline Anionic Fast Ion Conduction, Science and technology of fast ion conductors*, Springer, 1989, pp. 23-50.
- [15] P.J. Gellings, H. Bouwmeester, *Handbook of solid state electrochemistry*, CRC press, 1997.
- [16] E.G. Seebauer, M.C. Kratzer, *Charged Semiconductor Defects: Structure, Thermodynamics and Diffusion*, Springer London, 2008.
- [17] H.L. Tuller, J. Schoonman, I. Riess, *Oxygen Ion and Mixed Conductors and Their Technological Applications*, Springer Netherlands, 2000.
- [18] N.Q. Minh, T. Takahashi, *Science and Technology of Ceramic Fuel Cells*, Elsevier Science, 1995.
- [19] C. Gaudillere, L. Navarrete, J.M. Serra, *Int. J. Hydrog. Energy*, 39 (2014) 3047-3054.
- [20] M. Feng, J.B. Goodenough, K. Huang, C. Milliken, *J. Power Sources*, 63 (1996) 47-51.
- [21] A. Weber, E. Ivers-Tiffée, *J. Power Sources*, 127 (2004) 273-283.
- [22] S.R. Wang, T. Kobayashi, M. Dokiya, T. Hashimoto, *J. Electrochem. Soc.*, 147 (2000) 3606-3609.
- [23] K. Huang, R.S. Tichy, J.B. Goodenough, *J. Am. Ceram. Soc.*, 81 (1998) 2565-2575.
- [24] Y. Arachi, H. Sakai, O. Yamamoto, Y. Takeda, N. Imanishai, *Solid State Ion.*, 121 (1999) 133-139.
- [25] I. EG&G Technical Services, *Fuel Cell Handbook (Sixth Edition)*, DIANE Publishing.
- [26] K.D. Kreuer, *Annual Review of Materials Research*, 33 (2003) 333-359.
- [27] H. Iwahara, *Solid State Ion.*, 77 (1995) 289-298.
- [28] H. Iwahara, Y. Asakura, K. Katahira, M. Tanaka, *Solid State Ion.*, 168 (2004) 299-310.
- [29] W.G. Coors, *J. Power Sources*, 118 (2003) 150-156.
- [30] N. Bonano, B. Ellis, M.N. Mahmood, *Solid State Ion.*, 44 (1991) 305-311.
- [31] J.M. Serra, W.A. Meulenbergh, *J. Am. Ceram. Soc.*, 90 (2007) 2082-2089.
- [32] N. Bonanos, K.S. Knight, B. Ellis, *Solid State Ion.*, 79 (1995) 161-170.
- [33] S.C. Singhal, K. Kendall, *High-temperature Solid Oxide Fuel Cells: Fundamentals, Design and Applications*, Elsevier Science, 2003.
- [34] L. Malavasi, C.A.J. Fisher, M.S. Islam, *Chemical Society Reviews*, 39 (2010) 4370-4387.

- [35] S. Escolastico, M. Ivanova, C. Solís, S. Roitsch, W.A. Meulenber, J.M. Serra, *RSC Advances*, 2 (2012) 4932-4943.
- [36] T. Norby, Y. Larring, *Current Opinion in Solid State and Materials Science*, 2 (1997) 593-599.
- [37] H. Iwahara, H. Uchida, K. Ono, K. Ogaki, *J. Electrochem. Soc.*, 135 (1988) 529-533.
- [38] K.D. Kreuer, *Solid State Ion.*, 97 (1997) 1-15.
- [39] R. Haugrud, C. Kjøseth, *Journal of Physics and Chemistry of Solids*, 69 (2008) 1758-1765.
- [40] C. Solís, S. Escolastico, R. Haugrud, J.M. Serra, *The Journal of Physical Chemistry C*, 115 (2011) 11124-11131.
- [41] S. Escolástico, C. Solís, T. Scherb, G. Schumacher, J.M. Serra, *Journal of Membrane Science*, 444 (2013) 276-284.
- [42] J.H. Kuo, H.U. Anderson, D.M. Sparlin, *J. Solid State Chem.*, 87 (1990) 55-63.
- [43] S.P. Jiang, Y. Yan, M. Lu, *Materials for High-Temperature Fuel Cells*, Wiley, 2013.
- [44] D. Fu, M. Itoh, *Ferroelectricity in Silver Perovskite Oxides*, INTECH Open Access Publisher, 2011.
- [45] G. Rijnders, *Nat Mater*, 13 (2014) 844-845.
- [46] B. Guan, W. Li, H. Zhang, X. Liu, *J. Electrochem. Soc.*, 162 (2015) F707-F712.
- [47] K. Zhao, Q. Xu, D.-P. Huang, M. Chen, B.-H. Kim, *Ionics*, 18 (2012) 75-83.
- [48] G. Amow, I.J. Davidson, S.J. Skinner, *Solid State Ion.*, 177 (2006) 1205-1210.
- [49] B.X. Huang, J. Malzbender, R.W. Steinbrech, *J. Mater. Sci.*, 46 (2011) 4937-4941.
- [50] M.A. Laguna-Bercero, N. Kinadjan, R. Sayers, H. El Shinawi, C. Greaves, S.J. Skinner, *Fuel Cells*, 11 (2011) 102-107.
- [51] A. Mehta, P.J. Heaney, *Phys. Rev. B*, 49 (1994) 563-571.
- [52] E.N. Naumovich, V.V. Kharton, *Theochem-J. Mol. Struct.*, 946 (2010) 57-64.
- [53] V.V. Kharton, A.P. Viskup, A.V. Kovalevsky, E.N. Naumovich, F.M.B. Marques, *Solid State Ion.*, 143 (2001) 337-353.
- [54] G. Amow, S.J. Skinner, *J. Solid State Electrochem.*, 10 (2006) 538-546.
- [55] J.M. Bassat, Boehm, E., Grenier, J. C., Mauvy, F., Dordor, P. and Pouchard, M., in: J. Huijsmans (Ed.) *5th European Solid Oxide Fuel Cell Forum*, 2002, pp. 586-593.
- [56] F.S. Baumann, Stuttgart University, Stuttgart, 2006.

-
- [57] J.T.S. Irvine, D. Neagu, M.C. Verbraeken, C. Chatzichristodoulou, C. Graves, M.B. Mogensen, *Nature Energy*, 1 (2016) 15014.
- [58] S.B. Adler, *Chem. Rev.*, 104 (2004) 4791-4843.
- [59] M. Vogler, A. Bieberle-Hütter, L. Gauckler, J. Warnatz, W.G. Bessler, *J. Electrochem. Soc.*, 156 (2009) B663-B672.

4

Methodology

4. Methodology

4.1. Material synthesis

In the last decades different synthesis methods have been employed for the solids preparation, due to the interest of the solids properties. The method chosen for any solid will not only depend on the solid composition but also on its final application. Three are the most common methods for solid synthesis: solid state reaction, Pechini method and co-precipitation method. In the following sections will be explained in detail.

4.1.1. Solid state reaction (SSR)

The simplest and the most common method for preparing solids is the ceramic method [1, 2]. This method consists of heating together two or more solids (non-volatiles), which react to form the desired solid. The rate of diffusion in solid state reactions can be improved by increasing temperature or by introducing defects. Since solid state reactions take place only at the interface of two solids, by raising temperature the interface reactions are promoted and the diffusion through the solid is accelerated. Even so, diffusion is often the limiting step. In general, the reaction occurs in the solid state, since the temperature of the reaction does not achieve the melting temperature of the solid. Regarding the introduction of defects, the idea consists of starting with reagents that can be decomposed prior or during reaction, such as carbonates or nitrates.

The nucleation rate is another important parameter in SSR and can be maximized by introducing reactants with similar crystal structure to the desired compound.

The procedure (Figure 4.1) consists of taking stoichiometric amounts of the binary oxides, grind them in a pestle or with a ball mill to give a uniform small particle size, to maximize the surface contact and minimize the distance that reactants have to diffuse. Taking into account that in SSRs large surface areas of the reagents are desired to maximize the contact between reactants, the pelletization of powder is used before the sintering to promote an intimate

contact between particles. Then, the resultant pellets are heated in a furnace for several hours to obtain a single phase.

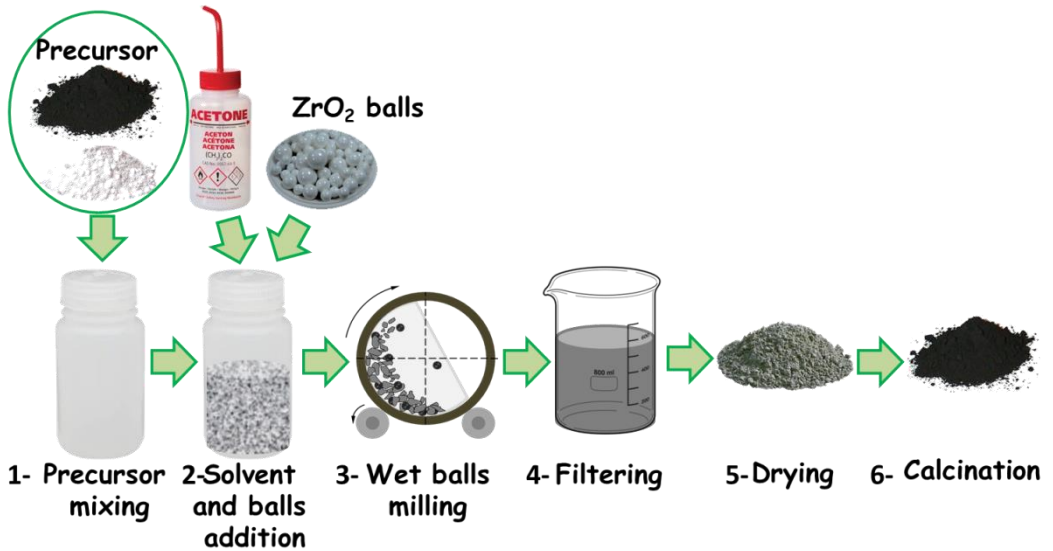


Figure 4.1: Solid State Reaction for pure multicomponent phase formation

Despite this method is widely employed due to the simplicity and low manufacturing cost, some disadvantages should be overcome. The most important are the low kinetics and the high temperatures required. Furthermore, there is low homogeneity of the samples with the presence of secondary phases and uncontrolled particle sizes [3]. However, with a good optimization, high quality ceramics can be obtained.

As has been described in the previous chapter, perovskites are one of the most widely employed materials for cells at high temperature. Since most perovskite oxides are stable at high temperature and are usually formed at temperature above 1273 K, SSR can be used for the perovskite formation. However, the perovskites powders obtained by solid state reactions usually exhibit a small surface area. As a result, different methods are preferred to obtain higher surface areas more useful for fuel cell applications.

4.1.2. Pechini

Pechini method (Figure 4.2) is a variation of sol-gel route where a highly homogeneous and finely dispersed oxide is obtained [4-6]. This technique only requires a beaker, a stirrer, inexpensive chemicals, hot plate and furnace. Inert atmospheres or control of water in the synthesis method is not required. This method includes a metal complex formation and polymerization of the organics agents. Firstly, precursors of the final compound composition are dissolved in distillate water. Then, a chelating agent, such as citric acid or EDTA is added to form stable metal complexes. The formation of citric complexes favors the homogeneous dispersion of the different ions and prevents the segregation of ions in later stages of the synthesis route. The solution is stirred and a polyalcohol, such as ethylene glycol (EG), is introduced for the polymerization process. Then, the temperature is increased to 100-130 °C to speed up the formation of polyester, due to the reaction of citric acid and the EG, resulting in a gelation of the reaction mixture and subsequent foaming. The organic part is subsequently eliminated at temperatures as low as 500 °C, thereby forming reactive oxides. Finally, the obtained powder is calcined at higher temperatures for the pure multicomponent phase formation.

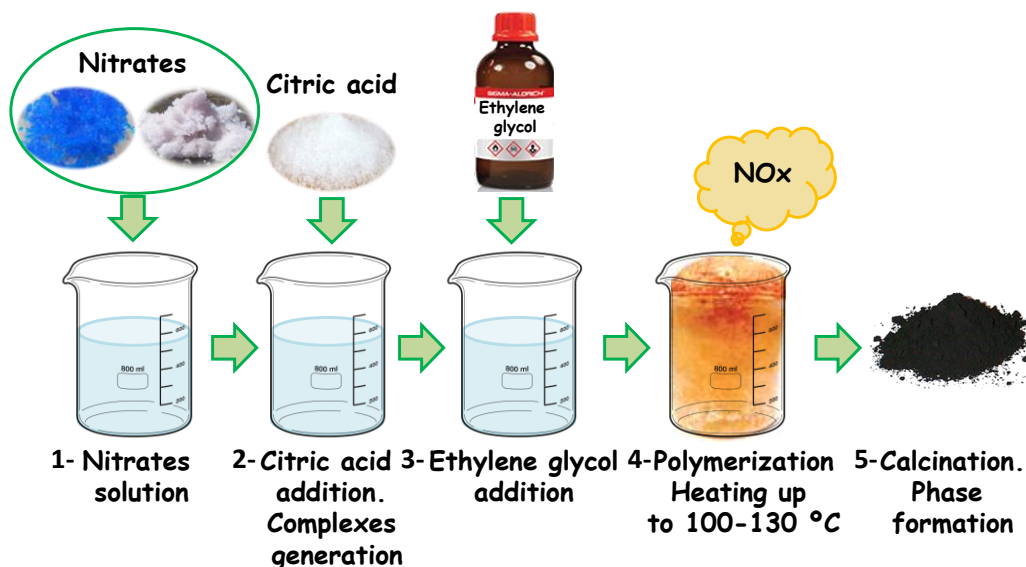


Figure 4.2: Pechini route for pure multicomponent phase formation.

4.1.3. Co-precipitation

The co-precipitation method allows the synthesis of nanometric size powders. In the co-precipitation route, stoichiometric amount of soluble salts of the metals ions is dissolved and then is precipitated as hydroxide, citrates, oxalates or formates [2]. Three are the main steps of the precipitation process, the liquid mixing, nucleation and crystal growth to form primary particles, and aggregation of the primary particles. The variation of the type of nucleation will depend on the concentration of the solution, temperature, surfactant used and co-precipitating agents. As a result, the variation of the parameters can lead to different particles sizes and aggregates [7]. The resultant mixture is filtrated, dried and calcined in the case of solid oxides (Figure 4.3), whereas the solid acids as CsH_2PO_4 are only dried (Figure 4.4).

Solid oxide formation method

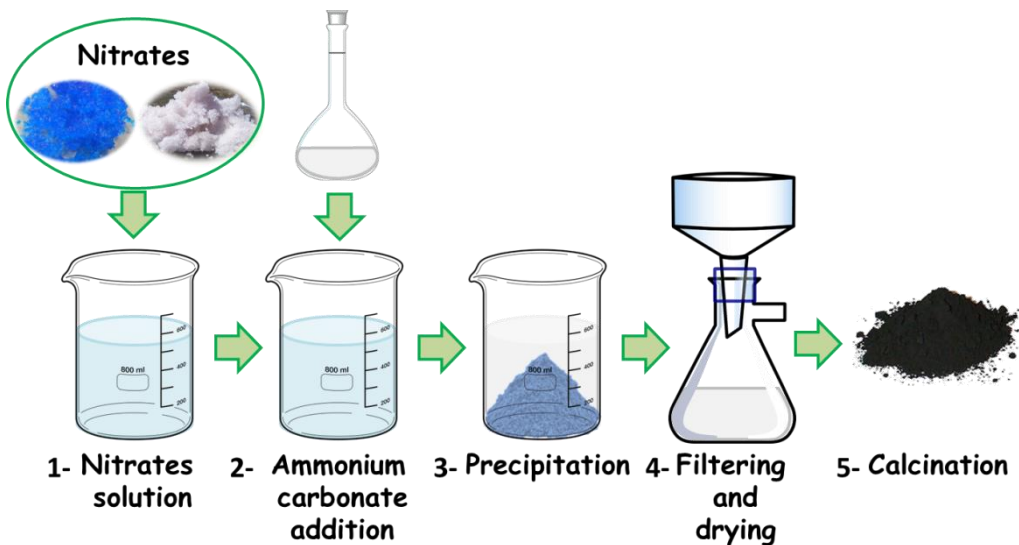


Figure 4.3: Co-precipitation route for pure solid oxide phase formation.

Solid acid formation method

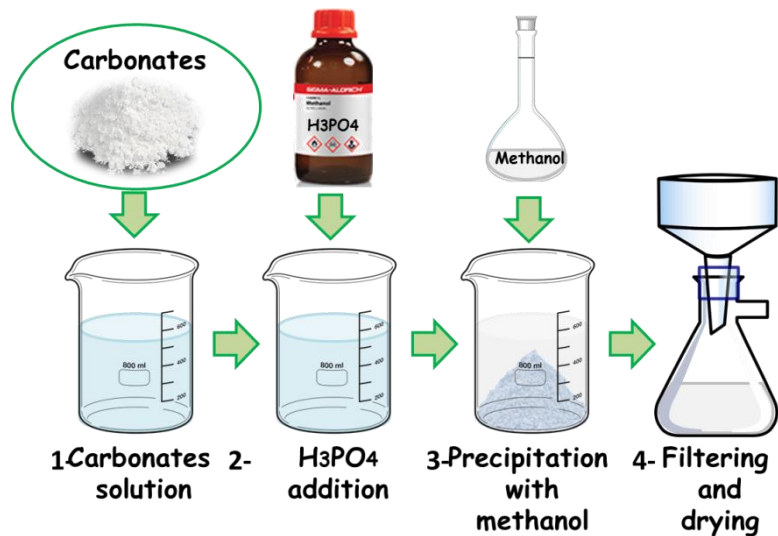


Figure 4.4: Precipitation route for pure solid acid phase formation.

4.2. Materials summary

The different compounds used in the present thesis, for the cell components, and the synthesis routes employed are listed in the table below. Furthermore, the maximum temperature achieved for the single phase formation are also included in the Table 4.1.

Compound	Abbreviation	Synthesis method	Final temp. (°C)	Observations
$\text{Ba}_{0.5}\text{Sr}_{0.5}\text{Co}_{0.8}\text{Fe}_{0.2}\text{O}_{3-6}$	BSCF	SSR	1150	
$\text{Ba}_{0.5}\text{Sr}_{0.5}(\text{Co}_{0.8}\text{Fe}_{0.2})_{0.97}\text{Y}_{0.03}\text{O}_{3-6}$	BSCF_Y	SSR	1150	
$\text{Ba}_{0.5}\text{Sr}_{0.5}(\text{Co}_{0.8}\text{Fe}_{0.2})_{0.97}\text{Zr}_{0.03}\text{O}_{3-6}$	BSCF_Zr	SSR	1150	
$\text{Ba}_{0.5}\text{Sr}_{0.5}(\text{Co}_{0.8}\text{Fe}_{0.2})_{0.97}\text{Sc}_{0.03}\text{O}_{3-6}$	BSCF_Sc	SSR	1150	
$\text{La}_2\text{NiO}_{4+6}$	LNO	Pechini	1350	
$\text{La}_{1.5}\text{Pr}_{0.5}\text{NiO}_{4+6}$	LPNO	Pechini	1350	
$\text{La}_2\text{Ni}_{0.8}\text{Co}_{0.2}\text{O}_{4+6}$	LNCO	Pechini	1350	
$\text{La}_{1.5}\text{Pr}_{0.5}\text{Ni}_{0.8}\text{Co}_{0.2}\text{O}_{4+6}$	LPNCO	Pechini	1350	
$\text{Nd}_2\text{NiO}_{4+6}$	NdNO	Pechini	1350	
LaPrNiO_{4+6}	LPNO11	Pechini	1350	
$\text{La}_{0.8}\text{Sr}_{0.2}\text{MnO}_{3-6}$	LSM			Commercial powder
$\text{Ce}_{0.8}\text{Gd}_{0.2}\text{O}_{2-6}$	GDC	Coprec.	800	
$\text{La}_{0.85}\text{Sr}_{0.15}\text{Cr}_{0.8}\text{Ni}_{0.2}\text{O}_{3-6}$	LSCNi	Pechini	900	
CsH_2PO_4	CDP	Prec. acid salts	80	
$\text{La}_{5.5}\text{WO}_{12-6}$	LWO			Commercial powder

Table 4.1: Synthesis conditions of the different compounds used.

4.3. Structural characterization

After the synthesis of the different compounds, some structural characterization should be performed. In the present thesis, all materials were checked by X-Ray Diffraction (XRD) to determine the crystalline phase. Those measurements were done to verify that single phases were obtained after synthesis and no reactivity between the different cells components was produced. Furthermore, the powders obtained after materials synthesis and the different cell components were studied by Scanning Electron Microscopy (SEM) and Field Emission Scanning Electron Microscopy (FESEM). Finally, thermogravimetric analyses (TGA) were employed for the characterization of some materials in specific conditions. A detailed description of the techniques used is included below.

4.3.1. X-Ray Diffraction (XRD)

X-ray diffraction technique is a non-destructive technique which reveals information about crystallographic structure, chemical composition, crystallite size (grain size) and preferred orientation [8].

X-rays are transverse electromagnetic radiations, similar to visible light, but with shorter wavelength. They are produced via interactions of the accelerated electrons of high energy with heavy metal target (the anode). When electrons hit this material, X-ray are generated at this point and radiated in all directions. When a monochromatic X-ray beam encounters a material, it interacts with the atoms [9]. The atomic lattice of the sample acts as a three-dimensional scattering grid producing the diffraction of the X-rays to specific angles. Because each crystalline material has a special atomic structure, it will diffract X-rays in a unique characteristic pattern. The angle (θ) and the spacing of the atoms (d) can be related with the wavelength (λ) by means of the Bragg equation:

$$\lambda = 2d \cdot \sin \theta \tag{4.1}$$

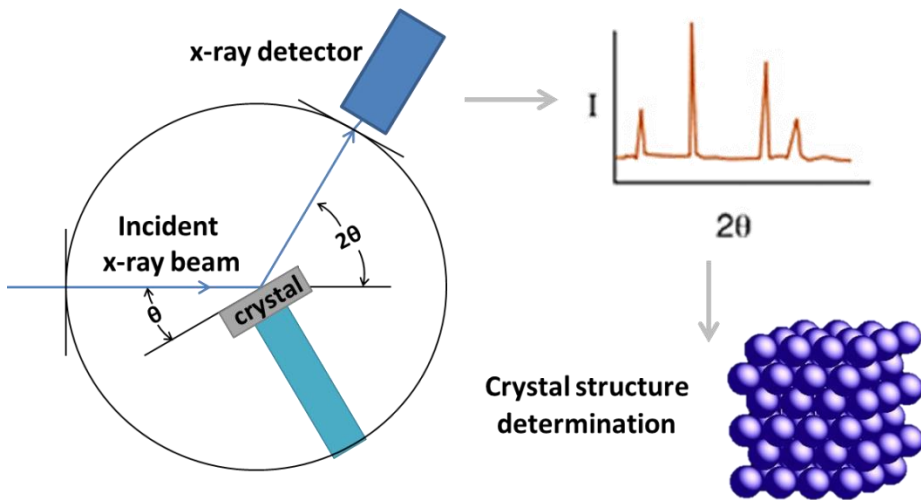


Figure 4.5: X-ray diffractometer and X-ray pattern for the crystal structure determination.

Figure 4.5 illustrates how crystalline structure can diffract X-rays with a specific angle. The detector reports the intensity (I) of the X-ray diffracted. The angles of diffraction are characterized by peaks, and the height of peaks is function of the interaction of the X-ray with the crystal and the intensity of the source. From the diffraction pattern, that includes angles and intensities, it can determine the type of material, since every crystalline material will give a characteristic diffraction pattern. Furthermore, the position of the diffracted peaks also provides information about the unit cell size and lattice parameters, since the atoms arrangement in the crystalline compound can be determined. In addition, information about the crystallite size and the microstrain can be obtained. Thus, the data generated from the X-ray diffraction can be interpreted and refined to obtain the crystal structure.

Crystals exhibit a regular, repetitive structure. The unit cell is the smallest volume element that by repetition in three dimensions describes the crystal. The unit cell can be defined by the cell edge lengths (a , b and c) and three angles (α , β and γ). Where α is the angle between b and c , β is the angle between a and c , and γ is the angle between a and b . Different combinations of these parameters release fourteen kinds of lattice systems [10] and that where defined by August Bravais. The fourteen kinds of lattice systems are summarized in Figure 4.6, and divided in the seven possible crystal systems.

The data collected from X-ray can provide structural information and determine the cells parameters.

XRD measurements in the present thesis were carried out in a PANalytical Cubix fast diffractometer by using CuK α 1,2 radiation. XRD patterns were recorded in the 2θ range from 20 to 90 ° and analyzed using the X'Pert HighScore Plus software.

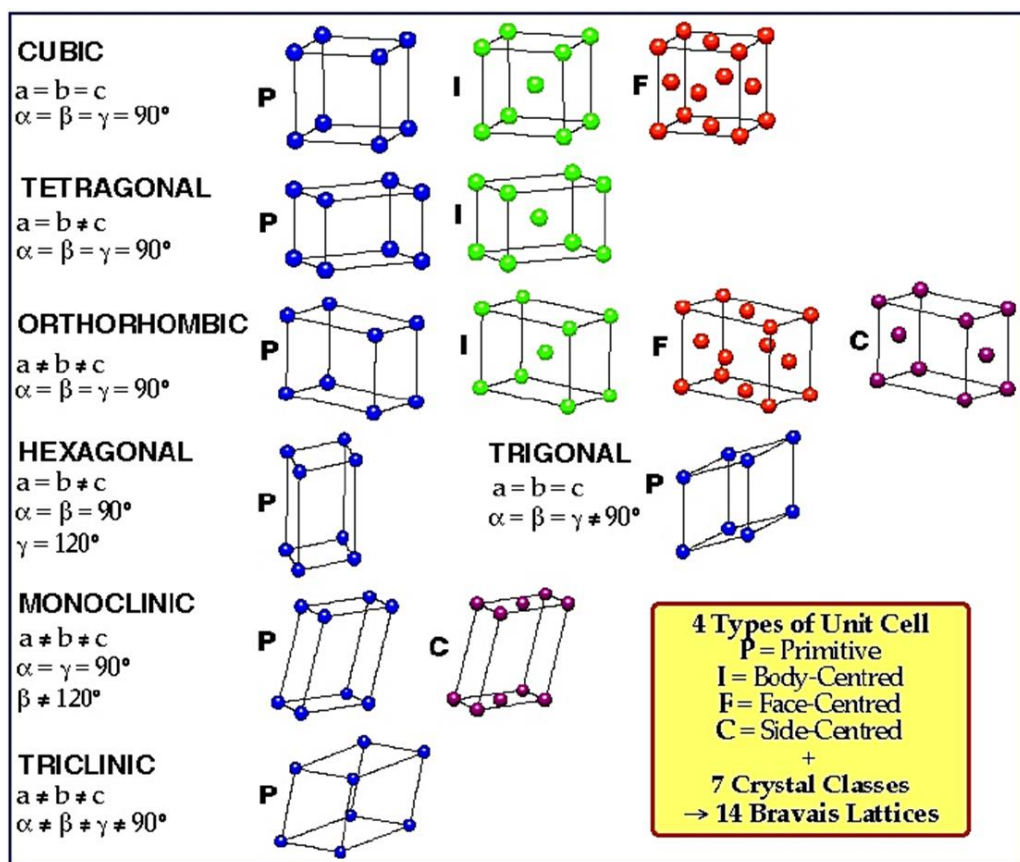


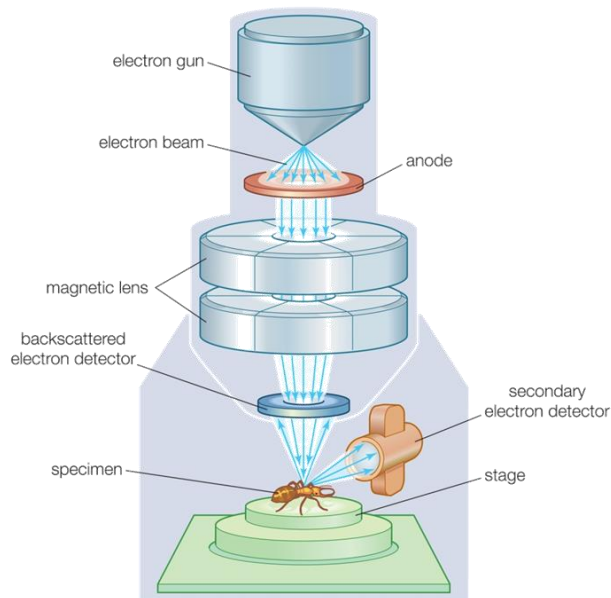
Figure 4.6: The 14 Bravais lattices

Lattice refinement techniques, such as Rietveld refinement, are a good support to provide accurate structural information. The Rietveld refinement is a structural refinement method but also can play an important role for the elucidation of crystal structures. The X-ray diffraction pattern can be simulated

using Rietveld refinement software. Different parameters can be varied, as site occupancies, atomic displacement parameters or unit cell coordinates to match the experimental data as much as possible to the simulated data. The Rietveld refinement can provide information, as the quantitative phase analysis, percentage of the crystallinity of the material, unit cell size, characterization of the cell with atomistic resolution, crystallite size and global residual strain.

4.3.2. Scanning Electron Microscopy (SEM)

Scanning Electron Microscopy (SEM) is a technique where electrons from a focused beam are rastered across the surface of the sample to create an image [2]. The electrons interact with the specimen, producing different signals that can be collected for the detector obtaining different information about the sample. The SEM column consist of an electron gun, two condenser lens, an objective lens, and electron detection system, and a set of deflectors, all operating in a vacuum [11].



© 2012 Encyclopædia Britannica, Inc.

Figure 4.7: SEM device description.

As is described in Figure 4.8, as the primary beam penetrates the specimen surface, it scatters as a variety of signals. The scattered electrons that escape from the atoms occupying the top surface specimen are known as secondary electrons (SE) and are created by inelastic collisions. The back scattered electrons (BSE), are scattered from deeper levels and are generated by multiple elastic collisions. Secondary electrons and backscattered electrons are usually used for imaging samples. Whereas SE are most valuable for showing topography and morphology of samples, BSE is most common to use it for drawing contrasts in composition in multiphase samples. X-ray is produced by inelastic collisions of the incident electrons with the electrons in the orbitals of the sample. Thus, the X-ray generated depends on the excited element by the electron beam. The X-ray can be used to determine the compositions of the sample, since is well-known the energetic levels of electrons in different shells for a certain element.

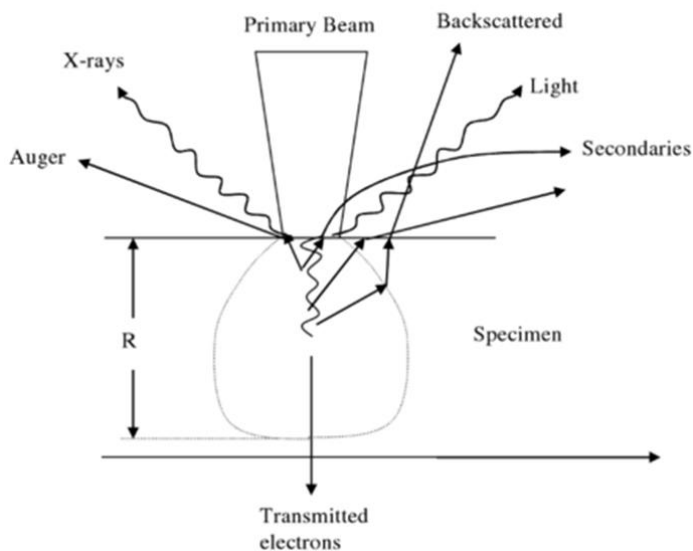


Figure 4.8: Interaction volume and emitted signals from beam/specimen interaction [11].

Field emission scanning electron microscopy (FESEM) is an equipment where the fundamentals are the same as SEM but the main difference is the emission source. In SEM the emission source is thermionic emitter whereas in FESEM is a field emitter. In thermionic emitters, electrical current is used to heat up the

filament, and the most common materials for filaments are Tungsten (W) and Lanthanum Hexaboride (LaB_6). In the case of FESEM, the emission is reached by placing the filament in a huge electrical potential gradient, and the filament material is usually Tungsten. Comparing between SEM and FESEM, the second equipment produces clearer and less electrostatically distorted images with higher spatial resolution.

SEM and FESEM techniques can be used in the electrochemical cells to characterize the cell components. Images of the morphology and topography can be obtained by SEM or FESEM with SE. In addition, the BSE is a useful technique to distinguish between phases in composite electrodes. Finally, X-ray generated from SEM or FESEM can allow the identification of possible elements diffusion or reactions between the components materials.

The SEM used in the present thesis was a JEOL JSM6300 electron microscope, whereas FESEM equipment was a ZEISS Ultra55.

4.3.3. Transmission Electron Microscopy (TEM)

Transmission electron microscopy (TEM) is a microscopy technique whereby an electron beam is accelerated and pass through a strong magnetic field that acts as a lens [12, 13]. The electron beam is transmitted through an ultra-thin specimen. Due to the interaction of electrons with the specimen, an image is formed, and is magnified and focused onto a detector. TEM was developed due to the limited image resolution in light microscopes. Since electrons are smaller than atoms that technique allows obtaining images below the atomic level. Contrast images are obtained as results of the electrons interaction with the sample; darker areas are product of heavier elements and denser areas (higher electron scattering). The orientation of crystals and crystal planes will produce a diffraction contrast.

Different information can be obtained from TEM: morphology of the specimen as shape, size and organization of particles, crystallographic information as the arrangement of atoms and compositional information.

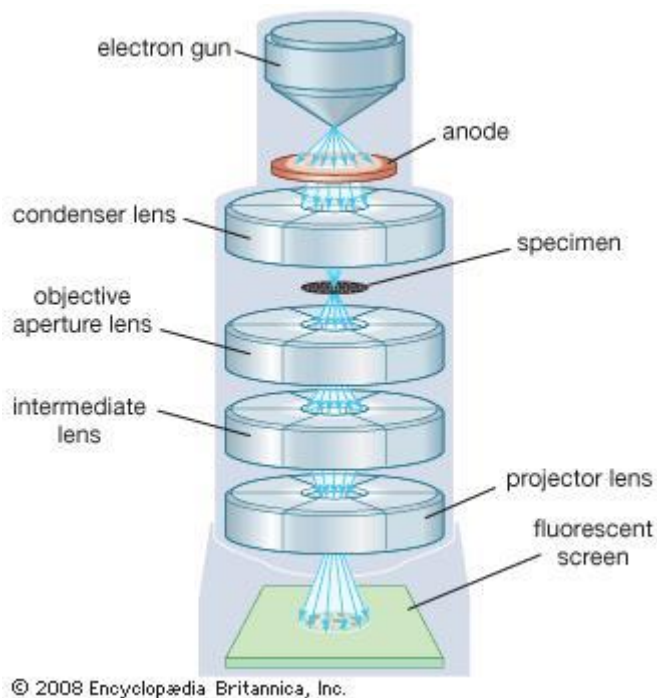


Figure 4.9: TEM device description.

Energy Dispersive X-Ray Analysis (EDX) is an x-ray technique used to identify the elemental composition of materials. EDX system is attached to SEM and TEM instruments. An electron vacancy in the inner part of atoms (which is usually full) is produced by the electron bombardment, and electron of outer part fills the vacancy generated. Characteristic X-Rays results from the electrons transitions in the inner part of the atoms. Quantitative analysis can be done by measuring the intensity of each element in the sample and for the same elements in calibration standards of known composition [14].

4.3.4. Thermogravimetric Analysis (TGA)

Thermogravimetric analysis (TGA) is an experimental technique where the mass change of substance is measured as function of increasing the temperature, or isothermally as a function of time [15]. Different atmospheres can be used for the measurements as nitrogen, air, others gases or in vacuum. The choice of the temperatures and the atmospheres of TGA will depend upon the type of information required about the sample. For instance, in

electrochemical cells is important to control the reactivity of the electrodes materials with the presence of CO_2 , thus a TGA can be performed in CO_2 containing atmospheres to know if the carbonation of the sample is produced. For instance, cathodes working in air atmospheres in fuel cell conditions should be stable with contents of CO_2 up to 1% (atmospheric air). However, electrodes for co-electrolysis mode have to be stable up to 15% of CO_2 . Furthermore, it can obtain the decomposition temperature of the sample, by measuring the mass change as function of temperature in a specific atmosphere.

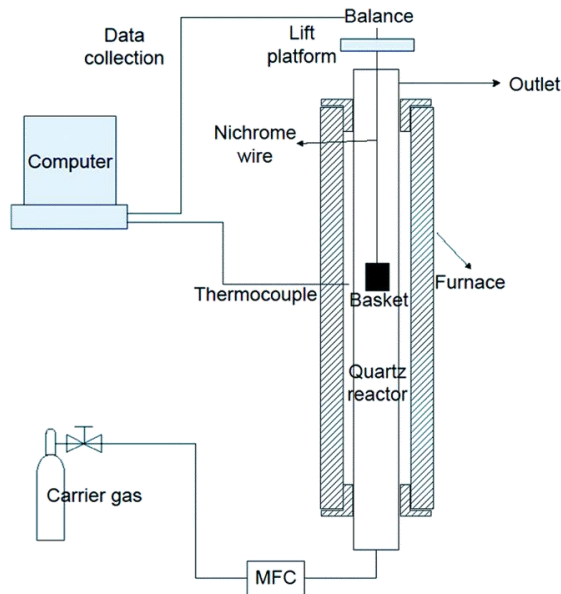


Figure 4.10: Schematic representation of the TGA equipment.

The results of TGA are usually presented as TGA curve in which mass or per cent of mass is plotted against time or temperature [16]. An additional plot of the first derivate of TGA will give information of the rate at which the mass changes. Furthermore, mass changes (loss or gain) will produce steps in TGA curves, which will be ascribed to the different possible effects. Some of the possible effects related with the materials studied in this thesis are described below:

- Evaporation of volatile compounds, as the loss of water.
- Oxidation of the compounds, as the oxidation of metals in air.

- Reduction of compounds in presence of hydrogen.
- Heterogeneous reactions, where the sample reacts with the surrounding atmosphere.
- Decomposition of carbonates, sulfates, nitrates, etc.

4.4. Sample preparation

Before the electrochemical characterization, all materials synthesized in the laboratory or purchased for that purpose were processed. Depending on the final characterization, different methods were used, and can be encompassed in two main processes: densification of samples and electrodes production.

4.4.1. Dense samples

Depending on the final and electrochemical application, two different types of dense samples were prepared. The main difference was the geometry of the samples. For DC conductivity measurements rectangular probes were obtained, whereas for the cells test dense discs were manufactured. The as prepared powder was mixed with acetone and zirconia balls. The mixture was ball milled during 12-15 h to decrease and homogenize the particle size. After milling, the solution was dried in order to eliminate the acetone. Powder was uniaxially pressed and subsequently calcined for the densification of the sample. The pressure of the press, the final temperature and time of annealing was different for each sample, depending on the composition of the powder and the particle size.

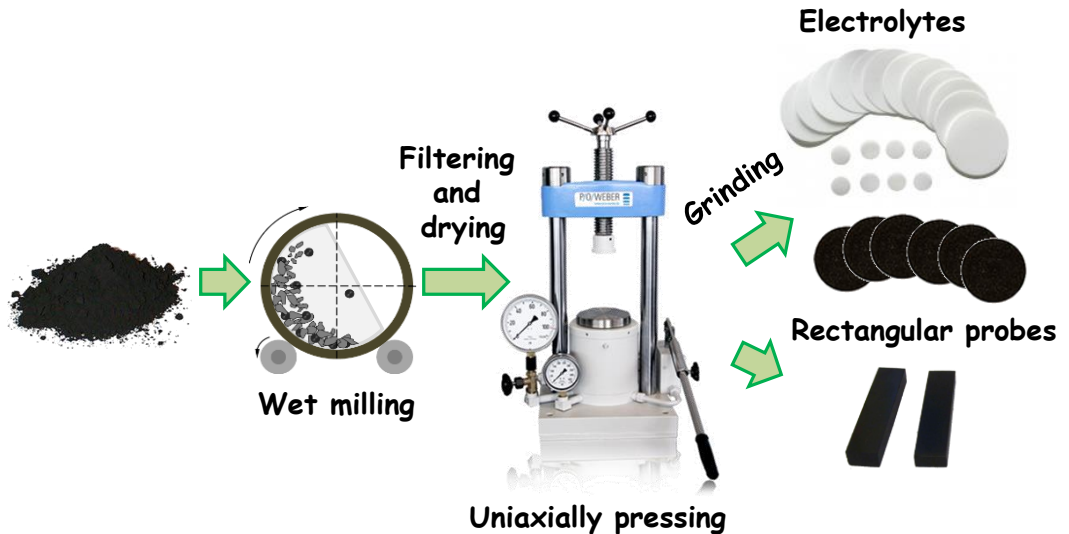


Figure 4.11: Main steps for rectangular probes and electrolytes densification.

The final dimensions of samples after calcination are temperature and composition dependent, since the contraction of the initial powder is different for each material. Additionally, the electrolyte samples were grinded and polished to obtain a very flat disc and to fit the sample with the measurement cell set-up (diameter of 15 mm).

The densification of the materials is one of the most important steps for its final application. For instance, electrolyte should be as dense as possible, since the leakage of gases from one side to the other in the electrochemical cell would reduce the performance. In the case of rectangular probes, the densification is very important for the accuracy of the DC-conductivity results. The possible porosity in samples should be taken into account for the correction of the final conductivity values. The firing temperature of the rectangular probes will be specified in the different chapters.

A summary of the electrolyte materials used in the thesis, with the pressure of the press and calcination temperature is shown in the following table:

Compound	Abbreviation	Press parameter	Final temperature calcination
CsH_2PO_4	CDP	40 kN (3min)	-
$\text{Ce}_{0.8}\text{Gd}_{0.2}\text{O}_{2-\delta} + 5\%\text{CoO}_x$	GDC	130 kN (3min)	1560 °C (4h)
$\text{La}_{5.5}\text{WO}_{12-\delta}$	LWO	40 kN (3min)	1560 °C (6h)

Table 4.2: Parameters for discs densification.

4.4.2. Electrodes preparation

The preparation of thick porous layers as electrodes was one of the most critical points in the fabrication steps during the present thesis. Different factors should be taken into account, and most of them have been described in the *Introduction chapter*. As a summary, the most important are: good porosity for gas diffusion, good attachment with the electrolyte but avoiding the reactivity between them, homogeneity of electrode and small particle size to increase the surface area for the electrochemical reactions.

The electrode configuration will depend on the starting materials and the following section is focused on the electrodes configuration used in the present thesis: single material electrodes, composite electrodes and backbone electrodes infiltrated by a catalyst.

Electrodes for high temperature electrochemical cells

The main steps followed for the electrodes fabrication for high temperature cells, are described in Figure 4.12. The as fabricated powder is ball milled with acetone and ZrO_2 balls. With this step is possible to obtain small particles size and a good homogeneity. After drying and rinsing the powder, this is grinded and sieved. If the intention is to obtain a composite electrode, both powders are mixed in a mortar and are sieved as well. Then, powder, an organic binder (ethyl cellulose) and a plasticizer are blended to make a viscous ink. To refine the powder and to obtain a uniform ink, a three-roll mill is employed. Later on, the slurry is deposited on the top of the electrolyte by screen printing. This technique is one of the most cheap deposition techniques. The procedure

consists of squeezing the slurry to pass through a 9 mm diameter screen. The thickness of the electrode will change as function of the number of times that this step is repeated and the type of screen employed. After drying the layer (temperature of 80 °C), it is possible to deposit another layer. The thickness of the layers obtained is $\approx 30 \mu\text{m}$ with an area $\approx 0.64 \text{ cm}^2$. After that, the layer is calcined at high temperature to obtain a good attachment between the electrode and the electrolyte. The sintering temperature will differ for each composition. Finally, a gold mesh is applied with the same technique on the top of the electrode and it is calcined at 900 °C during 2h, the gold mesh will allow a good contact between the electrode and the set-up current collector. For some of the electrodes tested, a catalyst was infiltrated in the electrode. For that purpose, a solution of the precursor, usually nitrates, is dropped in the electrode and after drying is fired to eliminate the nitrates, obtaining an oxide.

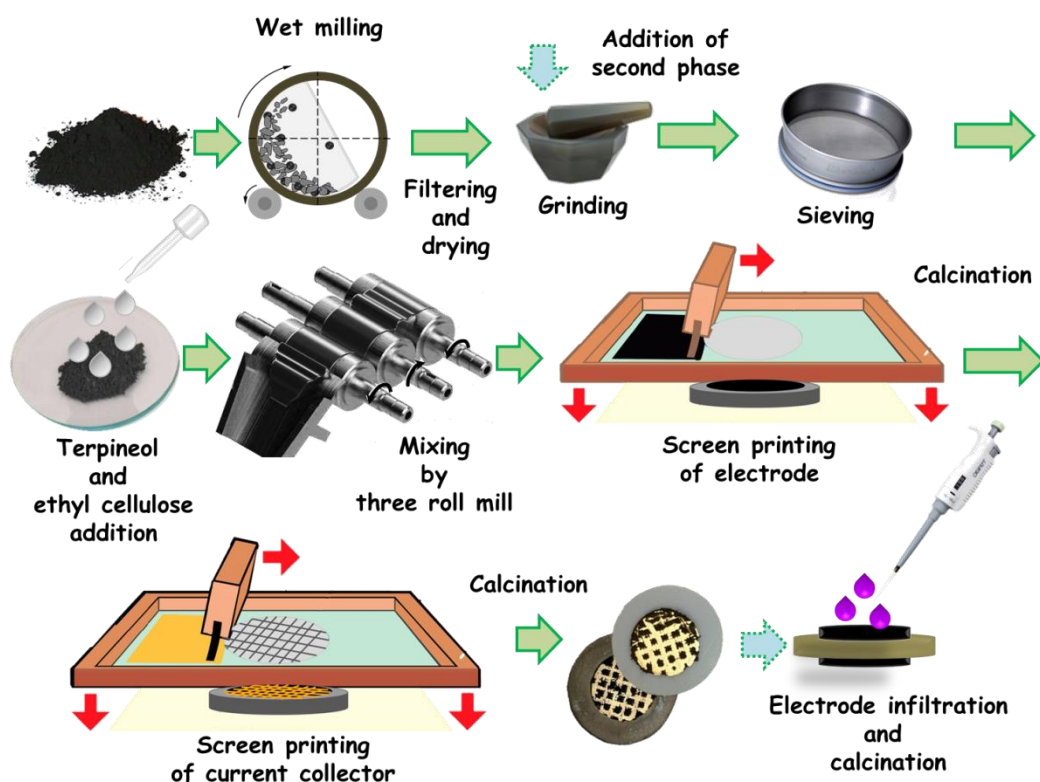


Figure 4.12: Main steps for high temperature electrodes fabrication.

Electrodes for low temperature electrochemical cells

Due to the restriction of the temperature for the electrolyte material for low temperature (CsH_2PO_4), different techniques were employed. The electrodes were obtained by using carbon paper or nickel substrate as scaffolds, or by preparing composite electrodes. In Figure 4.13 are briefly described the main steps followed for the low temperature electrodes production. In the first method, drawn with green arrows, the scaffold of carbon paper or nickel substrate is immersed in a solution with the electrocatalyst dissolved. Then, an ultrasound bath is used during 10 minutes to ensure that the solution goes into the bulk and the precursor is covering the whole material surface. Then, the support is taken from the solution and is dried. After n-times repetitions (depending on the precursor) the support is annealed under oxidizing or reducing conditions. If the final catalyst is a metal, hydrogen will be used whereas oxides will be obtained by calcining in air.

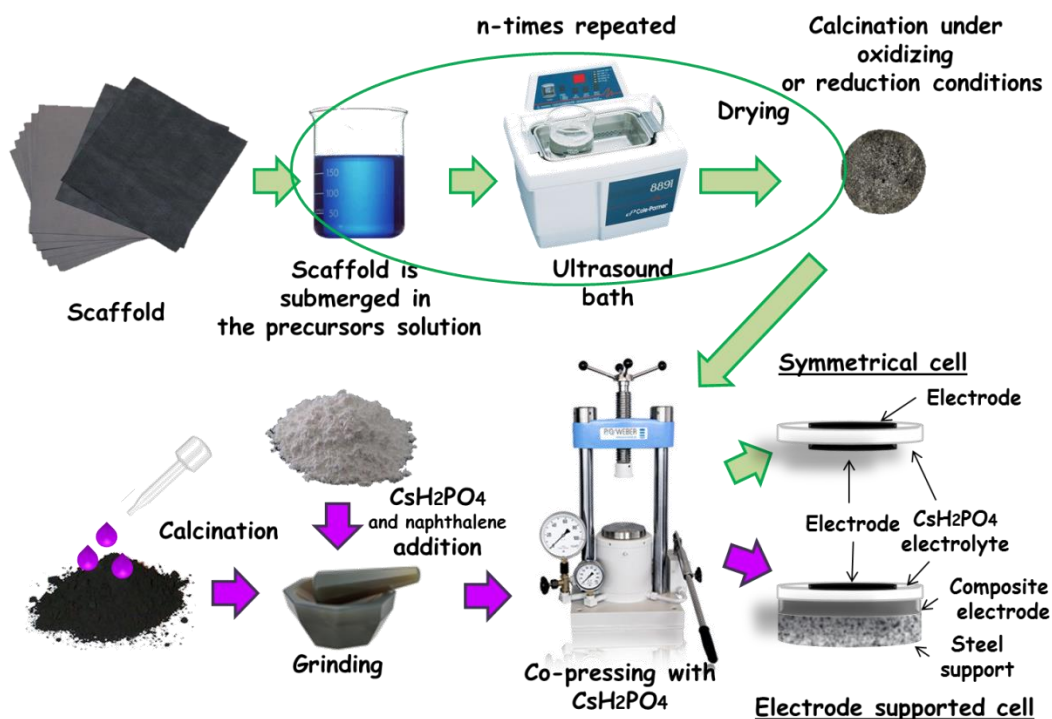


Figure 4.13: Main steps for low temperature electrode fabrication.

In the second method, described by purple arrows (Figure 4.13), a composite electrode is obtained by mixing the electrolyte material (CsH_2PO_4), naphthalene and carbon impregnated with some precursors (previously calcined). The mixture is homogenized by a mortar and is finally co-pressed with the powder for the electrolyte and the other electrode. In this type of cells a steel support is usually used for the mechanical stability of the sample. Naphthalene is evaporated in the reactor and is used as porous former additive in the electrode.

During the present thesis the electrodes, for both range of operation temperature, were tested as symmetrical cells, using the same electrode material for both sides of the electrolyte or in a fully-assembled cell, with different electrodes on both sides.

4.5. Electrochemical characterization

After sample preparation, different electrochemical characterization were performed in order to test the materials synthesized and to be able to optimize materials by tailoring their properties depending on the test results.

4.5.1. DC total electrical conductivity

Electrical conductivity measurements were carried out by standard four-point DC technique. For that purpose, rectangular bars were made as was explain in section 4.4.1 *Dense samples*. Silver wires and paste were used for the electrical current contact and lead as shown in the following picture:

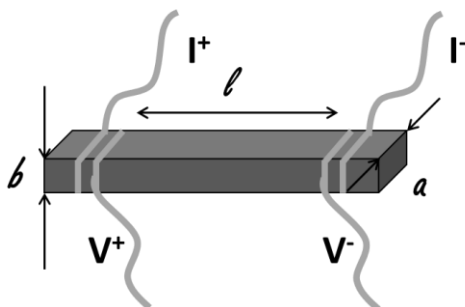


Figure 4.14: Rectangular bar configuration for DC total electrical conductivity.

Measurements were carried out in different oxygen partial pressure in the range of 400-800 °C, by cooling down with a slope of 1°C/min. The oxygen partial pressure was maintained during all range of temperatures and the samples were maintained at the highest temperature to achieve the stabilization of the conductivity before cooling down the samples. The oxygen partial pressure was checked by an oxygen sensor and the gas mixture was supplied by Linde calibrated gases. The rectangular bars were tested in a set-up able to measure different samples simultaneously (Figure 4.15 (a) and (b)).

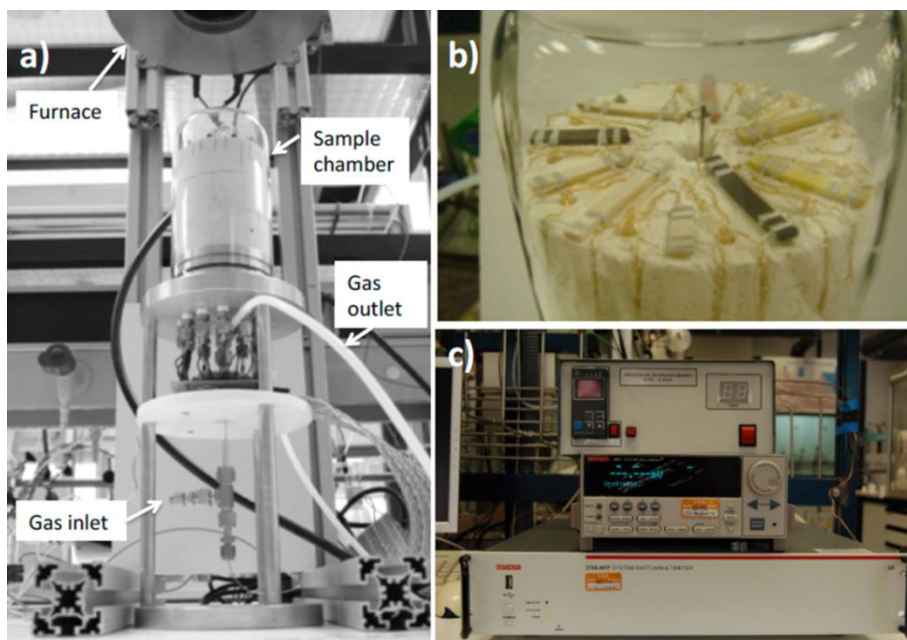


Figure 4.15: (a) Multisample DC conductivity measurement set-up, (b) chamber of the DC conductivity set-up and (c) furnace controller, programmable current source (Keithley 2601) and sixteen channel multimeter (Keithley 3706), from top to bottom.

A current DC ramp was applied to the outer wires of the sample with a Keithley 2601 programmable. The voltage difference between the inner wires was detected with a Keithley 3706 multimeter (Figure 4.15 (c)). In order to avoid the thermal effect and non-ohmic response, the voltage was measured by applying the current on both sides. From the slope of the I-V curves, collected from the equipment, was calculated the resistance exhibited by the sample. Taking into account the Ohm's law (Equation (4.2)) and the resistance

calculated, was possible to determine the total electrical conductivity (σ_{Total}) of the sample:

$$E = I \cdot R \quad (4.2)$$

$$\sigma_{\text{Total}} = \frac{l}{a \cdot b} \cdot \frac{1}{R} \quad (4.3)$$

Where a , b and l , are the rectangular bar dimensions; being a and b the width and thickness of the sample, respectively, whereas l is the distance between contacts, as is described in Figure 4.14.

The results can be analyzed in terms of the Arrhenius behavior since the measurements are thermally activated:

$$\sigma(T) = \frac{A_M}{T} \exp\left(\frac{-E_a}{k \cdot T}\right) \quad (4.4)$$

Being E_a , the activation energy, k the Boltzmann constant and A_M is a material constant. Or can be studied as function of the oxygen partial pressure, elucidating the conductivity mechanism; electron transport, electron hole transport, ionic conductivity, mixed conductivity, etc. For that purpose, it should be taken into account the formulas and the slopes of the $\sigma = f(pO_2)$ dependence shown in the *Chapter 3: Introduction*, section 3.2.2.

4.5.2. Electrochemical Impedance Spectroscopy (EIS)

In the electrochemical impedance spectroscopy an alternating current or voltages is applied to a sample, as function of frequency (Figure 4.16 (a)). The response will give information of the electrochemical processes, since each process in the cell takes place with a characteristic frequency.

In DC theory, where the resistance is independent of the frequency, AC current and voltage signals through a resistor are in phase with each other and the current and voltage follow the Ohm's law (Equation (4.2)). However, when these premises are not fulfilled and the behavior of samples is more complex, it is necessary to use impedance measurements. In EIS measurements the

dependence of the frequency is not zero, and it can be written an analogous equation:

$$E = I \cdot Z \quad (4.5)$$

The voltage excitation signal can be written as a function of time as follows:

$$E_t = E_0 \sin(\omega t) \quad (4.6)$$

Where E_t is the voltage at time t , E_0 is the amplitude of the signal and ω is the radial frequency. The relation between radial frequency and frequency in Hertz, is expressed by the next equation:

$$\omega = 2\pi f \quad (4.7)$$

In a linear system, the current response signal (I_t) is shifted in phase φ with different amplitude (I_0):

$$I_t = I_0 \sin(\omega t + \varphi) \quad (4.8)$$

Taking into account the Equations (4.5), (4.6) and (4.8), the impedance can be written as:

$$Z = \frac{E_0 \sin(\omega t)}{I_0 \sin(\omega t + \varphi)} = Z_0 \cdot \frac{\sin(\omega t)}{\sin(\omega t + \varphi)} \quad (4.9)$$

And the impedance as a complex function:

$$Z(\omega) = \frac{E}{I} = Z_0 \exp(j\varphi) = Z_0 \cdot \exp(\cos \varphi + j \sin \varphi) \quad (4.10)$$

As can be ascribed from Equation (4.10), the impedance is described by an imaginary part and real part. If is plotted the imaginary part on the y-axis and the real impedance on the x-axis, the result is the Nyquist plot that is shown in Figure 4.16 (b).

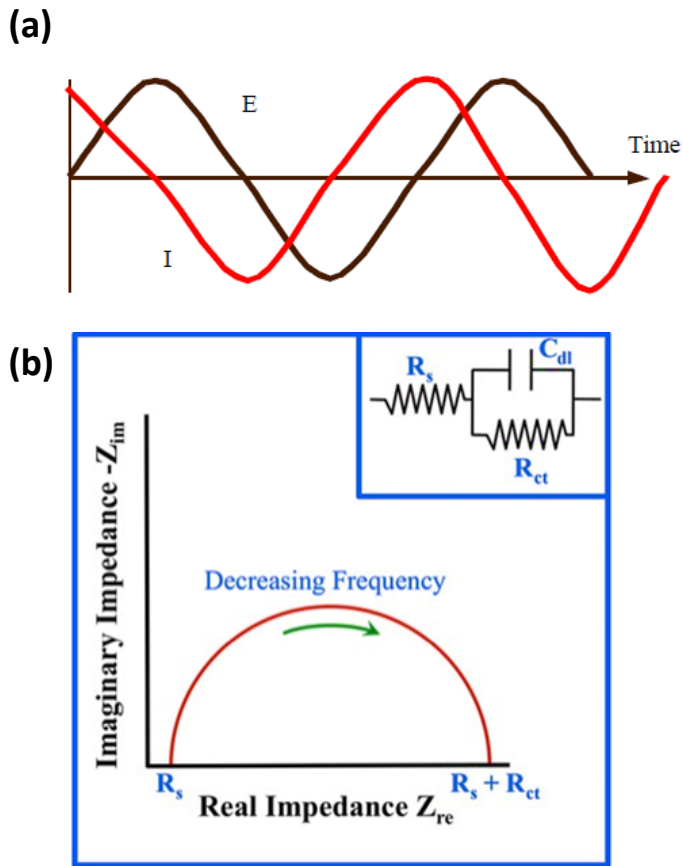


Figure 4.16: (a) Characteristic signal applied and response in an EIS measurement and (b) impedance results as function of the imaginary and real impedance. Inset represents the equivalent electrical circuit fitting for the EIS measurement response.

Usually, the most widespread methodology for the analysis of the EIS results consists of plotting the results and the subsequent fitting with equivalent electrical circuits. An example is shown in Figure 4.16 (b). This method allows distinguishing the different processes in the electrochemical cell. Each process take place with a characteristic frequency, for instance, electron or electron holes transport are almost instantaneous and take place at high frequencies. However, slower processes as the gas diffusion have a low associated frequency.

A summary of the most common electrical components employed for the equivalent electrical circuit fitting is presented below:

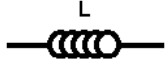

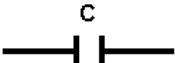

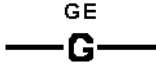

<i>Circuit element</i>	<i>Drawing</i>	<i>Impedance</i>	<i>Parameters</i>
<i>Inductor</i>		$(j\omega L)$	
<i>Resistance</i>		R	
<i>Capacitor</i>		$\frac{1}{(j\omega C)}$	
<i>Constant phase element</i>		$\frac{1}{T(l\omega)^P}$	CPE-T CPE-P
<i>Gerischer element</i>		$\frac{1}{Y_0\sqrt{2}} \sqrt{\frac{\omega^2 + K_a^2 + K_a}{\omega^2 + K_a^2}}$ $-i \sqrt{\frac{\omega^2 + K_a^2 - K_a}{\omega^2 + K_a^2}}$	GE-T= Y_0 GE-P= K_a
<i>Finite length Warburg</i>		$\frac{R \cdot \tanh([l T \omega]^P)}{(l T \omega)^P}$	Ws-R Ws-T Ws-P

Table 4.3: The most common circuit elements used for the equivalent electrical circuit fittings. Where l is the square root (-1) and ω the angular frequency of the AC signal.

Different combinations of the electrical components should be used depending on the material tested and the mechanisms that are occurring in the cell. Since the equivalent circuit depends on the material and the limiting processes, a detailed explanation will be done in each results chapter.

The acquisition data and the sinusoidal voltage/current signal were performed using the Solartron 1470E, as a source of voltage and current. The response was analyzed by 1455A frequency response analyzer. The Solartron equipment has two pair of wires, one for the current transport (+CE, counter electrode and -WE, working electrode) and the other for the voltage (+Re1, reference

electrode 1 and $-Re2$ reference electrode 2). Those wires are connected to platinum wires, that work as current collector, since are in contact with the sample as is shown below:

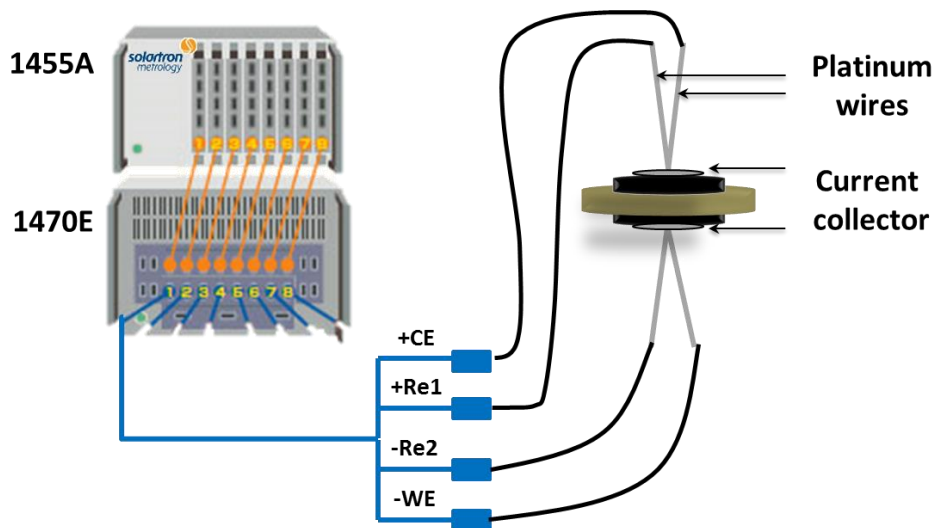


Figure 4.17: Connections between the Solartron equipment 1470E and 1455A module, with the electrochemical cell.

4.5.3. Fuel cell mode

After characterization and test of the material as electrode in single chamber symmetrical cells, using the same material on both sides of the electrolyte, the electrode materials were used in fully-assembled fuel cells. Cells, were composed of two different electrodes materials (in the case of high temperature fuel cells or some low temperature fuel cells) or the same material (in some of the low temperature fuel cells), acting each one as cathode and anode, respectively. The performance of a fuel cell can be assessed by the current-voltage curves [17]. In this type of measurements, the voltage response of a given current load is studied. The real performance of fuel cell is less than the ideal performance given by thermodynamics, due to the losses. Then, overall cell voltage can be written as follows [18-20]:

$$E_{cell} = E - \eta_A - \eta_{\Omega} - \eta_C \quad (4.11)$$

When there is no current load in the cell, the cell voltage measured is the open circuit voltage (OCV). In the OCV the overall reaction of the cell is in equilibrium. However, as the current load is increased, the overall cell voltage decreases as is described in Equation (4.11) and this is consequence of the three main polarization losses:

- η_A , activation polarization. An energetic barrier should be overcome for the reactive species to be active for the electrochemical reaction. In this region there is a big reduction of the overall cell potential (Figure 4.18a).
- η_Ω , ohmic polarization. These losses are the consequence of the ionic conductivity of the electrolyte, electronic or/and ionic conductivity of electrodes, electronic conductivity of current collectors and the contact between the different cell components. In this region of the i-V curves, the cell voltage follows a pseudo-linear fall.
- η_C , concentration polarization or mass transport. This contribution becomes important when the reaction of the cell is limited by the mass transport. The mass transport limitations can happen when the rate of reactants addition or products elimination is lower than the current demand. In this part of the i-V curves there is a huge decrease of the overall cell voltage.

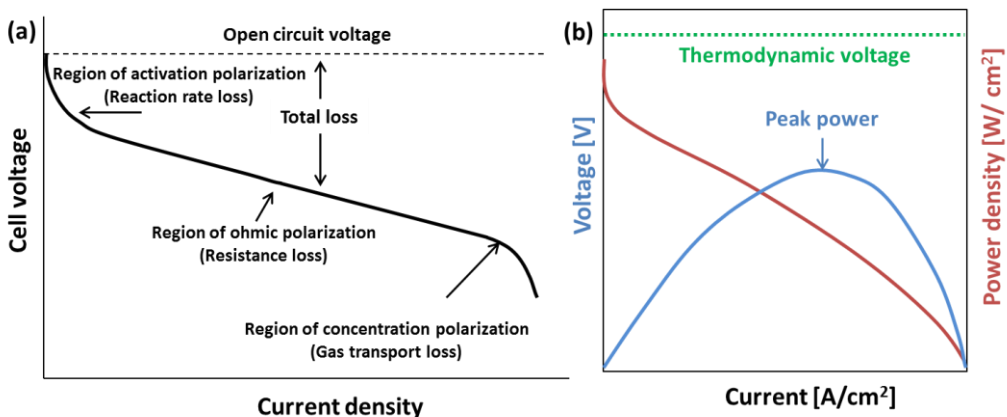


Figure 4.18: (a) Description of the i-V curves of a fuel cell with the different losses and (b) combined fuel cell i-V and power density curves.

Usually the i-V curves of a electrochemical cell are accompanied by the power density curves. The power density (P) can be calculated by the next relation:

$$P \left[\frac{W}{cm^2} \right] = V [V] \cdot \frac{I [A]}{S [cm^2]} \quad (4.12)$$

Where I is the current load and the S is the active area of the cell.

As happens in the i-V curves, in the Power density curves there are different regimes [21]. The power density increases with increasing the current, then, P achieves a maximum and then falls for higher current densities. Fuel cells are designed to operate at current densities below or at the maximum power density.

The acquisition of the i-V curves were performed by the Solartron equipment mentioned in the EIS section. Furthermore, EIS measurements were carried out in different regions in the i-V curves in order to understand how mechanisms changes as function of the current applied. For that purpose, a constant DC current was applied during the EIS measurements.

4.5.4. Electrolyzer mode

Some of the cells tested as fuel cells were tested in electrolysis or co-electrolysis mode, for that purpose a current load was applied to the cell (Figure 4.19). As has been explained above for the fuel cell curves, due to the similarity of processes, three domains can be distinguished in the electrolysis polarization curves as well. The differences in the curve domains are function of the losses that are created in the cell. Those losses reduce the efficiency of the cell, and can be divided in three: activation, ohmic and concentration losses (Figure 4.19). Furthermore, some samples can achieve almost constant voltages with a big reduction of the total resistance at high current densities. That fact can be related with the electroreduction of the electrolyte material producing the electronic conductivity in the electrolyte [22]. In some cases that electroreduction of the electrolyte can be recovered by increasing the oxygen content or reducing the current densities, other times, the change is irreversible.

The overall voltage of the electrolyzer can be defined by the Equation (4.11).

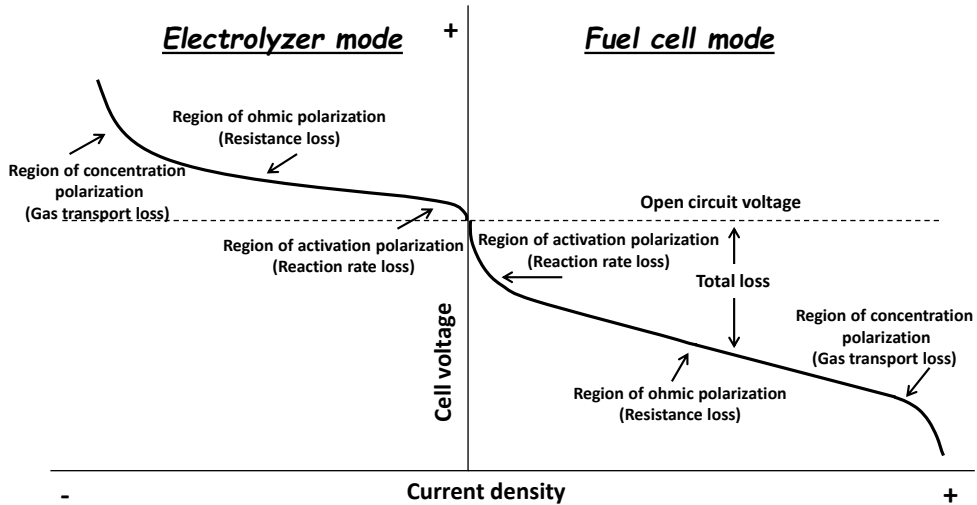


Figure 4.19: Description of the i-V curves of an electrochemical cell with the different losses in the electrolyzer and fuel cell mode.

Usually, the results in the electrolysis mode are studied by mean of the i-V curves, but the Faraday's efficiency and the energy efficiency should be studied as well. The Faraday's efficiency expresses the quantity of current applied to the cell which is converted in the desired reaction. In order to determine this efficiency the experimental amount of hydrogen (steam electrolysis) or/and CO (co-electrolysis) produced has to be quantified. Then, the Faraday's efficiency is written as:

$$\eta_F = \frac{V_{exp}}{V_{theor}} \quad (4.13)$$

being V_{exp} and V_{theor} the volume of hydrogen or CO experimentally and theoretically determined. V_{theor} can be calculated from the experimental data by using the formula:

$$V_{theor} = \frac{I}{n \cdot F} \quad (4.14)$$

Where I is the current applied in Amperes, n are the number of electrons involved in the electrochemical reaction and F is the Faraday's constant in Coulombs.

In the case of co-electrolysis the determination of the Faraday's efficiency is not as simple as shown before, since more than one electrochemical reaction is involved. As a result, the energy efficiency of the process (η_{ener}) will be calculated from current used for the H_2 (I_{H_2}) and CO (I_{CO}) production.

$$I_{H_2} = n \cdot F \cdot V_{H_2 \text{ exp}} \quad (4.15)$$

$$I_{CO} = n \cdot F \cdot V_{CO \text{ exp}} \quad (4.16)$$

$$\eta_{ener} = \frac{I_{H_2} + I_{CO}}{I} \quad (4.17)$$

4.5.5. High temperature set-up

For the measurement of high operation temperature samples, the ITQ designed a set-up that is shown in Figure 4.20. The four flow mass controllers allow working with different feed compositions, whereas the valves of the set-up permit to by-pass some streams to the analyzer equipment, or change between the cathode or anode outlet stream for composition analysis. As is shown in Figure 4.20, three analytic devices are connected with the electrochemical set-up; the gas chromatograph, the mass spectrometer and the Solartron modules. The first two, were used to characterize the outlet stream in terms of compositions. The gas chromatography can separate and analyze the compounds of a gas stream without the decomposition of them. This equipment was used as composition quantitative technique. The mass spectrometer can also separate the different compounds, but in this case the chemical species are ionized and are classify as function of their mass to charge ratio. However, this technique was used predominately as a qualitative technique, controlling the variation of the different masses as function of time. Finally, Solartron modules were connected to the cell as has been explained in the *section 4.5.2*. This device was used for the different electrochemical characterization, as the EIS measurements, Voltammetry or i-V curves for the electrolysis or fuel cell mode.

The samples were placed in a quartz reactor (detail of the reactor is shown in Figure 4.21) due to the high operation temperature (400-1000 °C). If the studied specimen was a symmetrical cell (one common atmosphere and identical electrode material on both electrolyte sides), the same inlet gas flow was introduced in the upper and lower part of the reactor. However, in the fully-assembled cells measured as fuel cells or electrolyzers, the cathode and anode were fed with different compositions gases. As to achieve a good chamber separation (cathode and anode) a pure metal or alloy metal sealing ring was used. The sealing step was the most critical point in the fully-assembled cells characterization. For the sealing, the temperature is increased near to the melting point of the metal, the ring is softened and the spring located in the top of the reactor permits the sealing between the sample and the quartz reactor. Platinum wires, used as electrical current contacts, passed through multibore alumina tubes (two wires for the bottom and two for the top of the cell) and were plugged between the sample and the Solartron connections. In order to avoid extra resistance in the electrochemical measurements, both platinum wires were in parallel but without any contact between them until the current collector, where wires were connected. Finally, to control the sample temperature, a thermocouple was placed in the same alumina tube.

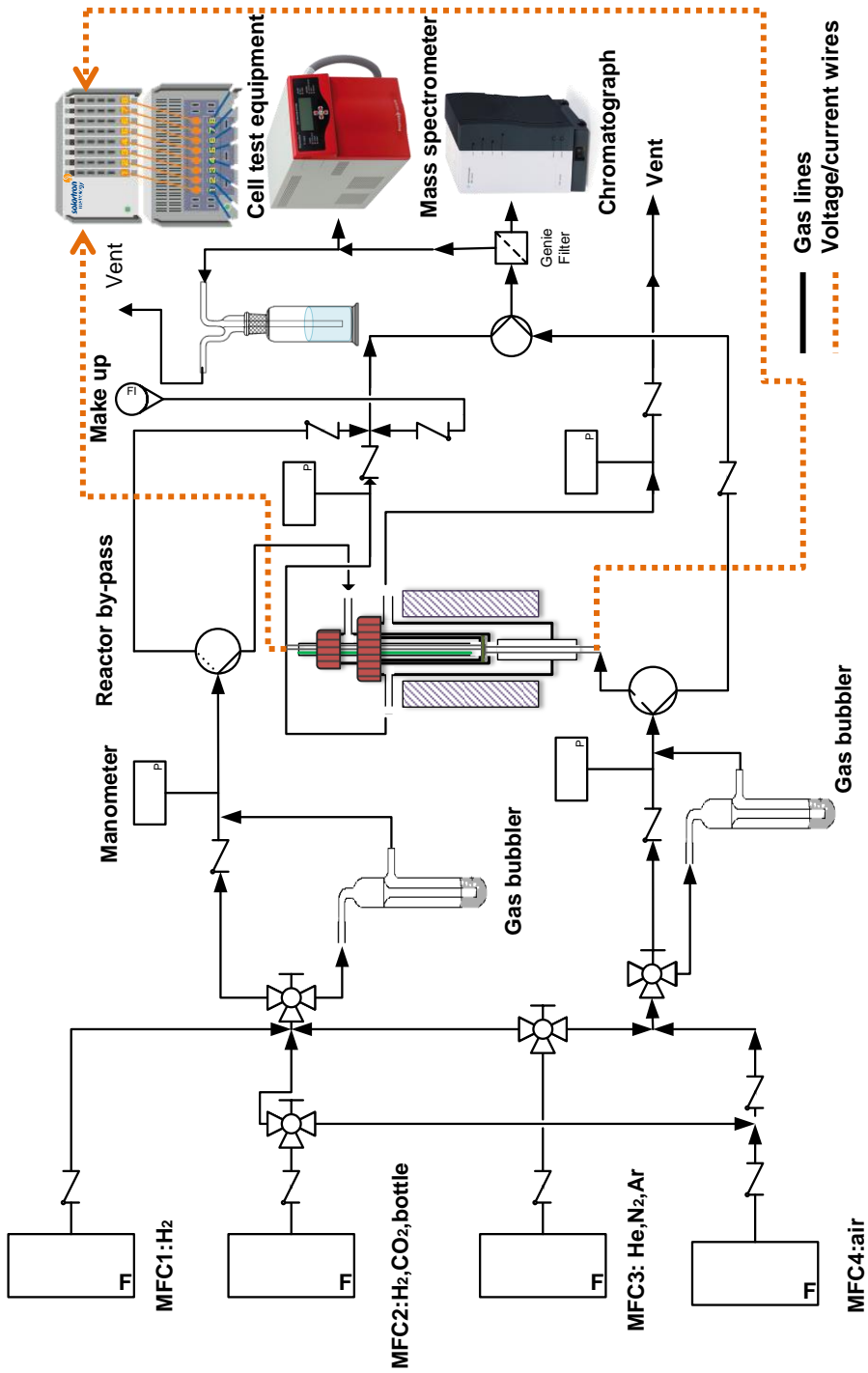


Figure 4.20: Set-up for high temperature cells characterization.

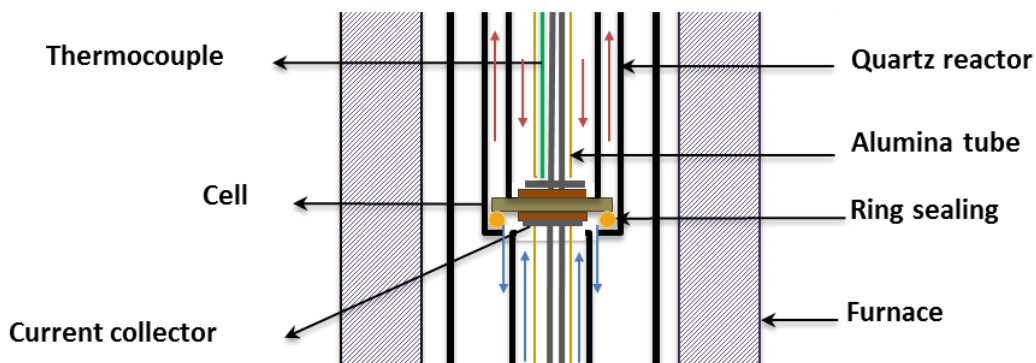


Figure 4.21: Detail of the reactor for high temperature.

4.5.6. Low temperature set-up

In the case of the samples for low temperature measurements, a similar set-up (Figure 4.22) was designed by the ITQ. In this case, due to the requirements of the system to work with high water partial pressure content, all system was heated to avoid the condensation of water. Furthermore, all parts of the setup were in steel giving the possibility to work with total pressures up to 20 bar. The internal pressure was controlled by two BPR valves, allowing to work from atmospheric pressure to high pressures. Four mass flow controllers were also used and the internal pressure of the system was checked by two manometers.

As has been explained in the high temperature set-up, the outlet gases were studied by a gas chromatograph and mass spectrometer. The Solartron also was connected with the sample, but by means of thin steel tubes in contact with the sample. The sealing between both chambers were obtained by a rubber ring.

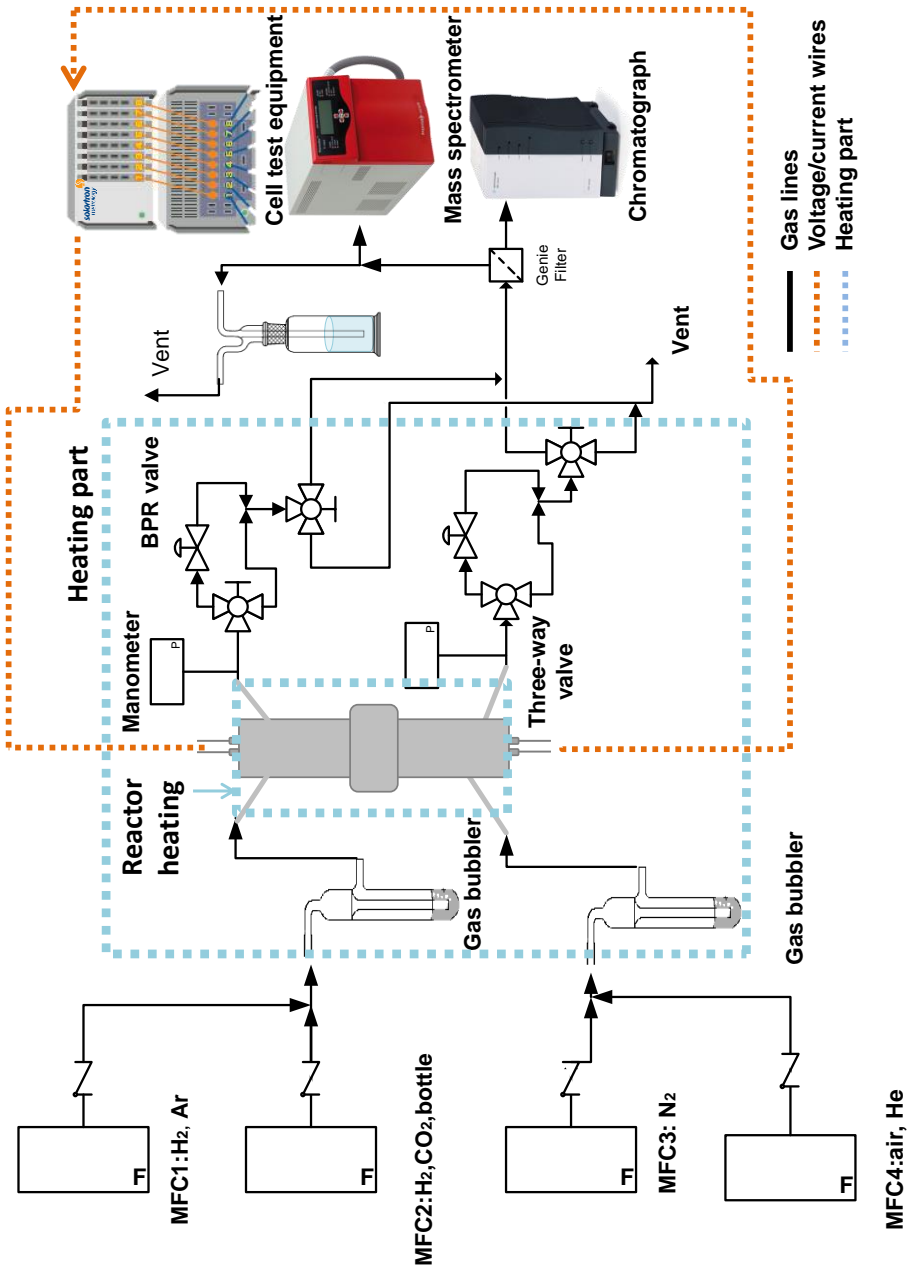


Figure 4.22: Set-up for low temperature cells characterization.

4.5.7. Gas chromatography

Gas chromatography (GC) is an analytical technique that measures the content of various components in a gas sample. The sample solution is injected into a column and swept to the detector by a carrier gas [23]. That carrier gas must have a high purity and be inert with the sample components. The separation of components will depend on its solubility in the gas phase. The temperature of the column and the affinity of each solute with the stationary phase will influence the partition of components. In fact, as molecules are continuously moving between stationary and mobile phase, the difference in retention time, will affect the partition. Consequently, components with different chemical and physical properties will arrive to the detector at different times.

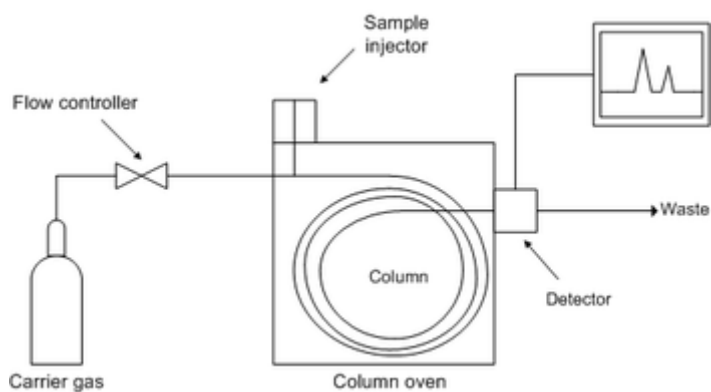


Figure 4.23: Schematic representation of the GC equipment [24].

To measure a sample with an unknown concentration, a standard sample with known concentration is injected into the instrument. Thus, the peak area and retention time of the standard sample is compared with the test sample to calculate the real concentration.

The gas chromatograph used in the present thesis was a Micro-GC CP-4900 with two columns, a Molsieve 5A and Pora PLOT Q columns.

4.5.8. Mass spectrometry

Mass spectrometry (MS) is an analytical technique which detects qualitatively and quantitatively the components in a gas stream. That technique can be divided in different stages:

- 1- Ionization: the mass spectrometer ionizes chemical species by knocking one or more electron off to give positive ion.
- 2- Acceleration: the ions are accelerated.
- 3- Deflection: the ions are deflected by a magnetic field and can be separated by their mass-to-charge ratio (m/z) [25].
- 4- Detection: a beam of ions pass through the electrical detector.

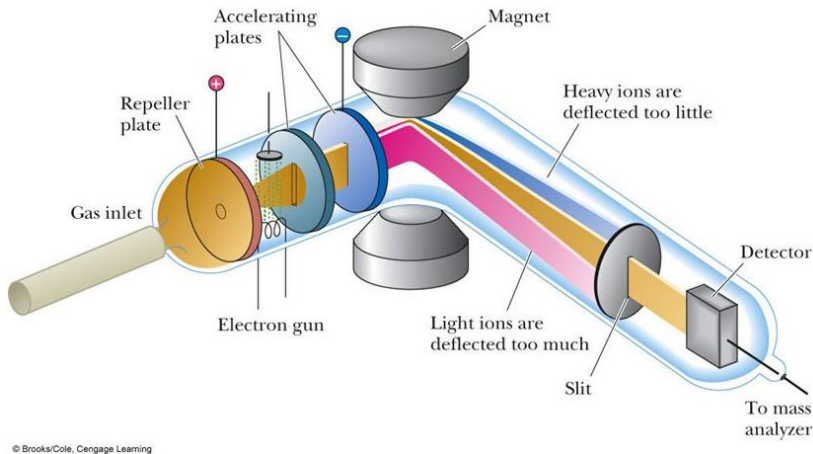


Figure 4.24: Schematic representation of the MS equipment [26].

The mass spectrometer selected for the measurements was a Pfeiffer Vacuum Omni Star GSD 320 O.

4.6. Summary

The cell components materials can be synthesized by three methods; solid state reaction, Pechini method or by co-precipitation. Depending on the method selected the final characteristics of powders can be different. Controlling some of the synthesis parameters, good particle size and homogeneity of the material with a single phase can be achieved. After

synthesis, the materials are structural characterized by X-Ray Diffraction and SEM or FESEM analysis. In some cases, TGA technique can be used to control the reactivity or decomposition of the sample in some special atmospheres. For the electrochemical characterization, dense samples and electrodes are manufacture. Being the temperature and calcination time the most important methodology parameters for the sample densification. In the case of the electrodes, a special attention should be paid in the microstructure, allowing enough porosity, good attachment with the electrolyte and big surface area. The final characterization of the samples includes the DC total electrical conductivity, the electrochemical impedance spectroscopy and test of the fully-assembled cells as fuel cell and/or electrolyzer cell. The DC total electrical conductivity allows discerning the type of conductivity, whereas the EIS measurements give information of the electrochemical mechanisms in the cell performance. Finally, in the fuel cell test the power density at different temperatures or atmospheres can be checked by means of the *i*-*V* curves. However in the electrolysis and co-electrolysis mode, the Faraday's efficiency is also important and can be calculated by measuring the real composition of the outlet stream.

4.7. References

- [1] T. Ishihara, *Perovskite Oxide for Solid Oxide Fuel Cells*, Springer US, 2009.
- [2] L.E. Smart, E.A. Moore, *Solid State Chemistry: An Introduction*, 2nd Edition, Taylor & Francis, 1995.
- [3] K.V. Ana Ecija, Aitor Larrañaga, Luis Ortega-San-Martín. and María Isabel Arriortua, *Synthetic Methods for Perovskite Materials– Structure and Morphology*, in: M. Yitzhak (Ed.) *Advances in Crystallization Processes*, 2012.
- [4] R.M.A. Roque-Malherbe, *The Physical Chemistry of Materials: Energy and Environmental Applications*, CRC Press, 2009.
- [5] S. Sakka, *Handbook of sol-gel science and technology*. 1. Sol-gel processing, Kluwer Academic Publishers, 2005.
- [6] A.M. Huízar-Félix, T. Hernández, S. de la Parra, J. Ibarra, B. Kharisov, *Powder Technology*, 229 (2012) 290-293.
- [7] K.P. de Jong, *Synthesis of Solid Catalysts*, Wiley, 2009.
- [8] A. Guinier, *X-ray Diffraction in Crystals, Imperfect Crystals, and Amorphous Bodies*, Dover, 1994.
- [9] B. Averill, P. Eldredge, *General Chemistry: Principles, Patterns, and Applications*, Ingram, 2011.

- [10] C. Suryanarayana, M.G. Norton, X-Ray Diffraction: A Practical Approach, Springer US, 2013.
- [11] A. Khursheed, Scanning Electron Microscope Optics and Spectrometers, World Scientific, 2011.
- [12] P. Zinin, University of Hawaii, www.soest.hawaii.edu/~zinin.
- [13] D.B. Williams, C.B. Carter, Transmission Electron Microscopy: A Textbook for Materials Science. Diffraction. II, Springer, 1996.
- [14] U.R.U.o. California, cfamm.ucr.edu/documents/eds-intro.pdf.
- [15] P.J. Haines, R.S.o. Chemistry, Principles of Thermal Analysis and Calorimetry, Royal Society of Chemistry, 2002.
- [16] P. Gabbott, Principles and Applications of Thermal Analysis, Wiley, 2008.
- [17] N.Q. Minh, T. Takahashi, Science and Technology of Ceramic Fuel Cells, Elsevier Science, 1995.
- [18] N.P. Brandon, S. Skinner, B.C.H. Steele, Annual Review of Materials Research, 2003, pp. 183-213.
- [19] D.A. Noren, M.A. Hoffman, J. Power Sources, 152 (2005) 175-181.
- [20] K. Sundmacher, L.K. Rihko-Struckmann, V. Galvita, Catal. Today, 104 (2005) 185-199.
- [21] S.M. Haile, Acta Materialia, 51 (2003) 5981-6000.
- [22] M.A. Laguna-Bercero, R. Campana, A. Larrea, J.A. Kilner, V.M. Orera, Fuel Cells, 11 (2011) 116-123.
- [23] E. Prichard, B. Stuart, R.S. Chemistry, Gas Chromatography, Royal Society of Chemistry, 2003.
- [24] <http://jahschem.wikispaces.com/gas+chromatography>.
- [25] J.H. Gross, P. Roepstorff, Mass Spectrometry: A Textbook, Springer Berlin Heidelberg, 2011.
- [26] G.M.L. Donald L. Pavia, George S. Kriz and James A. Vyvyan, Introduction to Spectroscopy, 5 th edition, 2015.

5

**Improvement of
BSCF performance by
B site dopants**

5. Improvement of BSCF performance by B site dopants

5.1. Introduction

In the last years, efforts have been focused on looking for new materials for intermediate temperature solid oxide fuel cells (IT-SOFC) cathodes, since traditional cathodes have poor activity for the oxygen reduction reaction (ORR). Specially, mixed ionic-electronic conducting (MIEC) materials have attracted great interest due to their excellent properties, as the electronic and ionic conductivity. Among the MIEC materials the ABO_3 perovskites-type materials have been extensively studied for fuel cell or oxygen permeation applications, due to their composition versatility. For instance, by partial substitution of trivalent cations in A site by divalent cations can generate oxygen vacancies increasing the ionic conductivity. On the other hand, multivalent metal ions in B site can improve the electronic conductivity [1]. $SrCo_{0.8}Fe_{0.2}O_{3-\delta}$ (SCF) was one of the first materials suggested as an oxygen transport membrane. Nevertheless SCF undergoes a phase transition, from cubic phase to brownmillerite, at low operation temperature and oxygen partial pressure. This new phase has low oxygen conductivity due to the ordered arrangement of oxygen vacancies in the structure. The partial substitution of Sr by Ba in SCF avoided the formation of brownmillerite with the variation of temperature and oxygen partial pressure, giving higher stability even improving the permeation rate. $Ba_{0.5}Sr_{0.5}Co_{0.8}Fe_{0.2}O_{3-\delta}$ (BSCF) was reported as promising MIEC perovskite [2] for oxygen permeation and cathode for IT-SOFC, due to its high transport rates. However, BSCF has one important drawback; the formation of carbonates in presence of CO_2 at intermediates temperatures (below 800 °C) [3, 4].

The introduction of different cations in A or/and B sites in the perovskite structure can tailor the properties. In the present study, different dopants (Y, Zr and Sc) were studied in B site. With the objective of improving the stability of the compound, cations with a fixed valence and similar ionic radius (Table 5.1) were selected. Furthermore, in the present chapter the influence on the cell performance will be studied.

Ion	Coordination	Oxidation state	Radius (Å)
Ba	12	+2	1.61
Sr	12	+2	1.44
Co	6	+2	0.65
Co	6	+2	0.745
Co	6	+3	0.545
Co	6	+3	0.61
Co	6	+4	0.53
Fe	6	+2	0.61
Fe	6	+2	0.76
Fe	6	+3	0.55
Fe	6	+3	0.645
Sc	6	+3	0.72
Y	6	+3	0.9
Zr	6	+4	0.745
O	4	-2	1.38

Table 5.1: Ion radii in BSCF [5].

Different $\text{Ba}_{0.5}\text{Sr}_{0.5}(\text{Co}_{0.8}\text{Fe}_{0.2})_{0.97}\text{B}_{0.03}\text{O}_{3-\delta}$ (B= Sc, Zr and Y) compounds were prepared following the solid state reaction explained in *Methodology chapter*. These powders were calcined at different stages and milled in each step in order to favor the homogenization of the final composition. The final annealing temperature was 1150 °C.

5.2. Results and discussion

5.2.1. Structural characterization

5.2.1.1. X-Ray diffraction

XRD patterns of the as-prepared $\text{Ba}_{0.5}\text{Sr}_{0.5}(\text{Co}_{0.8}\text{Fe}_{0.2})_{0.97}\text{B}_{0.03}\text{O}_{3-\delta}$ (B= Sc, Zr and Y) materials are depicted in Figure 5.1. The materials are labeled as follows: $\text{Ba}_{0.5}\text{Sr}_{0.5}\text{Co}_{0.8}\text{Fe}_{0.2}\text{O}_{3-\delta}$ (BSCF), $\text{Ba}_{0.5}\text{Sr}_{0.5}(\text{Co}_{0.8}\text{Fe}_{0.2})_{0.97}\text{Y}_{0.03}\text{O}_{3-\delta}$ (BSCF_Y), $\text{Ba}_{0.5}\text{Sr}_{0.5}(\text{Co}_{0.8}\text{Fe}_{0.2})_{0.97}\text{Sc}_{0.03}\text{O}_{3-\delta}$ (BSCF_Sc) and $\text{Ba}_{0.5}\text{Sr}_{0.5}(\text{Co}_{0.8}\text{Fe}_{0.2})_{0.97}\text{Zr}_{0.03}\text{O}_{3-\delta}$ (BSCF_Zr). The diffraction peaks can be assigned to a cubic perovskite phase [6,

7] and no traces of other phases can be detected to the limit of the XRD equipment resolution. Therefore, all dopants are well incorporated in the structure.

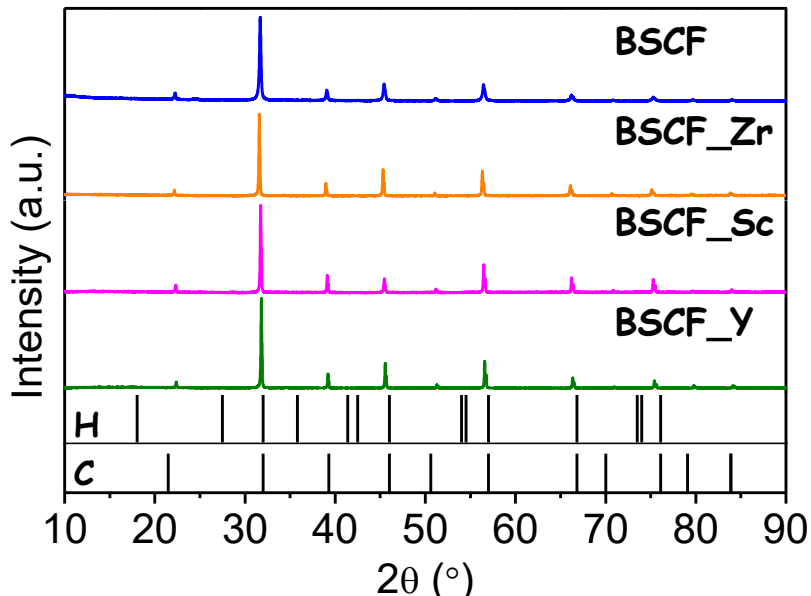


Figure 5.1: XRD pattern of $\text{Ba}_{0.5}\text{Sr}_{0.5}(\text{Co}_{0.8}\text{Fe}_{0.2})_{0.97}\text{B}_{0.03}\text{O}_{3-\delta}$ (B= Sc, Zr and Y) after calcination at 1150 °C.

It has been widely reported the instability of BSCF when is exposed to temperatures below 800 °C for long periods of time in air [6, 8-10]. The cubic phase (C) is not stable in air below 800 °C and hexagonal phases grow with time. Furthermore, it has been reported that in membranes the new hexagonal phases (H) appear in the grain boundary and the oxygen permeation fluxes decrease due to the production of barriers for the oxygen transport [9].

The stability of the different materials was studied by comparing the XRD patterns before and after a temperature treatment. The stability was performed with powder of the $\text{Ba}_{0.5}\text{Sr}_{0.5}(\text{Co}_{0.8}\text{Fe}_{0.2})_{0.97}\text{B}_{0.03}\text{O}_{3-\delta}$ compounds in synthetic air at 750 °C during two weeks. As can be ascribed from Figure 5.2, after the temperature treatment new peaks appear and can be assigned to a hexagonal phase. However, all doped compounds show better stability than the parent one (BSCF). The number of peaks and intensities corresponding to the hexagonal phase in the XRD pattern of doped compounds is less than in

the BSCF. Some authors have studied the effect of B-site dopants in the electrochemical performance and the oxygen permeation fluxes of BSCF based compounds, showing the improvement of the stability for long periods of time at intermediate operation temperatures [11-14]. It seems that introducing dopants in B site the stability of the cubic phase is improved.

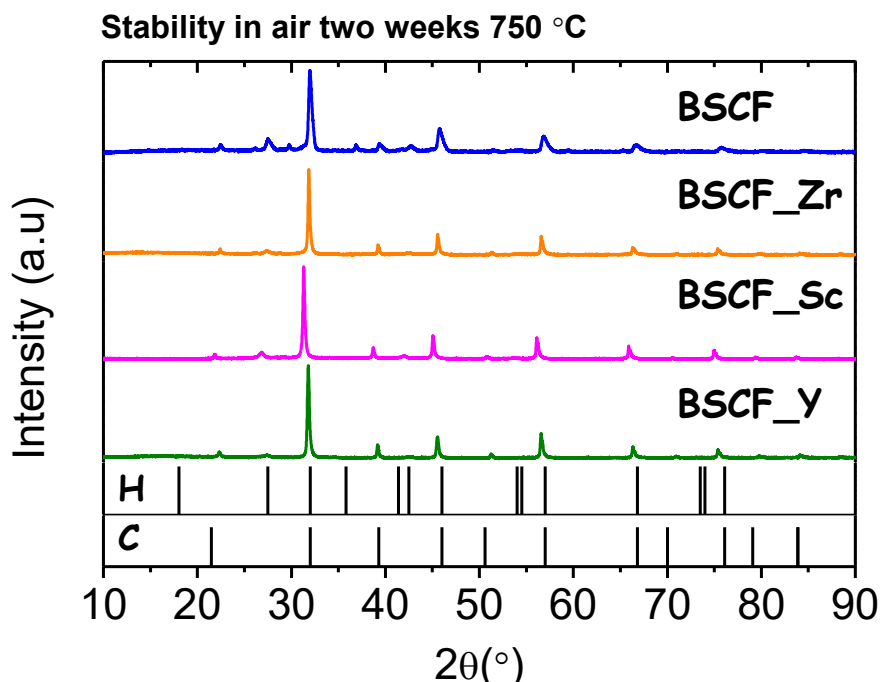


Figure 5.2: XRD pattern of $\text{Ba}_{0.5}\text{Sr}_{0.5}(\text{Co}_{0.8}\text{Fe}_{0.2})_{0.97}\text{B}_{0.03}\text{O}_{3-\delta}$ (B= Sc, Zr and Y) after stability test at 750°C during two weeks.

5.2.1.2. Thermogravimetric analysis in CO_2 atmosphere

As has been explained in the introduction, one of the main problems of this type of perovskites is the stability in presence of CO_2 . A thermogravimetric analysis as function of temperature with a containing CO_2 atmosphere was performed. The results of the analysis for $\text{Ba}_{0.5}\text{Sr}_{0.5}(\text{Co}_{0.8}\text{Fe}_{0.2})_{0.97}\text{B}_{0.03}\text{O}_{3-\delta}$ (B= Sc, Zr and Y) series are presented in Figure 5.3. As can be ascribed from Figure 5.3, five different regions can be distinguished:

- *Region 1* (RT- 275°C), there is a weight loss which can attributed to the material dehydration.

- *Region 2 (275 °C- 475 °C)*, the weight is almost constant.
- *Region 3 (475 °C- 775 °C)*, the weight of the sample starts to augment at 475 °C until achieve a maximum. The temperature of the maximum varies as function of the compounds, being at 775 °C for the undoped material, whereas the rest of materials have it at 800°C. Carbonates are generated in this region.
- *Region 4 (775 °C- 925 °C)*, carbonates produced in Region 3 are decomposed when the temperature is increased above 800 °C. Material transforms back from the carbonate to the perovskite phase, with a huge mass reduction.
- *Region 5 (925 °C-1000 °C)*, the high operation temperature force the oxygen vacancy formation within the perovskite, small loss of weight is obtained.

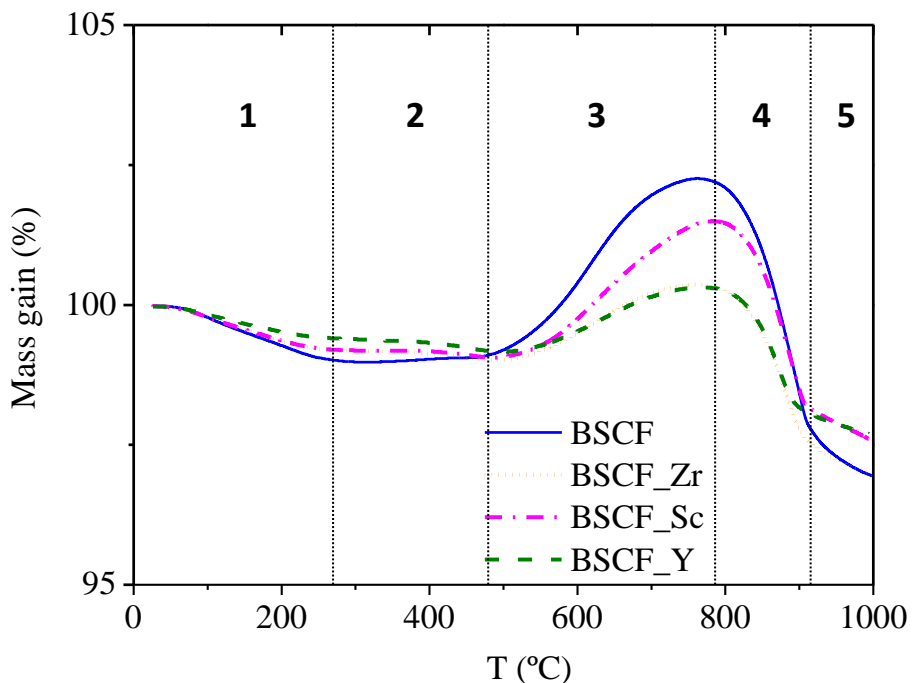


Figure 5.3: TG analysis of $\text{Ba}_{0.5}\text{Sr}_{0.5}(\text{Co}_{0.8}\text{Fe}_{0.2})_{0.97}\text{B}_{0.03}\text{O}_{3-\delta}$ (B= Sc, Zr and Y) in presence of CO_2 .

5.2.1.3. Total DC electrical conductivity

The electrical conductivity of the different compounds was measured using the four-point DC method, and the results are presented in Figure 5.4. The BSCF doped with Sc shown the highest conductivity in air from 500-800 °C (Figure 5.4 (a)), whereas BSCF and BSCF_Y have similar performance at high temperatures. However, BSCF_Zr exhibits the lowest electrical conductivity at high temperatures, but below 500 °C the Zirconium doped sample improve the BSCF parent material conductivity. The lower conductivity of BSCF_Zr can be related with the Zr oxidation state (+4). It seems that the oxygen vacancies are reduced and therefore the total DC conductivity is not improving by doping with Zr.

In addition, the electrical conductivity as function of the oxygen partial pressure (pO_2) at two different temperatures (600 °C and 800 °C) is drawn in Figure 5.4 (b).

The slope values (n_T) of $\log(\sigma)$ vs. $\log(pO_2)$ of the different materials is displayed in Table 5.2. The dependence of pO_2 and σ is in the range of $1/4 < n_T < 1/6$, indicating a p-type conductivity. The conductivity increases by increasing the pO_2 , since oxygen vacancies are occupied and electron holes are created as follows [15, 16]:



	$n_{600\text{ °C}}$	$n_{800\text{ °C}}$
BSCF_Y	0.27	0.14
BSCF_Zr	0.26	0.13
BSCF_Sc	0.27	0.14
BSCF	0.28	0.15

Table 5.2: n values of $\log(\sigma)$ vs. $\log(pO_2)$

At low temperatures, the ionic conductivity is negligible and the p-type electronic conductivity dominates. However at high temperatures, samples release oxygen producing oxygen vacancies and producing the concomitant

reduction of electrons holes and the electronic conductivity. That reduction in the electronic conductivity reduces the n value (Table 5.2).

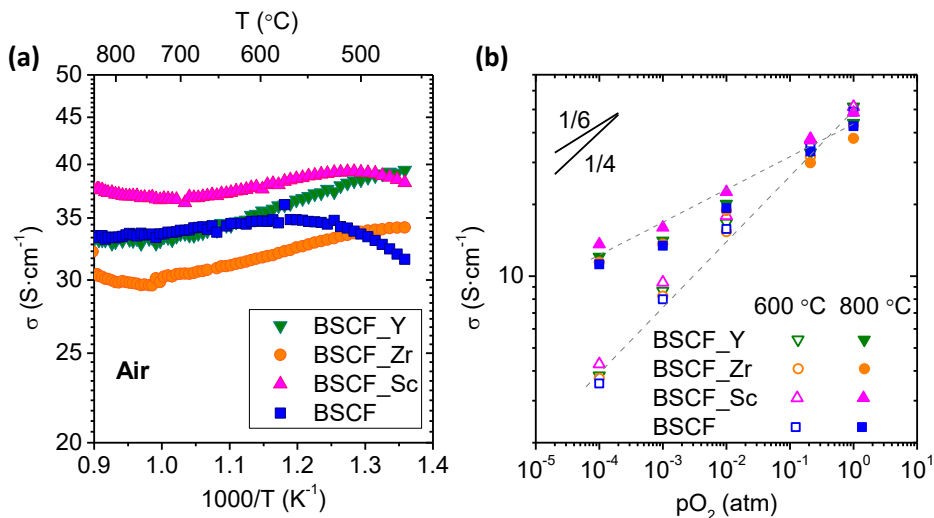


Figure 5.4: Total DC conductivity (a) as function of temperature in dry air and (b) as function of oxygen partial pressure.

5.2.2. Symmetrical cells characterization

5.2.2.1. Electrode microstructure

It has been widely studied the compatibility of BSCF with different electrolyte materials. In the case of yttrium stabilized zirconia (YSZ) some reaction is shown when calcination temperature is above 800 $^{\circ}\text{C}$, appearing new peaks in the XRD pattern. In addition, BSCF is totally decomposed when is used with YSZ electrolyte material at 950 $^{\circ}\text{C}$ [17]. To ensure good attachment between electrode and electrolyte, annealing temperatures higher than 800 $^{\circ}\text{C}$ are required. Thus, other electrolyte materials should be selected in order to avoid the BSCF decomposition. Gadolinium doped ceria (GDC) has been proposed as an alternative electrolyte for BSCF electrodes, due to its higher compatibility and ionic conductivity and fast oxygen surface exchange kinetics compared to YSZ at intermediate temperatures (400-600 $^{\circ}\text{C}$) [18, 19]. Furthermore, the thermal and chemical expansion coefficient (TEC) of BSCF is higher than YSZ and GDC, being nearly twice of both electrolyte materials [19]. This high TEC of most of the cobalt rich compounds produces mismatch of the electrode and

electrolyte material, resulting in a BSCF cathode delamination from the electrolyte. In the present thesis, in order to avoid those TEC problems, the BSCF-doped materials were mixed with $\text{Ce}_{0.8}\text{Gd}_{0.2}\text{O}_{2-\delta}$ in 50 % of weight. The composite electrodes were calcined at $950\text{ }^\circ\text{C}$, obtaining a good adhesion to the electrolyte. SEM micrographs of the cross section of the symmetrical cells after calcination at $950\text{ }^\circ\text{C}$ (2 hours) are shown in Figure 5.5. The four electrodes have a similar microstructure, with bigger particles related with BSCF-doped electrodes, whereas GDC particles are smaller. However, the porosity of the electrodes is good enough for gas diffusion. In the following parts of the chapter, a deeper analysis of oxygen mechanisms (activation, reduction, etc.) will be done. On top of all samples it can differentiate a gold thin layer ($\sim 1.5\text{ }\mu\text{m}$) and the thickness of electrodes are $\approx 30\text{ }\mu\text{m}$. Furthermore, the electrolyte has high density with close porosity, not affecting the electrochemical measurements.

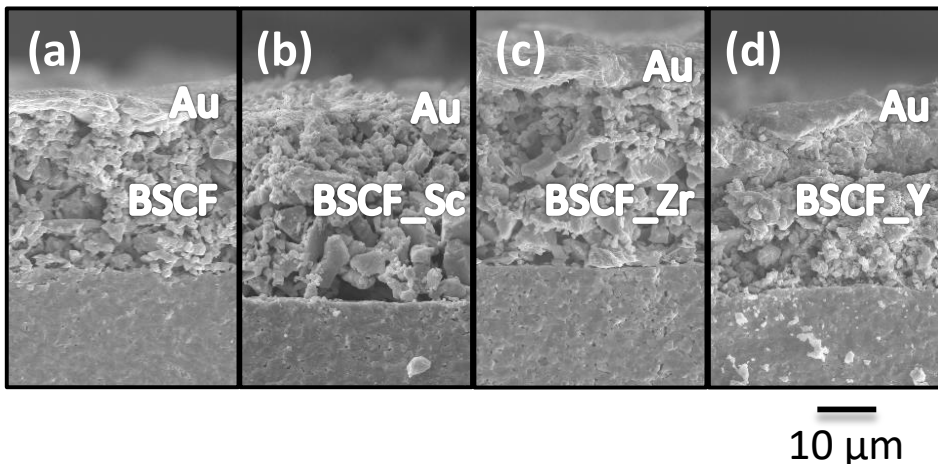


Figure 5.5: SEM micrographs of $\text{Ba}_{0.5}\text{Sr}_{0.5}(\text{Co}_{0.8}\text{Fe}_{0.2})_{0.97}\text{B}_{0.03}\text{O}_{3-\delta}$ /GDC electrodes after calcination at $950\text{ }^\circ\text{C}$. All composites were supported on GDC+Co_x electrolytes.

The results in all figures from this point were labeled with the single BSCF-doped compounds name, but results correspond to the composite electrodes.

5.2.2.2. Polarization resistance

5.2.2.2.1. Operation temperature influence

In order to determine the polarization resistance of the different materials synthesized working as cathodes in fuel cells, EIS measurements were performed. For that purpose, symmetrical cells with the same material on both sides of GDC electrolyte were manufactured. Since all electrodes were calcined at 950 °C the EIS measurements started at 900 °C, and then the temperature was decreased in gradients of 50 °C. The lowest temperature measured was dependent on the cell performance. The same atmosphere was introduced in both chambers of reactor. The maximum oxygen partial pressure was 0.21 atm and the lowest was 0.01 atm. The gas rate was kept in 50 ml/min in each electrode-side.

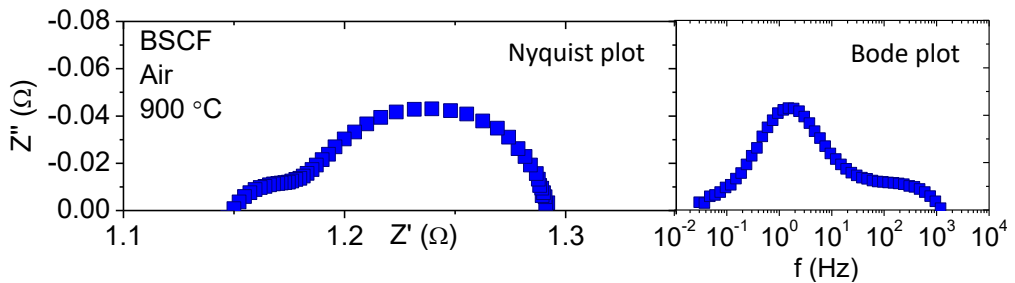


Figure 5.6: Nyquist and Bode plot obtained by means of the EIS measurements, left and right, respectively.

From the data of EIS measurements a Nyquist and Bode plot can be extracted (Figure 5.6). In the Nyquist plot the resistance of the electrolyte and electrode can be distinguished. The ohmic resistance can be determined from the cut in the x-axis in the left side of the arcs (Nyquist plot), whereas the electrodes resistance (polarization resistance) is marked by the real impedance (Z') under the arcs. In this thesis, polarization resistance (R_p) has been defined as the specific resistance per unit area. The polarization resistance of the GDC/BSCF composite and the different doped materials is shown as function of the operation temperature in Figure 5.7.

The polarization resistance of the different electrodes materials is represented as function of temperature in an Arrhenius-type plot. As can be inferred from Figure 5.7, the performance, *i.e.*, R_p , is improved by doping in B site with a 3%.

This effect is more important at high temperatures, at lower temperatures the resistance of BSCF, BSCF_Zr and BSCF-Y composites converge to the similar polarization resistance values. Nevertheless, the BSCF doped in B-site by Scandium reduces the polarization resistance in all range of temperatures measured, when is compared with the parent GDC/BSCF electrode. Additionally, the introduction of an ionic phase as GDC can improve the cell performance when is applied at low temperature [20], since the ionic conductivity of BSCF with decreasing temperature and the width of the TPB zone becomes narrower.

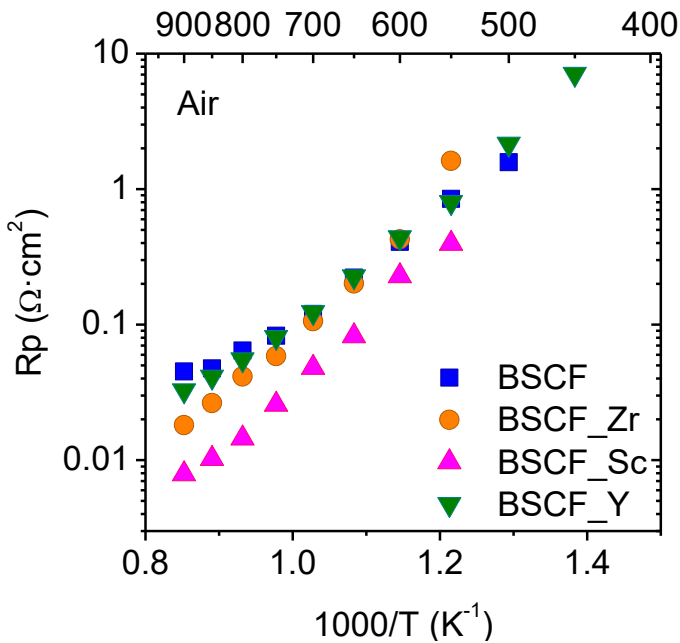


Figure 5.7: Polarization resistance of $\text{Ba}_{0.5}\text{Sr}_{0.5}(\text{Co}_{0.8}\text{Fe}_{0.2})_{0.97}\text{B}_{0.03}\text{O}_{3-6}$ /GDC electrodes in air as function of temperature.

The Arrhenius plot allows the determination of the activation energy (E_a) of each material in synthetic air. The four samples measured have a variation in the activation energy with the temperature (Table 5.3), increasing for low temperatures (750-450 °C). It seems that there are two different regimes in the polarization resistance, which are temperature dependent, and are correlated with the change in the activation energy. The electrocatalytic activity of the perovskite electrodes is usually influenced by the elements in B

site, since they can participate in the redox cycles [21] by improving the oxygen reduction reaction (ORR). For instance, Co and Fe in BSCF, can change the oxidation state; $\text{Co}^{+3} \leftrightarrow \text{Co}^{+4}$ and $\text{Fe}^{+3} \leftrightarrow \text{Fe}^{+4}$. By doping with elements with a fixed oxidation state (Zr, Sc and Y), the activation energy increases (Table 5.3). When BSCF is doped with Sc and Y with a +3 oxidation state the E_a is smaller than the Zr doped material with +4. This behavior can be related with the oxygen vacancies generated ($V_{\text{O}}^{\cdot\cdot}$) by the extrinsic defects created in the BSCF phase by Sc and Zr (+3 oxidation state). In the case of Zr with a +4 valence, no additional $V_{\text{O}}^{\cdot\cdot}$ can be generated, increasing the E_a . The same behavior is observed for both ranges of temperatures. Additionally, the particle size, porosity and distribution of both phases can influence the TPB length and consequently the cell performance and the activation energy variation of the different compounds. On the other hand, the phase transition of BSCF material, reported below 800 °C, can cause the E_a variation for low temperatures.

<i>Compound</i>	<i>E_{a1} [900-750 °C] (eV)</i>	<i>E_{a2} [750-450 °C] (eV)</i>
<i>BSCF/GDC</i>	0.50	0.81
<i>BSCF_Sc/GDC</i>	0.66	1.02
<i>BSCF_Zr/GDC</i>	0.82	1.24
<i>BSCF_Y/GDC</i>	0.63	0.96

Table 5.3: Activation energy of $\text{Ba}_{0.5}\text{Sr}_{0.5}(\text{Co}_{0.8}\text{Fe}_{0.2})_{0.97}\text{B}_{0.03}\text{O}_{3-\delta}$ /GDC electrodes in synthetic air. E_{a1} related with high operation temperature and E_{a2} with low temperature.

In order to identify limiting mechanisms in both ranges of temperature, a deep analysis of the EIS results will be performed. Figure 5.8 presents the EIS spectra of the different composites at two different temperatures in air (Nyquist and Bode plots). The real resistance associated to the ohmic resistance of the electrolyte has been subtracted with the aim of comparing directly the electrodes arcs. The ohmic resistance of the electrolyte is temperature dependent, having a higher resistance at lower temperatures. As can be ascribed from Figure 5.8, the addition of the different dopants can improve the performance of the cell, by reducing the resistance at low-medium frequencies. This effect is more significant at high temperature (900 °C) whereas this significant reduction is more obvious for the Sc doped BSCF.

Furthermore, the limiting processes in the cathode performance are shifted to higher frequencies when temperature is decreased. Nyquist and Bode plots suggest that the limiting mechanism in the oxygen reduction reaction takes place at low-medium frequencies. Usually the low-medium frequencies are related with surface processes, O_2 incorporation into the bulk and adsorption and/or partial reduction of oxygen on the MIEC electrode [22].

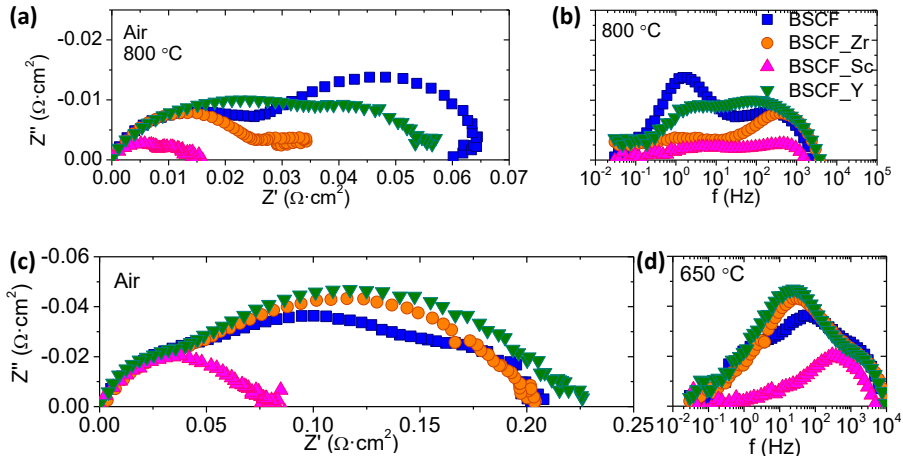


Figure 5.8: EIS spectra of $Ba_{0.5}Sr_{0.5}(Co_{0.8}Fe_{0.2})_{0.97}B_{0.03}O_{3-\delta}/GDC$ electrodes in synthetic air. (a) Nyquist and (b) Bode plot at 800 °C. (c) Nyquist and (d) Bode plot at 650 °C.

As has been explained in the *Methodology Chapter*, by fitting the EIS spectrum to an equivalent electrical circuit is possible to distinguish between the different limiting processes in the cathode and obtain information about intrinsic properties of materials as the conductivity, dielectric constant, chemical diffusion coefficient, etc. Two arcs for the parent BSCF composite can be differentiated from Figure 5.8 (a) at high temperature. However, at lower temperatures (650 °C), three arcs can be clearly seen, so two different equivalent circuits have to be used. The equivalent circuits used comprise an inductance (L) related with the electrical contacts and device. An ohmic resistance (R_{Ω}) associated with the conductivity of the electrolyte and two or three Constant Phase Element (CPE) in parallel with a resistance. The CPE is not a real capacitance, and is represented in the Nyquist plot as a depressed arc and has a characteristic value of n , this value is related with the heterogeneity of the imaginary part. When n is equal to 1, the CPE is became a real

capacitor, this value is limited between 0 and 1. The roughness of the material, the distribution of the reaction rate on the surface, due to the active site distribution, variation of the composition along the electrode and a not good current distribution can be some of the possible causes not to have a real capacitor. The equivalent circuits employed for the fitting are displayed in Figure 5.9. In the case of high temperature, two resistances are the limiting: low (LF) and medium frequency (MF). At lower temperature a third resistance associated with high frequency (HF) is incorporated.

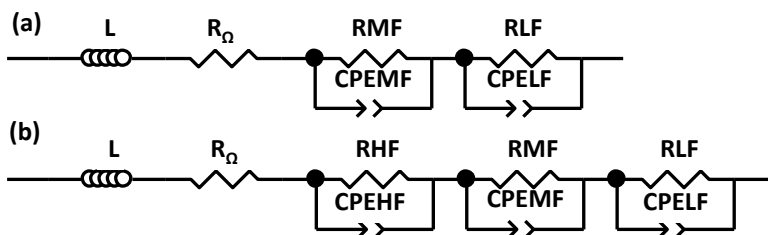


Figure 5.9: Equivalent electrical circuit used for the fitting at high temperature (a) and low temperature (b).

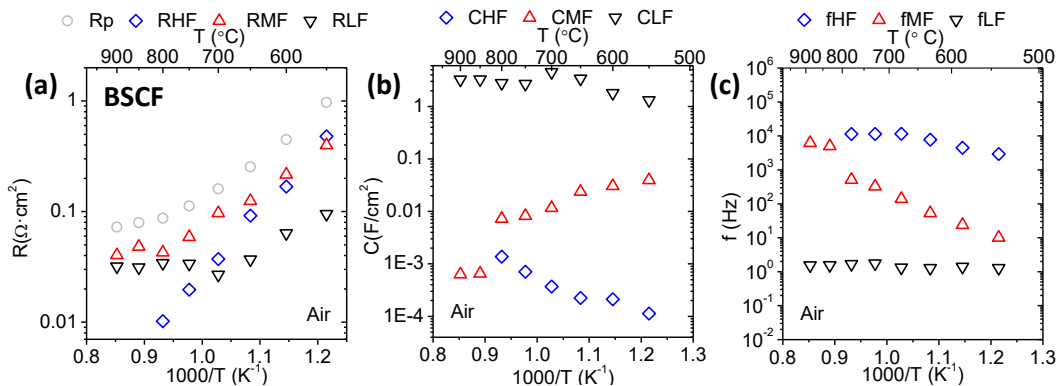


Figure 5.10: Results from the fitting with an equivalent electrical circuit for GDC/BSCF composite as function of temperature. (a) Resistance, (b) capacitance and (c) associated frequency.

The results obtained from the fitting of the equivalent electrical circuit of GDC/BSCF as function of temperature are shown in Figure 5.10. Fitting parameters can be divided in two ranges of temperature; 900 °C to 700 °C and 700 °C to 550 °C. The resistance at high frequency (HF) that is almost negligible at high temperatures becomes dominant at low temperatures (550 °C). The crossing of

LF and HF in Figure 5.10 (a) matches with the change in the activation energy observed in the Arrhenius plot (Figure 5.7). This increase of the HF resistances fits perfectly with the results observed in the Nyquist plot, where arcs are shifted to higher frequencies when the temperature is reduced.

The LF contribution remains almost constant from 900 °C to 650 °C, and becomes the smallest resistance at low operation temperature. The HF resistance is negligible at high temperatures, but at lower temperatures (700 °C to 550 °C), has the same order of magnitude than MF resistances. The LF contribution has the particularity that is almost constant in all range of temperature. Also, the frequency and capacitance associated show small variations, 1 to 2 Hz and 1 to 4 F/cm². Setevich *et al.*, [23] reported the same behavior for the BSCF composite and suggested no dependence between this resistance and the microstructure of the electrode and the possible second phases formed due to the heating treatments.

Nevertheless, the contribution of the MF contribution has a huge variation in terms of resistance, frequency and capacitance in the operation range. The resistance changes from 0.04 to 0.4 Ω/cm², whereas the frequency has a value of 6 kHz at 900 °C and the corresponding value at low temperatures (550 °C) is 10 Hz. Additionally, the capacitance change from 0.0006 to 0.04 F/cm². However, this MF contribution is microstructure and electrode configuration dependent and is thermally activated [23]. Then, R_{MF} is electrode microstructure dependent and therefore will be influenced by the TPB length [23, 24]. This contribution is usually present in the impedance spectra and is often found to be the dominant contribution in composite materials, as is the actual case. It is important to emphasize at this point, that the main objective of introduce Sc, Zr and Y in the B site is the stability of the material phase. Moreover, dopants in B site were able to improve the performance.

Finally, the HF contribution is also temperature dependent, with high frequency related processes from 10 to 2 kHz. The HF capacitance is 0.001 F/cm² at the highest temperature whereas at low temperature is 0.0001 F/cm². The HF contribution is originated from the O²⁻ transfer in the electrode/electrolyte interface [25]. The results obtained in the present thesis match with the frequency and capacitances associated shown by Dusastre *et*

al., [26]. As the temperature is decreased the conductivity of the electrolyte material is reduced, increasing the R_{HF} , since this HF contribution is affected by the GB in the GDC electrolyte [27].

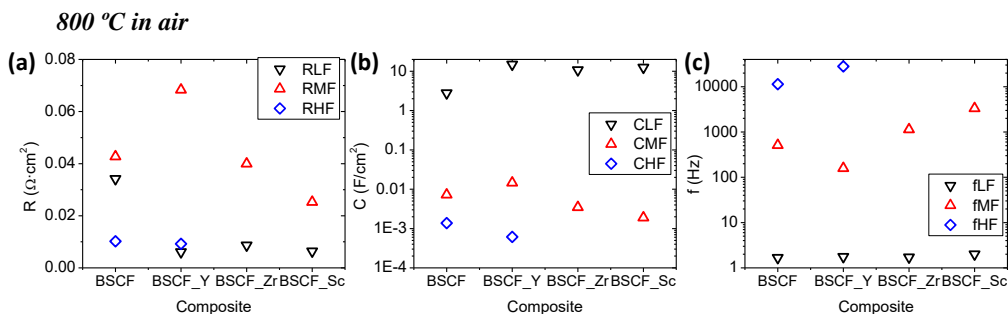


Figure 5.11: Equivalent electrical circuit fitting results; (a) resistance, (b) capacitance and (c) frequency of different processes at 800 °C in air.

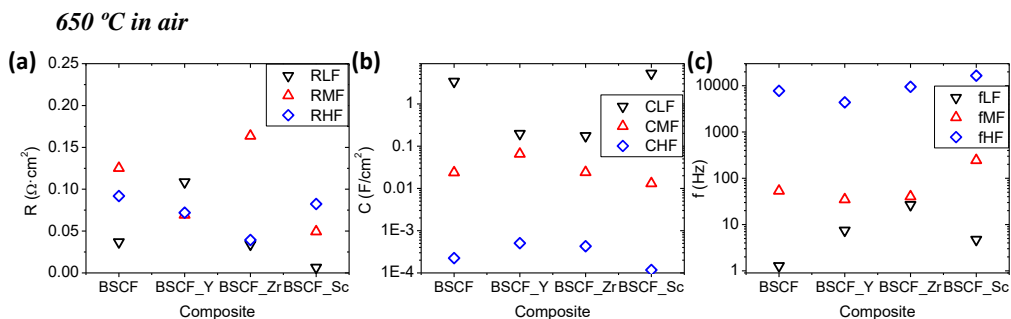


Figure 5.12: Equivalent electrical circuit fitting results; (a) resistance, (b) capacitance and (c) frequency of different processes at 650 °C in air.

After identifying the type of limiting steps in the parent composite (GDC/BSCF), it is important to elucidate which are the changes introduced by doping in B site. As has been explained before, there is an activation energy change around 700 °C, consequently, it has been selected two temperatures (800 °C and 650 °C) for the fitting of an equivalent circuit.

At 800 °C when 3% of Zr or Y is introduced in the structure in B site, the resistance at LF is reduced. As it has been measured [28, 29], the oxygen exchange coefficient (k_{chem}) and chemical diffusion coefficient (D_{chem}) are improved with 3% of Zr and Y. Furthermore, the introduction of dopants can

stabilize the K_{chem} and D_{chem} as function of time of at least for BSCF-Zr [28]. However at 650 °C the material doped with Y increases the resistance at low frequency, related with surface processes. Consequently, the results suggest that the reduction of Fe and Co and the subsequently radii enlargement, are not benefited for the presence of big cations as Y (Table 5.1). Thus, the surface processes could not be improved by the redox cycles.

The frequency associated with LF processes at high temperatures is almost constant for all materials, highlighting a common limiting process for all materials. However, the addition of dopants in the structure reduces the related resistance. The associated capacitance goes from 0.2 F/cm² to 20 F/cm² for both ranges of temperature.

The contribution at medium frequencies changes for each compound, being the highest resistance at 800 °C for Y-doped compounds, but it becomes the highest at 650 °C for Zr-doped compound (showing the lowest total DC conductivity). This MF resistance can be related with the length of the TPB. It is likely that the oxygen vacancies are dominating this resistance at low temperature. Regarding the oxidation state and the equilibrium of charges in the compound, when BSCF is doped by Zr with a +4 oxidation state the capability of compound to form oxygen vacancies is reduced, however with compounds with +3 as oxidation state, oxygen vacancies are forced to be produced in order to maintain the cubic structure and the electroneutrality of the sample. Then, the resistance at MF at 650 °C decreases: BSCF_Zr>BSCF>BSCF_Y>BSCF_Sc. The medium frequency resistances suffer a big change in terms of frequency and capacitance, where the values vary from 80 Hz to 1000 Hz and 0.001-0.1 F/cm², respectively.

The HF resistance can be related with the composite/GDC electrolyte interface resistance. At high temperature, only BSCF and BSCF_Y show the HF resistance and is the lowest limiting contribution. However, as the temperature is reduced and the ionic conductivity of the electrolyte material decreases, the HF resistance becomes more important even dominating the Sc-doped BSCF performance. The frequencies associated with HF resistance have the same range for all materials and temperatures, being around 10.000 Hz, and the capacitance range is the same for both temperatures ($1 \cdot 10^{-4}$ - $1 \cdot 10^{-3}$ F/cm²).

5.2.2.2.2. Oxygen partial pressure influence on the cell performance

The oxygen reduction reaction of a mixed ionic-electronic conductor consists of (1) gas diffusion of O₂ molecules inside the electrode, (2) surface reaction, (3) oxygen ion diffusion through the electrode bulk, (4) transfer of O²⁻ in the electrode/electrolyte interface. Separately, the surface reaction can be divided in the following stages; (1) O₂ molecule adsorption on the electrode surface (2) oxygen molecule dissociation into the oxygen ions and (3) oxygen ions incorporation in the MIEC material. The RLF can be attributed to the surface reactions [22, 23] and a deeper analysis should be performed in order to discern which process from the mentioned surface stages is limiting the cell performance.

Trying to better understand the origin of the arcs in the impedance spectra, isothermal experiments varying the oxygen partial pressure were performed. The analysis of the different contributions as a function of the oxygen partial pressure (pO₂) has been widely studied [30-32]:

$$R_i \propto pO_2^{-m_i} \quad (5.2)$$

Where m_i is an exponent related with the oxygen species involved in the limiting processes [30-32].

- $m=1$, molecular oxygen is involved in the limiting step.



- $m=1/2$, the atomic oxygen is the limiting step.



- $m=1/4$, the charge transfer is involved in the limiting step.



For that study, two different temperatures were selected in order to check if the limiting steps in the ORR change as function of the temperature. As has been discussed above, there is a change in the activation energy around 700 °C, which can be related with the BSCF phase transition from cubic to hexagonal at low temperatures. The temperatures selected for a deeper

analysis were 900 and 650 °C. Furthermore, equivalent circuits were employed to distinguish between the different contributions. Depending on the temperature two or three constant phase element in parallel with three resistances (Figure 5.9) were used. The results for the parent electrode (BSCF composite) and the best performance electrode (BSCF_Sc composite) are shown in Figure 5.13 and Figure 5.14, respectively.

As can be ascribed from Figure 5.13 and Figure 5.14, RHF is not pO_2 dependent. Therefore the HF arc is not related with molecular nor atomic oxygen, some authors have attributed this resistance with the oxygen transfer ion from the TPB to the electrolyte [33, 34]. This resistance is consequence of a reaction between electrode and electrolyte [22] or due to the lower ionic conductivity of the electrolyte compared with the electrode [35]. The value of 0.18 for BSCF_Sc composite at HF it seems consequence of the error obtained in the fitting with the equivalent circuit, since both arcs are coupled and the size of the HF arc is small. So, the theory suggested for the HF resistance as a function of the temperature is validated in this point. Therefore, the O^{2-} transfer in the electrode/electrolyte interface is the limiting step at HF.

The polarization resistance corresponding to low frequency arc showed strong dependence on pO_2 with an exponent between 0.7-0.87 for both compounds and temperatures. This high value suggests that the rate-determining step is the adsorption process of the molecular oxygen in the electrode [23, 36, 37]. This result confirms the assumption suggested above where the low frequency was assigned to surface processes in the oxygen reduction reaction.

Finally, the contribution at medium frequencies, that is distinguished at low temperatures, has a smaller oxygen partial pressure dependence, that can be ascribed to a charge transfer process ($m=1/4$), related with the p-type conductivity of the material ($1/6 < n < 1/4$). In the case of the BSCF_Sc composite the dependence of 0.32 for the resistance as a function of the pO_2 have been interpreted as the atomic oxygen diffusion process followed by a charge transfer [38, 39]. As has been mentioned before, the instability of the BSCF compound as function of the temperature affects the performance of the material. When the operation temperature is maintained below 800 °C there is phase change from a single cubic phase to a mixed hexagonal-cubic phase. This

change is attributed to the change of the oxidation state of the transition metal cations (mainly Co) [40]. As it has been reported for dense membranes [9, 41], the hexagonal phase appears at the grain boundary reducing the oxygen permeation, this effect can be extrapolated for electrodes, producing the phase change in the grain surface, reducing and/or changing the TPB and producing the resistance at this MF at 650 °C.

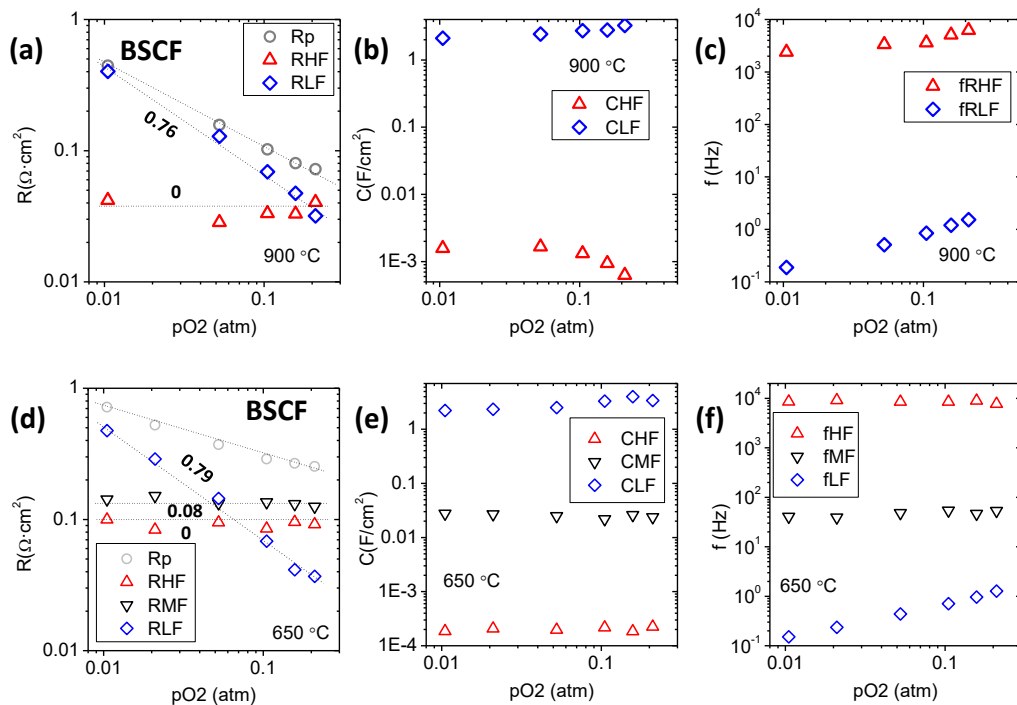


Figure 5.13: Equivalent electrical circuit fitting results for BSCF composite electrode; (a) resistance, (b) capacitance and (c) frequency of different processes at 900 °C in air and (d) resistance, (e) capacitance and (f) frequency of different processes at 650 °C in air.

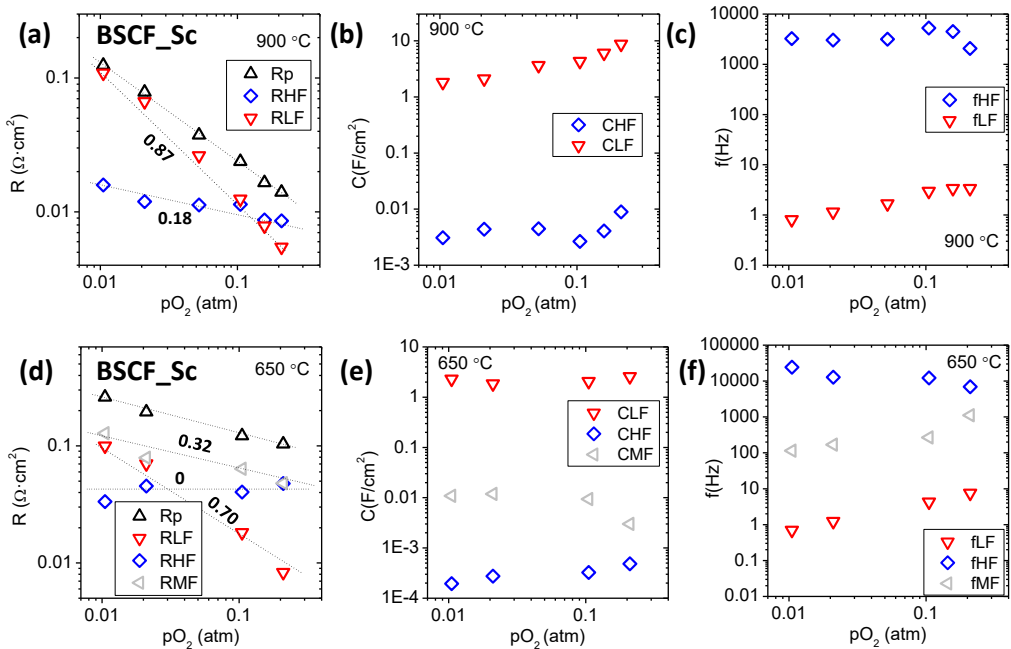


Figure 5.14: Equivalent electrical circuit fitting results for BSCF_Sc composite electrode; (a) resistance, (b) capacitance and (c) frequency of different processes at 900 °C in air and (d) resistance, (e) capacitance and (f) frequency of different processes at 650 °C in air.

5.2.2.2.3. CO₂ containing atmosphere influence on the cell performance

BSCF compounds suffer carbonation in presence of CO₂ below 800 °C, as has been shown in the TG measurements. In order to check the CO₂ effect on the electrode performance, the reference and the best electrode, were tested in CO₂ containing atmospheres. As can be ascribed from Figure 5.14 (a), when the CO₂ is fed in the reactor the polarization resistance increases as a function of time, but when CO₂-free atmosphere is reintroduced in the chamber the polarization resistance comes again to its initial value. The electrochemical impedance spectrum allows discerning what is changing in the electrode performance. As shown in Figure 5.15 (b). It seems that the resistance at high frequency is maintained whereas the resistance at low and medium frequency increases with the presence of CO₂. Fitting with an equivalent circuit permits to confirm the results observed in the Bode and Nyquist plots. The resistance at high frequency (HF) is maintained (Table 5.4), whereas at medium and low

frequency is increased. Since the LF processes take place at the same frequency for both conditions, it seems that there is a competitive diffusion of O_2 and CO_2 for the active sites. However for MF the resistance is shifted to lower frequencies and the resistance value is doubled, indicating a big influence of the charge transfer at the TPB, probably assigned to the surface carbonation and reduction of the TPB length. The same effect is observed for the material doped with Sc indicating that the HF processes (interface electrode-electrolyte) are maintained for both atmospheres and the surface and charge transfer processes (LF and MF, respectively) are harmed with the CO_2 presence.

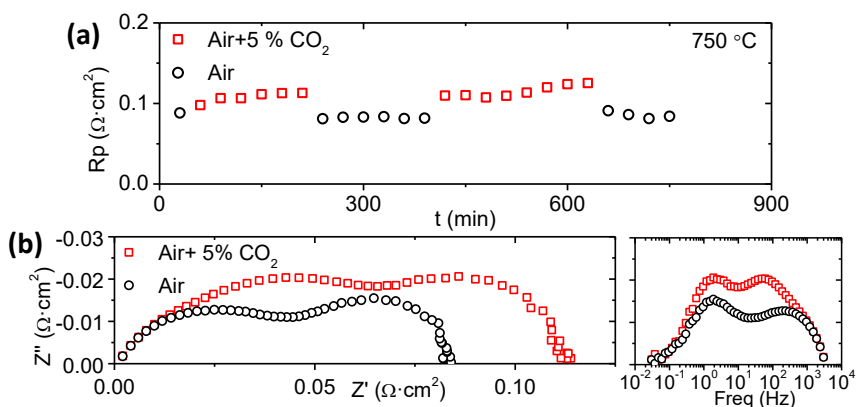


Figure 5.15: Influence of CO_2 containing atmosphere in the cell performance on BSCF ; (a) polarization resistance as function of time, (b) Nyquist plot and (b) Bode plot in CO_2 presence and free atmosphere.

	R_p $\Omega \cdot cm^2$	LF			MF			HF		
		R $\Omega \cdot cm^2$	C F/cm^2	f Hz	R $\Omega \cdot cm^2$	C F/cm^2	F Hz	R $\Omega \cdot cm^2$	C F/cm^2	f Hz
Air	0.105	0.035	2.66	1.71	0.031	0.037	136	0.039	0.001	3999
Air+5% CO_2	0.147	0.048	1.94	1.71	0.060	0.059	45	0.039	0.001	3999

Table 5.4: Equivalent electrical circuit fitting results for BSCF in air and air and CO_2 .

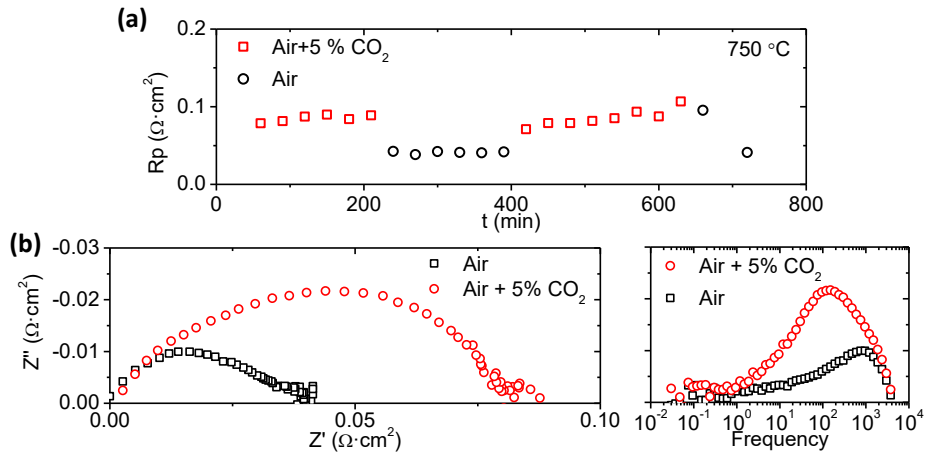


Figure 5.16: Influence of CO₂ containing atmosphere in the cell performance on BSCF_Sc ; (a) polarization resistance as function of time, (b) Nyquist plot and (b) Bode plot in CO₂ presence and free atmosphere.

5.2.3. Fuel cell characterization

The best material tested as composite electrode (BSCF_Sc/GDC) was used in a fully-assembled fuel cell (Figure 5.17). For that purpose, an anode supported fuel cell was used. The anode consisted of a Ni-YSZ anode, a thin YSZ layer as electrolyte and a GDC layer deposited by screenprinting to avoid the reactivity between cathode and electrolyte materials. A metal ring was employed to separate both chambers (anode and cathode) in a quartz reactor. The anode was fed with pure hydrogen or different concentrations, whereas the cathode inlet gas was air or different oxygen partial pressure. Furthermore, the influence of other operation parameters was tested, as the water partial pressure, the total flow and temperature. Electrochemical measurements including Current Density-Voltage (i-V), Current Density-Power Density (i-P), Open Circuit Voltage (OCV) and Electrochemical Impedance Spectroscopy (EIS) were made using the Solartron Analytical 1470E Cell Test System.

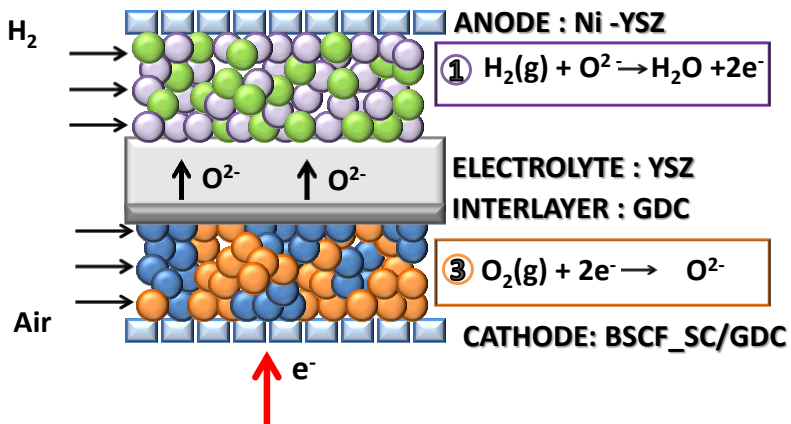
FUEL CELL MODE

Figure 5.17: Fuel cell mode system configuration.

5.2.3.1. Influence of the operation temperature

Cell performance in fuel cell mode was evaluated from 700 °C to 400 °C, from the highest to the lowest temperature. *i*-V and *i*-P curves for the Ni-YSZ/YSZ/GDC/BSFC_Sc-GDC sample are shown in Figure 5.18. The open circuit voltage (OCV) values are 1.08 V and 1.14 V at 700 °C and 550 °C, respectively, under fuel cell conditions. The OCV is originated from the oxygen concentration gradient across the electrolyte and determined by Nernst's equation (Equation (3.6), *Introduction Chapter*). The cell performance increases with increasing operating temperature, as expected. The sample presents peak power density of 882, 546, 278, 124, 47, 16 and 5 mW/cm² from 700 °C to 400 °C, with gradient of 50 °C.

As can be ascribed from Figure 5.18, for the highest tested temperatures (700 °C and 650 °C), the three regimes in the *i*-V curves can be distinguished; activation, ohmic resistance and polarization for concentration. As the temperature is reduced, the ohmic regime becomes more dominant with higher slopes.

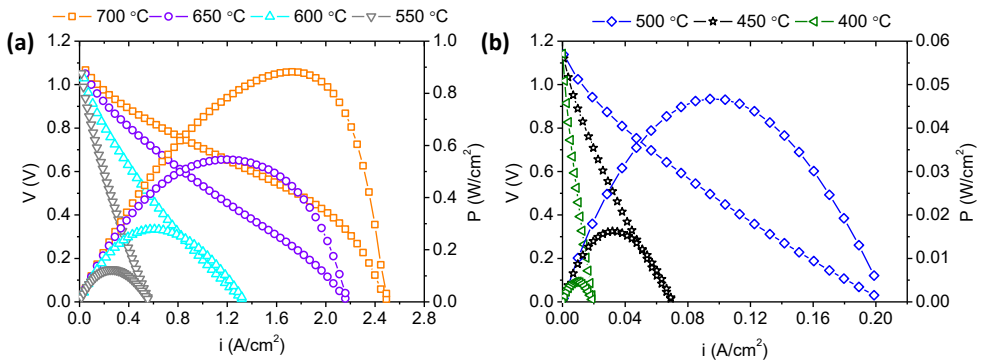


Figure 5.18: i-P and i-V curves of the Ni-YSZ/YSZ/GDC/(BSFC_Sc/GDC) at different temperatures working with wet H₂ (2.5 % vol. H₂O) and pure air.

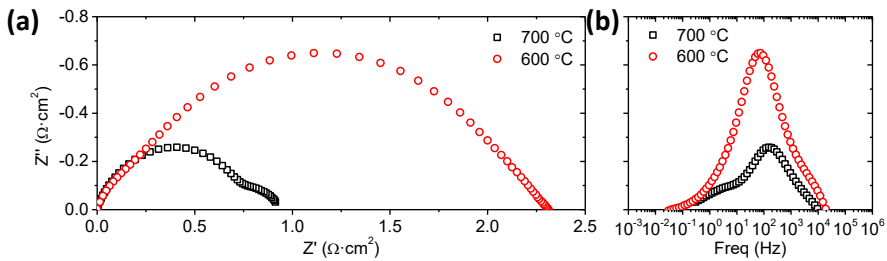


Figure 5.19: Nyquist and Bode plot obtained from the results of the EIS spectra in fuel cell mode near to the OCV.

EIS for the cell under SOFC mode at 700 °C and 600 °C are given in Figure 5.19. The ohmic resistances related with the electrolyte are 0.23 and 0.65 Ω·cm² at 700 and 600 °C, respectively, and have been subtracted from the EIS spectra (defined as the intersection of the arc with the x-axis in the left-side). The resistance associated with the electrolyte has been eliminated in the Nyquist plot in order to compare directly the electrodes contribution. Here, both electrodes (anode and cathode) are involved in the total electrode polarization resistance, thus the adsorption, incorporation and diffusion of hydrogen and oxygen species over the electrocatalyst anode sites and over the ionic conducting materials, respectively have to be taken into account. As can be ascribed from the graphs and the ohmic resistance values, the resistance of the electrodes is higher than the electrolyte resistance, indicating that the electrodes are limiting the cell performance. The electrodes resistance increases by reducing the temperature and the limiting resistance takes place

at medium frequencies. This frequency range (MF) fits with the results obtained for the BSCF_Sc/GDC tested as cathode in the symmetrical cell configuration at intermediate temperature. Thus, the EIS results indicate a possible phase transition on the BSCF_Sc material electrode surface or a change in the transport properties of composite phases.

5.2.3.2. Influence of p_{O_2} , p_{H_2} and p_{H_2O} in the fuel cell performance

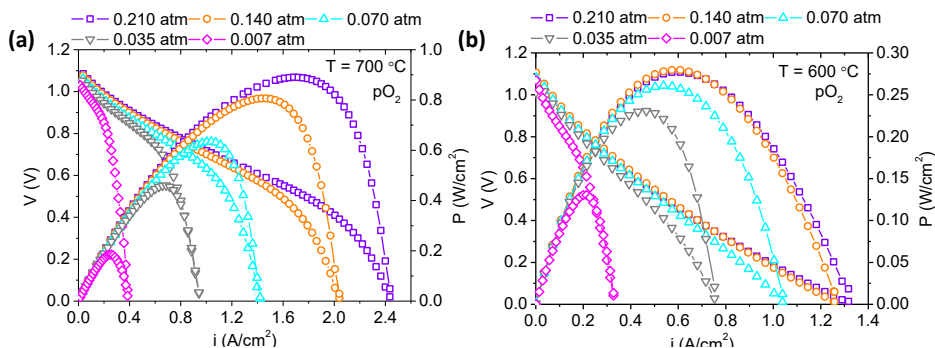


Figure 5.20: i-P and i-V curves of the Ni-YSZ/YSZ/GDC/(BSCF_Sc/GDC) at different oxygen partial pressure working with wet H_2 (2.5 % vol. H_2O) (a) at 700 °C and (b) 600 °C.

The influence of the oxygen partial pressure (p_{O_2}) on the cell performance was checked at two different temperatures. For the highest temperature (Figure 5.20 (a)) the influence of the oxygen partial is more detrimental, by reducing the power density more than 75 %, from 890 mW/cm^2 to 185 mW/cm^2 with a p_{O_2} of 0.007 atm. However, at 600 °C the power density only decreases 50 % at the same p_{O_2} (0.007 atm), changing from 277 mW/cm^2 to 130 mW/cm^2 . This behavior can be explained by the difference in the i-V curves shape. At the highest temperature, it can appreciate the polarization for concentration, indicating the importance of the oxygen concentration in the inlet stream. To extract some conclusions the oxygen utilization was calculated.

Oxygen utilization was calculated for the different oxygen partial pressures and temperatures and the results are shown in Table 5.5 and Table 5.6. Where FO_2 is the oxygen flow introduced in the cathode and FO_2^o the oxygen used in the cathode. The oxygen utilization (U_{O_2}) is calculated from the Faraday's equation and taking into account the oxygen reduction reaction as follows:



$$F_{O_2}^\circ = \frac{I}{n \cdot C} = \frac{I \cdot 22400 \cdot 60}{4 \cdot 96500} \quad (5.7)$$

$$U_{O_2} = \frac{F_{O_2}^\circ}{F_{O_2}} \cdot 100 \quad (5.8)$$

The oxygen utilization increases as the oxygen content in the cell is reduced. Furthermore, U_{O_2} is reduced at lower temperatures, indicating that the reduction of the temperature decreases the activity of the cathode and the oxygen requirements. At low temperatures it is only possible to appreciate the ohmic resistance in the i-V curves. Additionally, the OCV variation (Equation (3.6)) is produced by the partial pressures difference in the cell, since the p_{O_2} is reduced and p_{H_2} remains constant, the OCV of the fuel cell drops, as expected.

p_{O_2} (atm)	F_{O_2} (ml/min)	i (A/cm ²)	$F_{O_2}^\circ$ (ml/min)	U_{O_2} (%)
0.210	31.50	2.43	5.38	17
0.140	21.00	2.03	4.50	21
0.070	10.50	1.43	3.17	30
0.035	5.25	0.95	2.10	40
0.007	1.05	0.34	0.75	72

Table 5.5: Oxygen utilization at 700 °C.

p_{O_2} (atm)	F_{O_2} (ml/min)	i (A/cm ²)	$F_{O_2}^\circ$ (ml/min)	U_{O_2} (%)
0.210	31.50	1.32	2.92	9
0.140	21.00	1.27	2.81	13
0.070	10.50	1.05	2.33	22
0.035	5.25	0.76	1.68	32
0.007	1.05	0.32	0.71	68

Table 5.6: Oxygen utilization at 600 °C.

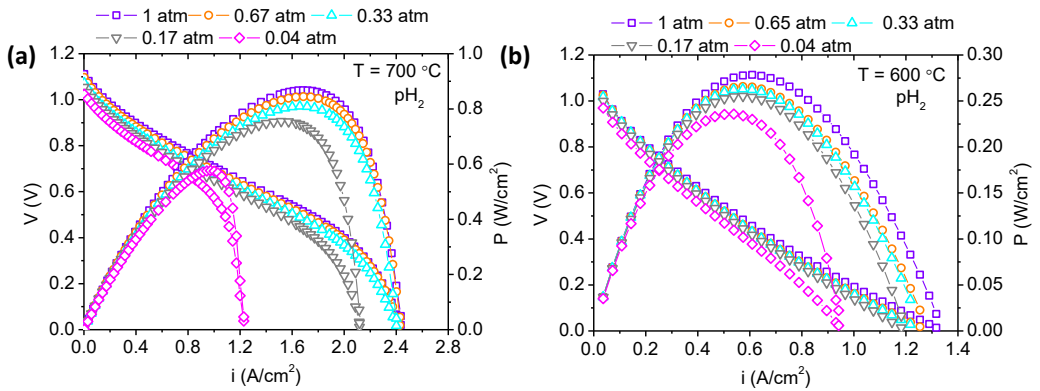


Figure 5.21: i-P and i-V curves of the Ni-YSZ/YSZ/GDC/(BSCF_Sc/GDC) at different wet hydrogen partial pressure (2.5 % vol. H₂O) working with air (a) at 700 °C and (b) 600 °C.

The same effect obtained for the oxidant is found by the fuel dilution, being more important the influence of the fuel fed at high temperatures. Similarly, the fuel utilization was determined as is described by equation (5.9), (5.10) and (5.11). Where F_{H_2} is the hydrogen flow rate introduced in the anode, $F_{H_2}^\circ$ the hydrogen used in the anode and U_{H_2} is the fuel utilization. In addition, the hydrogen partial pressure influence seems not to be as limiting as the oxygen partial pressure. For instance, with a hydrogen partial pressure of 0.04 atm the power density decreases to 576 mW/cm² whereas for 0.035 atm of O₂ the power density is 475 mW/cm², due to bigger fuel utilization (89%). Furthermore, the fuel utilization increases by reducing p_{H_2} , but drops by reducing the temperature (Table 5.7 and Table 5.8).



$$F_{H_2}^\circ = \frac{I}{n \cdot C} = \frac{I \cdot 22400 \cdot 60}{2 \cdot 96500} \quad (5.10)$$

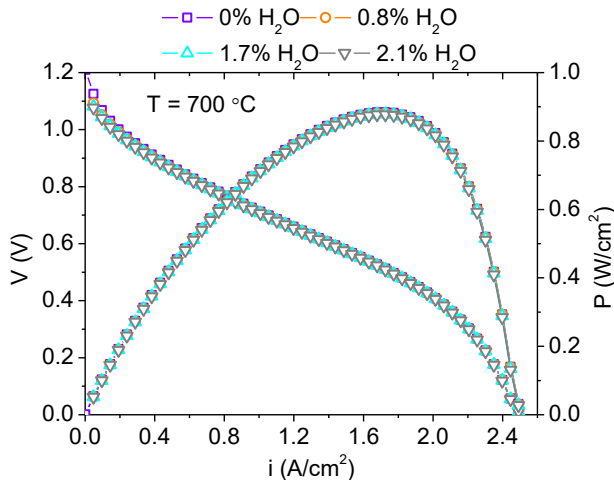
$$U_{H_2} = \frac{F_{H_2}^\circ}{F_{H_2}} \cdot 100 \quad (5.11)$$

p_{H_2} (atm)	F_{H_2} (ml/min)	i (A/cm ²)	$F_{H_2}^\circ$ (ml/min)	U_{H_2} (%)
1.00	150.0	2.43	10.77	7
0.67	100.5	2.42	10.72	11
0.33	49.5	2.41	10.68	22
0.17	25.5	2.12	9.39	37
0.04	6.0	1.20	5.32	89

Table 5.7: Hydrogen utilization at 700 °C.

p_{H_2} (atm)	F_{H_2} (ml/min)	i (A/cm ²)	$F_{H_2}^\circ$ (ml/min)	U_{H_2} (%)
1.00	150.0	1.32	5.85	4
0.67	100.5	1.28	5.67	6
0.33	49.5	1.27	5.63	11
0.17	25.5	1.21	5.36	21
0.04	6.0	0.95	4.21	70

Table 5.8: Hydrogen utilization at 600 °C.

Figure 5.22: i-P and i-V curves of the Ni-YSZ/YSZ/GDC/(BSFC_Sc/GDC) at different water partial pressure working with wet H₂ and pure air.

The influence of the steam content was also studied. As is shown in the Figure 5.22, the cell power density at 700 °C is maintained and the biggest difference

is observed in the OCV value. The higher pO_2 difference between the two electrodes increases the OCV value of the sample working without steam.

5.2.3.3. Total flow influence on the fuel cell performance

Finally, the effect of the total fuel and oxidant flows rate in the inlet stream was studied (Figure 5.23). In this case, it is evident that the highest influence of the total flow takes place at high temperatures, whereas at low temperatures the total flow in the fuel cell performance is independent. The shape of the i - V curves is equal for all flows at 700 °C, but for the smallest flows, the polarization for concentration regime starts before, exhibiting lower power densities. This effect cannot be ascribed to the presence of a leakage in the sample, since the OCV remains constant for all total flows studied. The power density difference between the different flow rates can be ascribed to the fuel/oxygen utilization. In order to check that fact, the fuel utilization was determined. The fuel utilization increases (Table 5.9) as the flow rate decreases, but the power density generation is diminished. Thus, for real applications, the cost balance should be determined in order to select the best conditions, high power densities or high fuel utilization. At low temperatures, the quantity of H_2 consumed is maintained, whereas the fuel utilization increases at low flow rates.

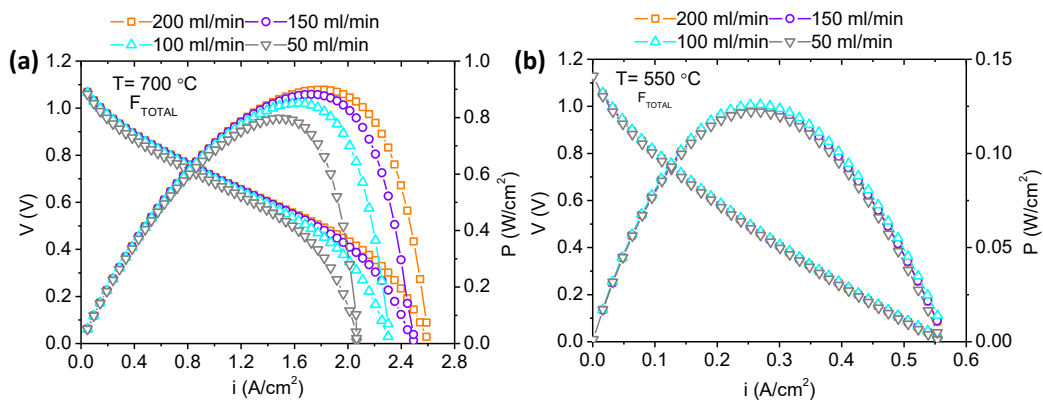


Figure 5.23: i - P and i - V curves of the Ni-YSZ/YSZ/GDC/(BSFC_Sc/GDC) at different total inlet flows working with wet H_2 (2.5 % vol. H_2O) and pure air (a) at 700 °C and (b) 550 °C.

pH ₂ (atm)	FH ₂ (ml/min)	i (A/cm ²)	FH ₂ ^o (ml/min)	U _{H2} (%)
1	200	2.60	11.52	6
1	150	2.43	10.77	7
1	100	2.31	10.23	10
1	50	2.08	9.21	18

Table 5.9: Hydrogen utilization at 700 °C with different flow rates.

pH ₂ (atm)	FH ₂ (ml/min)	i (A/cm ²)	FH ₂ ^o (ml/min)	U _{H2} (%)
1	200	0.55	2.44	1
1	150	0.55	2.44	2
1	100	0.55	2.44	2
1	50	0.55	2.44	5

Table 5.10: Hydrogen utilization at 550 °C with different flow rates.

5.2.3.4. Stability on the cell performance

One of the most important parameters of the cells development is the stability in real operation conditions. For that purpose, the cell stability over time at 600 °C was checked with a current of 0.5 A (0.78 A/cm²). The power density was measured for 2.5 days. The power density was increasing with time achieving a constant value of 285 mW/cm² (Figure 5.24). This value fits with power density obtained in the i-P curve at 600 °C.

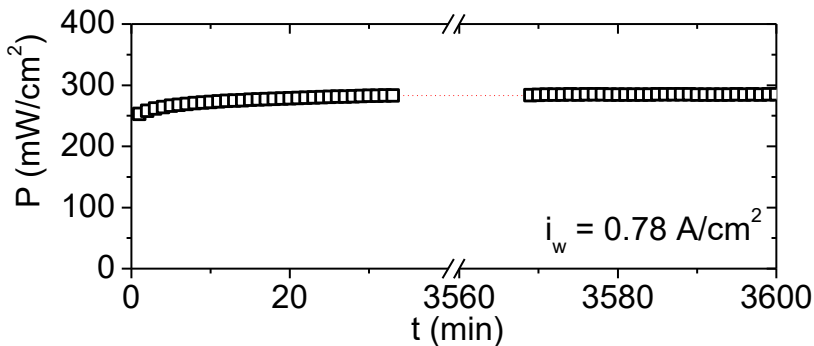


Figure 5.24: Stability of the fully-assembled fuel cell Ni-YSZ/YSZ/GDC/(BSFC_Sc-GDC) working with wet H₂ (2.5 % vol. H₂O) at 600 °C and pure air at a constant current density of 0.78 A/cm².

To compare and explain the difference in the obtained results, EIS measurements were performed at the beginning and at the end of the stability test. Two different measurements were recorded, one near the OCV and another at 0.2 A. For the EIS near the OCV the resistance obtained at medium frequency decreases with time, there is an activation of the electrode with time. However, at higher frequencies the EIS spectrum is almost constant, appearing a small resistance at very low frequencies. This change can be associated with surface processes, *i.e.*, a small densification of the electrodes with lower gas diffusion or surface change of BSCF_{Sc}, due to the phase transformation (from cubic to hexagonal).

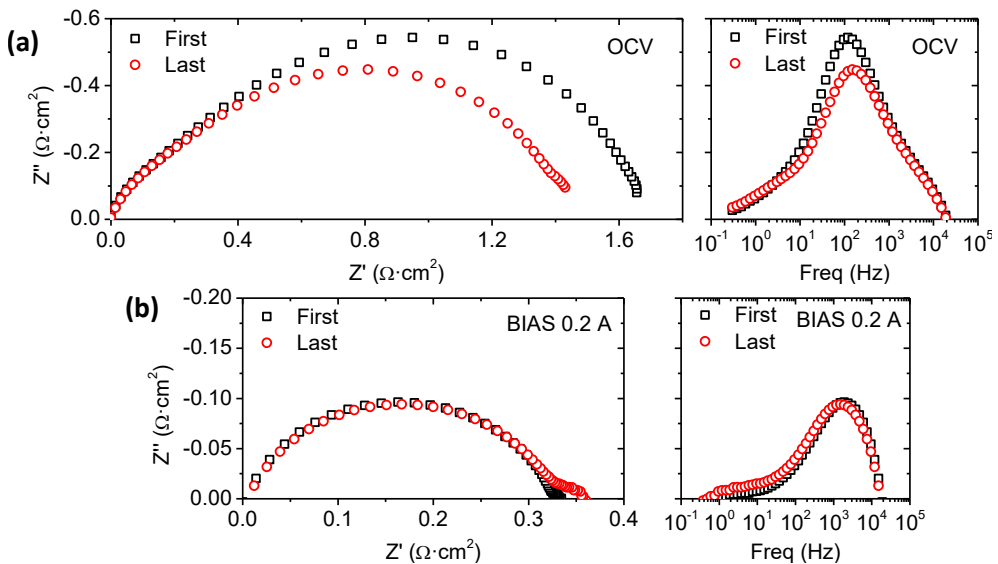


Figure 5.25: Nyquist and Bode plot obtained from the results of the EIS spectra in fuel cell mode near to (a) the OCV and (b) with a BIAS of 0.2 A at the beginning and the end of the stability test at 600 °C.

Therefore, it can be concluded that the materials tested as fully-assembled fuel cell is stable in real operation conditions, and have a good cell performance.

5.2.4. Electrolyzer characterization

5.2.4.1. Steam electrolysis

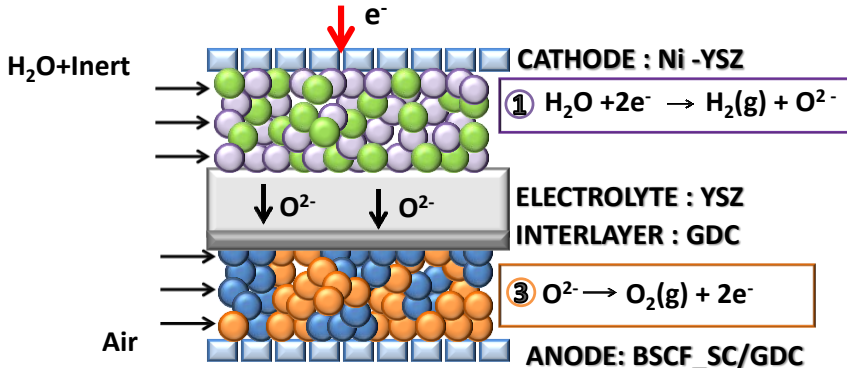


Figure 5.26: Electrolysis mode system.

At the beginning of the present thesis it was not possible to check the cell performance in electrolysis mode, but after few years two analysis units were incorporated in the high temperature set-up; a mass spectrometer and a gas chromatograph. The new equipment allowed checking the stability of the hydrogen and carbon monoxide production, and the Faradic efficiency of the cell. Thus, a new sample Ni-YSZ/YSZ/GDC/(BSFC_Sc-GDC) was manufactured and measured. The sample power density was checked again at different temperatures:

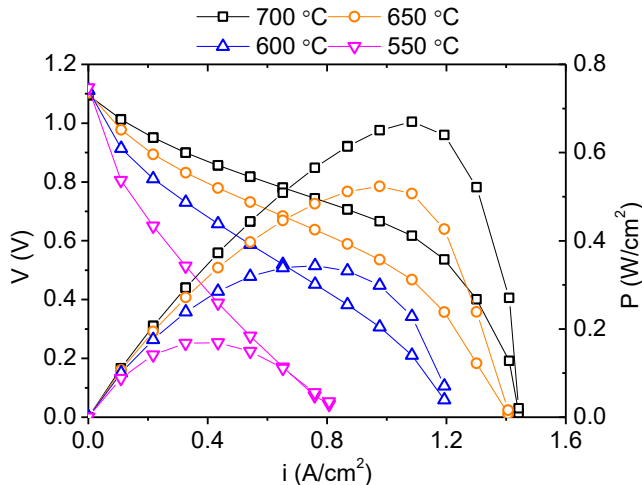


Figure 5.27: i - P and i - V curves of the Ni-YSZ/YSZ/GDC/BSFC_Sc-GDC at different temperatures working with wet H_2 (2.5 % vol. H_2O) and pure air.

After testing the sample in fuel cell mode, the temperature was increased again until 700 °C. H₂O electrolysis was performed at three different temperatures 700, 600 and 500 °C. Figure 5.28 represents the H₂ production determined by a mass spectrometer in the cathode outlet stream during the electrolysis experiments. Cathode was fed with 100 ml/min of wet argon with a 2.5 % vol. of H₂O. A constant current density was applied during 30 minutes, after that, the wet Ar flow was maintained. Hydrogen is produced and detected from a low imposed current density as 16 mA/cm² or 8 mA/cm², and that production increases with the applied current density. An important aspect is the steady production of hydrogen whatever the imposed current density (Figure 5.28). The range of the current density applied in the cells was function of the operation temperature. As the temperature is reduced, the resistance of electrodes and electrolyte increases producing higher cell overpotential and not allowing higher current densities.

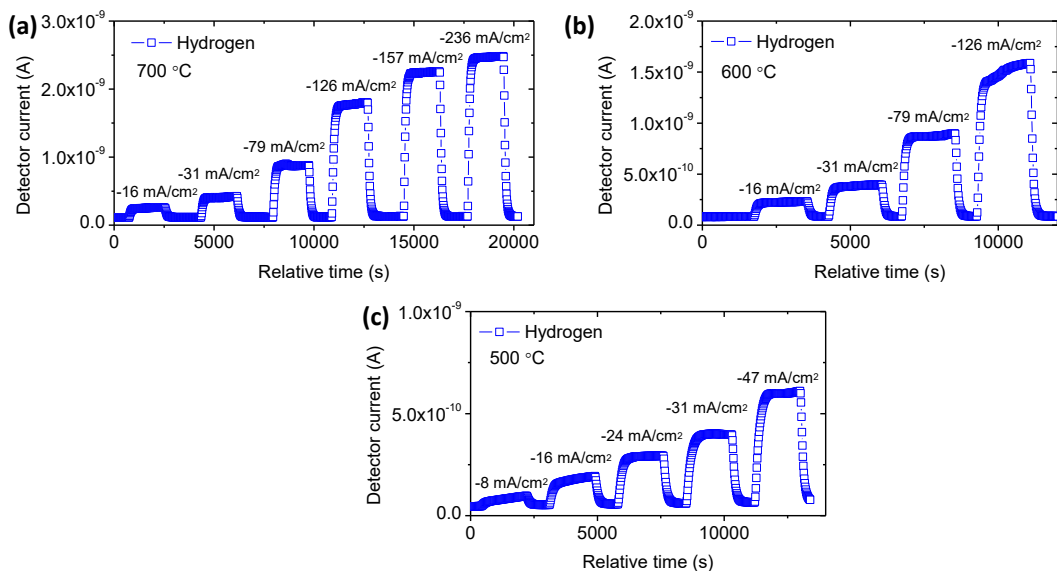


Figure 5.28: Mass spectrometer results of the steam electrolysis at different temperatures; (a) 700 °C (b) 600 °C and (c) 500 °C. Values in the graph are the current densities applied.

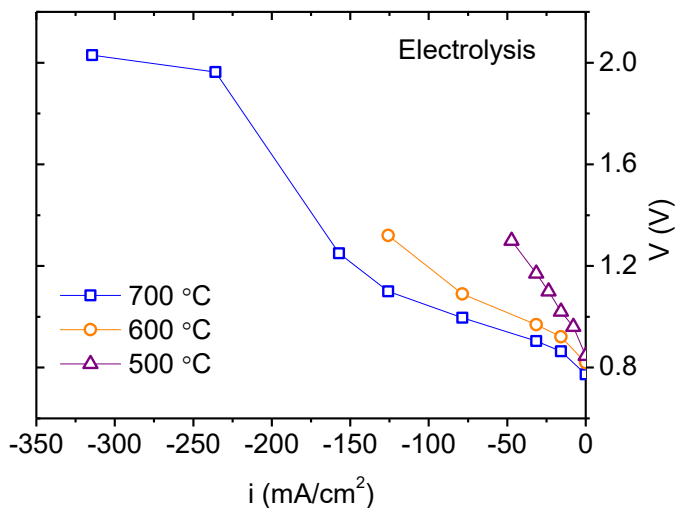


Figure 5.29: i-V curves for the steam electrolysis.

Figure 5.29 represents the overpotential observed for each current density. The negative sign of the current density indicates that the current is applied and is not produced by the cell. At 700 °C three different regimes can be distinguished, at low, medium and high currents. At low currents (near the OCV) there is a big change in the cell overpotential with the current, after that the slope of the overpotential voltage decreases and above 200 mA/cm² the cell overpotential has a little variation with the current density, indicating small change in the total resistance. It has been reported a similar behavior for cells working with YSZ as electrolyte at high current densities, and that effect has been assigned to the promotion of electronic conductivity in the thin YSZ electrolyte [42]. This effect is observed in the present cell (at high current densities) for voltages lower than the electroreduction voltage of 2.3V [43]. Furthermore, this effect is reversible for low levels of electroreduction, and the material can come back to the original state by applying lower currents or increasing the oxygen potential. Thus, the criterion in the electrolysis and co-electrolysis experiment in the present thesis was not increase too much the cell voltage in order not to achieve an irreversible electroreduction of the YSZ. With the gas chromatograph was possible to quantify the hydrogen produced in the steam electrolysis process and the results for three different temperatures are shown in Figure 5.30.

The Faradic efficiency (Equation (4.13)) in steam electrolysis was determined from the expected hydrogen production, calculated according to the Faraday's equation (Equation (4.14)) and the experimental hydrogen production determined during the stationary step of the electrolysis by the gas chromatograph. At low imposed current densities, the efficiency is higher than 90 %. For higher values of current density, the gap between the experimental and the theoretical values increases, producing a low Faradic efficiency. Two can be the explanations. Firstly, the YSZ electrolyte material becomes a mixed ionic-electronic conductivity under high cell overvoltage, and this could be detrimental to the cell efficiency. As a result of this electronic conductivity, a so-called current leakage takes place, *i.e.*, a proportion of the applied current could by-pass the expected electrolysis process and directly crosses over the electrolyte, producing this low Faradic efficiency. Secondly, a weak gas leakage produced between both compartments of the cell could result in the transfer of hydrogen from cathode to anode. This hydrogen could react with the oxygen in the anode producing H_2O and reducing the Faradic efficiency. Both types of leakages could explain the difference between the theoretical and the experimental hydrogen production. Nevertheless, this gap increases with the imposed current, it seems that the process related with the electroreduction of the YSZ (creating a MIEC electrolyte) remains predominant. Moreover, when the cell voltage is around 2 V (at 700 °C) the efficiency decreases drastically, this behavior can be assigned to the electronic conductivity of the electrolyte, as has been described before [42-44].

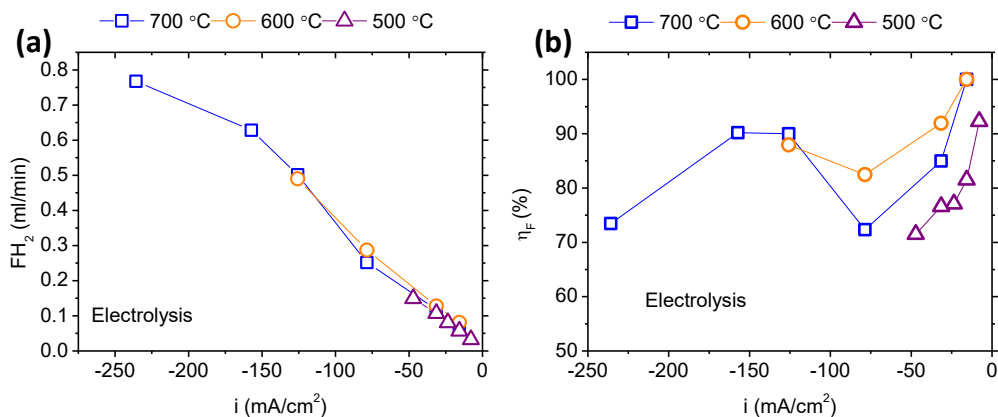


Figure 5.30: (a) Hydrogen production and (b) Faradic efficiency (η_F) for the steam electrolysis working at 700°C, 600°C and 500 °C.

5.2.4.2. Co-electrolysis

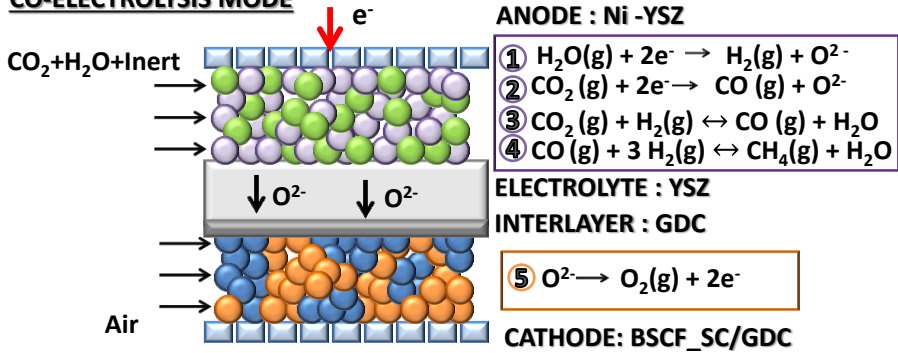
CO-ELECTROLYSIS MODE

Figure 5.31: Co-electrolysis mode system.

CO can be produced as well by CO_2 electrochemical reduction (Reaction (5.12)) and/or by the kinetically rapid Reverse Water Gas Shift reaction in the presence of hydrogen (Reaction (5.13)):



Being $V_{\text{O}}^{\cdot\cdot}$ the oxygen vacancies in the YSZ, e^- the electrons involved in the reaction and $\text{O}_{\text{O}}^{\times}$ an oxygen ion in oxygen position, written by the Kröger-Vink notation. The same test as for the water electrolysis was performed for co-electrolysis of water and CO_2 . To this end, a constant flow rate of 10 ml/min of CO_2 , 2.5 % vol. H_2O and argon (100 ml/min as total flow), was introduced in the fuel side, whereas air was supplied to the oxidant electrode. Four different temperatures were investigated and the different products obtained by the electrolysis were quantified and determined by mass spectroscopy and gas chromatography. The results of the cell voltage for the different currents applied to the cell are presented in Figure 5.32. As was happening in the H_2O electrolysis, when the temperature is diminished, the cell voltage increases, for the same value of current. The same explanation could be done in this point, since the polarization resistance of electrodes and the ohmic resistance of the electrolyte increases by reducing the temperature. That will increase the cell voltage determined by the Nernst's (Equation (4.11)).

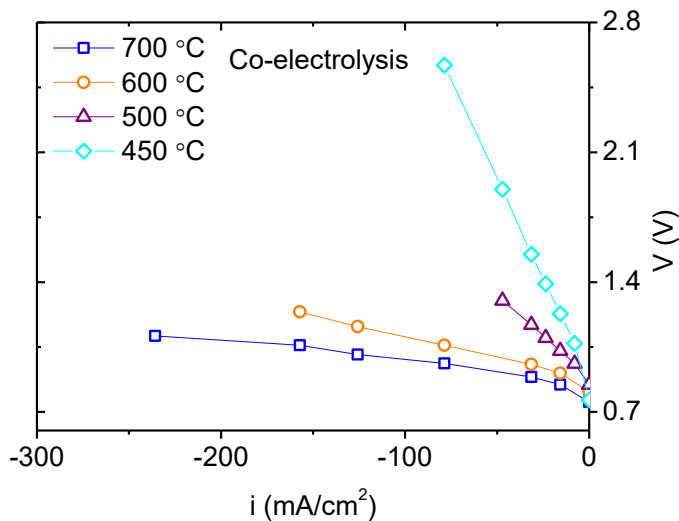


Figure 5.32: i-V curves for the cell working in a co-electrolysis mode.

The results recorded from the mass spectrometer are shown in Figure 5.33. The values in the graph represent the current density introduced in each step, in mA/cm². In this case, three masses were followed by the equipment, being 2 (Hydrogen), 28 (CO or CO₂) and 29 (CO). As can be observed from the graphs, the maximum production comes from the hydrogen, being stable with time with a quick electrolysis current response. The signal of mass 28 and 29 increases when the current is applied at 700 °C, those change signals can be attributed to the CO production by the electroreduction of CO₂ and the reversible water gas shift reaction. The same behavior was observed in the case of 600 °C, being more obvious at higher current densities. However, at 500 °C was not possible to discern the CO production by the change in the signal of mass 28 or/and 29. The thermodynamics of CO₂ and H₂O reduction (Figure 5.34) shows that from temperatures below 827 °C it is more favorable the water reduction reaction than the CO₂ reduction. Since CO₂ electrolysis is less favorable than the H₂O electrolysis [45-48], it should be expected that part of the CO produced comes from RWGSR or be consumed in the Water Gas Shift reaction (WGSR) reaction. Then, the thermodynamics, kinetics and the low current density applied at 500 °C do not allow the CO₂ electroreduction.

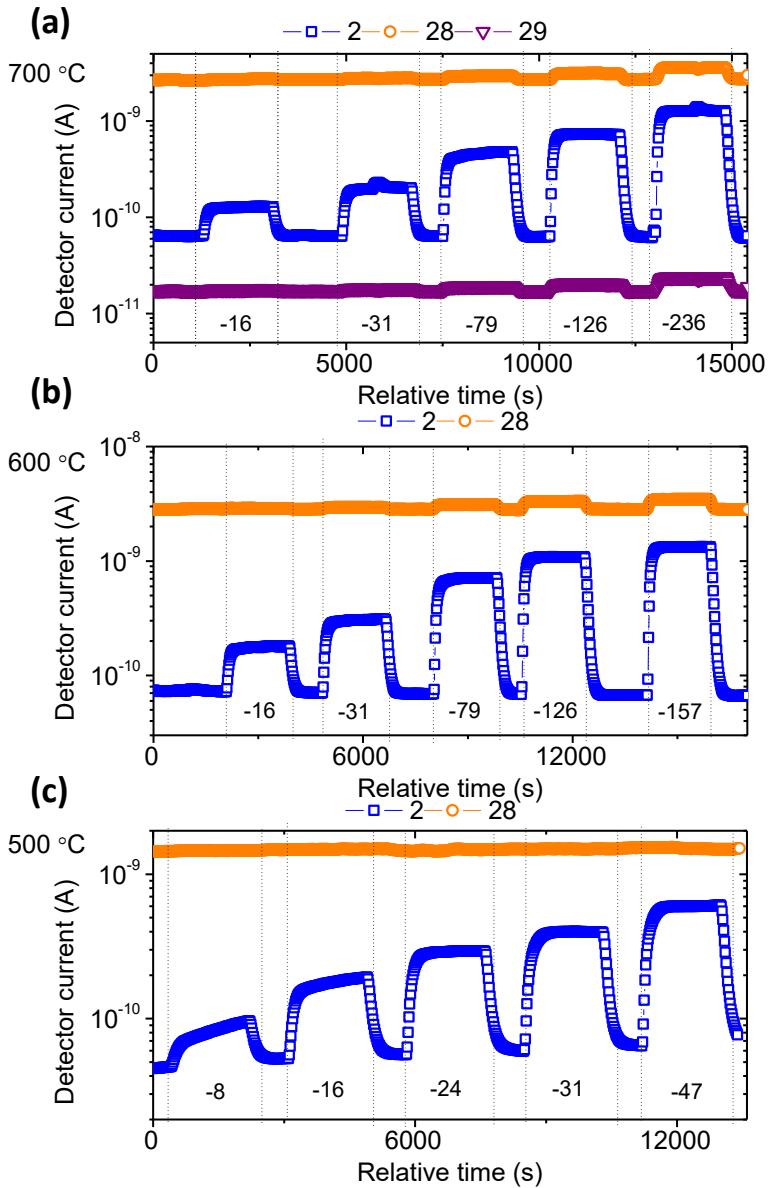


Figure 5.33: Mass spectrometer results of the co-electrolysis at different temperatures; (a) 700 °C (b) 600 °C and (c) 500 °C.

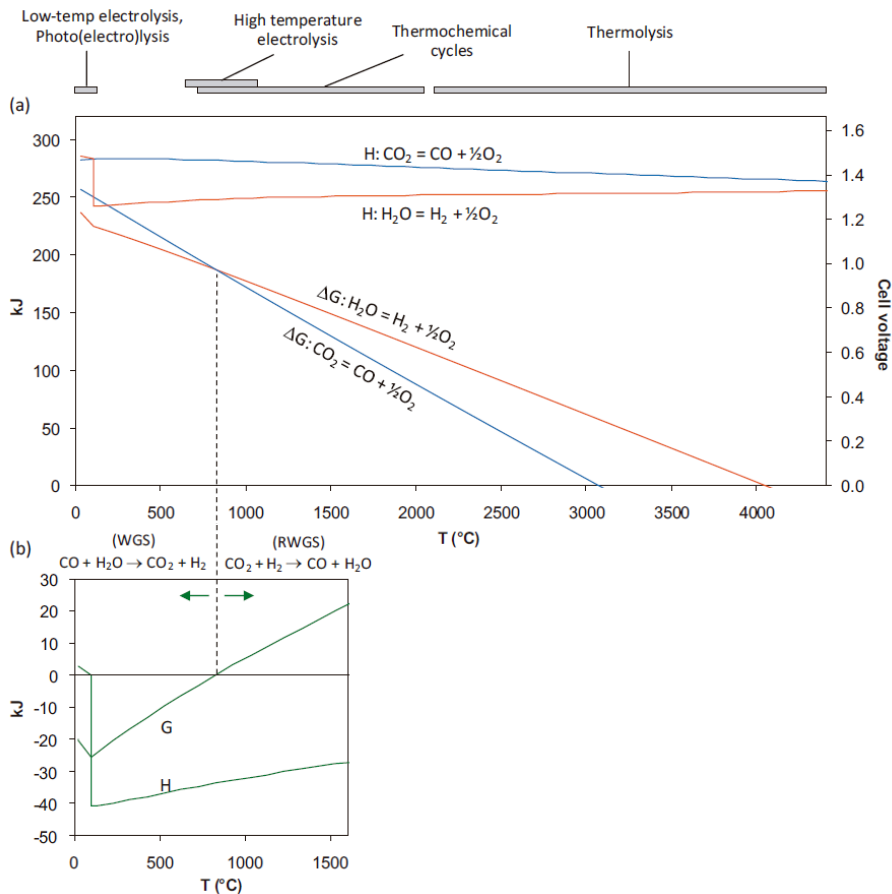


Figure 5.34: (a) Thermodynamics of the CO_2 and H_2 reduction reactions and (b) water-gas shift [49].

In addition, the operation temperature of the electrolyzer was decreased until 450°C , and apart from the mass 2, 28 and 29, the signal of mass 15 (CH_4) was followed in the outlet stream by a mass spectrometer. The signal of hydrogen increases as function of the current density applied (Figure 5.35 (a)). Furthermore, at 79 mA/cm^2 the signal of mass 15 increases, indicating the production of methane. In order to obtain higher signal from the mass spectrometer and the gas chromatograph, the total flow was decreased by half (50 ml/min) compared to the initial flow (Figure 5.35 (b)). When the applied current increases the signal of methane increases but the hydrogen signal is maintained. It is important to remain that four moles of hydrogen has to be consumed to produce a mole of methane.

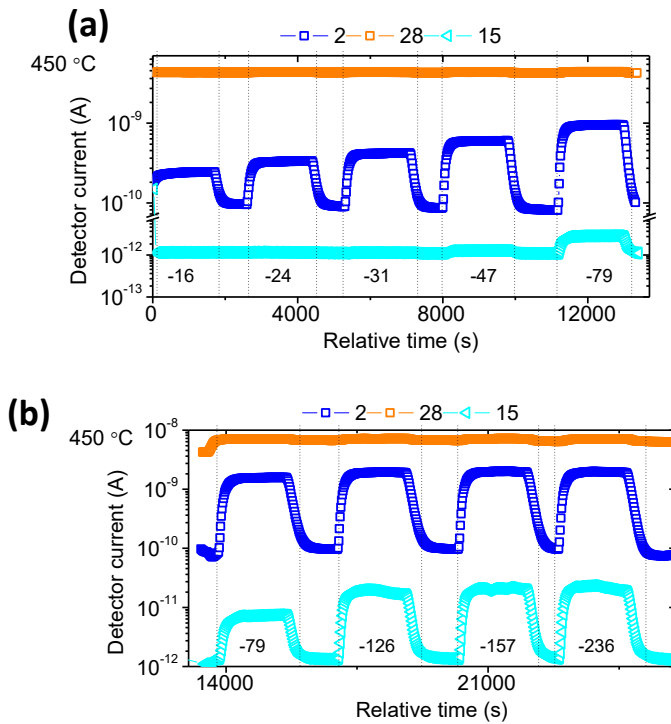


Figure 5.35: Mass spectrometer results of the co-electrolysis at 450 °C with a total flow of (a) 100 ml/min and (b) 50 ml/min. The percentage of each reactant is maintained.

As to confirm the results obtained by the mass spectrometer equipment, gas chromatography was used for all temperatures measured. As can be inferred from Figure 5.36 (b), as the temperature increases the selectivity to CO is enhanced, since the CO₂ reduction is thermodynamically activated at high temperatures [49]. Regarding the hydrogen production, all temperatures show similar behavior except for 450 °C. At 450 °C there is a big change in the hydrogen production, current densities higher than 79 mA/cm² does not produce bigger amounts of hydrogen. These results fit with the production of methane shown in the Figure 5.36 (c). The quantity of methane is increased by applying higher currents. The capability of this cell to produce methane and hydrogen simultaneously and the activity of Ni-YSZ for the methanation process should be highlighted.

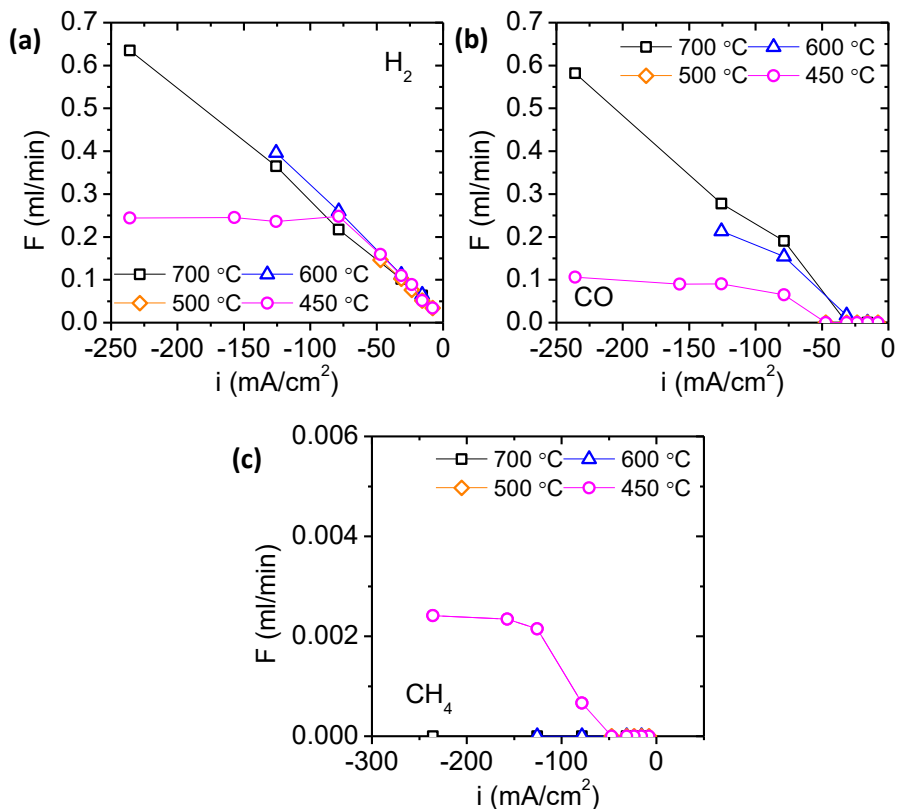
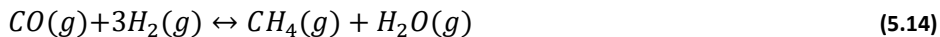


Figure 5.36: (a) Hydrogen (b) carbon monoxide and (c) methane production working at 700, 600 °C, 500 °C and 450 °C.

In order to check if the CO, H₂ and CH₄ production follows the thermodynamic equilibrium, the RWGSR and the methanation equilibrium have been taken into account:



The results determined by the equilibrium are plotted in Figure 5.37. The CH₄ production does not achieve the equilibrium, whereas the CO production overcomes the equilibrium. Thus, not all CO produced is converted to CH₄, the Ni-YSZ catalyst is not enough active to shift the Equation (5.14) to the equilibrium.

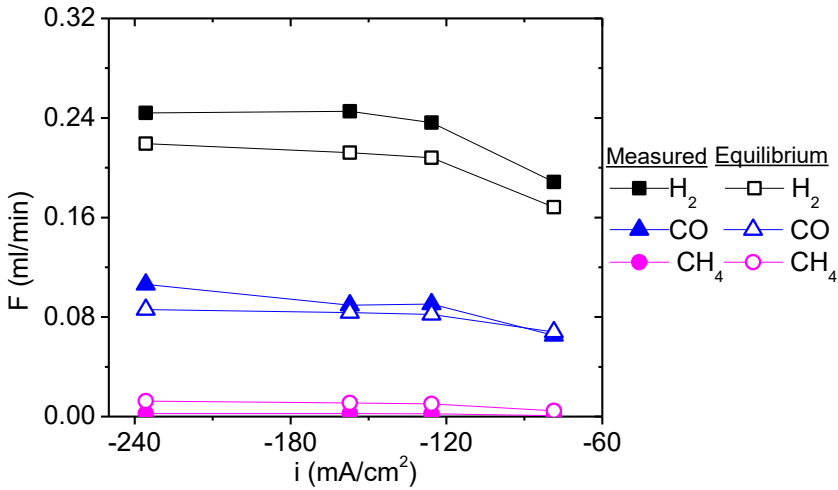


Figure 5.37: Results of the flow rate obtained during the Co-electrolysis mode at 450 °C and the corresponding values in the equilibrium.

Finally, co-electrolysis efficiency (Equation (4.17)) was calculated, for that purpose the current required for the hydrogen and CO production (Equation (4.15) and (4.16), respectively) was determined. For the hydrogen determination the hydrogen used for the CH₄ generation at 450 °C was also included. As can be inferred from Figure 5.38, for the highest temperatures the efficiency is around 100%, but when the temperature is reduced, the efficiency starts to diminish. In the case of 500 °C, it seems that the limit of CO detection in the gas chromatograph is not enough to measure the CO produced, thereby lower efficiencies are achieved. However at 450 °C, as the current density increases the cell efficiency is diminished. The cell voltage at that conditions, is higher than the electroreduction voltage of YSZ (2.3 V) and an electrons leakage of through the YSZ electrolyte can be produced, reducing the cell efficiency.

$$I_{H_2} = n \cdot F \cdot V_{H_2 \text{ exp}} \quad (4.15)$$

$$I_{CO} = n \cdot F \cdot V_{CO \text{ exp}} \quad (4.16)$$

$$\eta_{ener} = \frac{I_{H_2} + I_{CO}}{I} \quad (4.17)$$

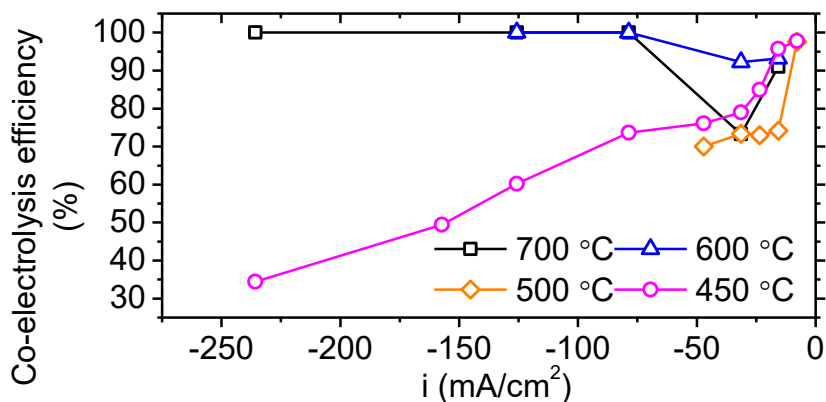


Figure 5.38: Co-electrolysis efficiency.

5.2.4.3. Electrolysis and co-electrolysis comparison

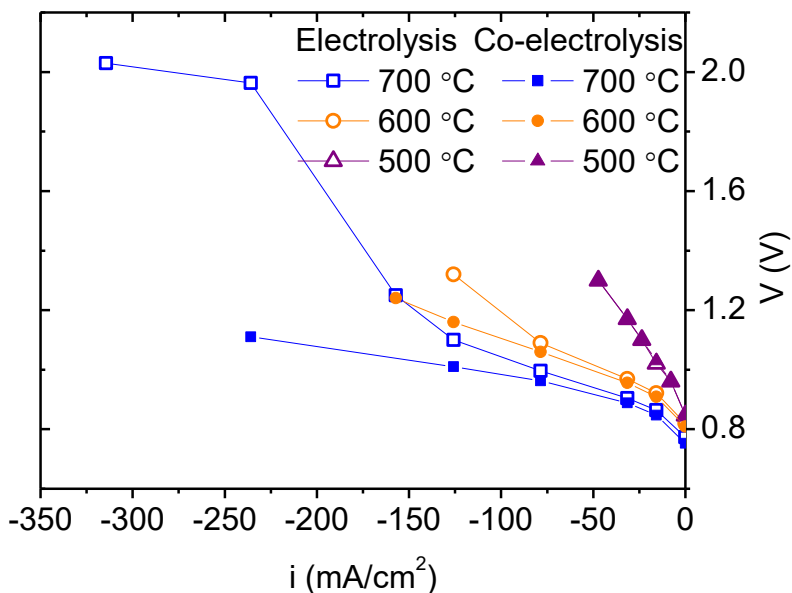


Figure 5.39: Comparison between i-V curves of electrolysis and co-electrolysis.

After the analysis of the different processes; electrolysis and co-electrolysis, it is necessary to compare between the voltages obtained from both modes in all temperature range. The i-V curves for H₂O and H₂O and CO₂ co-electrolysis are

represented in Figure 5.39. For the highest temperatures, the co-electrolysis process produces lower cell voltages [47, 50] and the efficiency of the cell increases. Consequently, the experiments performed reveal that co-electrolysis is kinetically favored rather than H₂O electrolysis at the current density range tested. Ni was found active for the electrochemical reduction of CO₂ at high temperature [46]. Furthermore, in the co-electrolysis mode the WGSR and RWGSR reaction should also be taken into account in the cell voltage. At 500 °C the voltage is almost the same for both modes of cell operation. As was explained above, at that temperature the CO production is not detected and only hydrogen is obtained. It seems that the cell voltage is mainly generated for the electroreduction of hydrogen and not for the presence of CO₂ in the inlet stream.

5.3. Conclusions

The parent Ba_{0.5}Sr_{0.5}Co_{0.8}Fe_{0.2}O_{3-δ} was doped with 3% of Sc, Zr and Y in B site. These elements were selected for their constant oxidation state in order to avoid phase change transition. However, after stability test at 750 °C in air, all compounds shown secondary phases ascribed to the hexagonal phase, being the parent Ba_{0.5}Sr_{0.5}Co_{0.8}Fe_{0.2}O_{3-δ} the most instable. Furthermore, the influence of CO₂ containing atmospheres was checked by TGA measurements. All compounds exhibited carbonation from 500 °C.

The electrochemical properties were studied for all materials synthesized. Regarding the total DC conductivity, all compounds shown a p-type conductivity and Ba_{0.5}Sr_{0.5}(Co_{0.8}Fe_{0.2})_{0.97}Sc_{0.03}O_{3-δ} exhibited the highest conductivity. Electrochemical impedance spectroscopy analysis shown one resistance at high frequencies, related with O²⁻ transport in the electrode-electrolyte, one resistance at medium frequencies, ascribed to the TPB length (usually present in composite electrodes) and one resistance at low frequency, due to the influence of the molecular oxygen adsorption. Despite the production of the hexagonal phase in the stability test, all materials showed better electrochemical performance than the parent BSCF. BSCF_Sc exhibited the best electrochemical results, and was tested in a fuel cell and electrolysis mode. A peak power density of 882 mW/cm² was achieved for the fuel cell working at 700 °C. The fuel/oxygen utilization suggested a lower utilization at

high partial pressures of O₂ and H₂, high flow rates and low temperatures. Finally, the electrolysis results showed a high Faraday's efficiencies for electrolysis and co-electrolysis mode. However, at high current densities the reduction of the electrolyte produces the current leakage and the resulting reduction of Faraday's efficiency. At temperatures as low as 450 °C, the simultaneous production of CO, CH₄ and H₂ took place in the Ni-YSZ electrode, showing catalytic activity of this composite material for the methanation reaction.

5.4. References

- [1] M. Burriel, C. Niedrig, W. Menesklou, S.F. Wagner, J. Santiso, E. Ivers-Tiffée, *Solid State Ion.*, 181 (2010) 602-608.
- [2] Z. Shao, S.M. Halle, *Nature*, 431 (2004) 170-173.
- [3] A. Yan, M. Cheng, Y. Dong, W. Yang, V. Maragou, S. Song, P. Tsiakaras, *Applied Catalysis B: Environmental*, 66 (2006) 64-71.
- [4] M.J. Scholten, J. Schoonman, J.C. van Miltenburg, H.A.J. Oonk, *Solid State Ion.*, 61 (1993) 83-91.
- [5] R.D. Shannon, *Acta Crystallographica Section A*, 32 (1976) 751-767.
- [6] Z. Shao, W. Yang, Y. Cong, H. Dong, J. Tong, G. Xiong, *Journal of Membrane Science*, 172 (2000) 177-188.
- [7] W. Zhou, R. Ran, Z. Shao, W. Zhuang, J. Jia, H. Gu, W. Jin, N. Xu, *Acta Materialia*, 56 (2008) 2687-2698.
- [8] C. Niedrig, S. Taufall, M. Burriel, W. Menesklou, S.F. Wagner, S. Baumann, E. Ivers-Tiffée, *Solid State Ion.*, 197 (2011) 25-31.
- [9] K. Efimov, Q. Xu, A. Feldhoff, *Chem. Mat.*, 22 (2010) 5866-5875.
- [10] D.N. Mueller, R.A. De Souza, T.E. Weirich, D. Roehrens, J. Mayer, M. Martin, *Physical Chemistry Chemical Physics*, 12 (2010) 10320-10328.
- [11] F. Wang, K. Igarashi, T. Nakamura, K. Yashiro, J. Mizusaki, K. Amezawa, *Solid State Ion.*
- [12] E.G. Babakhani, J. Towfighi, L. Shirazi, A. Nakhaeipour, A. Zamaniyan, Z. Shafiei, *Journal of Materials Science and Technology*, 28 (2012) 177-183.
- [13] J.M. Porras-Vazquez, P.R. Slater, *J. Power Sources*, 209 (2012) 180-183.
- [14] C. Kwak, D.W. Jung, D.-H. Yeon, J.S. Kim, H.J. Park, S.-J. Ahn, S. Seo, S.M. Lee, *RSC Advances*, 3 (2013) 10669-10672.
- [15] J.I. Jung, S.T. Misture, D.D. Edwards, *Solid State Ion.*, 181 (2010) 1287-1293.
- [16] J.I. Jung, S.T. Misture, D.D. Edwards, *J. Electroceram.*, 24 (2010) 261-269.

- [17] Z. Duan, M. Yang, A. Yan, Z. Hou, Y. Dong, Y. Chong, M. Cheng, W. Yang, J. Power Sources, 160 (2006) 57-64.
- [18] E.P. Murray, S.A. Barnett, Solid State Ion., 143 (2001) 265-273.
- [19] Z. Qingshan, J. Tongan, W. Yong, Solid State Ion., 177 (2006) 1199-1204.
- [20] W.G. Wang, M. Mogensen, Solid State Ion., 176 (2005) 457-462.
- [21] M.A. Peña, J.L.G. Fierro, Chem. Rev., 101 (2001) 1981-2018.
- [22] S.B. Adler, Chem. Rev., 104 (2004) 4791-4843.
- [23] C. Setevich, F. Prado, A. Caneiro, J. Solid State Electrochem., (2016) 1-11.
- [24] M.J. Jorgensen, M. Mogensen, J. Electrochem. Soc., 148 (2001) A433-A442.
- [25] F.S. Baumann, J. Fleig, H.U. Habermeier, J. Maier, Solid State Ion., 177 (2006) 3187-3191.
- [26] V. Dusastre, J.A. Kilner, Solid State Ion., 126 (1999) 163-174.
- [27] J. Nielsen, T. Jacobsen, M. Wandel, Electrochim. Acta, 56 (2011) 7963-7974.
- [28] C.-Y. Yoo, University of Twente, 2012.
- [29] P.F. Haworth, S. Smart, J.M. Serra, J.C. Diniz Da Costa, Physical Chemistry Chemical Physics, 14 (2012) 9104-9111.
- [30] Y. Takeda, R. Kanno, M. Noda, Y. Tomida, O. Yamamoto, J. Electrochem. Soc., 134 (1987) 2656-2661.
- [31] R. Peng, T. Wu, W. Liu, X. Liu, G. Meng, J. Mater. Chem., 20 (2010) 6218-6225.
- [32] M.J. Escudero, A. Aguadero, J.A. Alonso, L. Daza, J. Electroanal. Chem., 611 (2007) 107-116.
- [33] R.R. Peng, T.Z. Wu, W. Liu, X.Q. Liu, G.Y. Meng, J. Mater. Chem., 20 (2010) 6218-6225.
- [34] J.-D. Kim, G.-D. Kim, J.-W. Moon, Y.-i. Park, W.-H. Lee, K. Kobayashi, M. Nagai, C.-E. Kim, Solid State Ion., 143 (2001) 379-389.
- [35] F. Mauvy, C. Lalanne, J.M. Bassat, J.C. Grenier, H. Zhao, L.H. Huo, P. Stevens, J. Electrochem. Soc., 153 (2006) A1547-A1553.
- [36] E.P. Murray, T. Tsai, S.A. Barnett, Solid State Ion., 110 (1998) 235-243.
- [37] B. Philippeau, F. Mauvy, C. Nicollet, S. Fourcade, J.C. Grenier, J. Solid State Electrochem., 19 (2015) 871-882.
- [38] D.Y. Wang, A.S. Nowick, J. Electrochem. Soc., 126 (1979) 1155-1165.
- [39] S.P.S. Badwal, H.J. de Bruin, A.D. Franklin, Solid State Ion., 9 (1983) 973-977.
- [40] Z. Yáng, J. Martynczuk, K. Efimov, A.S. Harvey, A. Infortuna, P. Kocher, L.J. Gauckler, Chem. Mat., 23 (2011) 3169-3175.
- [41] P. Müller, Karlsruhe Institut für Technologie 2013.

- [42] M.A. Laguna-Bercero, R. Campana, A. Larrea, J.A. Kilner, V.M. Orera, *Fuel Cells*, 11 (2011) 116-123.
- [43] W. Weppner, *J. Electroanal. Chem.*, 84 (1977) 339-350.
- [44] D.A. Wright, J.S. Thorp, A. Aypar, H.P. Buckley, *J. Mater. Sci.*, 8 (1973) 876-882.
- [45] C.M. Stoots, J.E. O'Brien, J.S. Herring, J.J. Hartvigsen, *Journal of Fuel Cell Science and Technology*, 6 (2009) 0110141-01101412.
- [46] Z. Zhan, L. Zhao, *J. Power Sources*, 195 (2010) 7250-7254.
- [47] Z. Zhan, W. Kobsiriphat, J.R. Wilson, M. Pillai, I. Kim, S.A. Barnett, *Energy and Fuels*, 23 (2009) 3089-3096.
- [48] C. Gaudillere, L. Navarrete, J.M. Serra, *Int. J. Hydrog. Energy*, 39 (2014) 3047-3054.
- [49] C. Graves, S.D. Ebbesen, M. Mogensen, K.S. Lackner, *Renewable and Sustainable Energy Reviews*, 15 (2011) 1-23.
- [50] C. Graves, S.D. Ebbesen, M. Mogensen, *Solid State Ion.*, 192 (2011) 398-403.

6



**electrodes for ionic
electrolytes**

6. La_{2-x}A_xNi_{1-y}B_yO_{4+δ} electrodes for ionic electrolytes

6.1. Introduction

Ruddlesden-Popper series with the general formula La_{n+1}Ni_nO_{3n+1} (Figure 6.1), has attracted great interest due to its excellent electrochemical properties [1, 2]. Those properties can be correlated with the anisotropic structure, consisting of rock-salt and perovskite layers interspersed [3-5]. The value of n in the general formula is related with the number of perovskite layers between two rock-salt layers. Due to its layered structure these compounds are able to accommodate hyperstoichiometric oxygen in the interstitial sites of the rock-salt layer [6], exhibiting good oxide ion conductivity at intermediate temperatures [7-10]. The highly anisotropic oxygen diffusion is produced *via* the interstitial oxygen defects in the lattice [11] and the cooperative diffusion in the vacancies in the perovskite layer [7]. Furthermore, the oxygen migration in the *ab*-plane is greater than the *c*-plane [12]. Those qualities make these compounds suitable as SOFC cathodes.

It has been reported that substituting La by other elements with smaller ionic radius could increase the quantity of oxygen hyperstoichiometric at the same oxygen partial pressure and temperature [13] due to the variation in the cell parameters. In order to improve the electrocatalytic activity [14, 15] of the cathode as well and due to the similar ionic radius (La= 1.216 Å and Pr= 1.179Å), Pr was introduced in the La site. As has been reported previously [16, 17], if the amount of Pr in the La site is low, the orthorhombic *Fmmm* space group of La₂NiO_{4+δ} is maintained, however, higher amounts of Pr will shift the structure to *Bmab* space group. Furthermore, this aforementioned change in the structure agrees with the chemical instability of higher Pr content nickelates compounds. As not to produce any crystal structure symmetry, low Pr contents have been investigated; 25 % and 50 %.

Regarding Ni position, Co was selected due to its similar ionic radius and the diffusion coefficient improvement ascribed from its high redox activity [18]. The amount of Co was selected in order to maintain the orthorhombic structure, since Co contents higher than 60% lead to a *Bmab* symmetry. In

addition, it has been widely reported the high influence of the Co increasing the TEC [19, 20], as a result only 20 % of Co was substituted in the structure.

Furthermore, a double substitution was carried out to check the synergetic influence of both cations (Pr and Co) in the nickelate behavior.

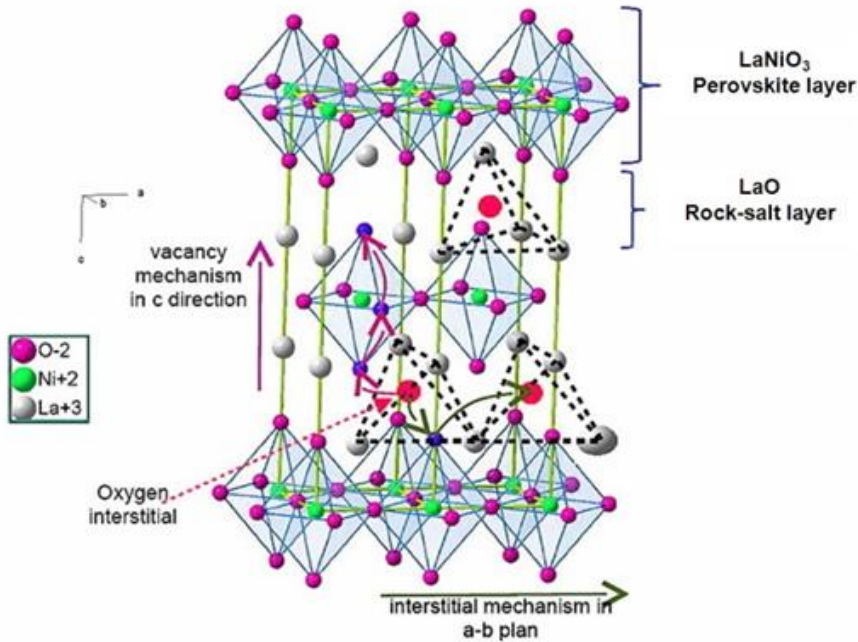


Figure 6.1: Ruddlesden-Popper structure for $\text{La}_2\text{NiO}_{4+\delta}$ [21].

6.2. Results and discussion

6.2.1. Characterization of $\text{La}_{2-x}\text{A}_x\text{Ni}_{1-y}\text{B}_y\text{O}_{4+\delta}$ compounds

6.2.1.1. Cell parameters and δ determination

After the synthesis of the different Ruddlesden-Popper materials by Pechini method, XRD measurements were performed for the identification of the crystalline phase. XRD patterns of the different compositions, labeled as in Table 6.1, are presented in the Figure 6.2. XRD patterns were recorded in the 2θ range from 20 to 90 °. The diffraction peaks of all samples can be assigned to the $\text{La}_2\text{NiO}_{4+\delta}$ phase [3, 22] with an orthorhombic structure [22-24].

<i>Compound</i>	<i>Abbreviation name</i>
La ₂ NiO _{4+δ}	LNO
La _{1.5} Pr _{0.5} NiO _{4+δ}	LPNO
La ₂ Ni _{0.8} Co _{0.2} O _{4+δ}	LNCO
LaPrNiO _{4+δ}	LPNO11
La _{1.5} Pr _{0.5} Ni _{0.8} Co _{0.2} O _{4+δ}	LPNCO
Nd ₂ NiO _{4+δ}	NdNO

Table 6.1: List of the different synthesized and its abbreviation name used in the text.

In order to investigate the influence of partial substitution of La position element by Pr on the crystal structure, Pr was introduced with different ratios. Firstly, 25 % of Pr (LPNO) was substituted in La site obtaining a single phase (Figure 6.2), *i.e.*, no traces of other oxides can be detected to the limit of X-ray diffraction equipment. However, the substitution of 50% La by Pr (LPNO11) in La site produces that some impurities appear. It seems that the transition from *Fmmm* space group to *Bmab*, due to the increasing Pr amount [16, 17], could produce these impurities. Regarding Co substitution, only 20 % was substituted in the Ni position, maintaining the orthorhombic structure of the parent La₂NiO_{4+δ}. Finally, a double substitution was carried out in both positions (LPNCO), as can be ascribed from the Figure 6.2 both cations are well incorporated, with a very small impurity in compounds with Co, which could be assigned to La₃Ni₂O₇.

In addition, the well-studied Nd₂NiO_{4+δ} was synthesized in order to compare with the new compositions obtained in the present thesis.

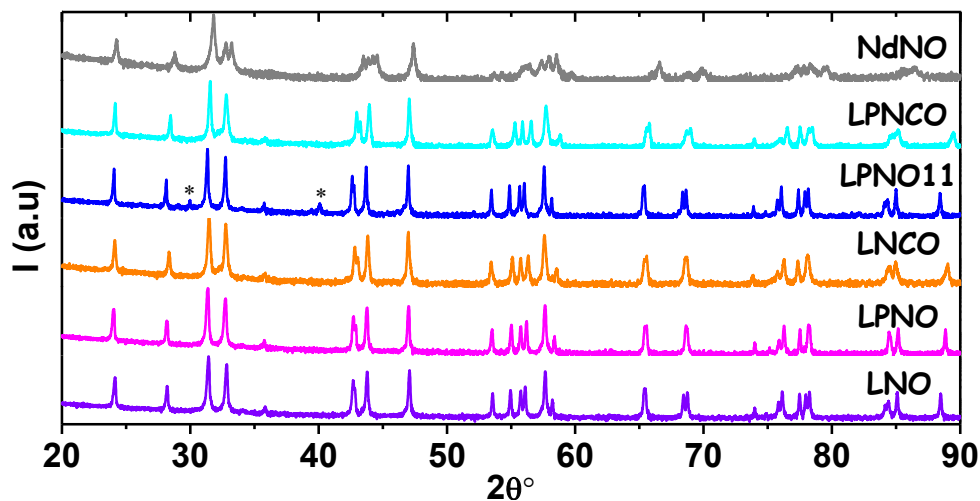


Figure 6.2: XRD patterns of $\text{La}_{2-x}\text{A}_x\text{Ni}_{1-y}\text{B}_y\text{O}_{4+\delta}$ after sintering recorded at room temperature. It is presented the logarithmic intensity of each compound. Impurities are marked on the graph (*).

The stability of these synthesized materials have been checked previously [25]. After two weeks of temperature treatment in air the powders do not show secondary phases over time.

In order to shed further light on the influence of the cations on the structure, the lattice parameters were obtained by Rietveld refinement [26], from the measurements obtained by Bruker D8 in Bragg-Brentano geometry. The Rietveld refinement results are shown in Figure 6.3. This method allows elucidating the structural changes induced by the introduction of the different cations. Both, the atomic radii and the bond type influence have been studied in terms of cell parameters and electrochemical properties for the different materials. For the cell refinement, the position and occupancies were assumed from Skinner *et al.* [27]. The structural parameters values obtained (Table 6.2) are in agreement with the values calculated by Rabenau *et al.*, [28] and Jogersen *et al.*, [29]. All materials prepared in this study exhibit an orthorhombic $Fmmm$ [17, 18, 29-31] space group at room temperature with La occupying the (0, 0, z) position, Ni occupying (0, 0, 0) and oxygen occupying four position variable fractional occupancies (Table 6.2).

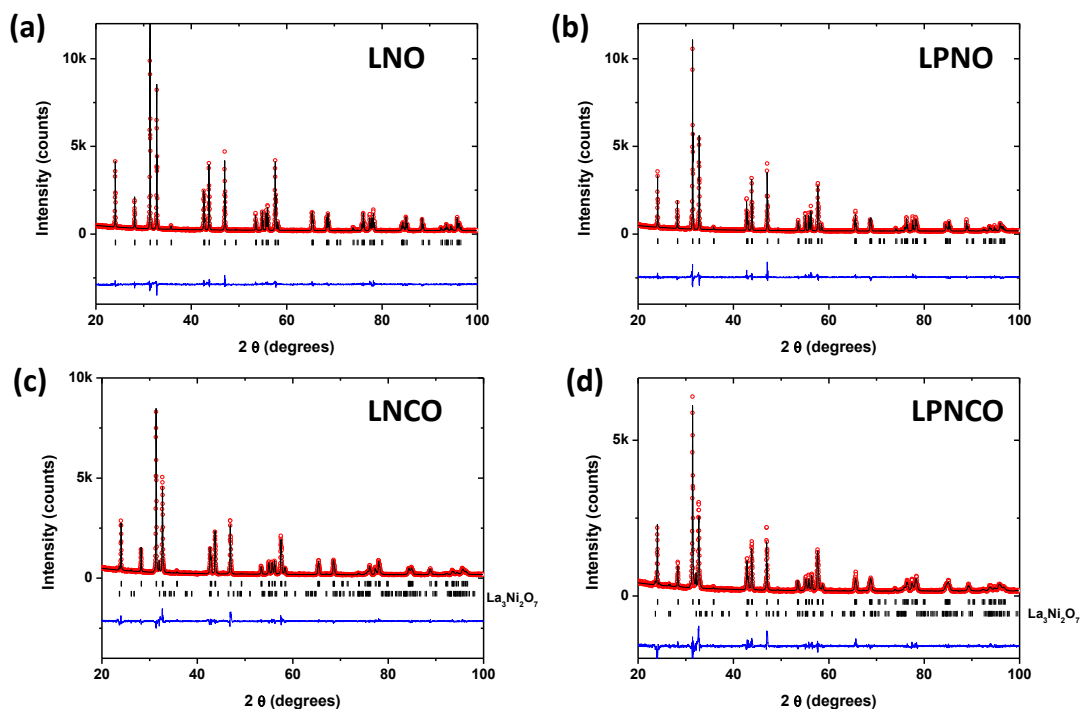


Figure 6.3: Rietveld refinements (lines) of La₂NiO_{4+δ} data (circles), shown above the corresponding difference patterns. Vertical bar indicate the Bragg positions.

The size and nature of the La and Ni site affect the structure and properties of this K₂NiF₄ type compounds. The size of the La-site ions with a 9 coordination state affects predominantly in *c* distances [32]. Partial substitution in La-site by smaller cations should decrease the *c* distance. The results are in agreement with this statement, since the introduction of Pr, with smaller ionic radius than La, produces a contraction of the *c* cell parameter [33] from 12.6842(2) to 12.6274(3) Å. Furthermore, Pr increases the Ni-O bond covalency and the La/Pr-O distance, as can be ascribed from Figure 6.4. On the other hand, a negligible reduction in the *a* and *b* cell parameters are induced when partial substitution with Pr is done. As a result a huge reduction in the cell volume is produced (Table 6.2).

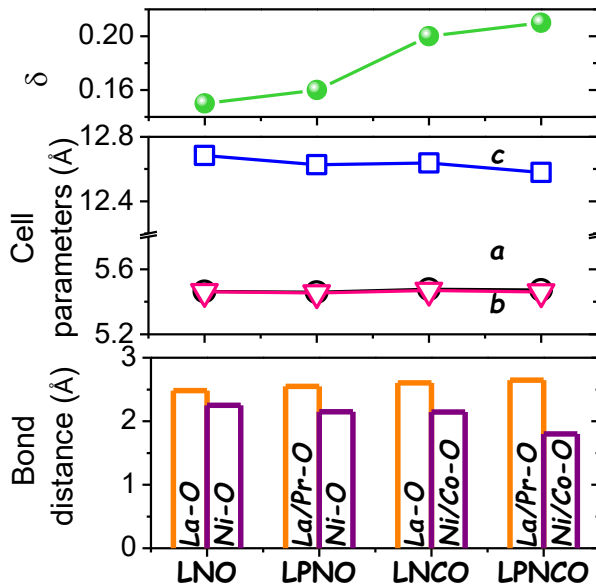


Figure 6.4: From top to bottom: oxygen hyperstoichiometry, cell parameters and bond distance obtained by the Rietveld refinement.

Regarding the Ni position, the partial substitution by Co produces a small change in the cell volume. In literature it has been discussed the variation of the covalency/iconicity nature of the Co-O bonds of this type of materials [34], associated with the transition metal spin state (HS –High Spin or LS- Low Spin) [31]. Co can be found with an oxidation state of +2 or/and +3 at room temperature and this Co^{+3} can adopt an intermediate spin state, producing a bond distance between LS and HS [35]. The ionic radius of Co in this case is close to the Ni radius. The variation of the oxidation state and the spin state makes difficult to calculate the real ionic radius of Co, consequently the possible values of the ionic radius of Co according to the spin state and oxidation state are shown in the Table 6.2. The introduction of Co increases the covalency of the Ni/Co-O bond and also the La-O bond distance as is shown in Figure 6.4, producing a cell change from the parent $\text{La}_2\text{NiO}_{4+\delta}$ material but with similar cell volume. Both effects produces the reduction in the c cell parameter but increases slightly the a and b length, as has been previously reported [36].

Compound	La ₂ NiO _{4+δ} La (+3)- 1.216	La _{1.5} Pr _{0.5} NiO _{4+δ} La(+3)- 1.216 Pr (+3)- 1.179	La ₂ Ni _{0.5} Co _{0.5} O _{4+δ} La (+3)- 1.216	La _{1.5} Pr _{0.5} Ni _{0.8} Co _{0.2} O _{4+δ} La(+3)- 1.216 Pr (+3)- 1.179
A position radii				
B position radii	Ni(+2)- 0.69	Ni(+2)- 0.69	Ni(+2)-0.69 Ni (+3)- 0.56LS/0.6HS Co (+2)- 0.65LS/0.745HS Co (+3)- 0.545LS/0.615HS	Ni(+2)- 0.69 Ni (+3)- 0.56LS/0.6HS Co (+2)- 0.65LS/0.745HS Co (+3)- 0.545LS/0.615HS
a (Å)	5.4636(2)	5.4586(1)	5.4778(3)	5.4732(5)
b (Å)	5.4622(2)	5.4535(1)	5.4690(3)	5.4604(5)
c (Å)	12.6842(2)	12.6274(3)	12.6383(6)	12.5791(10)
α=β=γ (°)	90	90	90	90
V (Å ³)	378.539	375.899	378.621	375.927
δ	0.15	0.16	0.2	0.21
La (8i)	x 0.0 y 0.0 z 0.361(1)	x 0.0 y 0.0 z 0.361(1)	x 0.0 y 0.0 z 0.361(1)	x 0.0 y 0.0 z 0.360(1)
Ni (4a)	x 0.0 y 0.0 z 0.0	x 0.0 y 0.0 z 0.0	x 0.0 y 0.0 z 0.0	x 0.0 y 0.0 z 0.0
O1 (8e)	x 0.25 y 0.25 z 0.0	x 0.25 y 0.25 z 0.0	x 0.25 y 0.25 z 0.0	x 0.25 y 0.25 z 0.0
O2 (16j)	x 0.25 y 0.25 z 0.207(6)	x 0.25 y 0.25 z 0.159(9)	x 0.25 y 0.25 z 0.086(9)	x 0.25 y 0.25 z -0.003(1)
O3 (8i)	x 0.0 y 0.0 z 0.170(16)	x 0.0 y 0.0 z 0.160(30)	x 0.0 y 0.0 z 0.141(7)	x 0.0 y 0.0 z 0.162(9)
O4 (32p)	x -0.00(8) y -0.06(1) z 0.176(5)	x -0.026(20) y -0.06(1) z 0.173(8)	x -0.001(2) y -0.038(16) z 0.179(2)	x 0.002(1) y -0.059(19) z 0.117(5)
La/Pr-O (Å)	2.483 (10)	2.550 (13)	2.605 (12)	2.649 (13)
Ni/Co-O (Å)	2.250 (23)	2.148 (12)	2.145 (10)	1.801 (11)
Rp (%)	5.42	6.99	6.85	8.54
Rwp (%)	7.19	9.24	9.07	11.5
Rexp (%)	5.10	5.73	5.56	6.01
RBragg (%)	5.13	7.08	6.57	7.80
χ ²	1.99	2.6	2.66	3.68

Table 6.2: Refined structural parameters for La_{2-x}A_xNi_{1-y}B_yO_{4+δ}. The data are refined in *F*/*mmm* orthorhombic space group. Numbers in parentheses are the standard deviations of the significant digits.

Finally, the synergetic effect of both Pr and Co is reflected in the reduction of the cell volume in the doubled substituted compound. It should be highlighted the important contraction in the c distance and the Ni/Co-O bond distance. Amow *et al.*, [36] suggested the reduction of the c cell parameter can be related with electronic state of cobalt ions and this change could be induced by the higher bonds covalency of Ni-site and the smaller La-site radius. On the other hand, this contraction in c parameter and Ni/Co-O bond length increases the La/Pr-O bond distance. All these changes produce the cell volume reduction.

Regardless of the cation introduced, the strength of the Ni/Co-O bond is enlarged while the La/Pr-O bond distance is increased, improving presumably the anisotropic diffusion of oxygen and the electrochemical properties as will be discussed below. Furthermore there is a bigger influence of Pr and Co in the c cell parameter, a and b are almost maintained.

Besides of X-ray diffraction measurements, the iodometric titration at room temperature was used to determine the oxygen hyperstoichiometry (δ) for LNO, LPNO, LNCO and LPNCO. $\text{Na}_2\text{S}_2\text{O}_3$ solution was used as reagent for the iodine titration and N_2 was flowed into the solution to avoid the reoxidation of the solution. Each compound can accommodate different quantity of hyperstoichiometric oxygen. LPNO allows incorporating higher content of oxygen ($\delta=0.16$) [17], since Pr has an oxidation state of +4/+3, smaller radii and also higher La/Pr-O distance than the pristine $\text{La}_2\text{NiO}_{4+\delta}$. In addition, it seems that the Ni/Co-O bond energy, the oxidation state of Co and the relatively bigger La-O distance permits to accommodate higher content of oxygen in the rock-salt layer as interstitial arriving until $\delta=0.2$ for LNCO. Finally LPNCO has the highest oxygen hyperstoichiometry being 0.21, the contribution of both cations in the structure can increase the oxygen content at room temperature (Figure 6.4).

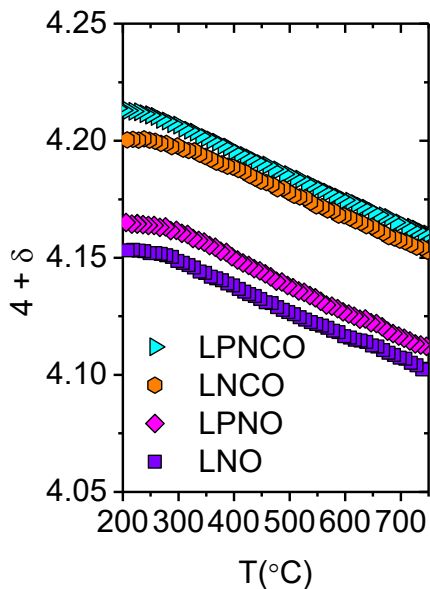


Figure 6.5: Oxygen hyperstoichiometry as function of temperature in air. Results obtained by TGA.

Finally, the variation of the oxygen hyperstoichiometry of LNO, LPNO, LNCO and LPNCO was measured by thermal gravimetric analysis. As can observe in Figure 6.5, the trend obtained at room temperature is maintained for all range of measured temperatures; *i.e.*, LPNCO > LNCO > LPNO > LNO. Furthermore, as the temperature is increased, the oxygen excess is reduced, due to release of oxygens in the compounds.

6.2.1.2. DC total conductivity measurement

Some authors have reported predominant p-type conductivity [37-40] of La₂NiO_{4+δ} based phases, where the electronic conductivity takes place by electron holes in the structure. Furthermore, the total ionic conductivity in oxides with K₂NiF₄ structure consists of two contributions; (a) the interstitial sites in the rock-salt-type layer, due to the sufficient space to accommodate an excess of oxygen at expense of the oxidation of the Ni sites cations, and (b) oxygen vacancies in the perovskite-like layer, both independent. The preferential oxide ion mechanism for these K₂NiF₄-based materials has been widely studied, being higher in the a-b plane (perovskite-like layer or rock-salt-layer) than in the c plane (between the different layers) [18, 39].

The total electrical conductivity of sintered bar-shaped samples at 1430 °C (5h) was determined under air using the four-probe DC technique in the 450-800 °C temperature range. The conductivity of each composition under air as a function of temperature is presented in Figure 6.6.

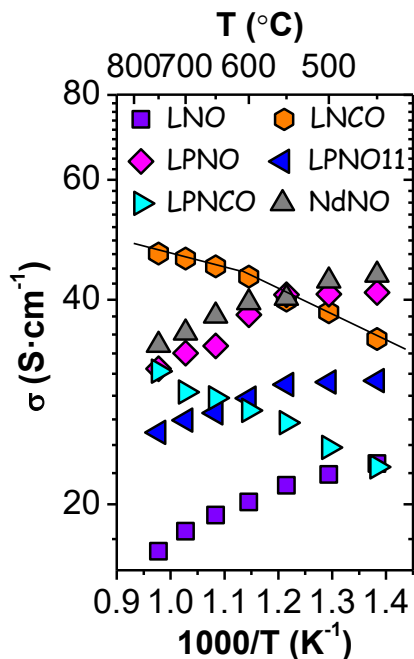


Figure 6.6: Total conductivity results in air for the different $\text{La}_{2-x}\text{A}_x\text{Ni}_{1-y}\text{B}_y\text{O}_{4+\delta}$ synthesized compounds.

Two different behaviors can be ascribed from the Figure 6.6 depending on whether Co is present in the compound structure or not. Firstly, compounds with Co undergo a change in the Ni/Co-O bond reduction upon heating, which can be related with the coordination environment variation. The higher redox activity of Co than Ni induces a change in the Ni/Co-O covalency and in the transport properties [31]. In the present thesis, the cobalt-containing compounds exhibit a continuous increase of conductivity with increasing temperature (Figure 6.6), that should be ascribed to the introduction of Co in Ni position, which increases the a distance, enhancing the oxygen mobility in the ab plane, and changes the Co/Ni-O bond distance (higher covalency), affecting the electronic behavior. As can be inferred from Figure 6.6, there is a change in the activation energy above 600 °C for LNCO and LPNCO. It has been reported [31] a variation in the activation energy for the oxide ion diffusion

mechanism. In addition, at high temperatures the reduction of the Co⁺³ ions prevailing (Ni/Co)⁺² ions will slightly diminish the oxygen hyperstoichiometry (as was determined by TG results (Figure 6.5)) or fraction of oxygen vacancies in the perovskite layer. This change would be related with the aforementioned effect on the loss of oxygen hyperstoichiometry, which involves a change from interstitial to vacancy conduction mechanism [31].

On the other hand, for compounds without Co there is a cation reduction when increasing the temperature, which results in the concomitant release of molecular oxygen, confirming the formation of oxygen vacancies at the expense of p-type electronic carriers [40] (electrons holes). Consequently at high temperatures the total conductivity decreases for these cobalt-free compounds (metal-like behavior), since the effect of the reduction of electron hole concentration prevails over the thermal activation of p-type conduction and the oxygen vacancies generation, as can be ascribed from Figure 6.6 for LNO, NdNO and LPNO.

All synthesized compounds present higher conductivity than the parent La₂NiO_{4+δ}, indicating an improvement of the conductivity by partial substitution in La and Ni site. Changes in the cell parameters (Table 6.2) produce some improvements in the total conductivity values. The introduction of Co in Ni position increases the *a* distance, thus enhancing the oxygen mobility in the *ab* plane and changing the Co/Ni-O bond distance (higher covalency). Both variations in the structure produce higher conductivity for the substituted material in all the temperature range tested compared to the parent non-substituted LNO compound. Nevertheless, the replacement by Pr reduces the cell parameters but increases the conductivity [33]. This can be associated with the improvement of electronic conductivity when shorter Ni-O bond distances are observed, since the electronic conductivity prevails to the oxygen conductivity in the measured temperature range.

As can be ascribed from Figure 6.6 LNCO compounds has the highest conductivity values at the cell operation temperature (900-600 °C), followed by NdNO and LPNO. It seems that the reduction in the cell volume, the change in the cell parameters, as was observed in the section, and some other possible changes (higher oxygen exchange and diffusion coefficient, higher electron holes concentration, etc.) lead to an improvement of the total conductivity of

the material. The total conductivity obtained for these materials makes them suitable as SOFC electrodes.

6.2.1.3. Electrochemical impedance spectroscopy measurements

6.2.1.3.1. Temperature influence on EIS results

In order to study the performance of the different materials as SOFC electrodes, powders of the different materials were milled to obtain a homogenous particle size for the ink preparation. Symmetrical cells were tested by means of EIS. Inks of different compounds were screen printed on both sides of GDC and calcined at 1050 °C (2h). SEM cross-section images of each compound after electrochemical measurements are shown in Figure 6.7. The porosity of the electrodes was adequate for gas diffusion and their thickness was around 22-30 μm .

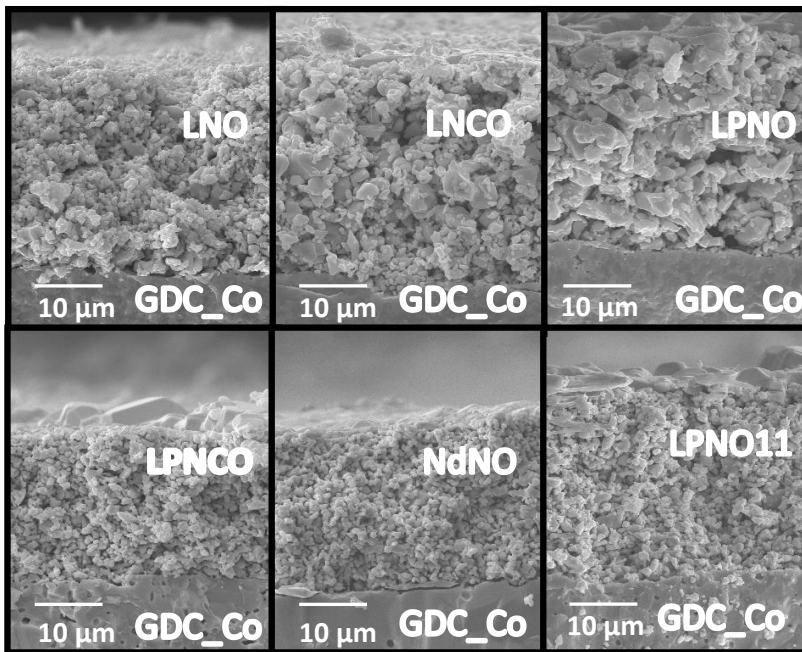


Figure 6.7: SEM micrographs of the different electrodes measured as symmetrical cells.

The enhancement of the electrocatalytic properties with the co-doping is shown in terms of the electrode polarization resistance (R_p) in the Figure 6.8. Full electrochemical impedance results were processed for obtaining the resistance assigned to each electrode (R_p). The contributions assigned to

electrolyte (function of temperature) and contacts related with the real resistance were not taken into account. The electrode resistance values were corrected with the area and divided by two to obtain the polarization resistance (R_p). It has been reported that by increasing the temperature the dissociation of molecular oxygen into atomic ion oxygen is favored [41], as well as the oxygen diffusion and surface oxygen coefficients [18, 30, 42]. Thus, as temperature increases, the overall R_p is decreased. Irrespective of the dopants, the corresponding polarization resistance for each synthesized compound is lower than the parent La₂NiO_{4+δ} resistance at the whole temperature range. This fact confirms that the substitution of La and Ni by Pr and Co significantly enhances the performance of the electrode. Thus, the improvement obtained by the variation of the cell parameters and the influence of the dopants was confirmed. The polarization resistance from the lowest to highest the value was obtained with NdNO, LPNCO, LPNO, LPNO11, LNCO and LNO.

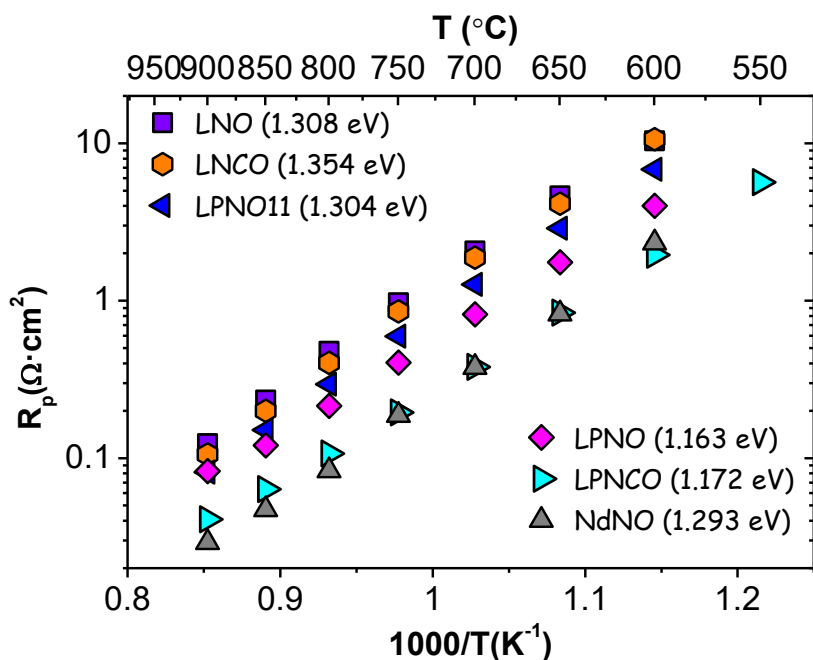


Figure 6.8: Polarization resistance values in an Arrhenius plot of the different MIEC electrodes in a temperature range from 900 °C to 600 °C. The numbers in parentheses are the activation energies (E_a) of each compound.

On the other hand, LNCO which exhibits the highest conductivity (900-600 °C) as shown in Figure 6.6, has the highest polarization resistance when compared with the other co-doped compounds. It can be concluded that there is not a direct relationship between total conductivity and polarization resistance behavior. This behavior can be explained in terms of the different factors that also affect the value of the polarization resistance, such as interface electrode-electrolyte, electrode microstructure or the electrocatalytic activity of the compound for the oxygen reduction reaction (ORR).

In addition, LPNO11 with some impurities in the compound, as was shown in the X-ray diffraction patterns, reduces the R_p in comparison with the parent LNO. Paying attention to the conductivity results (Figure 6.6) there is also an improvement for this compound too. The enhancement of the LPNO11 compound was confirmed despite the small impurities, but any conclusion can be extracted from the results, since the enhancement could come from the small impurities (nanoparticles, catalyst, etc.).

In addition, there is not a big difference in terms of the activation energy for all compounds. The lowest E_a is obtained for the compounds with Pr in the structure (Figure 6.8). The introduction of Pr improves the electrocatalytic activity for oxygen reaction reduction and that fact has been reported for different authors [14, 15, 33, 43]. Indeed, LPNCO electrode shows the best electrochemical results at lower temperatures with similar performance than the well-studied $\text{Nd}_2\text{NiO}_{4+\delta}$ at the highest tested temperatures. The double substituted compound (LPNCO) has both the electrocatalytic improvement of Pr [14, 15, 33, 43] and the reduction of Co(Ni)-o-Co(Ni) bond induced by the Co partial substitution which improves the total conductivity of the compound.

6.2.1.3.2. Co-doped influence on EIS results

The synthesized materials, with the partial substitution in La and Ni positions, improve the performance as SOFC cathodes of the parent LNO. In order to understand this enhancement, EIS spectra recorded at 750 °C were fitted using an equivalent electrical circuit. LPNO11 was not selected in order to focus only on single phases; LNO, LPNO, LNCO and LPNCO. All compounds were fitted by $\text{LR}_\Omega\text{-(RLF1-CPELF1)-(RLF2-CPELF2)}$ circuit, where L is the inductance related to the platinum wires and equipment connections. R_Ω is a real resistance

associated with the electrolyte resistance (dependent on the operation temperature), and CPEs are Constant Phase Elements.

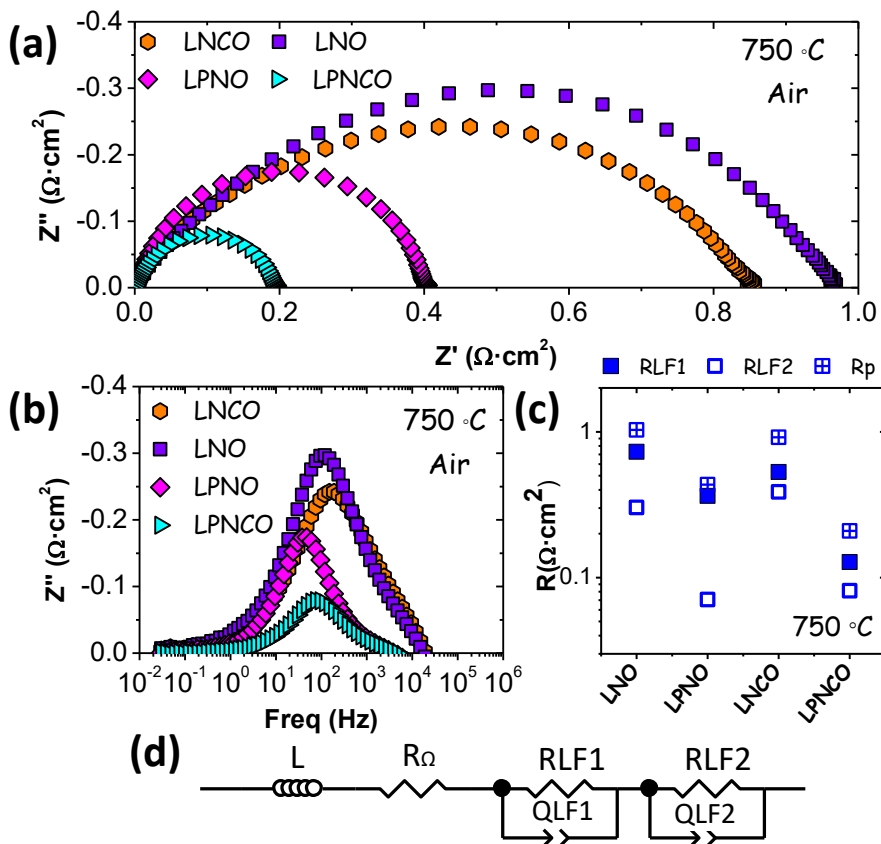


Figure 6.9: (a) Nyquist and (b) Bode plots at 750 °C for the different electrodes in air(c) Results of the equivalent electrical circuit fitting at 750 °C (d). Schematic representation of the equivalent electrical circuit used for the EIS fitting.

Two different contributions can be distinguished in the Nyquist plot for all compounds at 750 °C (Figure 6.9 (a) and (b)), both related to low frequency processes (43-657 Hz). The capacitances associated for LF processes are in the range of $5 \cdot 10^{-3}$ and $2 \cdot 10^{-1}$ F/cm² and are in accordance with the values obtained by Mauvy *et al.*, [41]. According to these capacitances, obtained from the equivalent electrical circuit fitting, and the results reported from some authors [41, 44-46], the arc at the lowest resistance (LF1) could be originated from molecular oxygen dissociation in the electrode surface, whereas LF2

could be related with the charge-transfer reaction occurring on the electrode/gas interface. As can be inferred from the graph (Figure 6.9 (c)), the incorporation of a dopant in La or Ni sites improves the performance of the electrode, obtaining lower polarization resistance values and enhancing LF1 and LF2 processes.

The reduction of RLF1 due to Pr incorporation could be ascribed to the enhancement of the catalytic properties [14, 15] associated with Pr mixed inherent valence (+3/+4) and the reduction in the activation energy of both the oxygen surface exchange coefficient (k_{chem}) and the oxygen diffusion coefficient (D_{chem}) [47]. Consequently, the oxygen dissociation reaction could be improved. Additionally, the partial substitution of La by Pr in the $\text{La}_2\text{NiO}_{4+\delta}$ structure, leads to a higher hyperstoichiometry ($\delta=0.16$) [48]. Furthermore, the mixed valence of Pr (+3/+4) can play an important role in the electronic conductivity promotion [49, 50] at the surface. As a result of both contributions a huge reduction in the RLF2 is obtained.

On the other hand, the introduction of Co in the Ni-site can slightly improve the polarization resistance related with LF1. As a general rule, the addition of Co in the parent La_2NiO_4 structure produces an enhancement in the oxygen surface exchange coefficient (k_{chem}) and the reduction of the activation enthalpy for this process [51-53]. Then, these kinds of materials have higher electrocatalytic activity than non-substituted compounds, and low frequency processes (molecular oxygen dissociation) are improved.

Moreover, the presence of both Co and Pr (LPNCO) in the structure can improve the performance of the symmetrical cell, obtaining the lowest polarization resistance, due to the accumulative properties effect of both dopants.

In addition, a stability test of LPNCO electrode was performed at high temperature (900 °C) by means of EIS measurements (Figure 6.10) recorded with time, obtaining a degradation slope as low as $1 \cdot 10^{-6} \Omega \cdot \text{cm}^2/\text{min}$, and it seems that this value can be related with the Solartron equipment error.

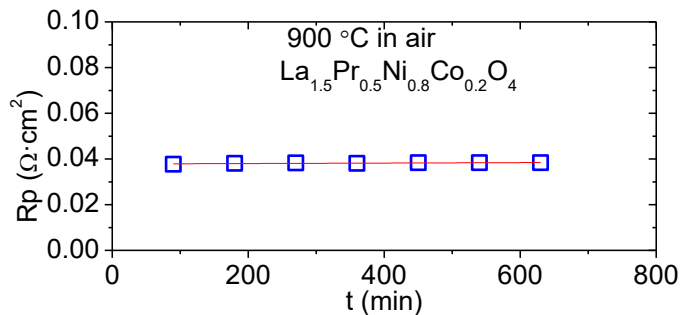


Figure 6.10: LPNCO electrode polarization resistance values as function of time in air at 900 °C.

6.2.1.3.3. LPNCO temperature influence on EIS results

Since LPNCO is the best electrode material synthesized, a deep study will be performed in order to distinguish the different processes that take place in the electrode. Firstly, the operation temperature influence was checked, thus, the EIS spectra as function of temperature were fitted by using an equivalent electrical circuit. Even though it seems that there is only one arc in the electrochemical impedance spectra (*e.g.*, the EIS spectrum of LPNCO at 750 °C, Figure 6.9 (a)), with a more in-depth analysis, two arcs can be distinguished. Both arcs are coupled and appear at the same frequency range (low frequency) making difficult to differentiate them. Then, the electrochemical impedance spectra were fitted by $LR_{\Omega}-(RLF1-CPELF1)-(RLF2-CPELF2)$ or $LR_{\Omega}(RLF1-CPELF1)-(RLF2-CPELF2)-(RHF-CPEHF)$ depending on the operation temperature, since at low temperatures another process takes place and it has been labeled at RHF.

Results obtained from the fitting of the different equivalent electrical circuits are shown in Figure 6.11. The low frequency processes (LF1 and LF2) have an associated capacitance that goes from $1 \cdot 10^{-2}$ to $8 \cdot 10^{-2}$ F·cm⁻², whereas the frequency range falls between $7 \cdot 10^{-2}$ and $5 \cdot 10^2$ Hz. Capacitance remains almost constant for LF1 and LF2, but the frequency has a different trend and decreases by decreasing the temperature. Predictably, lower temperatures make processes slow; consequently lower frequencies should be expected.

On the other hand, an additional resistance with higher frequencies ($1 \cdot 10^5$ - $6 \cdot 10^5$ Hz) and lower capacitances ($1 \cdot 10^{-7}$ - $8 \cdot 10^{-7}$ F·cm⁻²) appears at temperatures below 550 °C. This resistance appears at 550 °C with negligible effect but becomes more important at temperatures below 450 °C. As many authors

have been reported previously [41, 45, 54, 55], the HF contribution can be assigned to the electrolyte material due to the bulk and gran boundary conductivity contribution. The difference between GDC and LPNCO materials, in terms of the ionic conductivity, acquires greater relevance at low temperatures. Since the conductivity of LPNCO is higher than the GDC electrolyte, ions are blocked in the electrode-electrolyte interface.

As can be inferred from the Figure 6.11, the low frequency processes (LF1 and LF2) are overlapped below 600 °C. Usually, LF processes can involve different stages in the ORR as; the molecular oxygen dissociation, oxygen adsorption, chemical diffusion through the bulk and charge transfer on the electrode surface (interface gas-electrode) [41, 45, 56, 57]. The capacitance values of low frequency contributions (CLF1 and CLF2) are non-dependent on the temperature (Figure 6.11). Not changes in the microstructure [58] and/or in the electrocatalytic activity of the electrode for the ORR could be assumed from this behavior. According to the capacitances obtained with the fitting and the results reported from some authors [41, 44-46], the arc with the lowest resistance (LF1) could be originated from molecular oxygen dissociation in the electrode, whereas LF2 could be related with the charge-transfer reaction occurring on the electrode/gas interface.

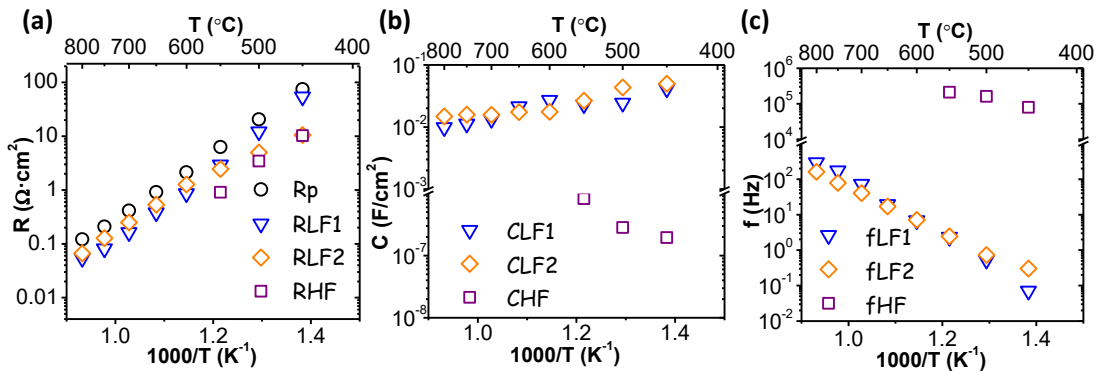


Figure 6.11: (a) Overall polarization resistance (R_p) and the different contributions, (b) capacitances associated and (c) frequencies after equivalent electrical circuit fitting of LPNCO as function of temperature in air.

6.2.1.3.4. LPNCO pO₂ influence on EIS results

As to check the pO₂ influence on the electrode performance, the different contributions at different oxygen partial pressures were studied by fitting the EIS spectra with an equivalent electrical circuit (Figure 6.12). The results obtained from the fitting of the equivalent circuits for two different temperatures (900 and 750 °C) are presented in Figure 6.12. Two arcs can be distinguished in the Nyquist plot (Figure 6.12) for all oxygen partial pressure tested at 900 °C, one related with a process at low frequencies (LF) and another with low-low frequencies (LLF). Thus, the following equivalent electrical circuit was employed; LR_Ω-(RLLF-CPELLF)-(RLF-CPELF). The resistance of the LF and LLF processes increases when the oxygen partial pressure decreases. However at 750 °C was necessary to use two different equivalent electrical circuits. One of them was composed of two resistances in parallel with two CPE whereas the second one was composed of three resistances (LR_Ω(RLLF-CPELLF)-(RLF1-CPELF1)-(RLF2-CPELF2)), two related with LF and another one with LLF.

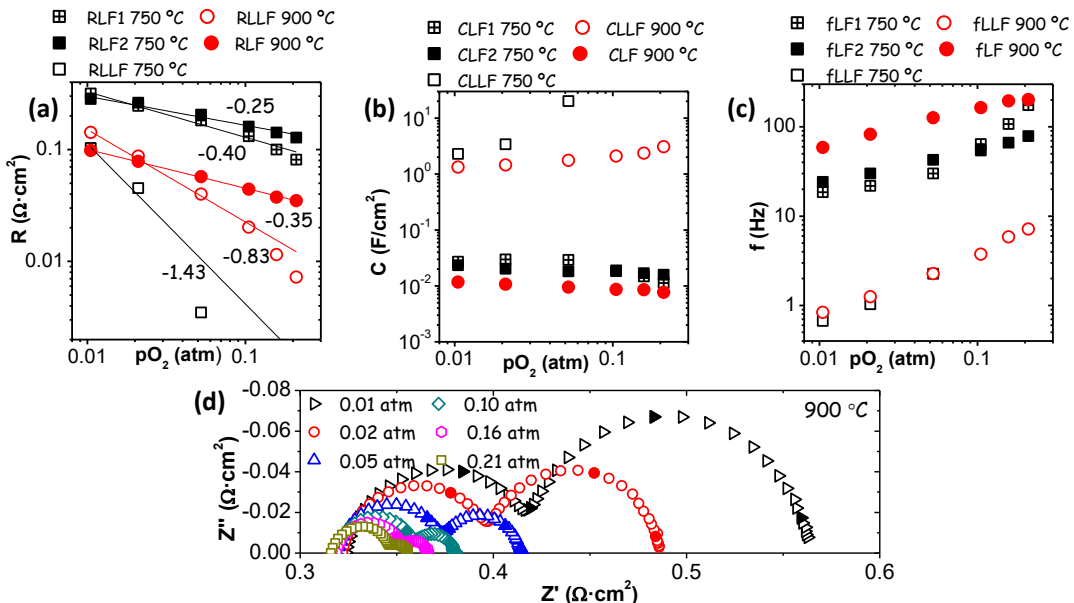


Figure 6.12: Equivalent electrical circuit fittings results: (a) resistance at low frequencies (LF) and medium frequencies (MF), (b) capacitance and (c) frequency at 750 °C and 900 °C at different pO₂. (d) EIS measurements at 900 °C with different pO₂ for LPNCO.

At low oxygen partial pressure (<0.02 atm) the highest contributions are LF1 and LLF for 750 °C and 900 °C, respectively (Figure 6.12). However, at higher oxygen partial pressures the resistance with higher frequencies becomes predominant, being LF2 at 750 °C and LF at 900 °C. In short, the arc at the much lower frequency side becomes dominant at low oxygen partial pressure, whereas at higher oxygen partial pressure the arc with higher frequency is more important (Figure 6.12 (d)). This behavior indicates a change in the rate-limiting process with the oxygen partial pressure. Mauvy *et al.*, [41] studied this phenomenon for $\text{Nd}_{1.95}\text{NiO}_{4+\delta}$, where the limiting process change with the oxygen partial pressure. They could check this trend working until a much lower oxygen partial pressure ($9.5 \cdot 10^{-4}$ atm). As have been explained above, low frequency resistances are usually related with the mechanisms in the oxygen reduction reaction on the electrode surface, as the molecular oxygen dissociation, oxygen adsorption and charge transfer reaction occurring on the electrode/gas interface [41, 56]. RLF, RLF1 and RLF2 resistances have a capacitance [59] around $8 \cdot 10^{-3}$ and $2 \cdot 10^{-2}$ F/cm² for all oxygen partial pressure range and at both temperatures. This capacitance does not vary significantly with the oxygen partial pressure, indicating that the surface properties of the electrode related with this LF range are maintained. Nevertheless, the LLF resistance has a capacitance much higher for both operation temperatures (Figure 6.12 (b)).

It is well known that the oxygen reduction in the cathodes of SOFC happens by different steps: (1) diffusion of O_2 molecules into the electrode, (2) adsorption-desorption of O_2 on the surface of the electrode, (3) dissociation of O_2 molecule into O species, (4) charge transfer from the electrode to O species, (5) incorporation of O^{2-} in the crystal lattice of the electrode, and (6) transport of O^{2-} ions from the electrode to the electrode/electrolyte interface [11].

In order to discern and confirm the nature of the limiting steps in this material and the species involved, the different resistances calculated were fitted with the $p\text{O}_2$ by means of the m parameter [1, 42, 56, 60-64]. As was described in the Improvement of BSCF performance by B site dopants (Chapter 5.2.2.2.2), this value can be correlated with the different species involved in the oxygen reduction reaction. When the molecular oxygen is involved, $m=1$, if the atomic oxygen is limiting the reaction, $m=1/2$ and if the charge transfer is the limiting

step, $m=1/4$. Furthermore, some authors have developed a dependence of $m=3/8$, being the atomic oxygen diffusion and charge transfer the limiting steps ($O_{ad} + e^- \leftrightarrow O^-_{ad}$).

The m values of the dependence between the oxygen partial pressure and the resistances for 900 and 750 °C are presented in the Figure 6.12 (a). The lowest frequency resistances at both temperatures (LLF) can be correlated with the process where the molecular oxygen is involved. Higher frequencies for 900 °C (LF) and 750 °C (LF1) with a m value $\approx 3/8$ can be related with the atomic oxygen diffusion and charge transfer on the electrode surface. Finally the highest frequency (LF2) that appears at 750 °C, with a value of $1/4$, can be correlated with the charge transfer as was listened before (Equation (5.5)). Additionally, the interstitial oxygen mechanism should be kept in mind for these type of compounds, since the charge transfer is also involved ($O'_{ad} + e' + V''_i \leftrightarrow O''_i + 2h$). Furthermore this value of $m = 1/4$ shows an adsorption mechanism that follows the Langmuir's isotherm [65].

It seems that at 750 °C the charge transfer process (LF2) prevails, appearing and being the limiting step in the ORR at high oxygen partial pressure. In addition, the oxygen dissociation mechanism (LLF) seems to be the lowest resistance at both temperatures at high pO_2 . However at 900 °C, LLF resistance becomes predominant at low oxygen partial pressure.

6.2.2. Fully-assembled cell

6.2.2.1. SEM micrographs characterization

Finally, the LPNCO material was tested as cathode in a fully-assembled solid oxide cell. The different layers of the fully-assembled fuel cell can be observed in Figure 6.13. LPNCO electrode is finely deposited on top of the screen-printed porous gadolinium doped ceria layer, no reaction between both materials can be noticed in the image at operation conditions [66]. This GDC interlayer was selected in order to avoid the reactivity with the YSZ electrolyte material. As can be ascribed from Figure 6.13 (a), there is a good attachment between all layers. As it is shown in the electrodes magnification image at the (Figure 6.13 (b)), the grain size of both electrode layers (LPNCO and Ni-YSZ) is very similar giving adequate porosity for gas diffusion. Furthermore, YSZ electrolyte layer,

with a thickness of $\sim 7 \mu\text{m}$, is fully dense, with some close porosity, whereas the GDC interlayer has $\sim 4 \mu\text{m}$ of thickness and is well connected with electrode and electrolyte (Figure 6.13 (a)).

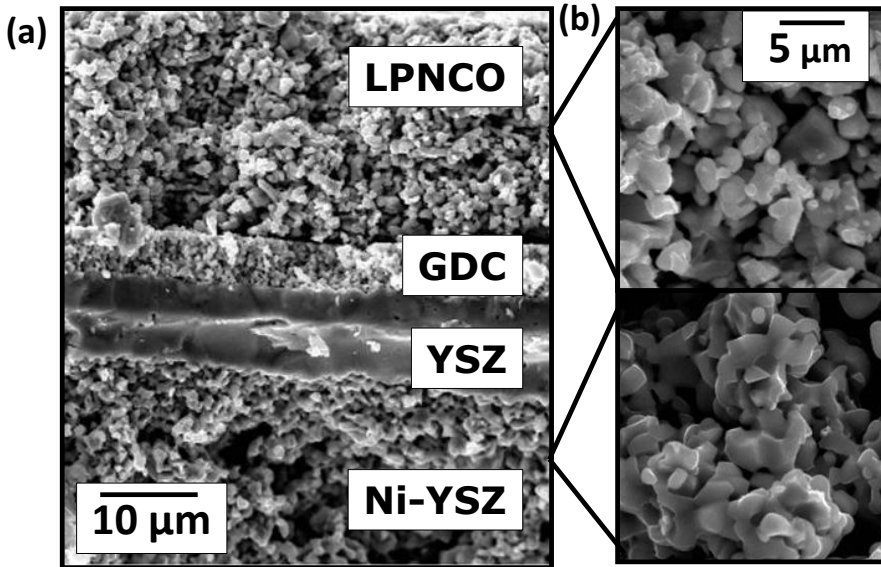


Figure 6.13: SEM micrographs of the fully-assembled fuel cell; Ni-YSZ/YSZ/GDC/LPNCO.

6.2.2.2. Fuel cell mode performance

The LPNCO/GDC/YSZ/Ni-YSZ fully-assembled fuel cell performance at different temperatures and working with humidified hydrogen and dry air in the anode and cathode, respectively, is shown in Figure 6.14. Maximum power densities achieved with these operating conditions are 385, 258 and 126 $\text{mW}\cdot\text{cm}^{-2}$ at 700, 650 and 600 °C, respectively. A high OCV value is maintained at all tested temperatures, indicating the goodness of the sample sealing. *i*-*V* curves for all range of temperatures measured shows predominantly the regime associated with the resistance of electrodes and electrocatalyst. However, the concentration polarization at the highest current densities can be inferred for the highest temperature.

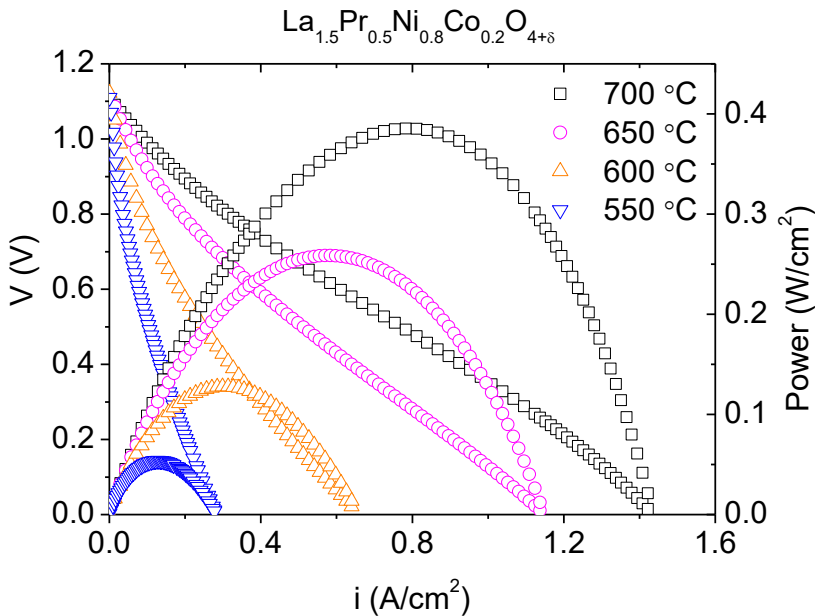


Figure 6.14: i - V and i - P curves for the fully assembled fuel cell at different temperatures, working with air in the cathode and wet hydrogen in the anode.

These results confirm that LPNCO electrode seems a suitable cathode for IT-SOFC applications. An *et al.*, [67] obtained power densities of $76 \text{ mW}\cdot\text{cm}^{-2}$ at $600 \text{ }^\circ\text{C}$ using a pure electronic conductor cathode (LSM) on Ni-YSZ/YSZ tape casted anodes, without any active layer. Nevertheless, Tsai *et al.*, [68] studied a composite cathode (LSM/YSZ) on a YSZ/Ni-YSZ anode cell with a $(\text{CeO}_2)_{0.84}(\text{Y}_2\text{O}_3)_{0.16}$ as interfacial layer, with a cell performance of $\sim 250 \text{ mW}\cdot\text{cm}^{-2}$ at 0.7 V and $700 \text{ }^\circ\text{C}$. However, the LPNCO-based SOFC, tested in the present thesis, shows a power density of $308 \text{ mW}\cdot\text{cm}^{-2}$ at the same voltage. On the other hand, a Ni-YSZ/YSZ/GDC anode supported fuel cell was measured by Serra *et al.*, [69], using a $\text{La}_{0.58}\text{Sr}_{0.4}\text{Fe}_{0.8}\text{Co}_{0.2}\text{O}_{3-\delta}$ (LSFC) cathode instead. They obtained a power density of $293 \text{ mW}\cdot\text{cm}^{-2}$ at 0.7 V , showing a similar performance than the LPNCO-based cell tested in this work. However, authors were aware that further improvement had to be done in the SOFC cathode microstructure in order to improve the overall cell performance.

6.2.2.3. Electrolysis mode

The same fully-assembled cell (LPNCO/GDC/YSZ/Ni-YSZ) was tested as steam electrolysis cell. The hydrogen flows produced in the steam electrolysis at 700 °C are shown in Figure 6.15 (b). The produced hydrogen flow was stable during the time that a constant current was applied to the cell. The theoretical value of hydrogen production was calculated according to the Faraday's equation and is plotted in Figure 6.15 (a). As can be ascribed from the Figure 6.15 (b) hydrogen is generated even at very low current densities, following the trend of the calculated by Faraday's. When the current density increases the efficiency of the steam electrolysis is reduced, increasing the gap between calculated and measured values (Figure 6.15 (b)). This reduction in the hydrogen production agrees with the change in the cell voltage trend. Current densities above of 80 mA·cm⁻² produce a huge cell voltage rise and as a result the cell voltage surpasses the thermoneutral voltage (V_{tn}) (1.28 V in these cell conditions) [70].

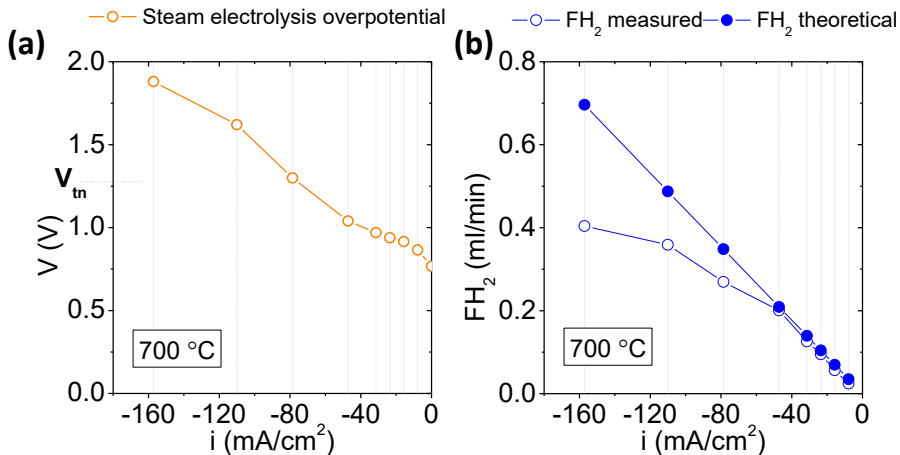


Figure 6.15: (a) i - V curves and (b) measured and theoretical hydrogen production in steam electrolysis mode.

As can be discerned from Figure 6.15 (a), when the cell overtakes the thermoneutral potential, the hydrogen production efficiency is reduced and the cell potential drastically increases. The first explanation might be attributed to the fact that the electrolysis is an endothermic process, and when the cell operates above thermoneutral voltage (exothermic mode) the

temperature increases and the electrical efficiency obtained is below 100 % [71-73]. The presence of electronic conductivity in YSZ in the electrolysis mode [74] could be another reason for the lower cell efficiency. Mogensen *et al.*, [75] calculated the electronic leak current densities as function of some parameters as voltage, temperature and electrolyte thickness. They found that higher electronic leakages are produced at higher temperatures, or/and higher voltages and/or thinner YSZ electrolytes. Taking into account the thickness of the electrolyte in the present work ($\approx 7 \mu\text{m}$) and the high voltages obtained above 80 mA/cm^2 , it seems appropriate to assign the low faradic efficiency (difference between the hydrogen obtained and the hydrogen calculated by the Faraday's law) to this electronic leakage and heating of the sample (since V_{tn} was overtaken).

6.2.2.4. Co-electrolysis mode

For the co-electrolysis test $180 \text{ mL}\cdot\text{min}^{-1}$ of Ar and $20 \text{ mL}\cdot\text{min}^{-1}$ of CO_2 were introduced in the Ni-YSZ cathode side. Different constant current densities were applied for 20 minutes.

The CO and H_2 flows obtained by co-electrolysis of CO_2 and water are presented in Figure 6.16 (b). As can be ascribed from the Figure 6.16 (b), the CO flow produced is higher than the hydrogen, under these experimental fed conditions. In contrast to water steam electrolysis, three reactions are involved in the $\text{H}_2\text{O}/\text{CO}_2$ co-electrolysis mode:



Due to the higher amount of CO_2 fed in the cathode chamber, it seems that the equilibrium of the WGSR reaction is shifted to the CO formation. As was described in the above section the water electrolysis takes place with high efficiency at low current densities, but in the co-electrolysis mode, part of the hydrogen produced is quickly recombined with CO_2 (Equation (6.3) producing additional CO to the amount obtained by electroreduction.

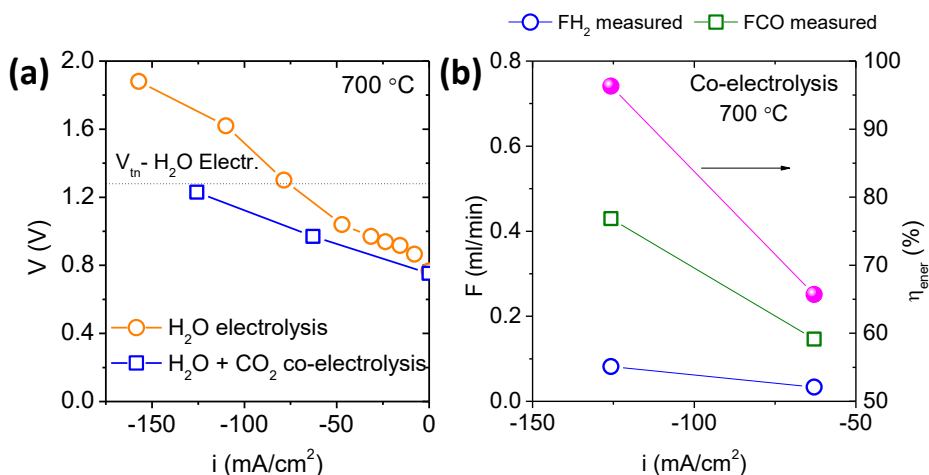


Figure 6.16: a) i - V curves for steam electrolysis and co-electrolysis and (b) measured hydrogen and carbon monoxide production in co-electrolysis mode.

The i - V curves for the LPNCO/GDC/YSZ/Ni-YSZ cell under electrolysis and co-electrolysis modes are shown in Figure 6.16 (a). Since the hydrogen generation is related with the current density by the Faraday's law [76, 77]. Lower voltages at high current densities will allow the production of higher amounts of hydrogen (and/or CO), increasing the efficiency. With this premise, the co-electrolysis mode exhibits better performance than steam electrolysis mode. For instance, at $\sim 120\text{ mA}\cdot\text{cm}^{-2}$ there is a difference of 0.4 V between single water and H₂O/CO₂ co-electrolysis (Figure 6.16 (a)). The optimal operation potential for water steam electrolysis and co-electrolysis should be close but below the thermoneutral potential, where cells operate without losing or requiring energy (adiabatically) [78-80]. When the cell is operated above the V_{tn} , the efficiency of the cell for the conversion of electricity into chemical energy decreases [81]. The thermoneutral potential of the water electrolysis at $700\text{ }^\circ\text{C}$ is 1.28 V whereas for "single" CO₂ electrolysis is 1.47 V [82]. Under co-electrolysis mode V_{tn} value should be appear in between both values.

In addition, the co-electrolysis mode efficiency was calculated with Equation (4.15), (4.16) and (4.17) and is presented in Figure 6.16 (b). At high current densities ($126\text{ mA}/\text{cm}^2$), the total efficiency of the process is around 96 %, all current applied produces hydrogen or carbon monoxide. However, at low current densities the efficiency decreases, indicating that the equilibrium of

the reactions does not turn to the H₂ and CO production, obtaining high CO₂ or H₂O content in the outlet stream.

6.2.2.5. Thermodynamic simulation of co-electrolysis

In order to corroborate the results obtained of the CO and H₂ produced under co-electrolysis mode, a thermodynamic simulation was done. The three reactions described above (Equation (6.1), (6.2) and (6.3)) were taken into account for the simulation. For this purpose ASPEN PLUS v8.0 software was employed. The operation conditions for the co-electrolysis mode were the same as used experimentally: temperature of 700 °C, system pressure of 1 atm, 20 mL·min⁻¹ of CO₂ and 2.5% vol. of H₂O. The final composition of the thermodynamic equilibrium was obtained by using a Gibbs reactor. The effect of current density applied on the equilibrium for the co-electrolysis mode at the operation condition is shown in the Figure 6.17, as the gas flow rate versus the current density.

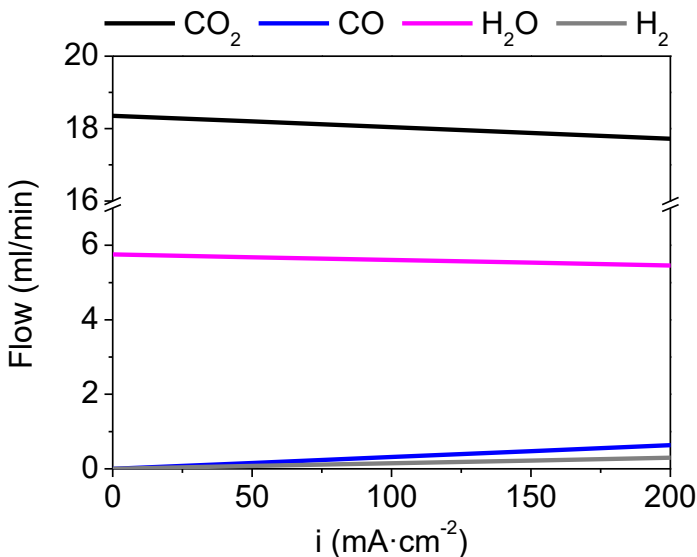


Figure 6.17: Thermodynamic results for the co-electrolysis simulation at 700 °C.

Higher current densities produces bigger difference between H₂ and CO flow rates, as can be inferred from the Figure 6.17. Indeed, the trend obtained by the experimental data (Figure 6.17) is maintained for the equilibrium results, where the CO production is higher than the H₂ and the difference increases

with the current density applied. Thus, it is demonstrated the effect of the WGS reaction mentioned above, where the introduction of CO_2 shift the equilibrium to the CO production at 700 °C.

6.3. Conclusions

This chapter summarizes the study of $\text{La}_{2-x}\text{A}_x\text{Ni}_{1-y}\text{B}_y\text{O}_{4+\delta}$ cathodes for IT-SOFC. The substitution of Pr in the La site and Co in Ni site induces the reduction of the length of c cell parameter, even though the orthorhombic $Fmmm$ structure is maintained. Additionally, Ni/Co-O bond distance is reduced and the electronic conductivity is improved whereas the enlargement of La/Pr-O bond and the higher hyperstoichiometry lead to a higher ionic conductivity, compared to the non-substituted parent material. On the other hand, all studied materials showed a p-type conductivity and the total conductivity behavior depended on the dopant. For instance, the Co substitution in the materials gives a non-metallic-like behavior (in the measured temperature range) whereas the cobalt-free compounds maintain the metal-like behavior of the parent $\text{La}_2\text{NiO}_{4+\delta}$.

These structural changes and the electrocatalytic properties of the selected dopants cations, play an important role in the improvement of the low frequency processes for the oxygen reduction reaction. This fact makes that these materials improve the fuel cell performance by reducing R_p for all compounds. The best cathode performance was obtained for $\text{La}_{1.5}\text{Pr}_{0.5}\text{Ni}_{0.8}\text{Co}_{0.2}\text{O}_{4+\delta}$ compound at tested temperatures, with similar recorded values than the well-studied $\text{Nd}_2\text{NiO}_{4+\delta}$ SOFC cathode.

On the other hand, temperature influence and oxygen partial pressure was studied by means of EIS and fitting with an equivalent electrical circuit. $\text{La}_{1.5}\text{Pr}_{0.5}\text{Ni}_{0.8}\text{Co}_{0.2}\text{O}_{4+\delta}$ changed the limiting mechanism when the oxygen partial pressure ($p\text{O}_2$) was decreased below 0.02 atm. Finally, the resistances at the different frequencies were fitted as function of $p\text{O}_2$. The relation between the resistance and $p\text{O}_2$ showed that the limiting steps, in the $\text{La}_{1.5}\text{Pr}_{0.5}\text{Ni}_{0.8}\text{Co}_{0.2}\text{O}_{4+\delta}$ electrode, were the molecular oxygen dissociation and charge transfer in the electrode surface.

The fuel cell performance with this La_{1.5}Pr_{0.5}Ni_{0.8}Co_{0.2}O_{4+δ} material as a cathode was similar to other state-of-the-art MIEC cathodes, obtaining values of 385 W·cm⁻² at 700°C for the Ni-YSZ/YSZ/GDC fully-assembled fuel cell.

Moreover, La_{1.5}Pr_{0.5}Ni_{0.8}Co_{0.2}O_{4+δ} tested as anode for electrolysis seems to be active for the oxygen oxidation during the electrolysis and co-electrolysis mode. Better performance in the co-electrolysis mode was obtained with lower cell voltages than the steam electrolysis. The produced ratio of H₂ and CO measured in the co-electrolysis mode test was demonstrated by a theoretical thermodynamic equilibrium simulation. Under co-electrolysis mode the CO amount produced was higher than the H₂ production, due to the WGS reaction involved.

6.4. References

- [1] B. Guan, W. Li, H. Zhang, X. Liu, *J. Electrochem. Soc.*, 162 (2015) F707-F712.
- [2] K. Zhao, Q. Xu, D.-P. Huang, M. Chen, B.-H. Kim, *Ionics*, 18 (2012) 75-83.
- [3] G. Amow, I.J. Davidson, S.J. Skinner, *Solid State Ion.*, 177 (2006) 1205-1210.
- [4] B.X. Huang, J. Malzbender, R.W. Steinbrech, *J. Mater. Sci.*, 46 (2011) 4937-4941.
- [5] M.A. Laguna-Bercero, N. Kinadjan, R. Sayers, H. El Shinawi, C. Greaves, S.J. Skinner, *Fuel Cells*, 11 (2011) 102-107.
- [6] A. Mehta, P.J. Heaney, *Phys. Rev. B*, 49 (1994) 563-571.
- [7] E.N. Naumovich, V.V. Kharton, *Theochem-J. Mol. Struct.*, 946 (2010) 57-64.
- [8] V.V. Kharton, A.P. Viskup, A.V. Kovalevsky, E.N. Naumovich, F.M.B. Marques, *Solid State Ion.*, 143 (2001) 337-353.
- [9] G. Amow, S.J. Skinner, *J. Solid State Electrochem.*, 10 (2006) 538-546.
- [10] J.M. Bassat, Boehm, E., Grenier, J. C., Mauvy, F., Dordor, P. and Pouchard, M., in: J. Huijsmans (Ed.) 5th European Solid Oxide Fuel Cell Forum, 2002, pp. 586–593.
- [11] F.S. Baumann, Stuttgart University, Stuttgart, 2006.
- [12] A. Chronos, B. Yildiz, A. Tarancon, D. Parfitt, J.A. Kilner, *Energy & Environmental Science*, 4 (2011) 2774-2789.
- [13] J. Rodriguezcarvajal, M.T. Fernandezdiaz, J.L. Martinez, *J. Phys.-Condes. Matter*, 3 (1991) 3215-3234.
- [14] J.M. Serra, V.B. Vert, *ChemSusChem*, 2 (2009) 957-961.
- [15] J.M. Serra, V.B. Vert, M. Betz, V.A.C. Haanappel, W.A. Meulenberg, F. Tietz, *J. Electrochem. Soc.*, 155 (2008) B207-B214.

- [16] A.F. Vaibhav Vibhu, Clément Nicollet, Sébastien Fourcade, Aline Rougier, Jean-Marc Bassat and Jean-Claude Grenier, 11th European SOFC & SOE forum, Lucern (Switzerland), 2014.
- [17] V. Vibhu, J.M. Bassat, A. Flura, C. Nicollet, J.C. Grenier, A. Rougier, ECS Transactions, 2015, pp. 825-835.
- [18] C.N. Munnings, S.J. Skinner, G. Amow, P.S. Whitfield, I.J. Davidson, Solid State Ion., 176 (2005) 1895-1901.
- [19] Y. Wang, H. Nie, S. Wang, T.-L. Wen, U. Guth, V. Valshook, Materials Letters, 60 (2006) 1174-1178.
- [20] H. Ullmann, N. Trofimenko, F. Tietz, D. Stöver, A. Ahmad-Khanlou, Solid State Ion., 138 (2000) 79-90.
- [21] A. Aguadero, L. Fawcett, S. Taub, R. Woolley, K.-T. Wu, N. Xu, J.A. Kilner, S.J. Skinner, J. Mater. Sci., 47 (2012) 3925-3948.
- [22] V.I. Voronin, I.F. Berger, V.A. Cherepanov, L.Y. Gavrilova, A.N. Petrov, A.I. Ancharov, B.P. Tolochko, S.G. Nikitenko, Nucl. Instrum. Methods Phys. Res. Sect. A-Accel. Spectrom. Dect. Assoc. Equip., 470 (2001) 202-209.
- [23] S. Takahashi, S. Nishimoto, M. Matsuda, M. Miyake, J. Am. Ceram. Soc., 93 (2010) 2329-2333.
- [24] A. Flura, S. Dru, C. Nicollet, V. Vibhu, S. Fourcade, E. Lebraud, A. Rougier, J.M. Bassat, J.C. Grenier, J. Solid State Chem., 228 (2015) 189-198.
- [25] C. Solís, L. Navarrete, J.M. Serra, J. Power Sources, 240 (2013) 691-697.
- [26] H. Rietveld, Journal of Applied Crystallography, 2 (1969) 65-71.
- [27] S.J. Skinner, Solid State Sciences, 5 (2003) 419-426.
- [28] A. Rabenau, P. Eckerlin, Acta Crystallographica, 11 (1958) 304-306.
- [29] J.D. Jorgensen, B. Dabrowski, S. Pei, D.R. Richards, D.G. Hinks, Phys. Rev. B, 40 (1989) 2187-2199.
- [30] V. Vibhu, A. Rougier, C. Nicollet, A. Flura, J.-C. Grenier, J.-M. Bassat, Solid State Ion., 278 (2015) 32-37.
- [31] S.J. Skinner, G. Amow, J. Solid State Chem., 180 (2007) 1977-1983.
- [32] I.B. Sharma, D. Singh, Bull. Mat. Sci., 21 (1998) 363-374.
- [33] S. Nishimoto, S. Takahashi, Y. Kameshima, M. Matsuda, M. Miyake, J. Ceram. Soc. Jpn., 119 (2011) 246-250.
- [34] H. Takahashi, F. Munakata, M. Yamanaka, Phys. Rev. B, 53 (1996) 3731-3740.
- [35] K. Asai, A. Yoneda, O. Yokokura, J.M. Tranquada, G. Shirane, K. Kohn, Journal of the Physical Society of Japan, 67 (1998) 290-296.
- [36] G. Amow, P.S. Whitfield, I.J. Davidson, R.P. Hammond, C.N. Munnings, S.J. Skinner, Ceramics International, 30 (2004) 1635-1639.

- [37] A.V. Kovalevsky, V.V. Kharton, A.A. Yaremchenko, Y.V. Pivak, E.V. Tsipis, S.O. Yakovlev, A.A. Markov, E.N. Naumovich, J.R. Frade, *J. Electroceram.*, 18 (2007) 205-218.
- [38] V.V. Vashook, Yushkevich, II, L.V. Kokhanovsky, L.V. Makhnach, S.P. Tolochko, I.F. Kononyuk, H. Ullmann, H. Altenburg, *Solid State Ion.*, 119 (1999) 23-30.
- [39] V.V. Kharton, A.A. Yaremchenko, A.L. Shaula, M.V. Patrakeev, E.N. Naumovich, D.I. Loginovich, J.R. Frade, F.M.B. Marques, *J. Solid State Chem.*, 177 (2004) 26-37.
- [40] M. Greenblatt, *Current Opinion in Solid State and Materials Science*, 2 (1997) 174-183.
- [41] F. Mauvy, C. Lalanne, J.M. Bassat, J.C. Grenier, H. Zhao, L.H. Huo, P. Stevens, *J. Electrochem. Soc.*, 153 (2006) A1547-A1553.
- [42] H. Zhao, F. Mauvy, C. Lalanne, J.M. Bassat, S. Fourcade, J.C. Grenier, *Solid State Ion.*, 179 (2008) 2000-2005.
- [43] H. Zhao, Q. Li, L.P. Sun, *Sci. China-Chem.*, 54 (2011) 898-910.
- [44] V. Dusastre, J.A. Kilner, *Solid State Ion.*, 126 (1999) 163-174.
- [45] S.B. Adler, *Chem. Rev.*, 104 (2004) 4791-4843.
- [46] J.C. Ruiz-Morales, D. Marrero-López, J.T.S. Irvine, P. Núñez, *Materials Research Bulletin*, 39 (2004) 1299-1318.
- [47] J.-M. Bassat, M. Burriel, M. Ceretti, P. Veber, J.-C. Grenier, W. Paulus, J.A. Kilner, *ECS Transactions*, 57 (2013) 1753-1760.
- [48] C. Allancon, P. Odier, J.M. Bassat, J.P. Loup, *J. Solid State Chem.*, 131 (1997) 167-172.
- [49] M. Balaguer, C. Solis, J.M. Serra, *J. Phys. Chem. C*, 116 (2012) 7975-7982.
- [50] M. Balaguer, C. Solis, J.M. Serra, *Chem. Mat.*, 23 (2011) 2333-2343.
- [51] J.A. Kilner, C.K.M. Shaw, *Solid State Ion.*, 154 (2002) 523-527.
- [52] C.N. Munnings, S.J. Skinner, G. Amow, P.S. Whitfield, I.J. Davidson, *Solid State Ion.*, 176 (2005) 1895-1901.
- [53] E. Boehm, J.M. Bassat, P. Dordor, F. Mauvy, J.C. Grenier, P. Stevens, *Solid State Ion.*, 176 (2005) 2717-2725.
- [54] H. Inaba, H. Tagawa, *Solid State Ion.*, 83 (1996) 1-16.
- [55] D.Y. Wang, A.S. Nowick, *J. Solid State Chem.*, 35 (1980) 325-333.
- [56] M.J. Escudero, A. Aguadero, J.A. Alonso, L. Daza, *J. Electroanal. Chem.*, 611 (2007) 107-116.
- [57] G.T. Kim, S. Wang, A.J. Jacobson, Z. Yuan, C. Chen, *J. Mater. Chem.*, 17 (2007) 1316-1320.
- [58] J. Dailly, S. Fourcade, A. Largeteau, F. Mauvy, J.C. Grenier, M. Marrony, *Electrochim. Acta*, 55 (2010) 5847-5853.

- [59] R. Sayers, M. Rieu, P. Lenormand, F. Ansart, J.A. Kilner, S.J. Skinner, *Solid State Ion.*, 192 (2011) 531-534.
- [60] R.R. Peng, T.Z. Wu, W. Liu, X.Q. Liu, G.Y. Meng, *J. Mater. Chem.*, 20 (2010) 6218-6225.
- [61] Y. Takeda, R. Kanno, M. Noda, Y. Tomida, O. Yamamoto, *J. Electrochem. Soc.*, 134 (1987) 2656-2661.
- [62] N. Grunbaum, L. Dessemond, J. Fouletier, F. Prado, L. Mogni, A. Caneiro, *Solid State Ion.*, 180 (2009) 1448-1452.
- [63] J.D. Kim, G.D. Kim, J.W. Moon, Y.I. Park, W.H. Lee, K. Kobayashi, M. Nagai, C.E. Kim, *Solid State Ion.*, 143 (2001) 379-389.
- [64] F.H. van Heuveln, H.J.M. Bouwmeester, *J. Electrochem. Soc.*, 144 (1997) 134-140.
- [65] D.Y. Wang, A.S. Nowick, *J. Electrochem. Soc.*, 126 (1979) 1155-1165.
- [66] A. Montenegro-Hernandez, J. Vega-Castillo, L. Mogni, A. Caneiro, *Int. J. Hydrog. Energy*, 36 (2011) 15704-15714.
- [67] C.M. An, J.H. Song, I. Kang, N. Sammes, *J. Power Sources*, 195 (2010) 821-824.
- [68] T. Tsai, S.A. Barnett, *Solid State Ion.*, 93 (1997) 207-217.
- [69] J.M. Serra, S. Uhlenbruck, W.A. Meulenber, H.P. Buchkremer, D. Stover, *Top. Catal.*, 40 (2006) 123-131.
- [70] Q. Li, Y. Zheng, W. Guan, L. Jin, C. Xu, W.G. Wang, *Int. J. Hydrog. Energy*.
- [71] S.D. Ebbesen, X. Sun, M.B. Mogensen, *Faraday Discuss.*, 182 (2015) 393-422.
- [72] M.N. Manage, E. Sorensen, S. Simons, D.J.L. Brett, *Chemical Engineering Research and Design*, 92 (2014) 1988-2005.
- [73] M.A. Laguna-Bercero, *J. Power Sources*, 203 (2012) 4-16.
- [74] M.A. Laguna-Bercero, R. Campana, A. Larrea, J.A. Kilner, V.M. Orera, *J. Electrochem. Soc.*, 157 (2010) B852-B855.
- [75] M. Mogensen, T. Jacobsen, *ECS Transactions*, 25 (2009) 1315-1320.
- [76] C.H. Yang, A. Coffin, F.L. Chen, *Int. J. Hydrog. Energy*, 35 (2010) 3221-3226.
- [77] R.M. Xing, Y.R. Wang, S.H. Liu, C. Jin, *J. Power Sources*, 208 (2012) 276-281.
- [78] P. Kazempoor, R.J. Braun, *Int. J. Hydrog. Energy*, 39 (2014) 5955-5971.
- [79] A. Brisse, J. Schefold, M. Zahid, *Int. J. Hydrog. Energy*, 33 (2008) 5375-5382.
- [80] X.F. Sun, M. Chen, S.H. Jensen, S.D. Ebbesen, C. Graves, M. Mogensen, *Int. J. Hydrog. Energy*, 37 (2012) 17101-17110.
- [81] S. Sunde, *Electrochim. Acta*, 42 (1997) 2637-2648.
- [82] S.H. Jensen, P.H. Larsen, M. Mogensen, *Int. J. Hydrog. Energy*, 32 (2007) 3253-3257.

7

**LSM electrode
improvement
strategies**

7. LSM electrode improvement strategies

7.1. Introduction

The reduction of the operation temperature of conventional SOFCs is very challenging but will be very beneficial to avoid the use of expensive building materials and to enlarge the stack lifetime. LSM ($\text{La}_{0.8}\text{Sr}_{0.2}\text{MnO}_{3-\delta}$) is still the material of choice for cathodes due to its stability, electronic conductivity and compatibility with different materials such as yttria stabilized zirconia (YSZ), doped ceria or perovskites. However, the optimal operation of this cathode is reached at high temperatures (above 800 °C) [1]. In order to reduce the operation temperature it is necessary to enlarge the three phase boundary (TPB) length, since LSM is an electronic conductor and the TPB is limited to the electrode-electrolyte region exposed to the gas [2]. In this way, a second phase can be used and mixed with LSM to enlarge the TPB length. For this purpose, YSZ is industrially preferred at high temperature since is compatible and one of the state-art materials. However, GDC ($\text{Ce}_{0.8}\text{Gd}_{0.2}\text{O}_{2-\delta}$) is a superior ionic conductor at intermediate temperatures (< 700 °C). Furthermore, GDC is compatible with LSM and mixed with LSM can promote the presence of percolative pathways for both electrons and ions [3-5]. This strategy will increase the TPB to the whole electrode thickness and improve the cathode performance at lower temperatures.

However, the performance of these composite cathodes is limited by surface related processes, such as oxygen dissociation and adsorption $\text{O}_{2(\text{g})} \rightarrow 2\text{O}_{\text{ad}}$ and $\text{O}_{\text{ad}} + \text{e}^- \rightarrow \text{O}_{\text{ad}}^-$ [3, 6, 7]. Thus, the use of a suitable catalyst is decisive for an efficient SOFC cathode development. In this chapter, Pr, Sm, Ce, Zr, Ba and Co oxides are brought onto the cathode and act as oxygen reduction catalysts due to their redox character and particular adsorption properties. In order to preserve the nanoscale of catalyst and good dispersion [8], the infiltration was performed on sintered and well-consolidated LSM-GDC electrodes, instead of incorporating it in the LSM-GDC cathode inks prior to electrode firing [9, 10].

7.2. Results and discussion

In order to improve the cell performance of the LSM state-of-the-art material, different strategies were followed (Figure 7.1). First, a composite electrode

was manufactured by mixing an electronic phase (LSM) and ionic phase (GDC). After that, different oxides were infiltrated in the LSM-GDC electrodes.

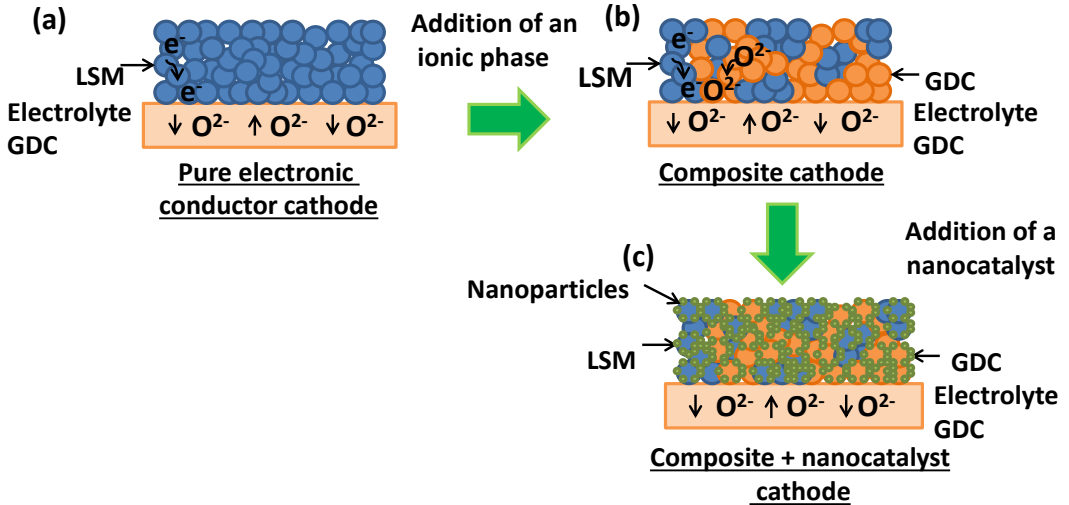


Figure 7.1: Improvement strategy for electrodes; (a) electronic conductor electrode, (b) composite electrode and (c) composite electrode and catalyst nanoparticles.

7.2.1. Symmetrical cells characterization

7.2.1.1. Phases compatibility

Firstly, in order to check the compatibility between LSM and GDC phases after electrode sinterization, powders of both phases were mixed by the agate mortar and calcined at 1150 °C during 2 hours. The Figure 7.2 shows the XRD pattern of the composite powder after calcination. As can be ascribed from the graph, both phases are compatible and no extra peaks from secondary phases are observed.

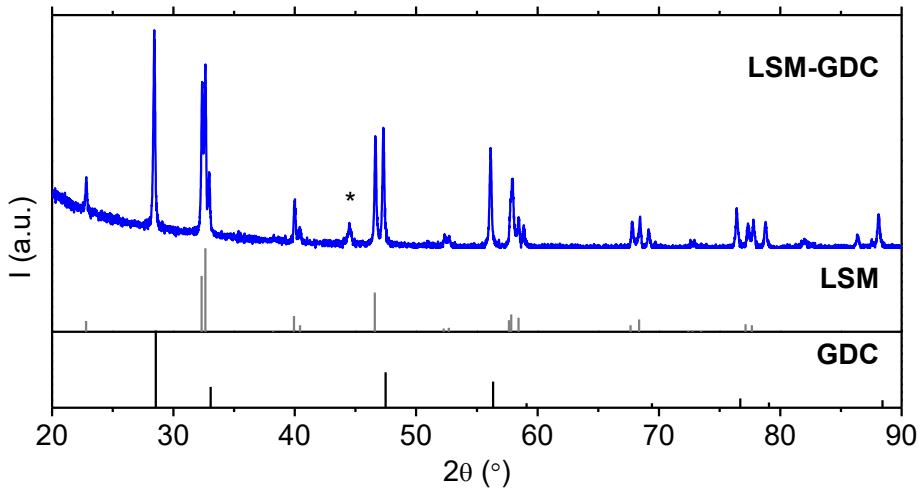


Figure 7.2: LSM and GDC compatibility test at 1150 °C (2h). * XRD holder.

7.2.1.2. XRD and FE-SEM characterization

Symmetrical cells were prepared by using cathodes based on LSM and LSM-GDC backbones. The ratio (in weight) LSM to ceria-based chosen for the composite electrode was 50/50 because it has been reported as the optimum for SOFC LSM-based cathodes purposes [11]. GDC powder was synthesized by co-precipitation method, whereas LSM powder was purchased from Fuel Cell Materials (USA). The inks obtained were applied on both sides of fully-dense GDC electrolytes. Porous electrodes (9 mm of diameter) were obtained after calcining screen-printed layers at 1150 °C for 2 hours. A top screen-printed gold mesh was further applied on LSM-GDC electrode in order to ensure proper current collection.

Different 2M solutions (ethanol-water) with adjusted surface tension were prepared with the different Co, Ba, Ce, Pr, Sm and Zr precursors for the electrodes infiltration. The solution was dropped on the electrode, and infiltration was carried out by capillarity.

The microstructure of the symmetrical cells manufactured is shown in the cross-section FE-SEM analysis (Figure 7.3) after EIS test, the back scattered electron analysis of the backbone, reveals that both phases are well distributed around the whole electrode. Thus, the TPB of the electrode should be enlarged

improving the cell performance. Furthermore, the electrode porosity appears to be adequate for gas diffusion, as will be assessed in the electrochemical testing.

As can be seen in the infiltrated electrodes, the whole electrode surface was covered (Figure 7.3) with different oxide catalysts, and the particles sizes range from 20 to 40 nm. The infiltrated particles are spherical, except for Pr which presents needle-like morphology.

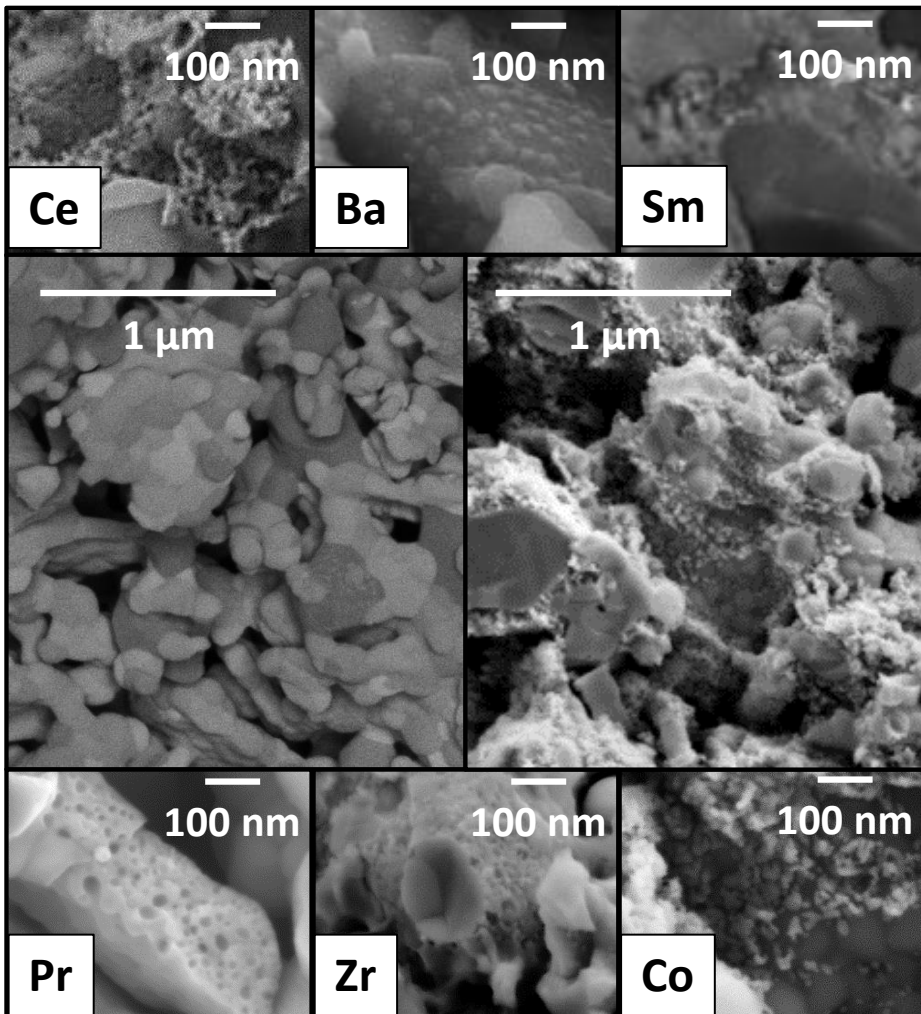


Figure 7.3: From left to right; back SEM backscattering electrons of the LSM-GDC backbone, Co backbone infiltrated. Infiltrated oxide SEM magnification; Pr, Zr, Co, Ce, Ba and Sm.

In order to check if there is a morphology change in the nanocatalyst infiltrated, FE-SEM images of a fresh electrode (after sintering 2 hours the nanocatalyst, in order to obtain the morphology at the beginning of the EIS measurements) and the electrode after EIS measurements are shown Figure 7.4. No coarsening is visible in the electrodes, which is an important factor in the stability of the electrode operation. Furthermore, the nanocatalyst size and morphology is retained after EIS test.

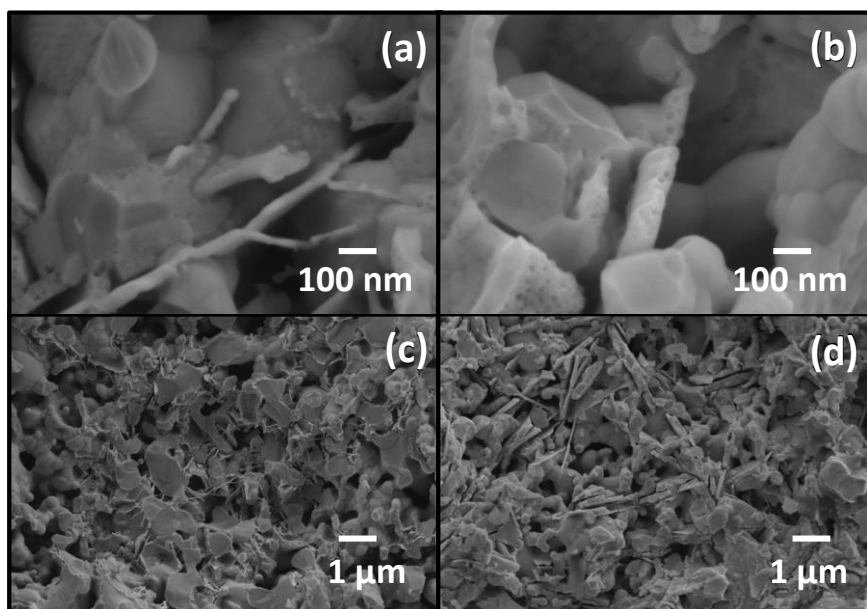


Figure 7.4: LSM-GDC infiltrated by Pr, calcined at 700 °C 2h (a) 100K X (c) 10 K X, LSM-GDC infiltrated by Pr, after EIS measurements (b) 100K X (d) 10 K X.

Additionally, electrodes were characterized by means of XRD and patterns are shown in Figure 7.5 (note the log scale in y-axis). The magnification of the patterns is necessary in order to discern the different oxides, due to the low intensity of the peaks. The patterns make possible to discern the different oxides obtained after the precursors calcination. Peaks that are not pointed in the figure were ascribed to LSM or GDC phases.

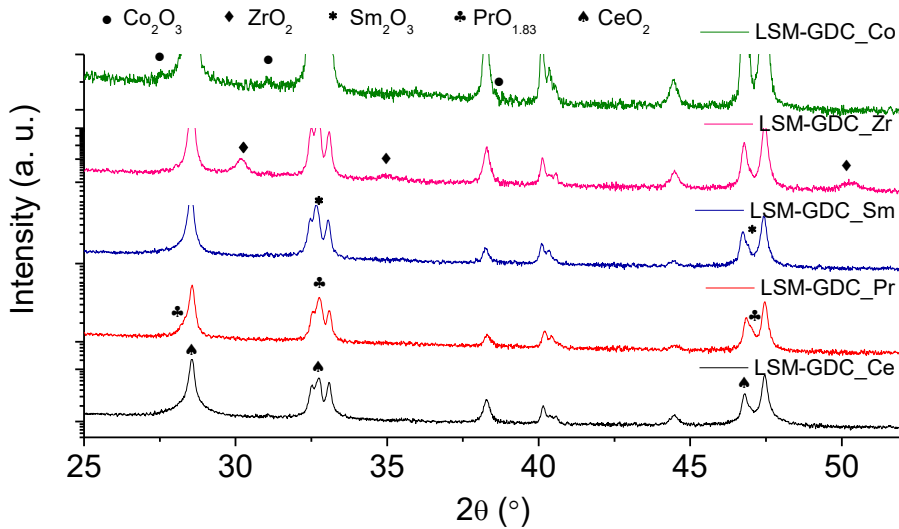


Figure 7.5: XRD of the electrodes after infiltration and calcination. Peaks of different oxides infiltrated are marked by symbols.

7.2.1.3. Polarization resistance determination

The electrochemical performance of the different promoted electrodes was studied by means of EIS on corresponding infiltrated symmetrical cells, which were compared with the LSM-GDC (blank) and LSM electrodes. LSM was measured at higher temperatures due to the worst performance. Comparing the polarization resistance (R_p) between LSM and LSM-GDC composite, the value decreases more than one order of magnitude by introducing the ionic phase. It seems that the TPB was enlarged along the whole electrode thickness improving the cell performance.

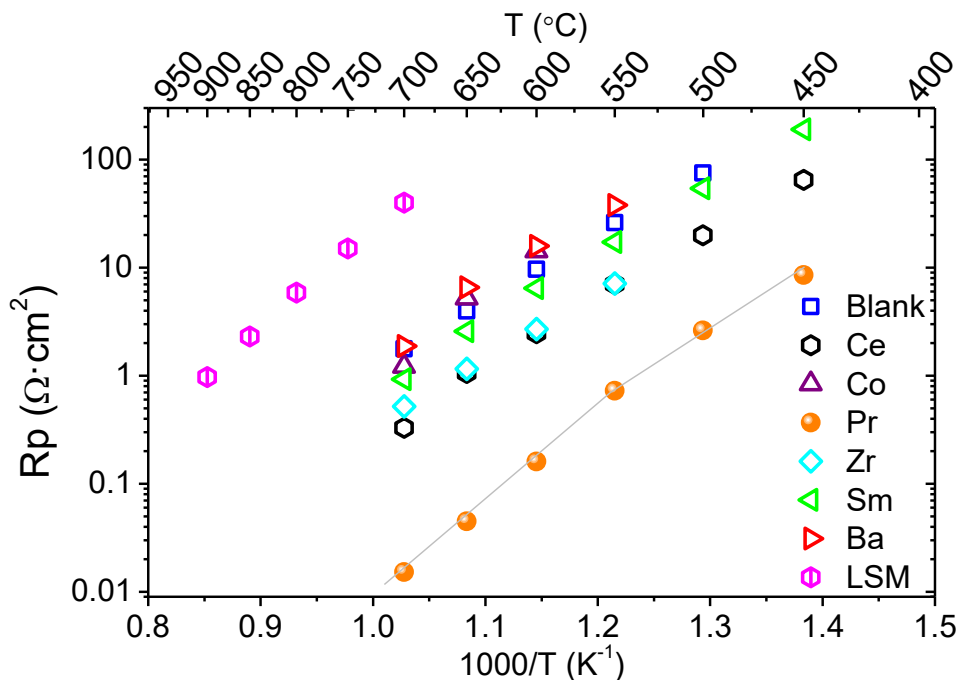


Figure 7.6: Arrhenius plot of the R_p obtained from the EIS measurements for the symmetrical cells in air. The composites infiltrated are labeled by the nanocatalyst infiltrated. Blank is the LSM-GDC composite and LSM is the parent electrode.

Furthermore, as can be inferred from the Figure 7.6 every nanocatalyst enhances the cell performance of the pristine sample, excepting Co and Ba. Pr exhibits exceptional promotion behavior, *i.e.*, the electrode polarization resistance diminishes two orders of magnitude with regard to the blank electrode. Other metal oxides show beneficial effects, namely, Ce, Zr and Sm infiltration leads to R_p 10, 5 and 2 times smaller, respectively. The derived activation energy (E_a) for all samples (Table 7.1) is very similar (1.14-1.22 eV), except for Co, which exhibits significantly higher E_a . Besides, Pr electrode shows a two-fold Arrhenius behavior: higher E_a value at high temperatures (700-550 °C); and at low temperature (550-450 °C) an E_a value within the quoted range observed for most infiltrated electrodes. Assuming that the backbone is identical for all samples, the changes in R_p are uniquely ascribed to the catalytic promotion. The particular E_a observed for the Pr electrode at higher temperatures evidences a change in its rate limiting step. Due to the high catalytic activity, the nature of the limiting step is presumably not related to surface oxygen reduction process. In addition, controlled phase transition of

this oxide has been widely investigated [12, 13]. Pr oxide undergoes a phase transition from the ordered $\text{PrO}_{1.833}$ at room temperature to disordered $\text{PrO}_{1.83}$ at increasing temperatures, which is reflected in the electrical conductivity behavior [14-16]. It seems that the variation of the E_a in the R_p coincides with this phase transition.

Infiltrated	E_a (eV)
Blank	1.18
Ce	1.14
Co	1.79
Pr	1.86
	1.20
Zr	1.20
Sm	1.22
Ba	1.14

Table 7.1: E_a (eV) of the cathodes in air.

Furthermore, the reproducibility of the results obtained by the infiltration was assessed by measuring three different cells infiltrated with Pr, obtaining practically the same electrochemical results (Figure 7.7).

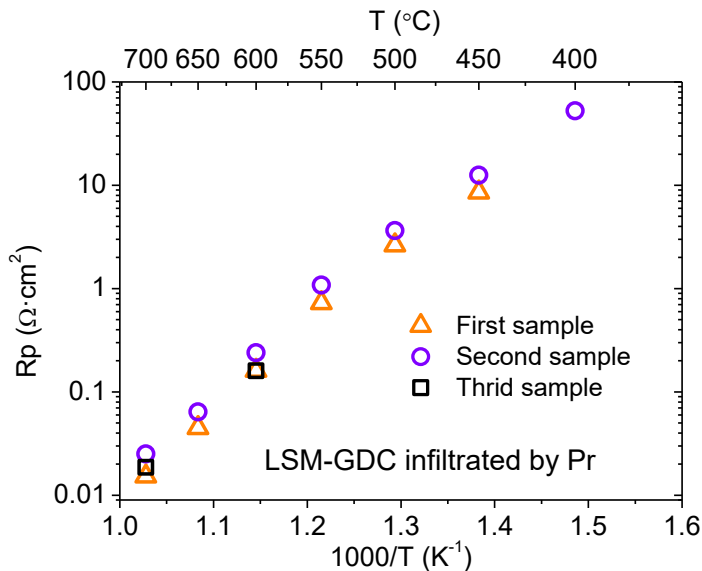


Figure 7.7: Reproducibility of the LSM-GDC electrodes infiltrated with Pr measured by symmetrical cells configuration.

7.2.1.3.1. LSM and LSM-GDC cathode electrochemical performance

In order to discern the different contributions of the resistance, EIS measurements were fitted to a double $R||CPE$ equivalent circuit (Figure 7.8 (a)) for LSM-GDC electrode whereas four $R||CPE$ elements were required (Figure 7.8 (b)) for the LSM electrode.

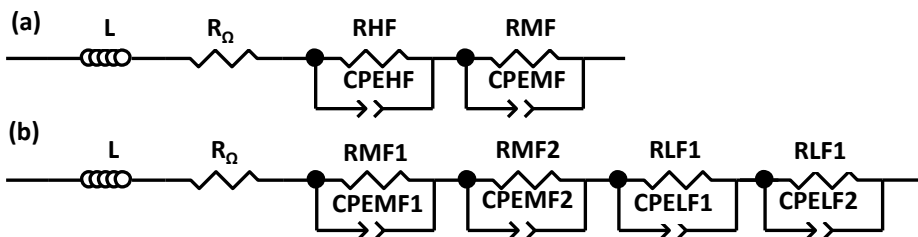


Figure 7.8: Equivalent circuits used for impedance spectra results fitting.

The electrochemical results of the symmetrical cell performance demonstrated the enhancement of the cell performance by reducing the R_p in more than one order of magnitude. The composite should improve the polarization resistance at medium and low frequencies, since the ionic phase can enlarge the TPB to the whole electrode thickness. EIS spectrum of the single phase material and composite electrode working at 700 °C in air are presented in Figure 7.9. As can be observed from the graph, LSM electrode shows four arcs in the EIS spectrum. The higher resistances are obtained at low (LF) and medium frequencies (MF) (Figure 7.9). Nevertheless, the LSM-GDC electrode exhibits only arcs at medium at high frequencies.

The fitting of the EIS spectra is presented in the Table 7.2. The dual phase composite reduces the resistances at medium and low frequencies. The low frequency processes are related with surface processes, and the incorporation of the ionic phase can improve the oxygen reduction reaction. Furthermore, the reduction at MF can be ascribed to the TPB length enlargement, since that resistance has been previously assigned with the TPB length [6]. Thus, the active area for the oxygen reduction is no limited to the electrode-electrolyte interface.

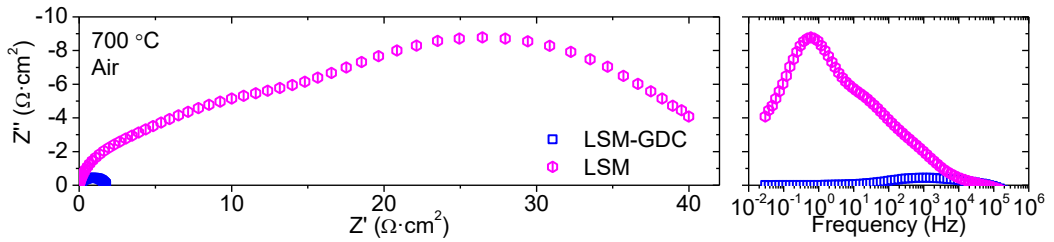


Figure 7.9: Electrochemical impedance spectra for LSM and LSM-GDC electrodes.

Frequency range	LSM			LSM-GDC		
	R ($\Omega \cdot \text{cm}^2$)	C (F/cm^2)	f (Hz)	R ($\Omega \cdot \text{cm}^2$)	C (F/cm^2)	f (Hz)
HF	-	-	-	0.91	$2.1 \cdot 10^{-5}$	8396
MF1	2.35	$7.7 \cdot 10^{-5}$	878	1.07	$2.0 \cdot 10^{-4}$	741
MF2	2.76	$3.3 \cdot 10^{-4}$	174	-	-	-
LF1	6.57	$9.4 \cdot 10^{-4}$	25.9	-	-	-
LF2	31.67	$9.7 \cdot 10^{-3}$	0.52	-	-	-

Table 7.2: Fitting results for the EIS spectrums for the symmetrical cells; LSM and LSM-GDC.

7.2.1.3.2. Stability of the infiltrated cathodes

Infiltrated	Degradation rate 700°C ($\Omega \cdot \text{cm}^{-2} \cdot \text{h}^{-1}$)
Blank	$5.87 \cdot 10^{-4}$
Ce	$2.00 \cdot 10^{-3}$
Co	$7.68 \cdot 10^{-3}$
Pr	$1.95 \cdot 10^{-4}$ (0-100 h) $-5.29 \cdot 10^{-6}$ (100-270 h)
Zr	$-3.42 \cdot 10^{-4}$
Sm	$1.41 \cdot 10^{-3}$
Ba	$1.38 \cdot 10^{-2}$

Table 7.3: Degradation rate of electrodes ($\Omega \cdot \text{cm}^{-2} \cdot \text{h}^{-1}$).

The stability of the infiltrated cathodes was tested at 700 °C for 1200 minutes, and the degradation rate is listed in Table 7.3. A very slight change in the R_p is obtained for all samples, which corroborates the stability of the infiltrated catalyst in the measured time. Exceptionally, Zr improves the cell performance with time, *i.e.*, R_p decreases, which is assigned to transient activation or

equilibration of the catalyst. A longer stability test was performed for the Pr electrode and it is also shown in the Table 7.3. Two different behaviors can be distinguished in Figure 7.10 (f). First there is an initial degradation or equilibration, but after 100 hours of operation, it disappears, as can be deduced from the almost constant R_p up to 275 h. In general, as concluded from the degradation rate values, all the catalysts show a first equilibration (activation and/or degradation) period until they reach their final state under the operation conditions (Figure 7.10), after which R_p remains constant.

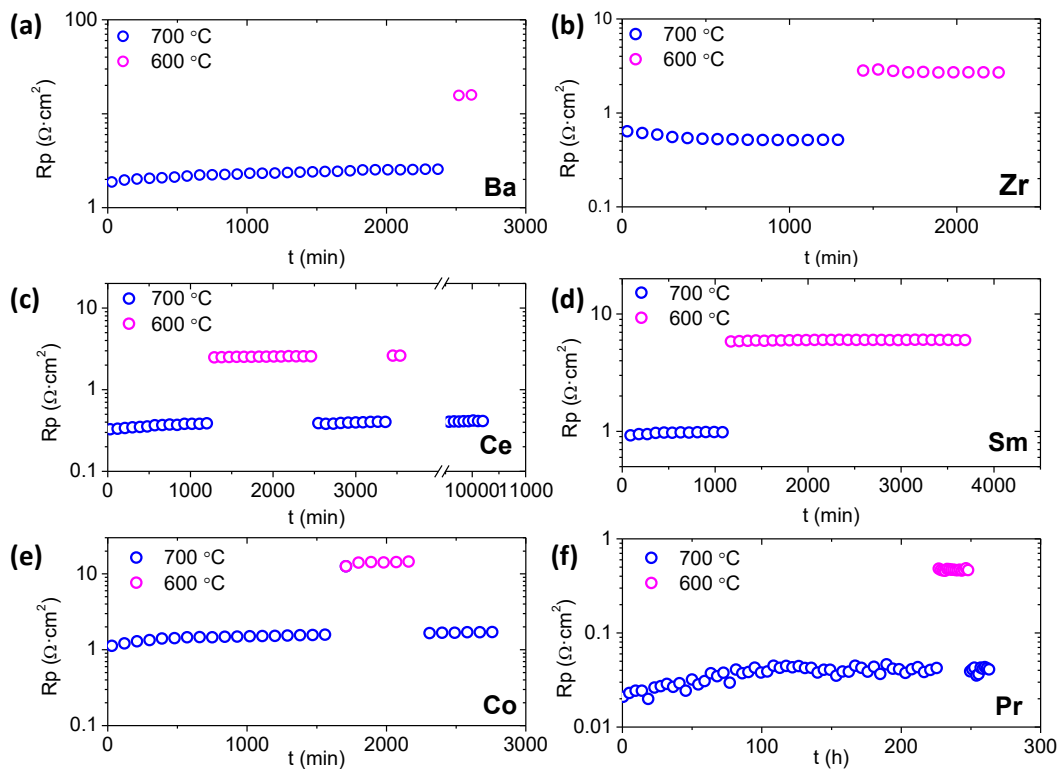


Figure 7.10: Polarization resistance of LSM-GDC infiltrated in the stability test.

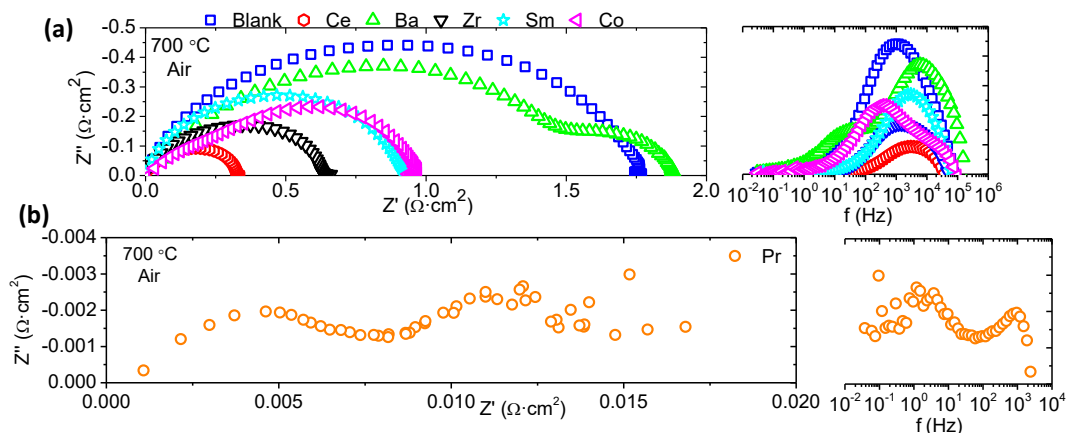


Figure 7.11: Electrochemical impedance spectra from the symmetrical cell analysis.

Regarding the electrodes infiltrated, the main changes in the cell performance should be attributed to the nanocatalyst incorporated in the electrode. Consequently, the fitting of the EIS spectrums by equivalent electrical circuit will shed light on the influence of the different catalysts. As was described above, the pristine (blank) electrode shows two contributions, *i.e.*, the highest one at medium frequencies (MF, 0.7-7 kHz), which limits the performance, and another one at high frequencies (HF, 8-220 kHz). MF contribution has been associated to the coupled dissociative adsorption, transfer of species at TPB and surface diffusion processes [6, 17, 18]. MF contributions are diminished through the infiltration with Pr, Ce, Zr and Sm catalysts, in this order from the highest to the lowest reached R_p magnitude. This effect is unambiguously assigned to the enhancement of the aforementioned surface related processes. On the other hand, HF processes become limiting in the electrode performance as the MF processes are progressively ameliorated thanks to the catalytic promotion. However, Ba and Co infiltrated electrodes present MF contributions bigger than that of the blank electrode that is directly attributed to the inhibition of surface related processes.

In addition, the stability of the different contributions was checked (Table 7.4). The MF resistance increases with operation time ($t_2=1200$ min), except for Zr that diminishes. Moreover, the frequency range associated with these surface processes is shifted towards lower values whereas the HF range remains more or less unaltered for all samples. Finally, after 1200 min the dominant

mechanism is still associated to HF processes, for Pr, Ce, Zr and Sm which agrees with the absence of catalytic surface deterioration (catalyst coarsening) revealed by SEM (Figure 7.4 (b) and (d)).

Infiltration oxide	t	RHF ($\Omega \cdot \text{cm}^2$)	RMF ($\Omega \cdot \text{cm}^2$)	RLF ($\Omega \cdot \text{cm}^2$)	fHF (Hz)	fMF (Hz)	fLF (Hz)
Blank	1	0.91	1.07	--	$8.40 \cdot 10^3$	742	
	2	0.90	1.08	--	$8.61 \cdot 10^3$	740	
Ce	1	0.36	0.12	--	$3.23 \cdot 10^4$	1814	
	2	0.41	0.16	--	$2.82 \cdot 10^4$	1307	
Co	1	0.53	1.05	--	$1.44 \cdot 10^5$	266	
	2	0.56	1.37	--	$1.31 \cdot 10^5$	185	
Pr	1	0.05	--	$4.45 \cdot 10^{-3}$	$3.84 \cdot 10^4$		2
	2	0.07	--	$5.58 \cdot 10^{-3}$	$3.07 \cdot 10^4$		2
Zr	1	0.41	0.31	--	$2.61 \cdot 10^4$	1050	
	2	0.40	0.28	--	$2.21 \cdot 10^4$	1011	
Sm	1	0.75	0.35	--	$9.69 \cdot 10^3$	1623	
	2	0.70	0.46	--	$9.64 \cdot 10^3$	1230	
Ba	1	0.43	1.43	$3.38 \cdot 10^{-1}$	$1.78 \cdot 10^5$	6494	17
	2	0.60	1.54	$7.80 \cdot 10^{-1}$	$2.21 \cdot 10^5$	5857	15

Table 7.4: Fitting results at t1= 30 min and t2 after 1200 min for the pristine and infiltrated samples.

7.2.1.3.3. Influence of oxygen partial pressure

To shed further light into the nature of the limiting steps in the oxygen reduction reaction (ORR), the best electrode (Pr infiltrated) and the blank sample were tested at different p_{O_2} . The blank sample presents three arc contributions at 600 °C, HF, MF and LF, while the Pr sample has only two contributions, HF and M-LF (medium-low frequency, 300-1500 Hz). Each contribution can be related with the oxygen partial pressure by the equation $R_i \propto P_{\text{O}_2}^{-m_i}$ and m clarifies the limiting step in the ORR [19, 20]. Figure 7.12 depicts the modelled resistances, capacitances and frequencies for the different contributions.

The non-infiltrated electrode shows a p_{O_2} independent ($m=0$) HF contribution,

which can be assigned to the ionic transport of the composite. The limiting processes associated to MF and LF slightly increase when decreasing the pO_2 with $m = 0.12$ and $3/8$, respectively. The value of $3/8$ is related with the partial reduction of the atomic oxygen ($O_{ad} + e^- \rightarrow O_{ad}^-$). However the m value 0.12 observed for MF processes originates from the combination of two different mechanisms, the transport of the partial reduced atomic oxygen to the TPB ($O_{ad}^- \rightarrow O_{TPB}^-$) $m=1/4$, and the total reduction of oxygen ($O_{TPB} + e^- \rightarrow O_{TPB}^{2-}$) with $m=0$.

The Pr infiltration decreases mainly the resistance at L-M frequencies and slightly the HF associated resistance, which in this case limits cathode performance. This HF contribution is also pO_2 independent as corresponds to the limiting ionic conductivity. The slight decrease of the resistance can be assigned to Pr oxide properties that promote the surface diffusion of oxygen species to be transported in contrast to the parent sample. Further, LF processes can be assigned to the transport of partial reduced atomic oxygen to the TPB ($m=1/4$) [20, 21].

The capacitances associated with the limiting processes can be divided in three groups depending on the range of frequencies for both materials. L and L-M frequencies processes, related with the transport of the partial reduced atomic oxygen to the TPB and the partial reduction of the atomic oxygen, have capacitances in the range of $3 \cdot 10^{-3}$ - $1 \cdot 10^{-2}$ F/cm². On the other hand, the HF processes have the lowest capacitances; 1.4 - $2.4 \cdot 10^{-4}$ F/cm². Finally, the medium frequencies; where the transport of the partial reduced atomic oxygen to TPB and the total reduction of oxygen is involved have a value of capacitance ~ 5 - $8 \cdot 10^{-5}$ F/cm².

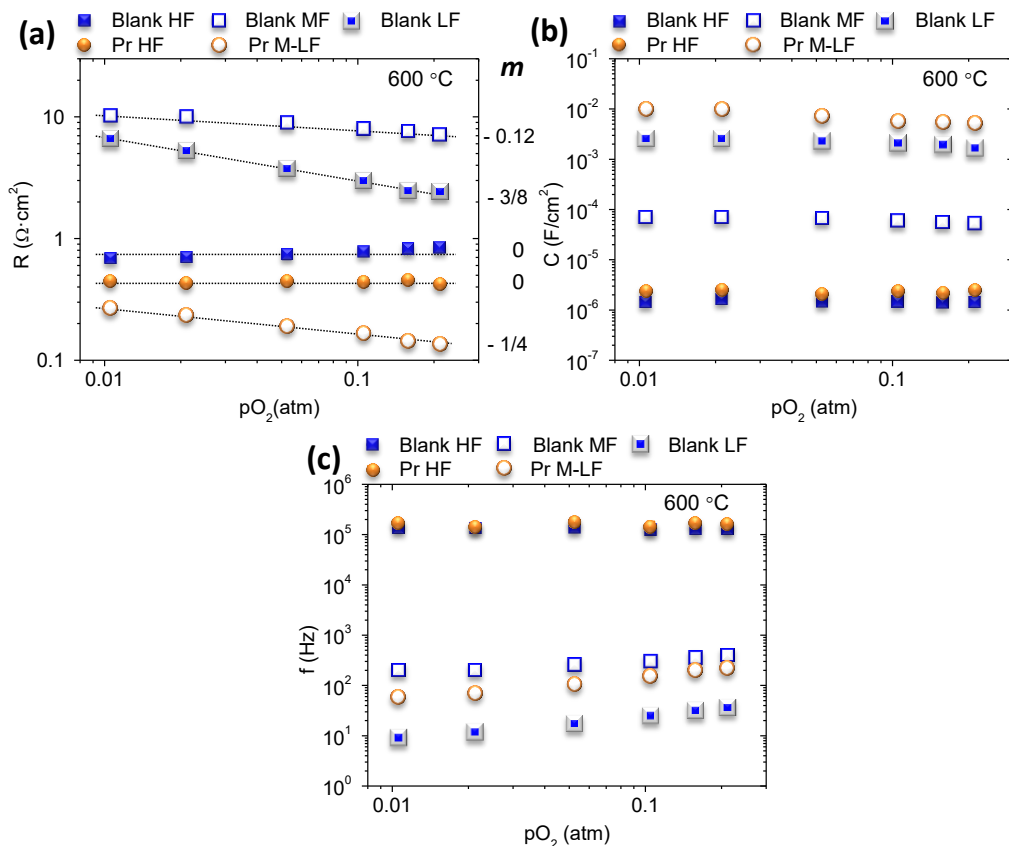


Figure 7.12: Fitting results of the (a) resistances (b) capacitances and (c) frequencies for High (HF), Medium (MF), Medium-Low (M-LF) and Low frequencies (LF) at 600°C for different pO_2 and m value for the different frequencies.

7.2.2. Fully-assembled cell performance

7.2.2.1. Fuel cell mode performance

To confirm the results obtained by symmetrical cells the best cathode and the blank were tested as fully-assembled fuel cell. For this purpose, an anode-supported cell based on Ni-YSZ anode and 8 μ m-thick YSZ electrolyte was used. The results of the fully-assembles fuel cells are drawn in Figure 7.13. In the case of the infiltrated sample is possible to observe the polarization for concentration in the last part of the i-V curves, whereas the blank composite i-V curve is limited by the ohmic resistance polarization. As the temperature is decreased, the cell performance is dominated by the resistance of the

electrodes and electrolyte material in all range of currents densities. No leakage of hydrogen was observed for both samples, achieving high OCV. The maximum power density obtained at 700 °C, by using air as oxidant feed and wet hydrogen as fuel, is five times bigger for the Pr-infiltrated cathode, reaching a peak value of 567 W/cm² at 700 °C.

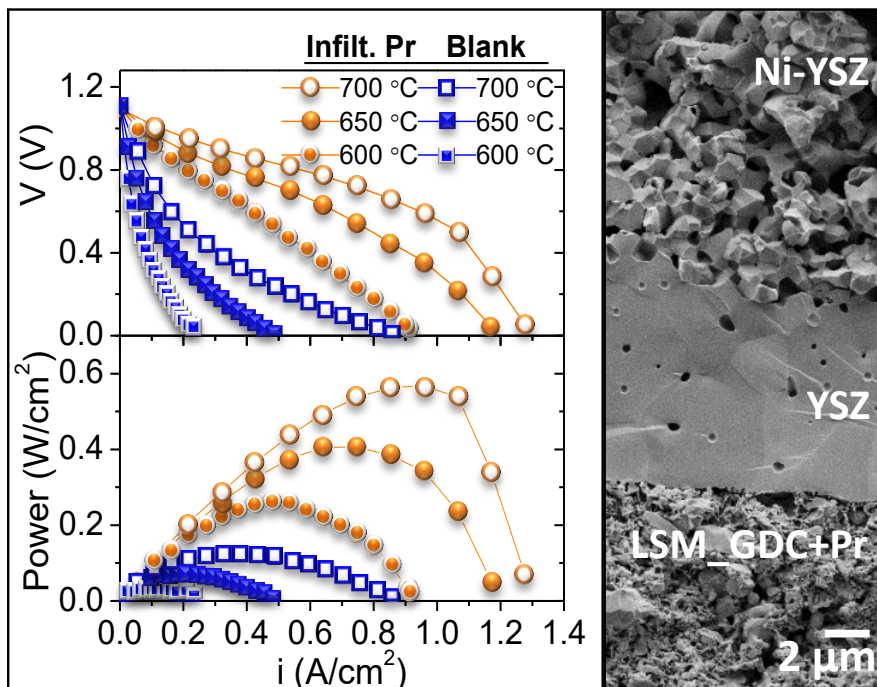


Figure 7.13: i-V and i-P curves for LSM-GDC/YSZ/Ni-YSZ and LSM-GDC+Pr/YSZ/Ni-YSZ.

As both samples were identical, excluding for the infiltration, an EIS measurement was performed in complete fuel cell mode near to the OCV at 700 °C. Table 3 shows the results of the fitting with the equivalent electrical circuit mentioned above (three R||CPE elements). All resistances decrease with the Pr infiltration; all processes increase the capacitance and change the characteristic frequency to slower values. Assuming that the contributions related with the electrolyte and electrode remained constant for both measurements, the cell improvement due to the Pr infiltration can only be related to the enhancement of the ORR. As explained for the symmetrical cells measurements, the blank cell is limited by MF surface related processes, and this behavior is maintained for the fully-assembled fuel cell. MF resistance

decreases more than 80% with the Pr infiltration, where dissociation and oxygen adsorption processes are improved. This reduction of the different contributions is responsible for the enhancement of the power density reached for the infiltrated SOFC.

Frequency range	LSM-GDC/YSZ/Ni-YSZ			LSM-GDC+Pr/YSZ/Ni-YSZ		
	R ($\Omega \cdot \text{cm}^2$)	C (F/cm^2)	f (Hz)	R ($\Omega \text{ cm}^2$)	C (F/cm^2)	f (Hz)
HF	0.17	$2.24 \cdot 10^{-5}$	$4.31 \cdot 10^4$	0.07	$2.89 \cdot 10^{-4}$	$7.59 \cdot 10^3$
MF	2.57	$3.10 \cdot 10^{-5}$	2005	0.47	$8.75 \cdot 10^{-4}$	384
LF	0.57	$1.09 \cdot 10^{-3}$	256	0.07	$3.75 \cdot 10^{-1}$	6

Table 7.5: Fitting results for the EIS spectrums recorded at the OCV in fully-assembled fuel cell at 700 °C.

7.2.2.2. Electrolysis mode performance

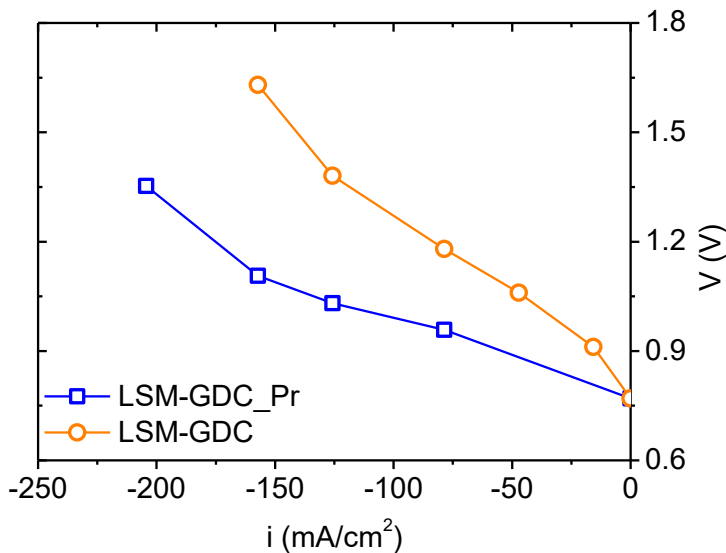


Figure 7.14: i-V curves of the steam electrolysis for the pristine and the Pr infiltrated anode.

After testing the samples in fuel cell mode, the temperature was increased until 700 °C. Steam electrolysis was performed at 700 °C for both samples. In Figure 7.14 is represented the voltage observed for each current density. The negative sign of the current density indicates that the current is applied and is

not produced by the cell. When small current densities are applied there is big increase of the overpotential. However, for higher currents densities but below 1.3 V the slope of the i - V curves are reduced. But for higher voltages (> 1.3 V) there is a huge augment of the cell voltage with the current density. In addition the sample with the praseodymium oxide infiltrated in the anode shows a better performance for the same range of current densities operation, *i.e.*, the cell voltage is smaller. This reduction in the cell voltage allows applying higher current densities, therefore higher quantities of hydrogen could be produced.

Figure 7.15 represents the H_2 production detected by a mass spectrometer in the cathode outlet stream during the electrolysis experiments. During the electrolysis tests constant current densities were applied during 30 minutes, and the cathode was feed with wet argon (2.5 % vol. H_2O). As shown in the Figure 7.15, hydrogen could be detected from low imposed current densities and the production was stable during the electrolysis time. In addition, there was a quick signal response as can appreciate from the graphs, with a huge augment or diminution depending if the current is applied or removed.

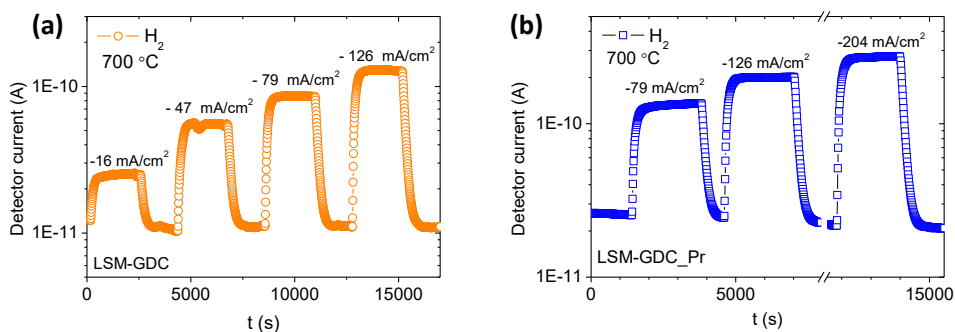


Figure 7.15: Mass spectrometer results of the steam electrolysis at 700 °C (a) for the LSM-GDC composite and (b) LSM-GDC infiltrated by praseodymium oxide.

In order to determine the Faradic efficiency of the steam electrolysis process, the hydrogen production was quantified by a gas chromatograph. Figure 7.16 shows the hydrogen production and Faradic efficiency for both cell (LSM-GDC/YSZ/Ni-YSZ and LSM-GDC+Pr/YSZ/Ni-YSZ) working as steam electrolyzer. The Faradic efficiency (η_F , in *Methodology chapter*) in the water electrolysis was determined from the expected hydrogen production calculated according

to the Faraday's equation (Equation (4.14)) and the experimental hydrogen production measured by the gas chromatograph during the stationary step of the steam electrolysis. Tested cells have high Faraday's efficiency, achieving values around 100 %, the variation of the efficiency can be caused by the experimental error, since no hydrogen leakage was detected. However, at 157 mA/cm^2 , the efficiency of the not infiltrated sample is reduced. This point fits with the highest increase in terms of cell overpotential (1.63 V). This behavior can be assigned to the electronic conductivity in the thin YSZ electrolyte, even though the present cell voltage is lower than the usual electroreduction voltage of YSZ (2.3 V) [22]., but the same effect was recorded for similar cells [22-24]. This effect is reversible for low levels of electroreduction.

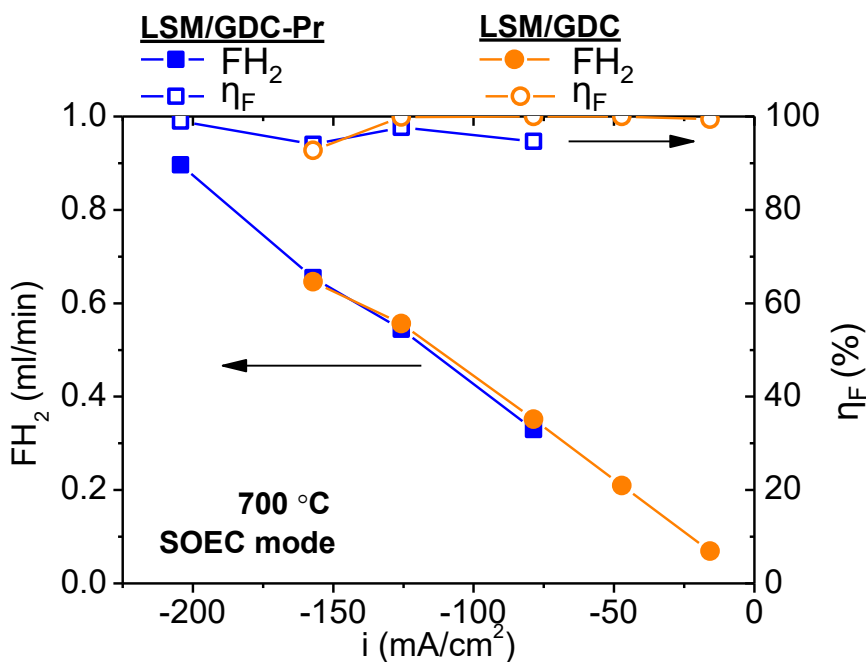


Figure 7.16: Faradic efficiency and hydrogen production in the steam electrolysis for LSM-GDC/YSZ/Ni-YSZ and LSM-GDC+Pr/YSZ/Ni-YSZ.

7.3. Conclusions

The performance of the LSM state-of-the-art was improved by introducing an ionic phase (GDC). The processes at low and medium frequencies could be enhanced by enlarging the TPB in the electrode. This robust LSM-GDC

composite was used as backbone electrode for the infiltration of different catalysts, Sm, Zr, Ce, Ba, Co and Pr, dispersed as oxide nanoparticles after firing. Catalysts candidates were screened using symmetric cells supported on GDC electrolyte. Sm, Zr, Ce and Pr catalysts improved the electrode performance by the reduction of the resistance at medium frequency, associated to surface processes. In contrast Co and Ba catalyst worsen the cell performance increasing the resistance at medium frequencies in the temperature operation range.

The stability of the operation with time for different activated cathodes was systematically studied. At first, a slight increase in the polarization resistance with time until was obtained, reaching a constant value. However, Zr catalyst showed a particular case, since the polarization resistance decreased with time. The modelling results as function of pO_2 revealed that the rate-limiting mechanism in the ORR was the surface transport of oxygen species towards the TPB.

Finally, the best infiltrated composite was tested in a fully assembled Ni-YSZ-supported cell. Firstly, the cell was tested in a fuel cell mode achieving a 5-fold improvement of the power density. Then, the cell was used as steam electrolyzer reducing the cell potential in 0.53 V for a current density of 157 mA/cm².

These results demonstrate the applicability of the infiltration for the fully-assembled cell working as a fuel cell or electrolyzer with the resulting improvement of the power density and reduction of the cell voltage, respectively.

7.4. References

- [1] S.P. Jiang, J. Mater. Sci., 43 (2008) 6799-6833.
- [2] S.B. Adler, Chem. Rev., 104 (2004) 4791-4843.
- [3] E.P. Murray, T. Tsai, S.A. Barnett, Solid State Ion., 110 (1998) 235-243.
- [4] M.J. Jorgensen, S. Primdahl, C. Bagger, M. Mogensen, Solid State Ion., 139 (2001) 1-11.
- [5] M. Balaguer, V.B. Vert, L. Navarrete, J.M. Serra, J. Power Sources, 223 (2013) 214-220.
- [6] M.J. Jorgensen, M. Mogensen, J. Electrochem. Soc., 148 (2001) A433-A442.

- [7] E.P. Murray, S.A. Barnett, *Solid State Ion.*, 143 (2001) 265-273.
- [8] C. Solis, M. Balaguer, F. Bozza, N. Bonanos, J.M. Serra, *Appl. Catal. B-Environ.*, 147 (2014) 203-207.
- [9] S.P. Jiang, *Mater. Sci. Eng. A-Struct. Mater. Prop. Microstruct. Process.*, 418 (2006) 199-210.
- [10] T.Z. Sholklapper, C.P. Jacobson, S.J. Visco, L.C. Dejonghe, *Fuel Cells*, 8 (2008) 303-312.
- [11] S.P. Jiang, W. Wang, *Solid State Ion.*, 176 (2005) 1351-1357.
- [12] B.G. Hyde, D.J.M. Bevan, L. Eyring, *Philosophical transactions of the Royal society A*, 2 (1964) 227.
- [13] B.G. Hyde, D.J.M. Bevan, L. Eyring, in: G.a.B. K. S. Vorres (Ed.), New York, 1966.
- [14] L. Eyring, N.C. Baenziger, *Journal of Applied Physics*, 33 (1962) 209.
- [15] G.V. Chandrashekhar, P.N. Mehrotra, G.V. Subba Rao, E.C. Subbarao, C.N.R. Rao, 63 (1967) 1295-1301.
- [16] R.G. Biswas, M. Rajendran, G.S. Walker, E. Williams, A.K. Bhattacharya, *J. Mater. Sci.*, 33 (1998) 3001-3007.
- [17] S.Z. Wang, Y. Jiang, Y.H. Zhang, J.W. Yan, W.Z. Li, *Solid State Ion.*, 113 (1998) 291-303.
- [18] F.H. vanHeuveln, H.J.M. Bouwmeester, *J. Electrochem. Soc.*, 144 (1997) 134-140.
- [19] M.J. Escudero, A. Aguadero, J.A. Alonso, L. Daza, *J. Electroanal. Chem.*, 611 (2007) 107-116.
- [20] R.R. Peng, T.Z. Wu, W. Liu, X.Q. Liu, G.Y. Meng, *J. Mater. Chem.*, 20 (2010) 6218-6225.
- [21] Y. Takeda, R. Kanno, M. Noda, Y. Tomida, O. Yamamoto, *J. Electrochem. Soc.*, 134 (1987) 2656-2661.
- [22] W. Weppner, *J. Electroanal. Chem.*, 84 (1977) 339-350.
- [23] M.A. Laguna-Bercero, R. Campana, A. Larrea, J.A. Kilner, V.M. Orera, *Fuel Cells*, 11 (2011) 116-123.
- [24] D.A. Wright, J.S. Thorp, A. Aypar, H.P. Buckley, *J. Mater. Sci.*, 8 (1973) 876-882.

8



electrodes for

protonic electrolyte

8. La_{2-x}A_xNi_{1-y}B_yO_{4-δ} electrodes for protonic electrolytes

8.1. Introduction

The growing interest in proton conducting solid oxide fuel cells (PC-SOFC) [1-4] research is principally due to their advantages compared to conventional oxygen-ion conducting solid oxide fuel cells (SOFCs): (1) their higher efficiency and fuel utilization, since protons react with oxygen in the cathode to form water diluting the air stream; and (2) the lower activation energy of proton transport together with the higher mobility of protons, which makes possible to reduce the operation temperature (500 - 700 °C) and permits the utilization of less expensive system components and increases their lifetime [5, 6].

Nowadays, different proton conducting materials, as doped SrCeO₃, BaCeO₃ and BaZrO₃ perovskites [2, 7, 8], LaNbO₄ scheelite [9] and La_{5.5}WO_{12-δ} defective fluorite [10], are being investigated as promising electrolytes for PC-SOFCs. Among these, La_{5.5}WO_{12-δ} (LWO) compound combines essential properties for a final application, as it exhibits reasonable high values of predominant protonic conductivity below 800 °C, low grain boundary resistance and high stability in operation conditions for long times under CO₂ and H₂S containing atmospheres [11-13].

In the present chapter, cathodes based on the mixed ionic-electronic (MIEC) conductor La₂NiO_{4+δ} are investigated. The use of MIEC materials as cathodes in PC-SOFC introduce pathways to transfer part of the dissociated oxygen ions through the bulk of the cathode to the TPBs to react with the protons (Figure 8.1). Thus, although the reacting areas are limited to the TPBs, the oxygen pathways to the TPBs are greatly enlarged, and this reduces the polarization resistance [14, 15].

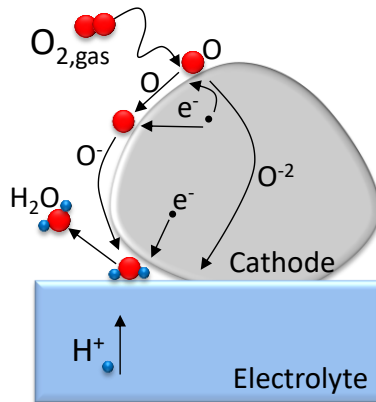


Figure 8.1: Schematic diagram of MIEC cathode reaction mechanisms for a LWO proton conducting electrolyte.

This chapter focuses on the nickelates studied used as cathodes in SOFC for its application as cathodes on LWO based PC-SOFCs. The materials selected were the pristine $\text{La}_2\text{NiO}_{4+\delta}$ (LNO), the Pr doped compounds: $\text{La}_{1.5}\text{Pr}_{0.5}\text{NiO}_{4+\delta}$ (LPN) and $\text{La}_{1.5}\text{Pr}_{0.5}\text{Ni}_{0.8}\text{Co}_{0.2}\text{O}_{4+\delta}$ (LPNCO) and $\text{Nd}_2\text{NiO}_{4+\delta}$ (NdNO). Additionally, $\text{La}_2\text{Ni}_{0.8}\text{Co}_{0.2}\text{O}_{4+\delta}$ (LNCO) used as cathode for SOFC was selected, but the difference in terms of thermal expansion coefficient (TEC) between LNCO and LWO, made the electrode detachment and EIS measurements were no possible.

After characterizing the powder and checking the compatibility with the LWO electrolyte, different symmetrical cells were prepared in order to study the electrochemical properties. Cathodes performance was studied by checking the influence of different parameters as the electrode sintering temperature, the use of dry and humidified conditions, or by preparing composite electrodes.

8.2. Results and discussion

8.2.1. Electrodes characterization

8.2.1.1. Reactivity test

Before the symmetrical cells processing and testing, the compatibility of LNO with the LWO electrolyte phase was checked. Figure 8.2 shows XRD patterns of a mixture of LNO and LWO 50 vol.% before and after being fired together at

1150 °C for 5 h. It can be observed that all the peaks correspond to the LNO and the LWO phases. XRD patterns of both materials are also plotted in Figure 8.2, where it can be observed that LWO powder presents a very small peak at 28.784° that corresponds to small traces of La₆W₂O₁₅ phase [16]. The absence of reaction between LNO and LWO phases up to the highest temperature used for cathode preparation is confirmed by this lack of new peaks after the treatment at high temperature.

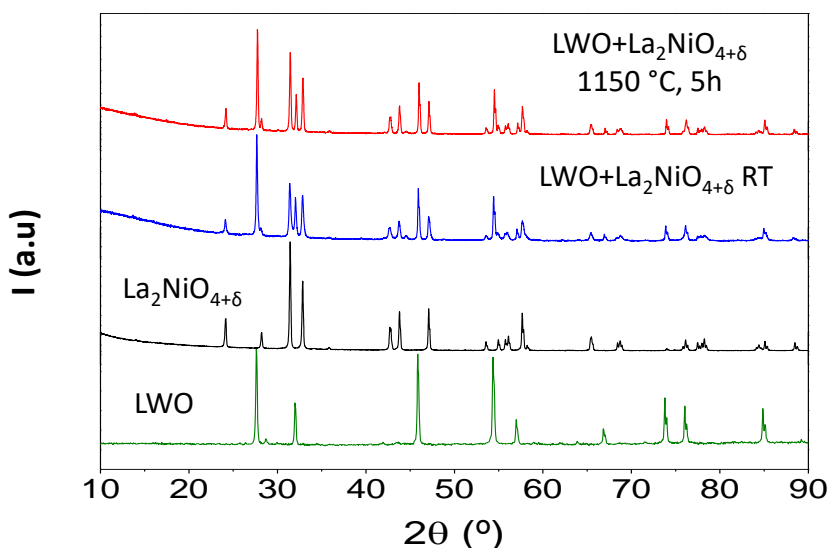


Figure 8.2: XRD patterns of LWO, La₂NiO_{4+δ} and a 50% mixture of both phases at room temperature and after being calcined at 1150 °C for 5 h.

8.2.1.2. Electrochemical characterization

Symmetrical cells of the different powders were prepared on dense LWO electrolytes. Porous ~30 μm electrodes were obtained by screen-printing the inks on both sides of the LWO electrolytes. Firing temperatures of the screen-printed cathode cells were 1150 °C, 1100 °C and 1050 °C in some cases, during 2 hours.

8.2.1.2.1. Influence of operation temperature

The cathode porosity and the electrolyte density was studied by SEM. As can be observed from cross-section image of the LPNCO cathode sintered at 1150 °C in Figure 8.3, the cathode looks very porous with relatively large surface area and shows a similar morphology as state-of-the-art SOFC cathodes.

Furthermore, the interface with the electrolyte is clean, with no visible reaction layers, as was checked by XRD (Figure 8.2) for LWO and LNO mixture.

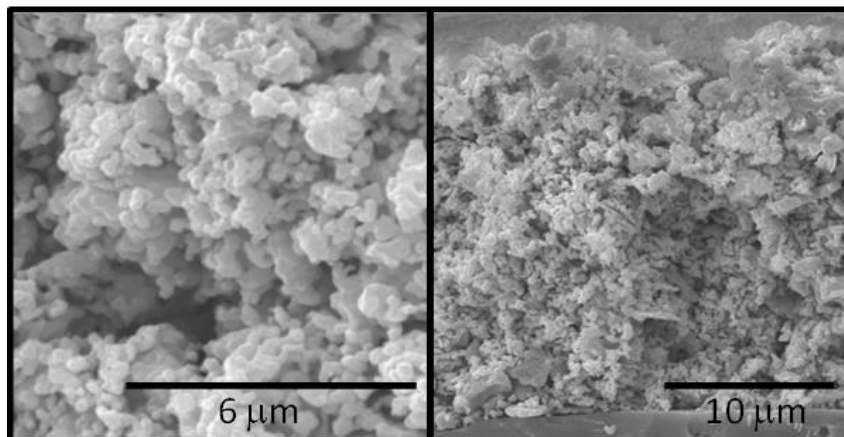


Figure 8.3: SEM analysis of the fracture cross-section of a cell (after electrochemical testing) consisting of a LWO dense electrolyte coated with LPNCO cathode at 1150 °C.

Electrochemical properties of the different cathodes, calcined at 1150 °C, can be analyzed from the polarization resistances (R_p) recorded in wet (2.5% H_2O) air as a function of temperature (Figure 8.4). The electrochemical behavior is notably improved by the incorporation of Pr and Co. For instance, a R_p value of $5.03 \Omega \cdot cm^2$ is achieved at 750 °C for LNO while the doped compounds show values of $1.03 \Omega \cdot cm^2$ and $0.93 \Omega \cdot cm^2$ for LPNO and LPNCO, respectively. On the other hand, the total substitution of Nd in the La position can reduce the polarization resistance until $2.65 \Omega \cdot cm^2$. The activation energy (E_a) of the NdNO is diminished to 1.3 V whereas the E_a remains constant (1.47 eV) when the Pr dopant is introduced in the La site (LPNO sample). However, when the Co dopant is also introduced in the Ni site together with the Pr, E_a is reduced slightly (1.44 eV). The best electrochemical properties are achieved for the LPNCO cathode in the range of operation conditions, which behaves somewhat better at low temperatures than the LPNO electrode.

The results obtained in the polarization resistance fits with the values obtained regarding the total conductivity (Figure 6.6). The doped compounds showed higher total conductivity in the measured temperature range than LNO. This improvement in the transport properties is reflected in lower polarization

resistance. Additionally, this effect can be ascribed to the reported catalytic effect of Co and Pr on the oxygen reduction reaction [17, 18].

However, NdNO with a similar total conductivity to LPNO (Figure 6.6) and a good electrochemistry performance as cathode in SOFCs [19, 20], does not show the same behavior as cathode for proton conductors. On the other hand, the activation energy is the lowest one and halves the polarization resistance of LNO.

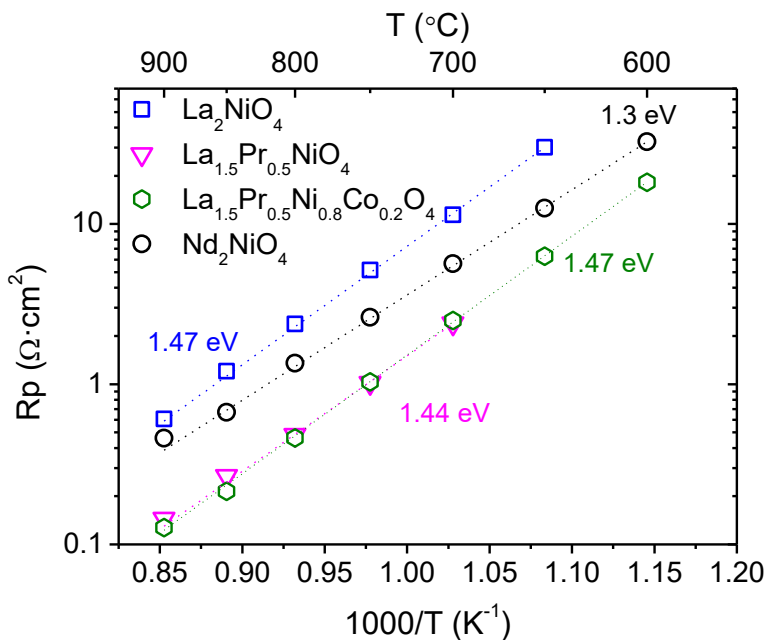


Figure 8.4: Polarization resistance as a function of $1000/T$ in wet synthetic air for LNO, LPNO, LPNCO and NdNO. Electrodes sintered at $1150\text{ }^{\circ}\text{C}$ (2h).

The impedance spectra recorded at $750\text{ }^{\circ}\text{C}$ in wet air for all cathodes sintered at $1150\text{ }^{\circ}\text{C}$ are represented in Figure 8.5 (a) and (b) (Nyquist and Bode plots, respectively). One, two or three different arcs can be distinguished depending on the material. Thus, electrochemical impedance data were modeled following an equivalent electrical circuit composed of one, two or three parallel $R||CPE$ elements, in series. Figure 8.6 (a) depict the modeled resistances (R) obtained from the EIS spectra of LNO, LPNO, LPNCO and NdNO cathodes measured in wet air. The results of capacitance and frequency are

shown in Figure 8.6 (b) and (c). All resistances can be divided in two groups depending on the range of frequency: medium frequencies (MF) from 0.1 to 10000 Hz and high frequencies (HF) with values higher than 10 kHz. LNO cathode shows one contribution at high frequencies and another at medium frequencies, being this last one the highest and limiting the cathode performance [21]. When the cathode composition is doped (with Pr and with Pr and Co), the HF contribution disappears while the MF contribution becomes smaller, giving rise to a better performance of the cathode. As mentioned above, this behavior is associated with the better transport properties of the doped compounds, which drastically reduces the HF contributions, typically associated with the total transport of the cathode materials. The cathode material doped with both Pr and Co (LPNCO) shows an additional but less pronounced improvement in the MF contribution, with respect to LPN cathode. Regarding the NdNO, it shows a resistance at high frequencies but smaller than LNO high frequency resistance. The total conductivity results of NdNO (Figure 6.6) shown higher values than LNO. Additionally, two different contributions appear at similar frequencies (at MF) for NdNO (Figure 8.5 (b)). It seems that the MF processes are not improved as for the Pr and Pr and Co doped compounds, showing a lower catalytic activity of NdNO.

The related capacitances associated with the limiting processes in the tested cathodes are summarized in Figure 8.6 (b). All processes that take place at medium frequencies have a capacitance between $1 \cdot 10^{-3}$ - 0.1 F/cm^2 . However the medium frequency process of LNO electrode has a smaller value of capacitance, and it is almost constant for all temperature range measured, with a value of $1 \cdot 10^{-4} \text{ F/cm}^2$. The high frequency processes of LNO and NdNO show smaller capacitance with a value between $1 \cdot 10^{-6}$ - $1 \cdot 10^{-4} \text{ F/cm}^2$.

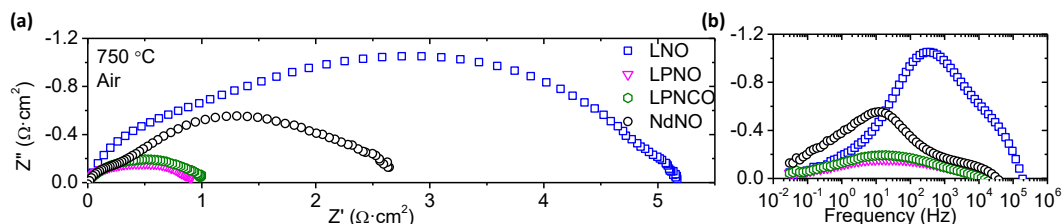


Figure 8.5: Impedance spectra, (a) Nyquist and (b) Bode plots, of LNO, LPNO, LPNCO and NdNO measured at 750 °C in wet synthetic air.

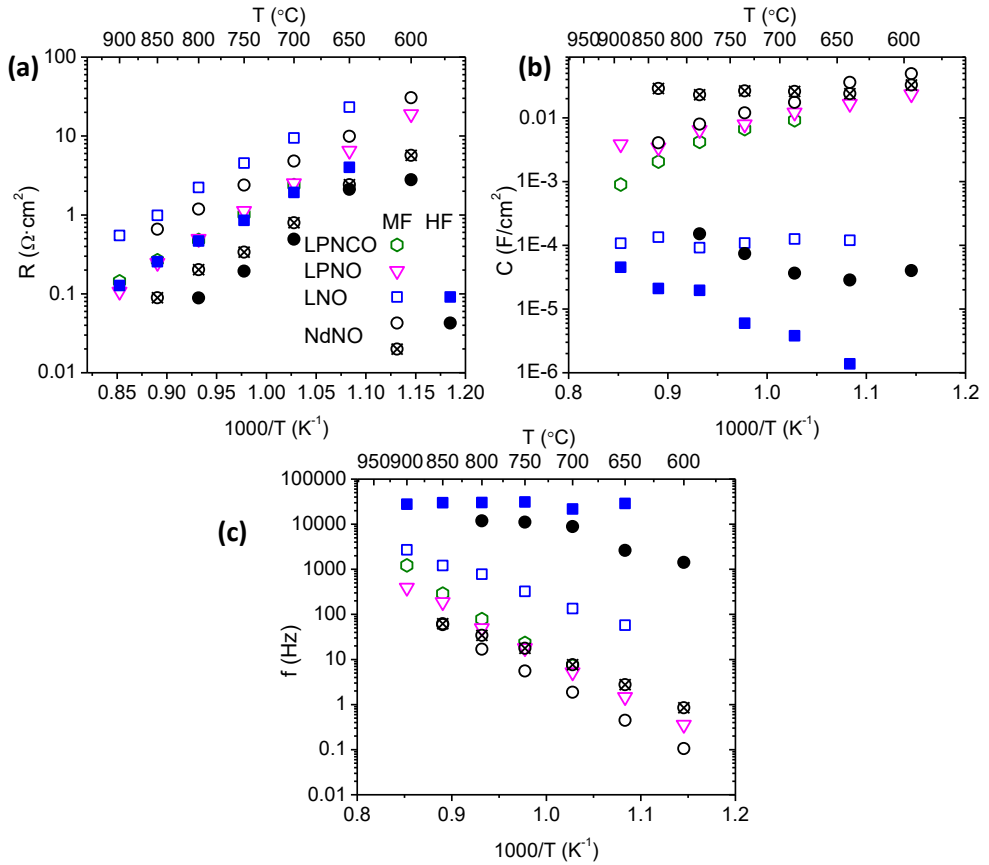


Figure 8.6: Modeled results of LNO, LPNO, LPNCO and NdNO (a) resistances, (b) capacitances (c) and frequencies as a function of the $1000/T$ in humidified air.

As it has been shown in Figure 8.1 , there are many elementary reactions that take place in the cathode on a proton conductor electrolyte and these are going to be summarized in the following table:

Elementary reactions steps	
$O_{2(g)} \rightarrow O_{2(ad)}$	Oxygen adsorption
$O_{2(ad)} \rightarrow 2O_{(ad)}$	Oxygen dissociation
$O_{(ad)} + e^- \rightarrow O_{(ad)}^-$	Oxygen reduction
$O_{(ad)} + 2e^- \rightarrow O_{(ad)}^{2-}$	
$O_{(ad)}^- \rightarrow O_{(TPB)}^-$	Surface diffusion
$O_{(ad)} \rightarrow O_{(TPB)}$	
$O_{(bulk)}^- \rightarrow O_{(TPB)}^-$	Bulk diffusion
$O_{(TPB)}^- + e^- \rightarrow O_{(TPB)}^{2-}$	Oxygen reduction at the TPB
$O_{(TPB)} + 2e^- \rightarrow O_{(TPB)}^{2-}$	
$2H_{(bulk)}^+ \rightarrow 2H_{(TPB)}^+$	Proton migration
$H_{(TPB)}^+ + O_{(TPB)}^{2-} \rightarrow OH_{(TPB)}^-$	Water formation
$OH_{(TPB)}^- + H_{(TPB)}^+ \rightarrow H_2O_{(TPB)}$	
$H_2O_{(TPB)} \rightarrow H_2O_{(g)}$	Water evaporation

Table 8.1: Elementary reaction steps in the cathode working with a protonic electrolyte [22].

The electrochemical impedance spectroscopy is a good tool to determine the limiting steps in the cathode performance. For fuel cells working with ion oxygen conducting electrolytes, the resistance (R) is proportional to the oxygen partial pressure (pO_2) by the m parameter [14, 23] by the following relation:

$$R_i \propto pO_2^{-m_i} \quad (8.1)$$

However, in the case of cathodes for proton conductor electrolytes, oxygen and water are also involved in the cathode reactions. Then, in the correlation the oxygen partial pressure (pO_2) and water partial pressure (pH_2O) have to be involved:

$$R_i \propto pO_2^{-m_i} \cdot pH_2O^{-n_i} \quad (8.2)$$

And the values of m and n determine the elementary reactions as follows:

	Elementary reactions steps	m_i	n_i
Step 1	$O_{2(g)} \rightarrow O_{2(ad)}$	1	0
Step 2	$O_{(ad)} + e^- \rightarrow O_{(ad)}^-$	3/8	0
Step 3	$O_{(ad)}^- \rightarrow O_{(TPB)}^-$	1/4	0
Step 4	$O_{(TPB)}^- + e^- \rightarrow O_{(TPB)}^{2-}$	0	0
Step 5	$H_{(bulk)}^+ \rightarrow H_{(TPB)}^+$	0	1/2
Step 6	$H_{(TPB)}^+ + O_{(TPB)}^{2-} \rightarrow OH_{(TPB)}^-$	0	1/2
Step 7	$OH_{(TPB)}^- + H_{(TPB)}^+ \rightarrow H_2O_{(TPB)}$	0	1/2
Step 8	$H_2O_{(TPB)} \rightarrow H_2O_{(g)}$	0	1/2

Table 8.2: Elementary reactions in the cathode and their order reaction respect to oxygen partial pressure (m_i) and water partial pressure(n_i).

In order to further analyze the different elementary cathode reaction steps, the calculated resistances as function of the oxygen partial pressure are depicted in Figure 8.7 (a), capacitances and frequencies are plotted in Figure 8.7 (b) and (c), respectively. All results of the electrodes calcined at 1150 °C and measured at 750 °C are presented in Figure 8.7. Generally, in protonic materials the overall total conductivity is dominated by proton transport in water vapour or/and hydrogen atmospheres below 600 °C [24]. However, at higher temperature the water desorption occurs increasing the concentration of oxygen vacancies and decreasing the proton defects. Thus, at this temperature range, oxygen ions conduction will take place via oxygen vacancies and interstitial oxygens. Then, this phenomenon will reduce the water formation and the oxygen surface reactions will dominate the elementary steps for temperatures above 600 °C [22]. Then, as the operation temperature selected for measurements was 750 °C, the relationship selected for the understanding of the limiting steps will be the Equation (8.1) and the results of the fitting of $R_i \propto pO_2^{-m_i}$ are shown in Table 8.3.

The increasing or unchanged resistance values for all materials tested at lower oxygen partial pressure indicates that there is not limitation of the oxygen bulk diffusion [22], then, other processes should be the limiting mechanisms. The HF associated processes only appear in the LNO and NdNO cathodes with very low associated capacitances (below $1 \cdot 10^{-4}$ F/cm²). The m value close to $\frac{1}{4}$ for

LNO at HF can be associated specifically to the bulk transport of LNO, which has the pO_2 dependency $-1/4$ as corresponds to a p -type electronic conductor [14, 15]. However, NdNO with a value of 0.11 seems to be related with the charge transfer as it is shown in Table 8.2 ($O_{(TPB)}^- + e^- \rightarrow O_{(TPB)}^{2-}$). The MF associated processes, limiting the LNO, LPN and LPNCO measured cathodes, have m values close to $1/4$ (0.28, 0.26 and 0.20, respectively). This pO_2 dependency and capacities of around 10^{-4} - 10^{-2} F/cm² can be related to ionic transport from TPB interface towards the electrolyte and not to electrode-electrolyte interfacial processes, since no pO_2 dependence would be expected in that case [21, 25, 26]. Additionally, the dependence of the oxygen partial pressure and the resistance at MF for NdNO has values of 0.41 and 0.34 that can be correlated with the oxygen reduction (step 2 in Table 8.2).

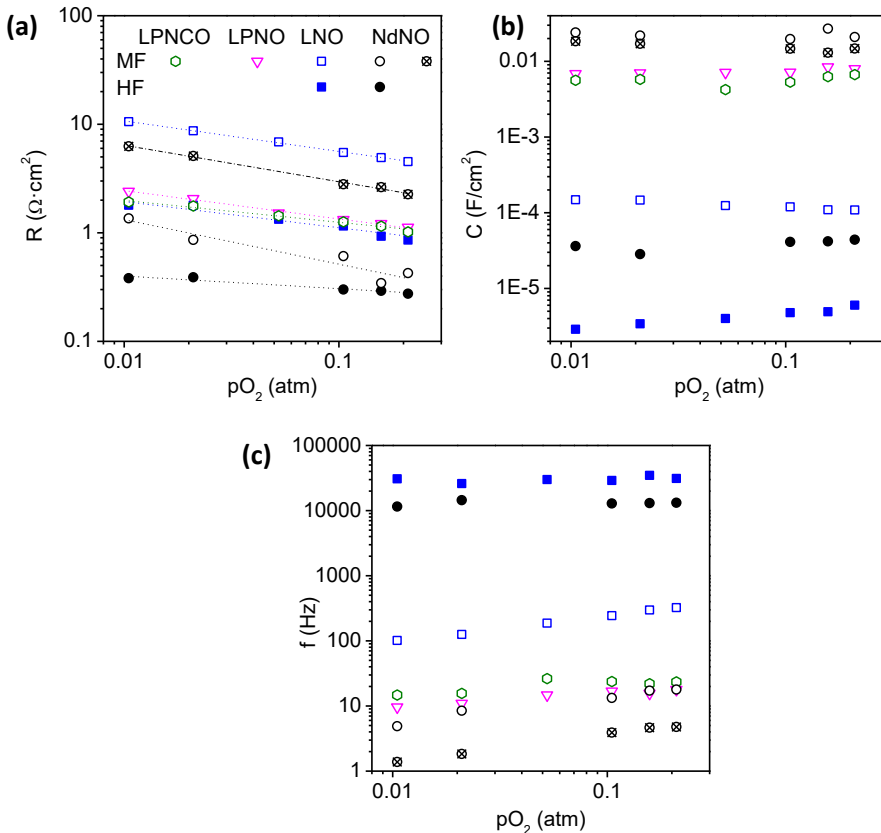


Figure 8.7: Modeled results of LNO, LPNO, LPNCO and NdNO electrodes sintered at 1150 °C; (a) resistances, (b) capacitances (c) and frequencies as a function of the pO_2 in humidified conditions.

	Electrode material			
	LNO	LPNO	LPNCO	NdNO
m_{HF}	0.24	-	-	0.11
m_{MF}	0.28	0.26	0.20	0.41/0.34

Table 8.3: m_i values from the fitting of $R_i \propto pO_2^{-m_i}$.

8.2.1.3. Influence of electrode sintering temperature

In order to further optimize cathodes performance, different sintering temperatures were analyzed. Figure 8.8 summarizes R_p of LPNCO cathode sintered at 1150 °C, 1100 °C and 1050 °C. The best performance is obtained for cathode sintered at 1050 °C ($R_p=0.62 \Omega \cdot \text{cm}^2$ at 750 °C in wet air) while the other two different temperatures result in similar performances (around $0.93 \Omega \cdot \text{cm}^2$). Additionally, when the sintering temperature of the electrode is reduced the activation energy decreases from 1.47 to 1.36 and 1.37 eV, that change can be ascribed to the higher active area for the oxygen reduction reaction. As similar impedance spectrum was obtained despite the sintering temperature, and taking into account that the total transport of the material not change, the electrode improvement can be ascribed to the higher porosity and lower grain sizes of the cathode sintered at lower temperature. Thus, the electrocatalytic surface area available for surface reactions is enlarged while the bounding among grains is preserved.

The results of EIS spectra fitting with an equivalent electrical circuit composed of $L-R_{\Omega}-R||CPE$ are plotted in Figure 8.9. The frequency at 1100 °C and 1050 °C are similar, however at 1150 °C the frequency is reduced. The same phenomenon was observed for LSM/YSZ with increasing the sintering temperature, the summit frequency of the arc decreases [27]. Furthermore, the decrease of sintering temperature reflects in the reduction of the associated capacity [27].

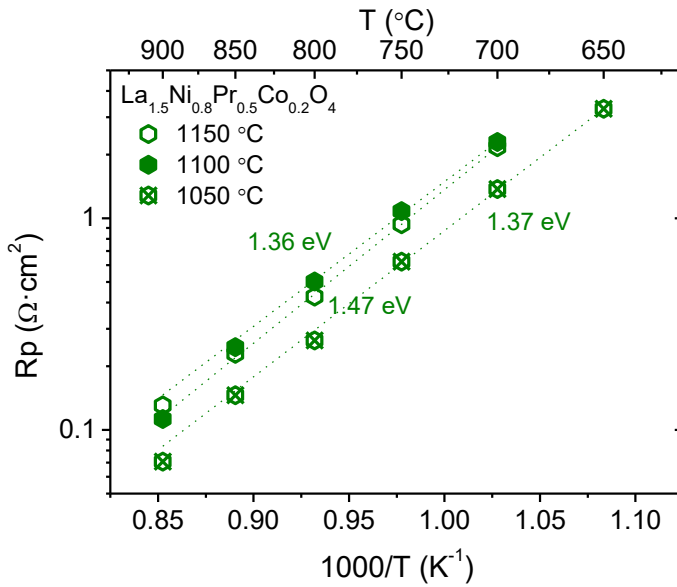


Figure 8.8: R_p as a function of $1000/T$ of $\text{La}_{1.5}\text{Pr}_{0.5}\text{Ni}_{0.8}\text{Co}_{0.2}\text{O}_{4+\delta}$ sintered at 1050 $^\circ\text{C}$, 1100 $^\circ\text{C}$ and 1150 $^\circ\text{C}$.

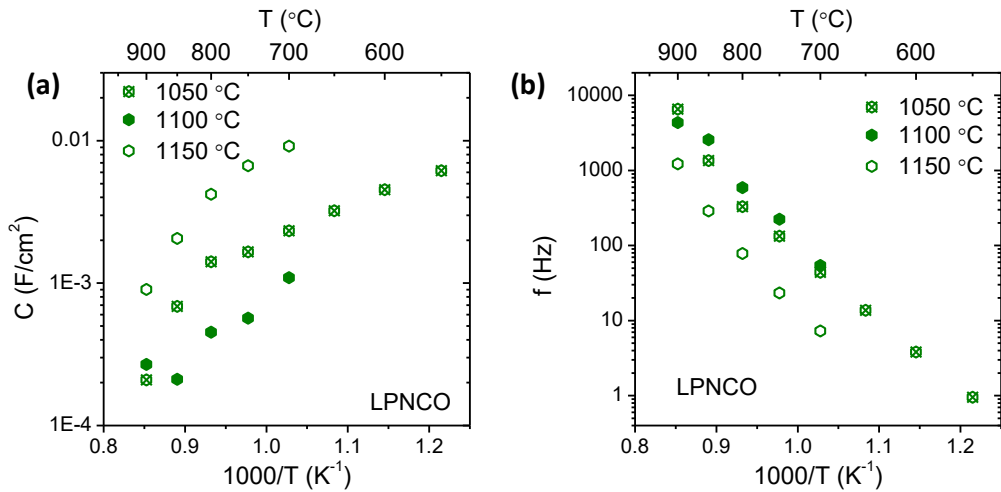


Figure 8.9: Modeled results of LPNCO electrode sintered at 1050, 1100 and 1150 $^\circ$; (a) capacitances and (b) frequencies as a function of the $1000/T$ in humidified air.

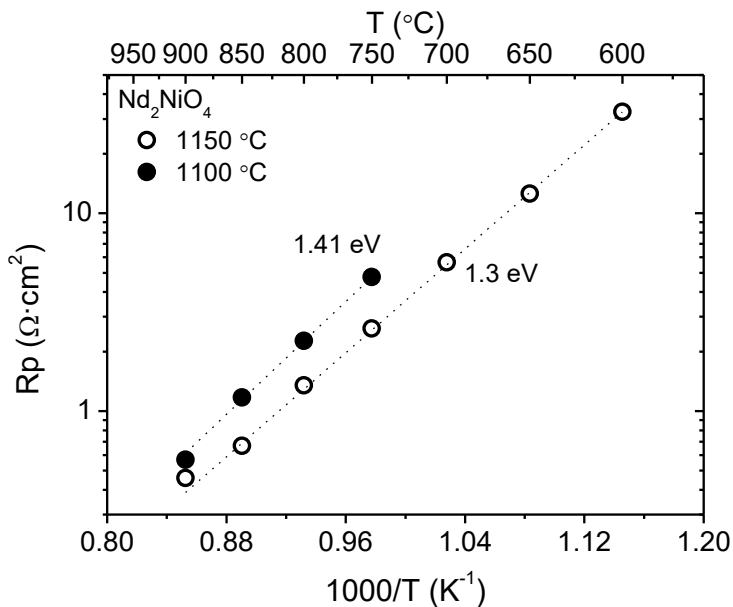


Figure 8.10: R_p as a function of $1000/T$ of $\text{Nd}_2\text{NiO}_{4+\delta}$ sintered at 1100°C and 1150°C

The cell performance is strongly affected by the electrode microstructure [28, 29]. Decreasing the sintering temperatures the TPB length can be enlarged since small grains are obtained, resulting in a lower polarization resistance. The best sintering temperature is a tradeoff between a long TPB and good electrical and optimal physical contact between electrode and electrolyte.

8.2.1.3.1. Influence of composite electrodes

In order to improve the cell performance, a composite electrode was manufactured. The cathode consisted of a mixture of the MIEC LPNO material and the electrolyte material (LWO). The volumetric ratio selected was 60:40 of LPNO:LWO [30]. With the incorporation of the protonic phase in the cathode the formation of water should not be limited to the electrode-electrolyte interface. The surface between the MIEC and LWO phases should be also active for the water formation (Figure 8.11).

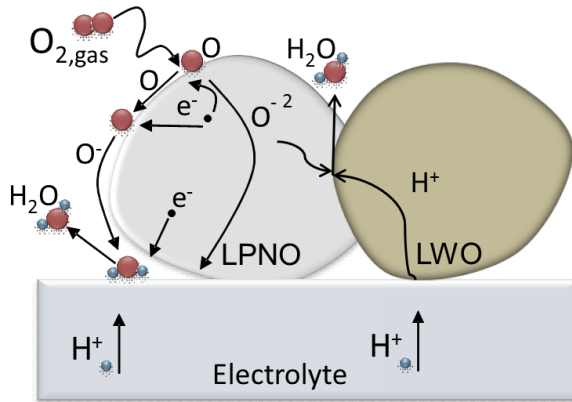


Figure 8.11: Schematic diagram of mechanisms in a MIEC/proton conductor composite cathode on a LWO proton conducting electrolyte.

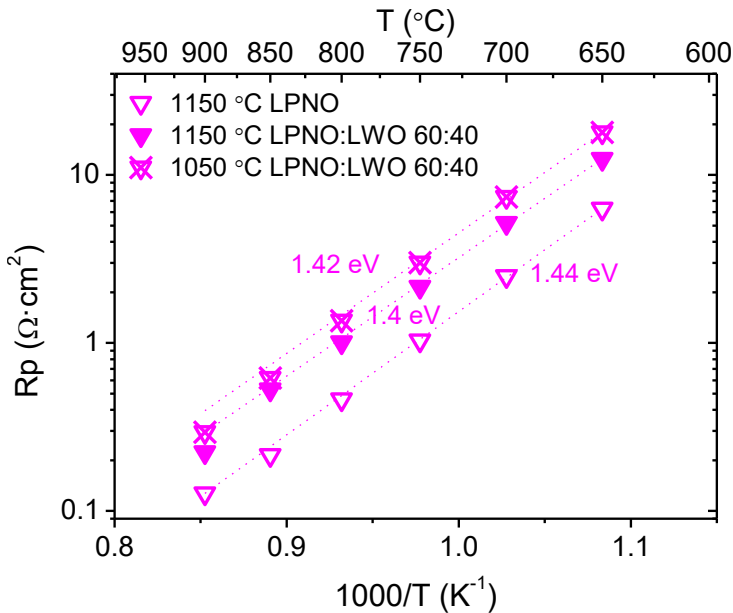


Figure 8.12: R_p as a function of $1000/T$ of LPNO sintered at 1150 and LPNO:LWO composite electrodes sintered at 1150 °C and 1050 °C.

The polarization resistance of the MIEC, and composite electrodes sintered at two different sintering temperatures in a symmetrical cell configuration are plotted as function of the operation temperature in Figure 8.12. When the protonic phase is incorporated in the electrode microstructure, the activation energy is reduced, indicating a change in mechanism. However, the polarization resistance increases for both sintering temperatures. As to shed

further light on the influence of the protonic phase incorporation, a fitting with an equivalent circuit was performed, and the results are presented in Table 8.4.

When the proton conductor is incorporated in the cathode microstructure an additional resistance appears at medium frequencies (846 Hz). As was mentioned before, above 600 °C the oxygen reduction reaction limits the cathode performance. By introducing the protonic phase, the oxygen ion and electrons conduction is restricted to the LPNO phase. Then, proton conducting phase incorporation will produce the dilution of LPNO and the reduction of the TPB, for the oxygen reduction reaction. Furthermore, the reduction of sintering temperature does not allow the improvement of the cell, probably due to the lower interaction of phases in the cathode and the worse electrode-electrolyte bonding.

Ts (°C)	LPNO:LWO vol.	RMF1 (W·cm ²)	CMF1 (F/cm ²)	fMF1 (Hz)	RMF2 (W·cm ²)	CMF2 (F/cm ²)	fMF2 (Hz)	Rp (W·cm ²)
1150	100:0	1.12	7.94·10 ⁻³	17	-	-	-	1.12
1150	60:40	1.44	3.25·10 ⁻²	3	1.11	1.68·10 ⁻⁴	846	2.55

Table 8.4: Modeled results of LPNO sintered at 1150 and LPNO:LWO composite electrode sintered at 1150 °C at 750 °C in humidified air.

Further studies should be performed in order to change the volumetric ratio and lower operation temperatures (below 600 °C) should be used to check the influence of the protonic material incorporation.

8.2.1.3.2. Dry conditions and isotopic effect influence

The influence of operation conditions were tested for all MIEC materials. All symmetrical cells were measured in wet and dry conditions. Furthermore, the isotopic effect was checked by measuring the samples in normal water (H₂O) and in heavy water (D₂O). The results will be presented separately for all materials.

8.2.1.3.2.1. La₂NiO_{4+δ}

Firstly, LNO was measured in dry and humidified conditions (H₂O and D₂O). The polarization results obtained from the EIS spectra are plotted in the Figure 8.13. When the cathode works in dry conditions the electrode performance

increases. This can be consequence of the presence of water in the TPB, affecting the oxygen reduction reaction or the water formation.

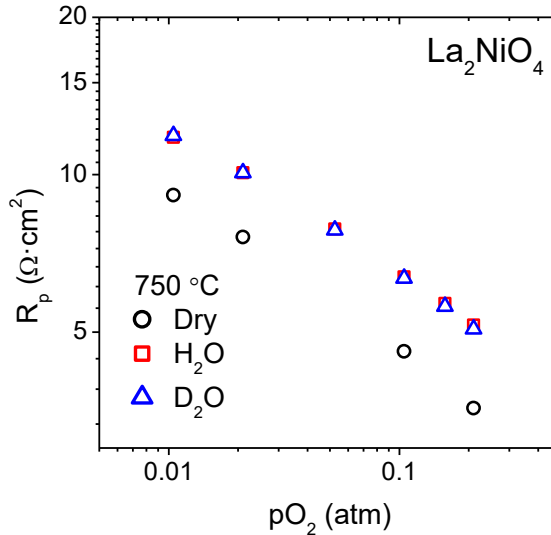


Figure 8.13: Polarization resistance of LNO as function of pO_2 in different humidified (H_2O and D_2O) and dry conditions.

The EIS spectra in the Nyquist and Bode type plots are drawn in Figure 8.14. The real resistance ascribed to the electrolyte and wires was subtracted for the direct comparison of electrodes. The shape of the EIS spectra for the three conditions is the same but the resistance that takes place at medium frequencies increases. In order to clarify the assumptions above mentioned, an equivalent electrical circuit composed of two resistances in parallel with two CPE was employed and the results are presented in Figure 8.15.

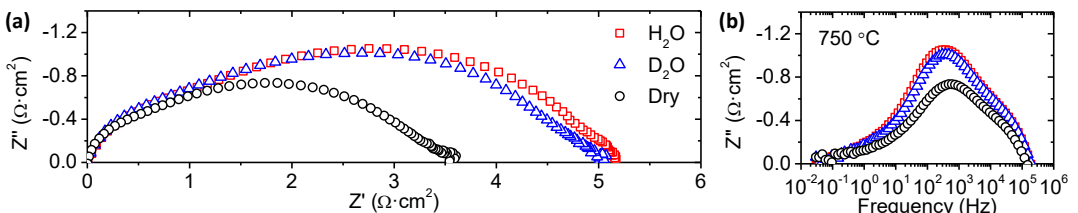
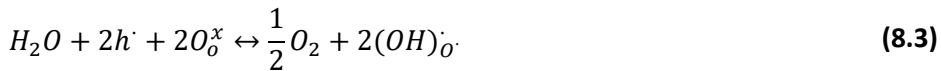


Figure 8.14: Impedance spectra, (a) Nyquist and (b) Bode plots, of $La_2NiO_{4+\delta}$ measured at $750^\circ C$ in air in different humidified (H_2O and D_2O) and dry conditions.

The resistance at high frequencies, related with the transport properties of the bulk, changes for all conditions, indicating that HF process is affected by the presence of the H₂O or D₂O. If H₂O is supposed to be incorporated in the structure, electron holes are consumed and the transport properties are worsened:



Regarding the MF, there is a reduction in the resistance when the symmetrical cell works in dry conditions (Figure 8.15 (a)) shifting to higher values the associated frequencies.

The m_i values of HF resistance obtained from the relationship of $R_i \propto \rho O_2^{-m_i}$ are 0.24, 0.38 and 0.44 for H₂O, D₂O and dry conditions, respectively. It seems that the m value with H₂O fits $\frac{1}{4}$ related with the electronic conductivity. In the case of D₂O, the limiting step at HF is related with the oxygen reduction ($m=3/8$). In that reaction ($O_{(ad)} + e^- \rightarrow O_{(ad)}^-$) electrons are involved as well. Thus, possible water incorporation could reduce the electron holes concentration.

Regarding MF processes, the m value is almost maintained (0.28, 0.28 and 0.30 for H₂O, D₂O and dry conditions, respectively), indicating that the same process takes place, but this is harmed by the presence of water or heavy water. This process is related with the ionic transport from TPB to the electrolyte, since water competes with oxygen in the TPB.

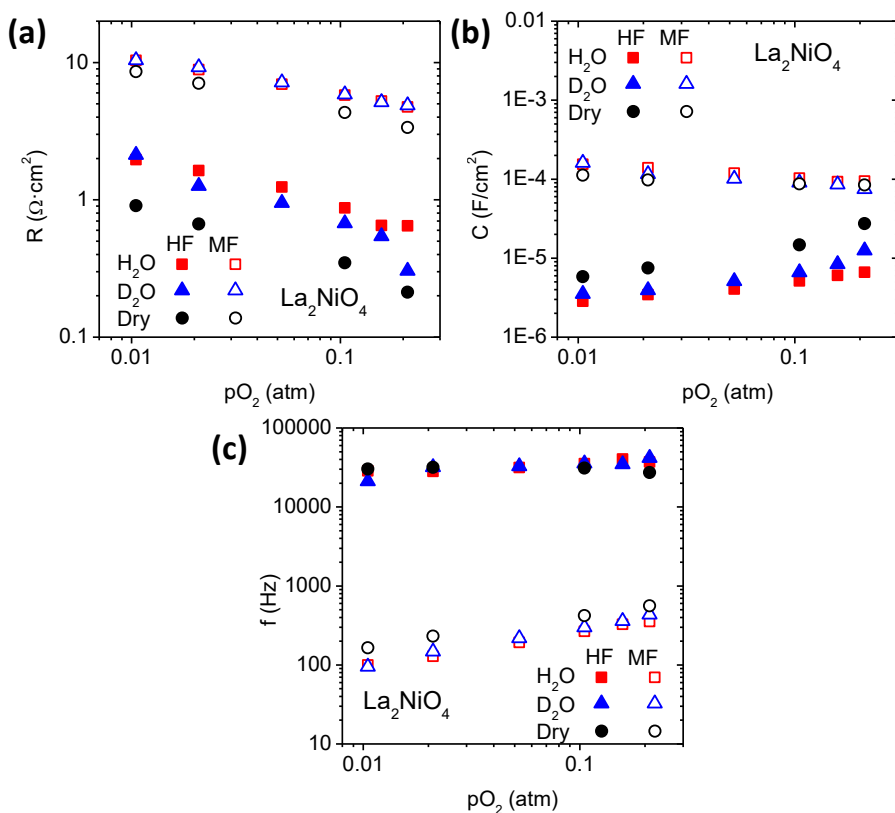


Figure 8.15: Modeled results of LNO electrode sintered at 1150 °C; (a) resistances, (b) capacitances (c) and frequencies as a function of the pO_2 in different humidified (H_2O and D_2O) and dry conditions.

8.2.1.3.2.2. $La_{1.5}Pr_{0.5}Ni_{0.8}Co_{0.2}O_{4+6}$

The same influence was tested for the double substituted nickelate. Figure 8.16 shows the results of the EIS spectra for the three conditions working in air at 750 °C. The resistance of the electrolyte was also subtracted in the electrochemical impedance spectra. In this case, the influence of the different operation conditions is totally different. When the electrode is working in humidified conditions the polarization resistance decreases. Additionally, regarding the isotopic effect, cell performance worsens when D_2O is used. As was done for the parent material (LNO), the results were fitted with an equivalent circuit, but only one resistance in parallel with a CPE was used. As the medium resistance increases, ($H_2O < D_2O < dry$), the frequency shifts to lower values and the capacity decreases in all tested oxygen partial pressure range.

These results could indicate that LPNCO exhibits some protonic conductivity, since there is an isotopic effect and the cell performance is diminished in dry conditions. Further investigation at lower temperatures should be performed in order to confirm the theory.

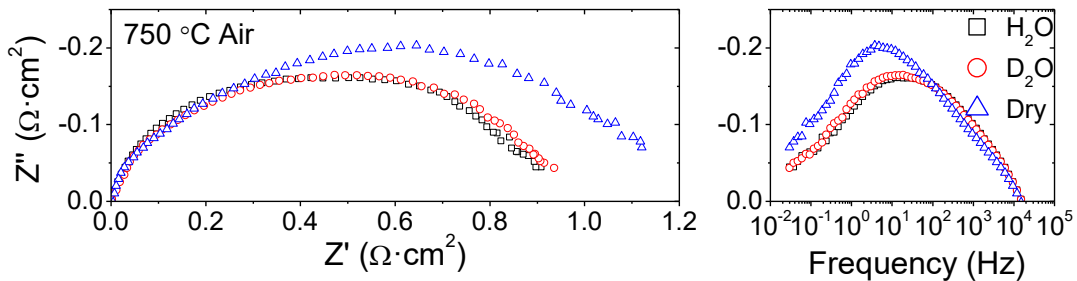


Figure 8.16: Impedance spectra, Nyquist (a) and bode (b) plots, of LPNCO measured at 750 °C in air in different humidified (H₂O and D₂O) and dry conditions.

Furthermore, the values obtained from the $R_i \propto pO_2^{-mi}$ dependence are 0.20, 0.22 and 0.21 for H₂O, D₂O and dry conditions, respectively (Figure 8.17 (a)). Thus, the limiting mechanism is the same but depending on the operation conditions the magnitude of the resistance varies. As the resistance is increasing (H₂O < D₂O < dry) the process is slower and the associated capacitance is higher.

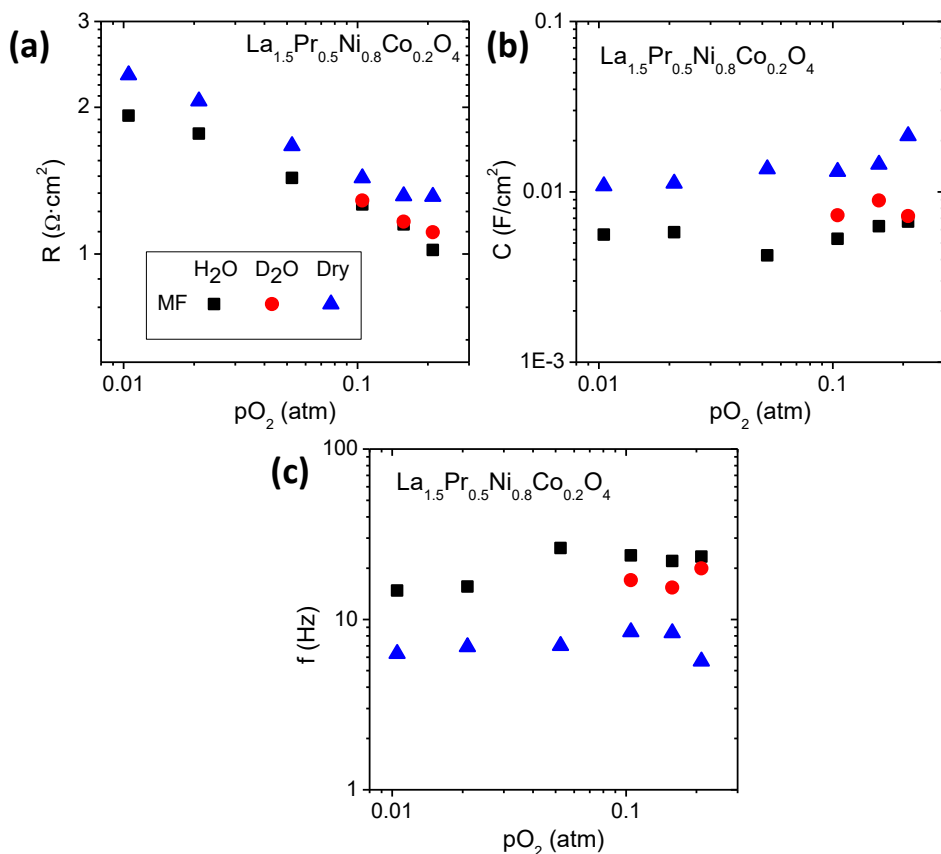


Figure 8.17: Modeled results of LPNCO electrode sintered at 1150 °C; (a) resistances, (b)capacitances (c) and frequencies as a function of the pO_2 in different humidified (H₂O and D₂O) and dry conditions.

8.2.1.3.2.3. $La_{1.5}Pr_{0.5}NiO_{4+6}$

The isotopic effect was also studied for the sample only doped with Pr in the La site. The results of the EIS measurements are plotted in Figure 8.18 (Nyquist and Bode plot), as can be seen, a slightly increase in the polarization resistance is produced when the symmetrical cell is operated with D₂O. The same phenomenon was shown in the double substituted compound (LPNCO). In order to confirm the theory, the EIS spectra were fitted to an equivalent electrical circuit with a resistance in parallel with a CPE. The resistance increases and the capacity and frequency are almost constant; indicating that

the limiting process is the same but is worsened. A small protonic conductivity can be suspected in the material doped with Pr in the La site.

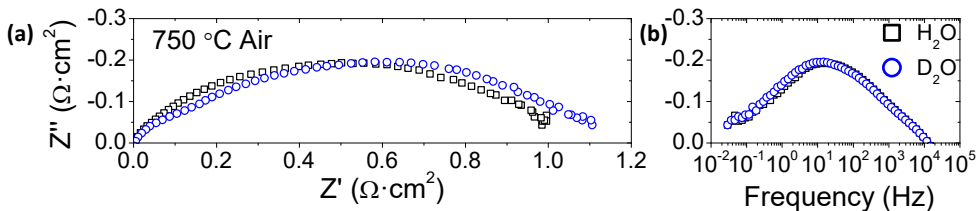


Figure 8.18: Impedance spectra, (a) Nyquist and (b) Bode plots, of LPNO electrode sintered at 1150 °C and measured at 750 °C in air in different humidified (H₂O and D₂O).

Conditions	R (W·cm ²)	C (F/cm ²)	F (Hz)
H ₂ O	1.12	7.94·10 ⁻³	18
D ₂ O	1.23	7.06·10 ⁻³	18

Table 8.5: Modeled results of LPNO sintered at 1150 °C measured in humidified air (H₂O and D₂O) at 750 °C.

8.2.1.3.2.4. Nd₂NiO_{4+δ}

NdNO electrode calcined at 1150 °C was tested at 750 °C in air in order to check the isotopic effect. As for LNO, the polarization resistance decreases when D₂O is used instead of H₂O, as it is observed in Figure 8.19.

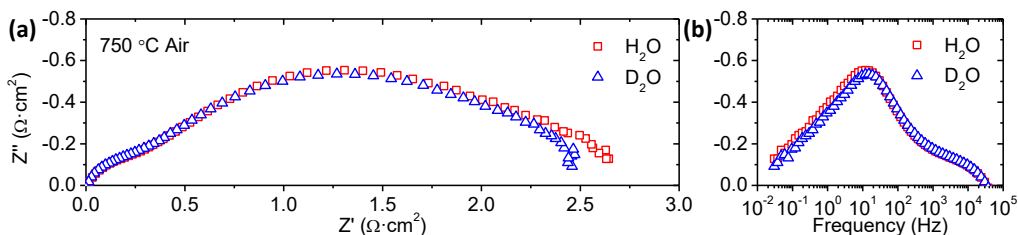


Figure 8.19: Impedance spectra, (a) Nyquist and (b) Bode plots, of NdNO electrode sintered at 1150 °C and measured at 750 °C in air in different humidified (H₂O and D₂O).

As was done in the case of the other symmetrical cells, the EIS spectra were fitted to an equivalent electrical circuit composed of three resistance in parallel with 3 CPE (Figure 8.20).

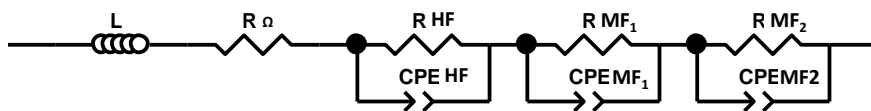


Figure 8.20: Equivalent electrical circuit used for the fitting of the NdNO EIS spectra.

Three different contributions were obtained, two at medium frequencies and another at HF. The HF and MF_1 resistances remain almost constant regardless of the humidification state, however the MF_2 resistance increases in $0.21 \text{ } \Omega \cdot \text{cm}^2$ with the presence of H_2O . The same effect was obtained for LNO. The surface reactions are negatively affected by the H_2O presence. Water competes with the oxygen molecules in the TPB and act as blocking molecules for the oxygen reduction reaction.

	RHF ($\text{W} \cdot \text{cm}^2$)	CHF (F/cm^2)	fHF (Hz)	RMF ₁ ($\text{W} \cdot \text{cm}^2$)	CMF ₁ (F/cm^2)	fMF ₁ (Hz)	RMF ₂ ($\text{W} \cdot \text{cm}^2$)	CMF ₂ (F/cm^2)	fMF ₂ (Hz)
H_2O	0.28	$4.39 \cdot 10^{-5}$	13192	0.43	0.021	18	2.26	0.015	4.76
D_2O	0.24	$6.03 \cdot 10^{-5}$	10909	0.49	0.017	19	2.05	0.011	7.19

Figure 8.21: Modeled results of NdNO sintered at $1150 \text{ } ^\circ\text{C}$ measured in humidified air (H_2O and D_2O) at $750 \text{ } ^\circ\text{C}$.

8.2.1.3.2.5. General remarks

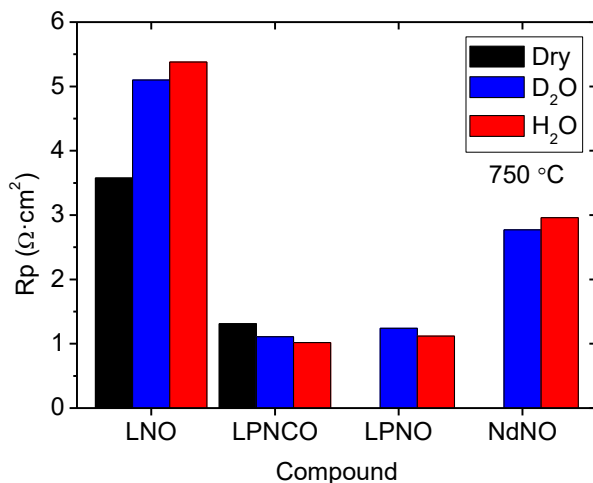


Figure 8.22: Summary of R_p in different humidified conditions at $750 \text{ } ^\circ\text{C}$ in air.

Two different behaviors were obtained for the electrode materials working in wet and dry conditions. LPNO and LPNCO apparently show a protonic effect, increasing the resistance in dry conditions. However, LNO and NdNO exhibit the opposite performance, in dry conditions or in D₂O the polarization resistance is decreased. Further studies were carried out as to shed further light.

Firstly, a thermogravimetric analysis was performed in dry conditions in order to check if the electrode materials were able to incorporate water in their structure. The experiment was done in dry air. The mass evolution was recorded with time as a function of temperature. The TGA measurements consisted of a first heating in dry air, then, the samples were cooled down in dry air and finally was heated again in the same conditions. The slope of cooling and heating was maintained in all experiment in 2 K/min. The results obtained are presented below.

The results obtained for the fresh samples show a mass reduction from 200 °C to 400 °C. However, that change cannot be observed for the samples heated again the second time. The loss in weight in the samples can be related with the presence of water in the sample, while at higher temperatures, it is related to O₂ release. In addition, that water seems to be incorporated in the structure, since if the water was outside the structure, lower temperatures (between 100 °C-200 °C) should be expected for the water evaporation. The same effect was obtained for other materials that pertain to the Ruddlesden-Popper series [31, 32].

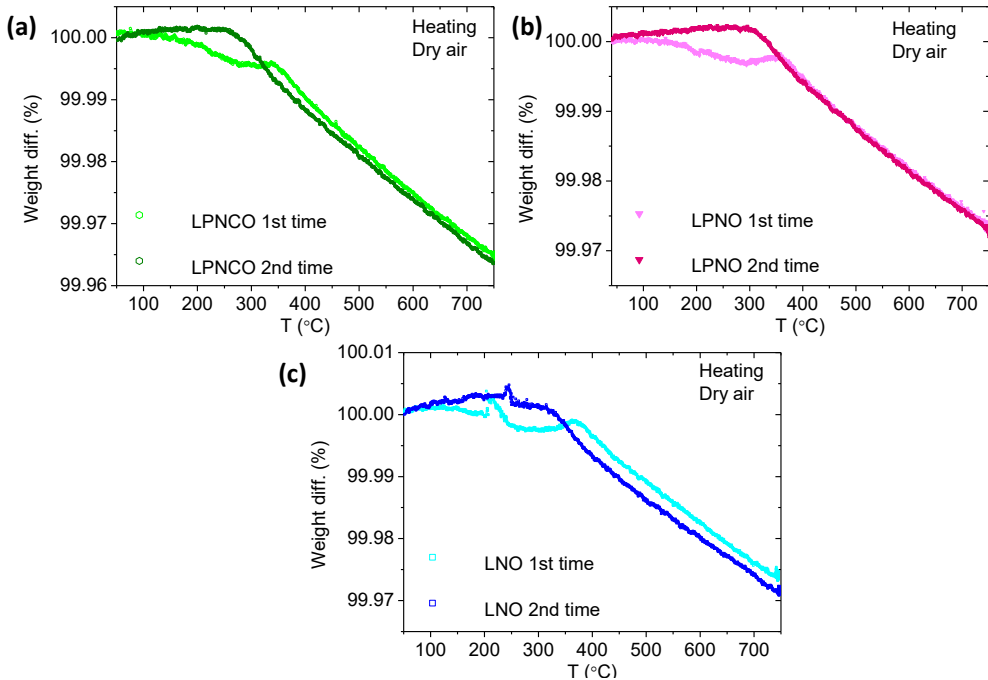
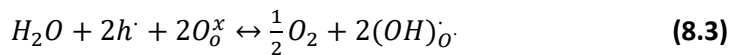


Figure 8.23: TGA results recorded in dry air when the samples were heated up, with the fresh samples (1st time) and heated again after cooled down the samples in dry conditions (2nd time).

Conductivity measurements were also carried on electrodes materials in order to understand better the results obtained in the EIS spectra. Total DC conductivity was checked for the materials in dry and wet conditions.

Two different behaviors were obtained from the conductivity measurements that fit with Rp results. NdNO shows higher conductivity in wet atmospheres at low temperatures whereas LPNO and LPNCO reduce slightly the conductivity when water is incorporated in the inlet gas. This effect suggests that water, is incorporated in the structure, and reduces the p-type conductivity:



The above results can suggest the proton conductivity of LPNO and LPNCO, as others Ruddlesden-Popper series compounds [33] and the detrimental effect of water in the NdNO and LNO performance.

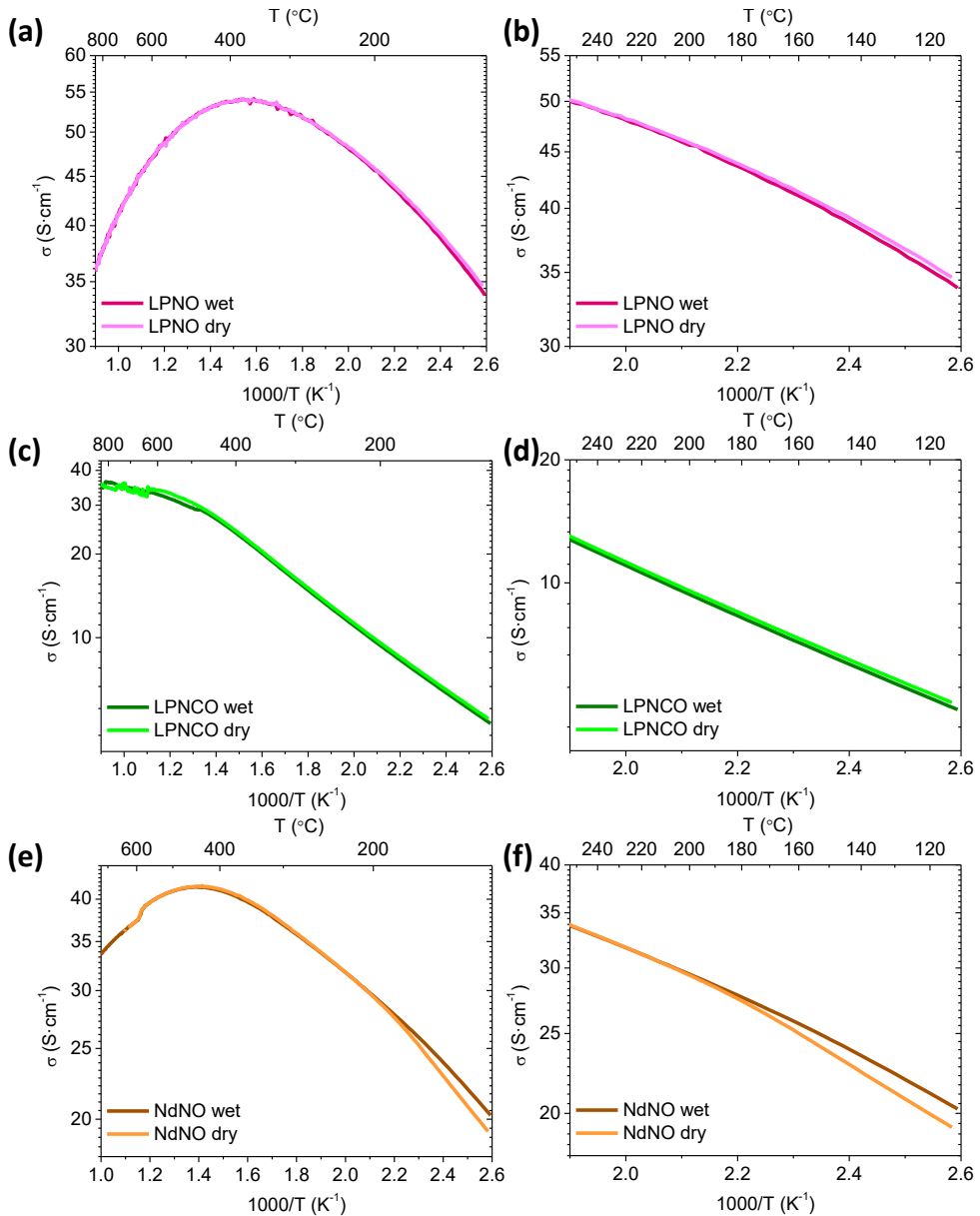


Figure 8.24: Total DC conductivity of (a) LPNO (c) LPNCO and (e) NdNO and zoom of conductivity at lower temperatures (b) LPNO (d) LPNCO and (f) NdNO in dry and wet (2.5 vol.% of H₂O) conditions.

8.3. Conclusions

$\text{La}_2\text{NiO}_{4+\delta}$ was investigated as potential cathode for PC-SOFC based on $\text{La}_{5.5}\text{WO}_{12-\delta}$ electrolyte. Once probed the chemical compatibility between cathode and electrolyte phases ($\text{La}_2\text{NiO}_{4+\delta}$ and $\text{La}_{5.5}\text{WO}_{12-\delta}$, respectively) the electrochemical properties of the cathode were improved by partially or totally substituting La and/or Ni. Specifically $\text{La}_{1.5}\text{Pr}_{0.5}\text{NiO}_{4+\delta}$ and $\text{La}_{1.5}\text{Pr}_{0.5}\text{Ni}_{0.8}\text{Co}_{0.2}\text{O}_{4+\delta}$ materials were considered and showed improved total conductivity and reduced polarization resistance, when they were tested as cathode in symmetrical cells. The microstructure optimization of $\text{La}_{1.5}\text{Pr}_{0.5}\text{Ni}_{0.8}\text{Co}_{0.2}\text{O}_{4+\delta}$ was completed by varying the firing temperature of the cathode. Additionally, a composite electrode was obtained by mixing $\text{La}_{1.5}\text{Pr}_{0.5}\text{NiO}_{4+\delta}$ with $\text{La}_{5.5}\text{WO}_{12-\delta}$. The performance of the cell increases and this was probably attributed to a non-optimal volume ratio between phases. Finally, all cathodes were tested in different conditions in order to study the H/D isotopic effect and this revealed that the incorporation of Pr in the La position gives rise to a small protonic conductivity. However, $\text{La}_2\text{NiO}_{4+\delta}$ and $\text{Nd}_2\text{NiO}_{4+\delta}$ electrodes improve their performance in dry condition, indicating that there is not a protonic conductivity.

The cathode performance of these mixed conductors was found to be limited by medium frequencies associated processes. $\text{La}_{1.5}\text{Pr}_{0.5}\text{Ni}_{0.8}\text{Co}_{0.2}\text{O}_{4+\delta}$ cathode sintered at 1050 °C exhibited the best electrochemical performance on a $\text{La}_{5.5}\text{WO}_{12-\delta}$ -based PC-SOFC, achieving $R_p=0.62 \Omega\cdot\text{cm}^2$ at 750 °C in wet air.

8.4. References

- [1] K.D. Kreuer, Annual Review of Materials Research, 33 (2003) 333-359.
- [2] H. Iwahara, Solid State Ionics, 77 (1995) 289-298.
- [3] H. Iwahara, Y. Asakura, K. Katahira, M. Tanaka, Solid State Ionics, 168 (2004) 299-310.
- [4] W.G. Coors, Journal of Power Sources, 118 (2003) 150-156.
- [5] N. Bonanos, B. Ellis, M.N. Mahmood, Solid State Ionics, 44 (1991) 305-311.
- [6] J.M. Serra, W.A. Meulenbergh, J. Am. Ceram. Soc., 90 (2007) 2082-2089.
- [7] N. Bonanos, K.S. Knight, B. Ellis, Solid State Ionics, 79 (1995) 161-170.
- [8] S. Escolastico, M. Ivanova, C. Solis, S. Roitsch, W.A. Meulenbergh, J.M. Serra, Rsc Advances, 2 (2012) 4932-4943.
- [9] R. Haugrud, T. Norby, Nature Materials, 5 (2006) 193-196.

- [10] R. Haugrud, C. Kjolseth, *Journal of Physics and Chemistry of Solids*, 69 (2008) 1758-1765.
- [11] C. Solis, S. Escolastico, R. Haugrud, J.M. Serra, *Journal of Physical Chemistry C*, 115 (2011) 11124-11131.
- [12] S. Escolastico, C. Solis, J.M. Serra, *Solid State Ionics*, 216 (2012) 31-35.
- [13] S. Escolastico, V.B. Vert, J.M. Serra, *Chemistry of Materials*, 21 (2009) 3079-3089.
- [14] R.R. Peng, T.Z. Wu, W. Liu, X.Q. Liu, G.Y. Meng, *J. Mater. Chem.*, 20 (2010) 6218-6225.
- [15] A. Grimaud, F. Mauvy, J.M. Bassat, S. Fourcade, M. Marrony, J.C. Grenier, *Journal of Materials Chemistry*, 22 (2012) 16017-16025.
- [16] J.S. M. Ivanova, J. M. Serra, C. Solis, W. A. Meulenberg, W. Fischer, S. Roitsch, H.-P. Buchkrmer, *Chemistry and Materials Research*, 2 (2012) 56.
- [17] J.M. Serra, V.B. Vert, *Journal of the Electrochemical Society*, 157 (2010) B1349-B1357.
- [18] J.M. Serra, V.B. Vert, *ChemSusChem*, 2 (2009) 957-961.
- [19] M.A. Laguna-Bercero, A.R. Hanifi, H. Monzón, J. Cunningham, T.H. Etsell, P. Sarkar, *Journal of Materials Chemistry A*, 2 (2014) 9764-9770.
- [20] A. Egger, E. Bucher, W. Sitte, *J. Electrochem. Soc.*, 158 (2011) B573-B579.
- [21] S.B. Adler, *Chem. Rev.*, 104 (2004) 4791-4843.
- [22] E. Fabbri, L. Bi, D. Pergolesi, E. Traversa, *Energy & Environmental Science*, 4 (2011) 4984-4993.
- [23] F. He, T.Z. Wu, R.R. Peng, C.R. Xia, *Journal of Power Sources*, 194 (2009) 263-268.
- [24] D. Pergolesi, E. Fabbri, A. D'Epifanio, E. Di Bartolomeo, A. Tebano, S. Sanna, S. Licocchia, G. Balestrino, E. Traversa, *Nat Mater*, 9 (2010) 846-852.
- [25] R. Baker, J. Guindet, M. Kleitz, *Journal of the Electrochemical Society*, 144 (1997) 2427-2432.
- [26] C. Solis, L. Navarrete, F. Bozza, N. Bonanos, J.M. Serra, *ChemSusChem*, Submitted.
- [27] M.J. Jorgensen, M. Mogensen, *J. Electrochem. Soc.*, 148 (2001) A433-A442.
- [28] L. Baqué, A. Caneiro, M.S. Moreno, A. Serquis, *Electrochem. Commun.*, 10 (2008) 1905-1908.
- [29] K. Chen, N. Ai, C. Lievens, J. Love, S.P. Jiang, *Electrochem. Commun.*, 23 (2012) 129-132.
- [30] C. Solís, L. Navarrete, S. Roitsch, J.M. Serra, *J. Mater. Chem.*, 22 (2012) 16051-16059.
- [31] M. Matvejeff, M. Lehtimäki, A. Hirasu, Y.H. Huang, H. Yamauchi, M. Karppinen, *Chem. Mat.*, 17 (2005) 2775-2779.

[32] N.A. Tarasova, I.E. Animitsa, *Russian Journal of Electrochemistry*, 51 (2015) 401-405.

[33] Z. Wang, W. Yang, S.P. Shafi, L. Bi, Z. Wang, R. Peng, C. Xia, W. Liu, Y. Lu, *Journal of Materials Chemistry A*, 3 (2015) 8405-8412.

9

**Cer-cer cathodes for
PC-SOFC**

9. Cer-cer cathodes for PC-SOFC

9.1. Introduction

Different proton conduction materials have been investigated as promising electrolytes for PC-SOFCs [1-4], and depending on the selected electrolyte material, compatible cathodes have to be developed. Recent works on PC-SOFC cathode performance have shown that the addition of a protonic conducting phase, normally the same material used as electrolyte, to a mostly electronic conducting cathode enables an important improvement of the electrochemical performance. This positive effect is ascribed to the fact that the protonic phase allows extending the three phase boundary (TPB) area from the electrode–electrolyte interface to the whole thickness of the cathode [5-11]. Furthermore, as the electrolyte material is part of the composite cathode, the electrode adhesion is improved and the thermal expansion coefficient (TEC) between the electrode and electrolyte is better adjusted and, therefore, improved mechanical properties and resistance to thermal cycling are generally attained.

Ceramic-ceramic (cer-cer) composites based on mixtures of different kinds of conducting materials, as, for instance, an electronic and a protonic conductor, have shown improved performances in proton conducting solid oxide fuel cells (PC-SOFC) cathodes operating at intermediate temperatures (500 °C-700 °C) [5-7, 9, 11, 12]. The present chapter aims to develop active cathodes for PC-SOFCs based on LWO electrolytes.

The electronic material LSM has been widely studied as cathode in Solid Oxide Fuel Cells. LSM exhibits a high electronic conductivity at high temperatures [13], conferring a good performance. However as has been explained in the first chapters of the present thesis, this type of material limits the TPB to the electrode–electrolyte interface. It seems that a second phase (LWO) incorporation will improve the cell performance, since the TPB length will be enlarged along the electrode (Figure 9.1). The studied cathodes in the present thesis comprise mixtures of two phases, *i.e.*, LSM as the main electronic conducting phase and electrocatalyst, and LWO as a proton conducting phase.

The electrochemical performance was optimized by studying the effect of the LSM–LWO ratio and sintering temperatures.

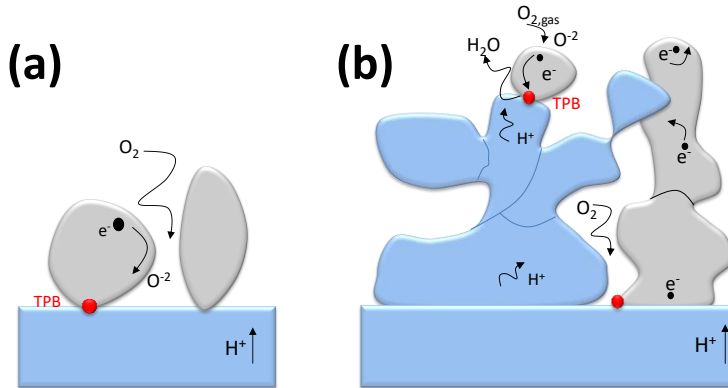


Figure 9.1: Scheme of the electrode mechanisms in (a) a pure electronic electrode and (b) in an electronic and protonic conductor cer-cer electrode.

However, the operation of this composite cathode is limited by surface processes. Reaction rate of surface steps can be significantly enhanced by tailoring their catalytic activity through the electrode surface impregnation with intrinsically catalytic nanoparticles, as was observed for LSM-GDC electrode.

The catalytic activity of different SOFC cathodes has been significantly improved by introducing catalytic nanoparticles such as Ag [14], $\text{Pr}_{0.6}\text{Sr}_{0.4}\text{CoO}_3$ [15], $\text{Ce}_{0.8}\text{Y}_{0.2}\text{O}_{1.9}$ [16] and CeO_2 and Co_3O_4 [17]. Furthermore, cathodes for PC-SOFCs based on doped barium cerate ($\text{BaZr}_{0.1}\text{Ce}_{0.7}\text{Y}_{0.2}\text{O}_{3-\delta}$) backbones have also been infiltrated with catalytic $\text{Sm}_{0.5}\text{Sr}_{0.5}\text{CoO}_{3-\delta}$ showing improved and stable performances, that enables lowering the operating temperatures [18]. 20% samarium-doped ceria (SDC) was selected as nanocatalyst. When this sintered cathode is infiltrated with SDC catalytic particles, two major effects are expected, *i.e.*, (1) new oxide-ion conduction pathways are generated on the electrode surface and (2) the overall catalytic processes are improved due to the high dispersion and the intrinsically higher catalytic redox activity of the SDC particles, compared with LSM and LWO. Indeed, ceria sites are known to

be active for oxygen reduction reaction and to boost molecular oxygen adsorption/desorption process [19].

9.2. Results and discussion

9.2.1. Compatibility test

The state-of-the-art cathode material (LSM) in SOFC was selected as starting point for the manufacture of PC-SOFC cathode. Firstly, the compatibility with the electrolyte material selected (LWO) was checked by XRD upon a heat treatment. For that purpose both powders: LSM and LWO were physically mixed, and XRD measurements were performed before calcination (at room temperature (RT)) and after 5 hours at 1150 °C. Figure 9.2 shows the XRD spectra of LSM/LWO 50% vol. at room temperature and after calcination at 1150 °C for 5 hours. XRD patterns of the single LWO sintered at 1300 °C and LSM sintered at 900 °C are also included. As can be ascribed from Figure 9.2 the cubic (LSM) and fluorite phase (LWO) are maintained after the annealing time. Furthermore, not extra peaks ascribed to secondary phase were detected in the limit of the XRD equipment detection. Thus, the compatibility is proved for the LSM and LWO mixture.

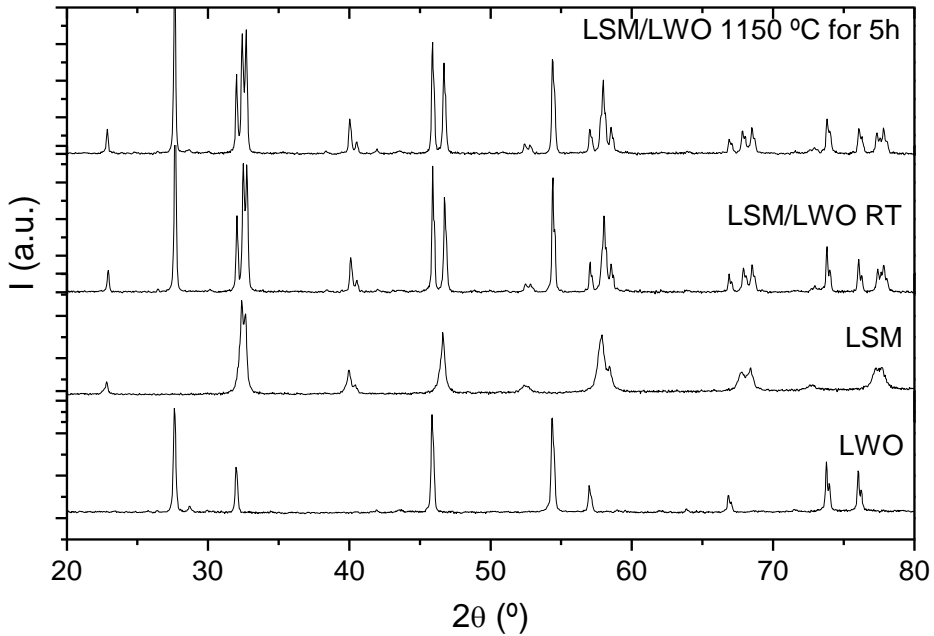


Figure 9.2: XRD pattern of LWO and LSM phases, mixture of LSM and LWO at room temperature and after calcination at 1150 °C for 5h.

9.2.2. Electrochemical characterization

9.2.2.1. Cathode sintering temperature influence

9.2.2.1.1. Microstructure characterization

First, LSM was tested as cathode on LWO and the calcining temperature selected was 1050 °C. Then, the second phase LWO was added, for that purpose both powders were mixed in 50 % in volume. The electrode ink was prepared by mixing terpeneol, ethyl cellulose and LSM and LWO powders. Homogenization of ink was done by a three roll milling. Finally, LSM/LWO ink was screenprinted on both sides of a fully dense LWO electrolyte and calcined at 1050 °C.

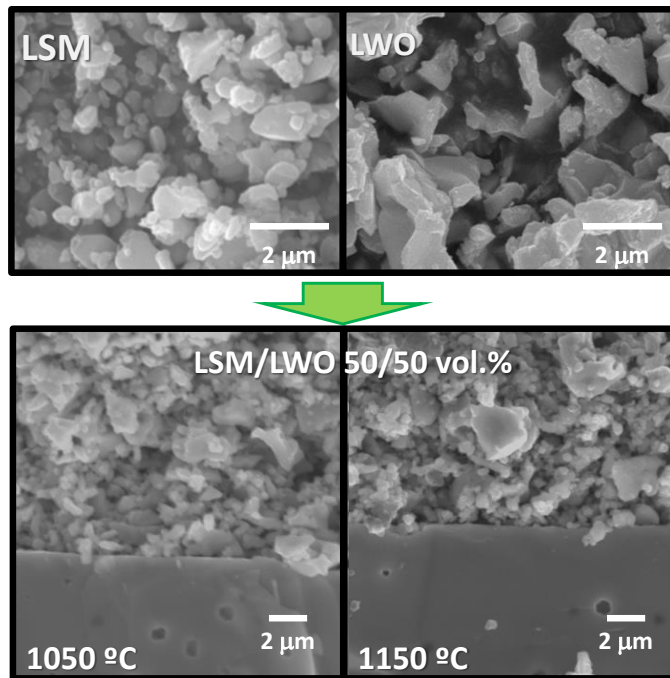


Figure 9.3: SEM images of LSM and LWO powders (top of the image) and LSM/LWO cer-cer cathode 50/50 vol. % (bottom of the image) sintered at 1050 °C and 1150 °C.

As the microstructure of the cathodes constitutes a key factor for the correct fuel cell performance, the sintering temperature was varied in order to analyze resulting differences. The sintering temperature should be enough to achieve a good adhesion between electrode and electrolyte, but not too high to ensure a sufficient porosity for gas diffusion. Hence, the sintering temperatures tested were 1050 °C and 1150 °C. Figure 9.3 presents the SEM micrographs corresponding to the initial powders for the cathode preparation, LSM and LWO, and the 50 vol. % LSM/LWO cer-cer cathodes sintered at 1050 and 1150 °C. LSM and LWO powders present similar grain size suitable for mixing them for the composite manufacture. From the cross-section image of the symmetrical cells, similar porosity of both electrodes can be observed, being enough for the gas diffusion. Furthermore, the high density of the electrolyte is also confirmed from the SEM images.

In addition, TEM images of the electrode calcined at the highest temperature were done in order to check the electrode-electrolyte interface. TEM images of

the cross section of LSM calcined at 1150 °C on LWO with the combination of three Energy Disperse X-Ray spectroscopy (EDX) spectra acquired in different sample regions are shown in Figure 9.4. On the left-hand side a part of the FIB-lamella shows the interface of LWO and LSM. A magnification of the interface is shown on the right-hand side. For both images, LWO is on left-hand side, whereas the LSM is on right-hand side. The EDX spectra were taken at three different positions and are indicated by numbers in the image. Spectrum 1 corresponds to the LWO region whereas the spectrum 2 was taken in the interface and spectrum 3 was acquired in the LSM side. Spectrum 1 and 3 show only the composition of LWO and LSM, respectively. However, spectrum 2 indicates that these particles mainly consist of LWO and only a small amount of Mn (2-3 at. %) is found. Some Mn cations might have diffused into the first grain of LWO layer or this can be result of the measuring inaccuracy or scattered radiation from the LSM phase. Thus, TEM analyses suggest good compatibility and adhesion between both phases.

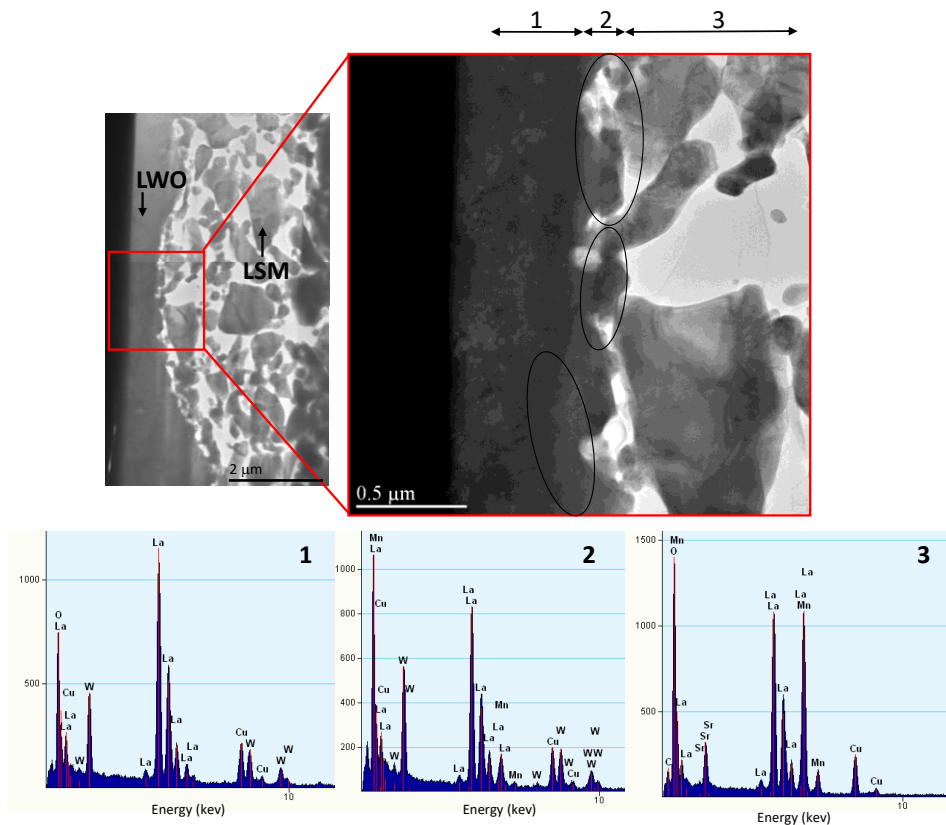


Figure 9.4: TEM images and EDX spectra of a FIB-lamella showing the cross section of a LSM cathode on the electrolyte calcined at 1150 °C.

9.2.2.1.2. Electrochemical analysis of cer-cer cathodes sintering temperature

After the compatibility study of phases, the electrochemical properties of the different firing temperatures of the cer-cer cathode were studied by using symmetrical cell configuration. Figure 9.5 shows the polarization resistance (R_p) recorded in wet (2.5% vol.) air as a function of temperature in an Arrhenius arrangement plot. The addition of the proton conductor material can reduce the polarization resistance in all range of temperatures (LSM/LWO 50/50 vol. 1050 °C). As was suggested above, the introduction of the proton conducting material can enlarge the TPB to the electrode thickness (Figure 9.1) and increase the performance of the electrode, as is shown in Figure 9.5 for all temperatures tested. Additionally, the electrode sintering temperature was

increased in order to check the influence on the polarization resistance of the cathode. Then, the same electrode mixture (50% in volume of each phase) was calcined at higher temperature; 1150 °C. It seems that higher temperature allows a better contact between phases in the electrode and also with the electrolyte material, keeping the microstructure for a good gas diffusion (Figure 9.3). In all cases, the activation energy is close to the parent LSM electrode [20].

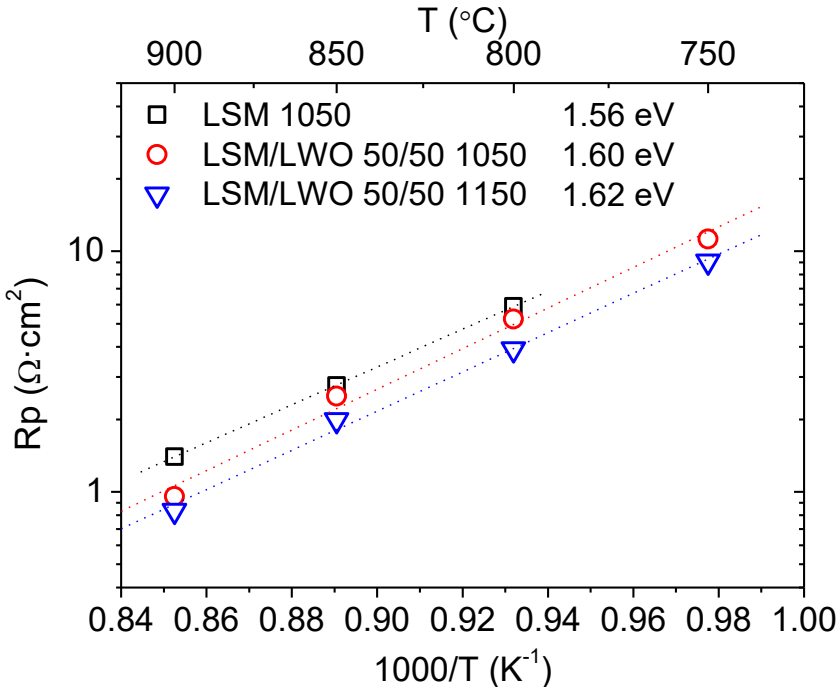


Figure 9.5: Polarization resistance as function of the temperature in wet air (2.5% vol. H₂O). Activation energy values are written on the right.

In order to check which processes were improved by the introduction of the proton conductor material, the EIS spectra results were fitted by an equivalent circuit. The best electrode and the reference electrode (LSM) fitting results are shown in Figure 9.7. The circuit was composed by three resistances in series in parallel with three constant phase elements:

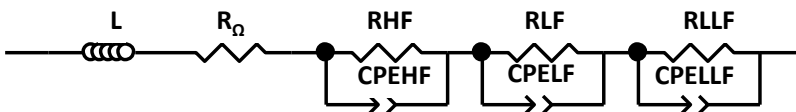


Figure 9.6: Equivalent electrical circuit used for the fitting of the EIS spectra.

Where L is the inductance ascribed to the wires and EIS device, R_{Ω} is the resistance associated with the real resistance of the electrolyte and wires and the three $R||CPE$ related with the limiting steps in the cathode; low (LF), low-low (LLF) and high frequencies (HF).

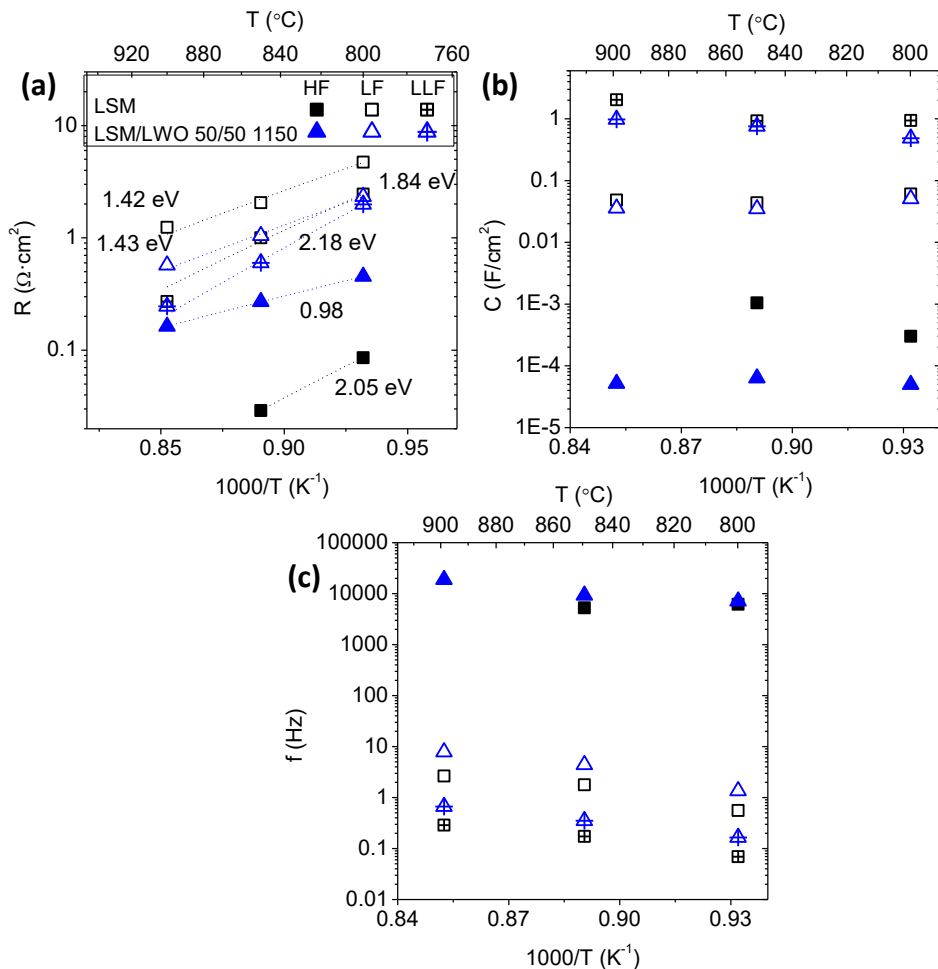


Figure 9.7: Results of the equivalent electrical circuit (a) resistances, (b) capacitances and (c) the related frequencies of the LSM and LSM/LWO composite in wet air as function of the temperature.

Figure 9.7 presents the obtained circuit parameters: (a) the modelled resistance (b) the pseudo-capacitance and (c) the frequency. Although there are significant dissimilarities between LSM and the composite cathode, the highest resistance values are found for LF processes in both electrodes in all

range of temperatures. However, the introduction of the proton conductor in the cathode originates the reduction in terms of resistance at LF. Furthermore, the LLF resistance is also reduced with the composite electrode in all range of operation temperature tested. In addition, the capacities of the low and low-low frequencies for both samples are very similar and the activation energy are almost the same, indicating that the limiting processes are equal for both samples, but can be improved by the proton conductor phase incorporation. The capacitance of LLF has a value associated between 0.5 to 2 F/cm². Whereas the LF capacitance is in between of 0.03 and 0.07 F/cm². Similar resistances and capacitances have been observed in other composite cathodes for conventional SOFCs and they have been assigned to adsorption and dissociation of oxygen molecules on the surface of the electrode [21].

Finally, the resistance at high frequencies (>7000 Hz) increases by introducing proton pathways. This phenomenon can be consequence of the dilution of the electronic phase, since the electronic conductivity of LWO is negligible, then the electrons paths are reduced. Usually, the quickest process as electrons transport takes place at high frequencies.

Sunde *et al.*, [22] studied the influence of different parameters in the impedance spectra of composite materials by computer modeling, having in mind the different types of interfaces created in composite electrodes. These calculations were carried out for anode composites, but the general remarks can be extrapolated to any electronic/ionic or protonic composite electrode, like the LSM/LWO cathode in this work.

Different types of interface can appear when electronic and protonic phases are mixed in the same electrode since each well dispersed phase can form a cluster (Figure 9.8): Type I is an interface formed between two clusters both ends of them are connected to both ends of the composite, *i.e.*, current collector and electrolyte. In Type II interface, clusters are connected to their corresponding bulk phase but not to the other. Type III interface presents at least one of the phases not connected to the corresponding bulk phase [23]. Types I and II will reduce the overall electrode resistance [22], but Type III will increase the polarization resistance of the electrode. The lack of percolation in

the electrode can affect the impedance and most likely appears at high frequency in the impedance spectra [22, 23].

It can be expected that the main interfaces found in electrodes with high distribution of both phases, as the LSM and LWO in the present thesis, should be like Type III or II. Thus, the HF contribution that appears for the composite electrode, suggests the presence of Type III interfaces.

Additionally, Jorgensen *et al.*, [21] discussed the possible reasons of the different arcs in a composite material electrode. They suggested that the arcs at high frequency can be originated for the transport of ions and intermediates in composite interfaces and can be minimized by ensuring the good percolation of both phases in the electrode. With this purpose different LSM/LWO ratios were studied and will be presented in the following section.

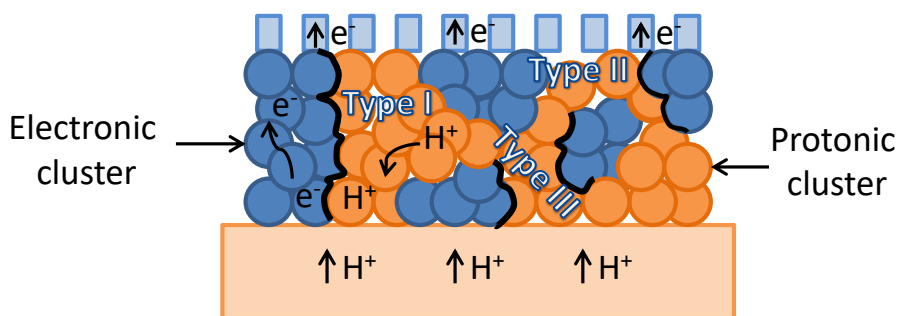


Figure 9.8: Type of clusters that can be originated in a composite electrode.

9.2.2.2. Influence of volume ratio on the electrode performance

Different LSM and LWO ratios were studied by calcining the electrode at 1150 °C. The polarization resistance results of the different electrodes working on LWO in a symmetrical cell configuration are plotted in Figure 9.9. As can be ascribed from the graph, the best electrode is the composite LSM/LWO 60/40 in volume, but exhibits the highest activation energy. Additionally, at low temperatures (750 °C) the polarization resistance value obtained for the composites with a ratio of 60/40 and 40/60 in volumes are very similar.

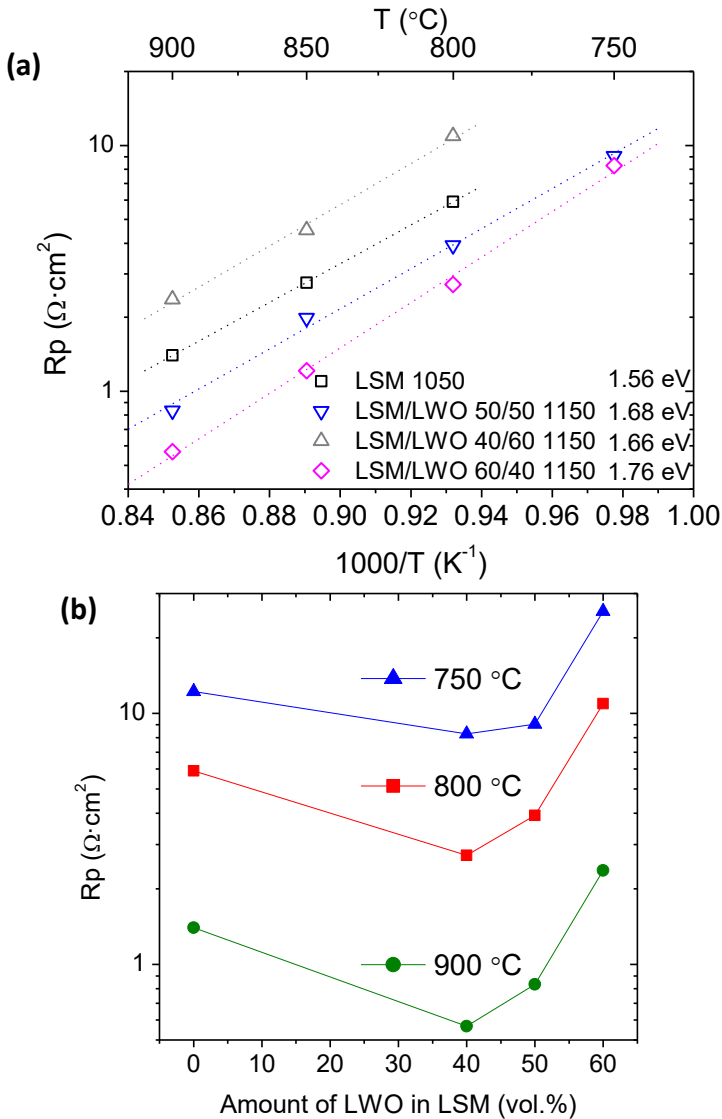


Figure 9.9: Polarization resistance as function of the LSM and LWO ratio in wet air (a) as function of the temperature and (b) as function of the phase's ratio.

On the other hand, when the addition of the protonic phase is higher than 50 vol. % (LSM/LWO 40/60) the polarization resistance is worsened with regard to the LSM electrode. This drop in the cathode electrochemical performance has been attributed for other cer-cer protonic cathodes to: (1) a restriction in the active electrode thickness due to the limited protonic conductivity of LWO particles, (2) the lower TPB length of this composition compared to that of the

optimum LSM/LWO ratio, and (3) a possible limitation of the electronic conductivity due to the lack of sufficient connectivity among LSM particles, due to the negligible electronic conductivity of LWO [11]. Thus, the limitations can be ascribed to the reduction of the TPB length and the threshold is not achieved with 40 % vol. of LSM.

In order to compare how the addition of the different phases affects the performance of the cell, the electrochemical impedance spectra of the different LSM/LWO volumetric ratios is plotted in Figure 9.10 (Nyquist and Bode plots). The spectra were recorded at two temperatures in wet air (2.5 vol. %).

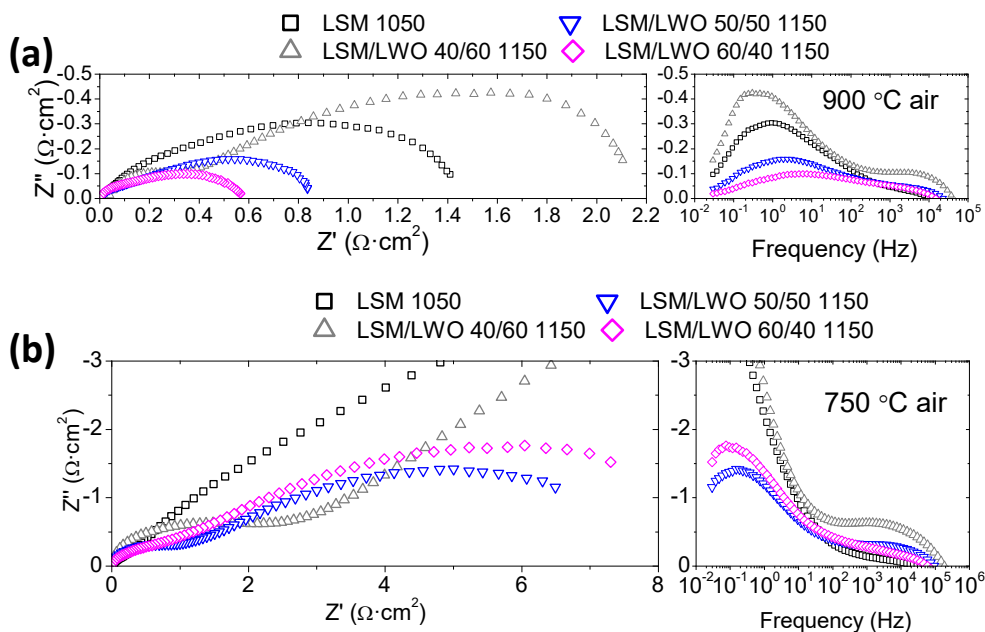


Figure 9.10: Nyquist and bode plot, left and right, respectively, of the different composites electrodes tested at (a)900 °C and (b)750 °C in wet air.

From these graphs at least two different contributions (two separated arcs) can be distinguished, one at LF and the other at HF. The behavior of the high frequency arc is maintained for both temperatures. As higher the proton phase volume, higher the resistance at high frequencies. Thus, at HF and from the lowest to highest contribution; LSM < LSM/LWO 60/40 < LSM/LWO 50/50 < LSM/LWO 40/60. As was suggested before, the HF resistance is originated from

charge carrier transport and ions and/or proton between the interfaces of different phases, and more likely to the transport of electrons in the electrode.

Regarding LF contributions, all electrodes seem to be principally limited by LF surface-associated processes as can be inferred from the higher magnitude of this arc. Additionally, the incorporation of the proton phase mainly affects the low frequency arcs. For instance, when LWO is introduced with a volume ratio higher than 50 % the LF arc increases, being higher than the pure electronic material. However, the LF LSM electrode resistance can be halved when 50 % or 40 % in volume of LWO is mixed in the electrode. The LF arc decreases as consequence of the higher available TPB length in the thickness of the cathode, due to the protonic phase incorporation, and thanks to the newly introduced protonic pathways. As a consequence, the LSM electrode is limited by LF processes and nearly no HF contribution is observed at some temperatures (Figure 9.7 and Figure 9.10). This behavior is associated with the lower TPB available for the surface reactions.

9.2.2.3. LSM/LWO 60/40 % v/v electrode limiting mechanisms

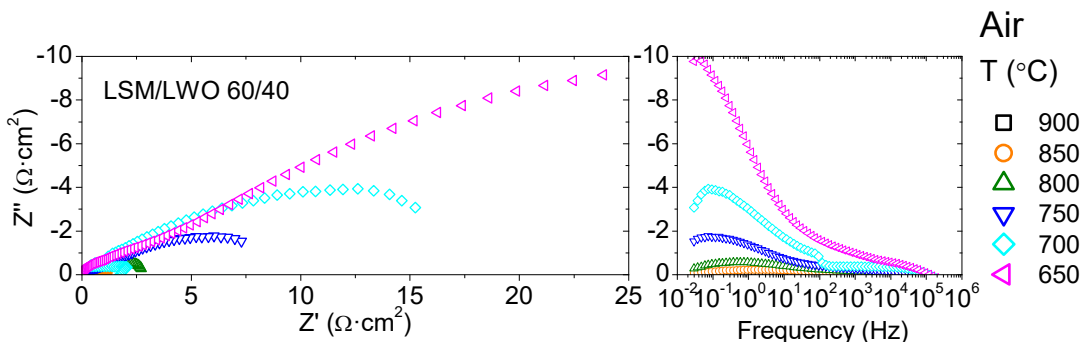


Figure 9.11: Nyquist and bode plot, left and right, respectively of LSM/LWO 60/40 composite cathode as function of the temperature in wet air.

After the different tests, it was found that the best electrode in the operation temperature range was LSM/LWO 60/40. Then, in the next section is going to explain the nature of the limiting steps in the electrode performance and the optimization of the electrode will be carry out by tailoring some of its properties.

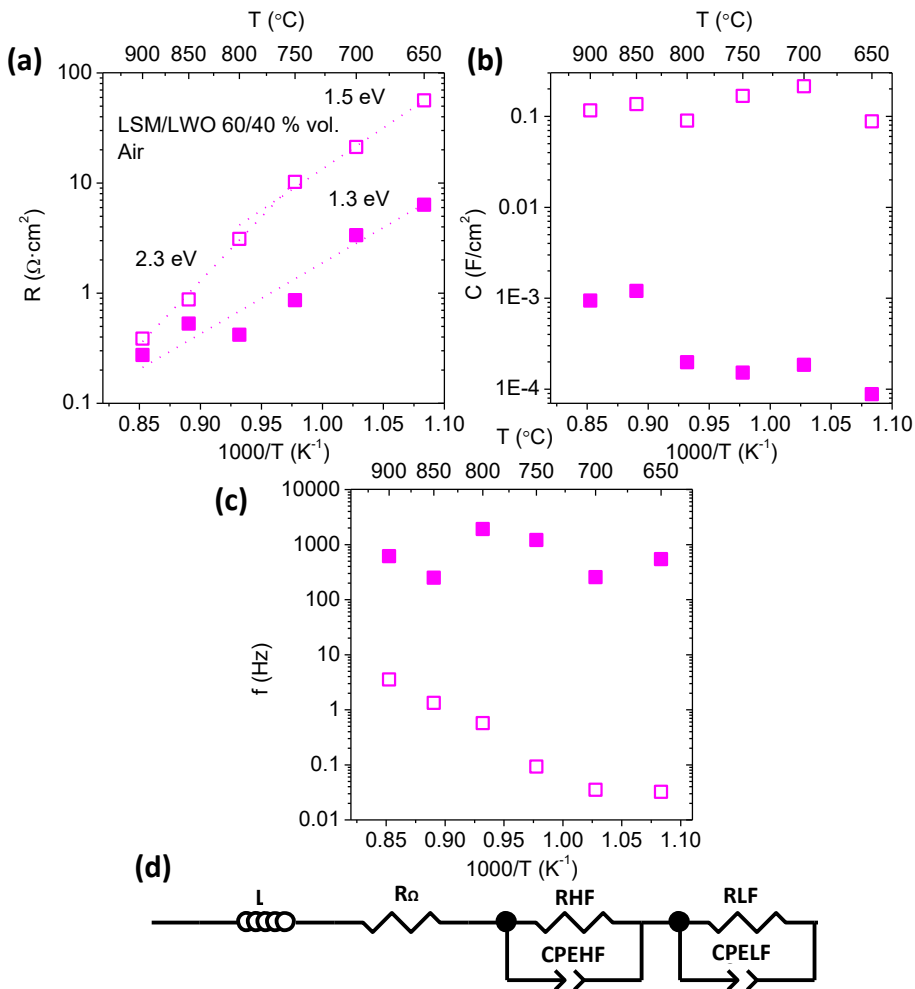


Figure 9.12: Results of the equivalent electrical circuit fitting of LSM/LWO 60/40 electrode as function of the temperature in wet air; (a) resistances, (b) capacitances and (c) associated frequencies.

The impedance spectra (Figure 9.11) were fitted with an equivalent electrical circuit composed of an inductance in series with a real resistance and two $R||CPE$ (Figure 9.12 (d)) and results are plotted in Figure 9.12. In all range of temperatures the LF resistance is limiting the electrode performance, with a small capacitance between $1 \cdot 10^{-4}$ to $1 \cdot 10^{-3}$ F/cm^2 and associated frequency below 10 Hz. Since the activation energy of the LF is higher than the HF, at low temperatures the gap between both contributions is bigger.

As was explained in *La_{2-x}A_xNi_{1-y}B_yO_{4-δ} electrodes for protonic electrolytes chapter*, three different elementary cathode reaction steps take place in PC-SOFC: (1) surface dissociative adsorption and diffusion of oxygen along with charge transfer, (2) proton migration from electrolyte to TPBs and (3) formation and desorption of H₂O [8, 24]. The dependence between the resistance and the oxygen partial pressure, keeping constant the p_{H₂O} can provide information about the nature of the species involved in the limiting steps. The relation between resistance and oxygen partial pressure depends on the parameter *m*:

$$R_i \propto pO_2^{-m_i} \quad (9.1)$$

The results of the fitting by two R||CPE are shown in Figure 9.13. The numbers above the dot lines are the *m* parameters values. As was described by Peng *et al.*, [25], different elementary reactions can limit the electrode performance but two of them seem to be present in this electrode composite study here:



Thus, the LF processes with a power dependence of 0.29 is associated with the transfer of the adsorbed oxygen to the TPB (Reaction (9.3)), whereas the HF dependence of 0.32 is related with the reduction of oxygen adsorbed (Reaction (9.2)). As was mentioned before, by the proton phase introduction the HF arc is increased, then it can suppose that the negligible electronic conductivity of LWO block the electrons and affect the reduction of adsorbed oxygen.

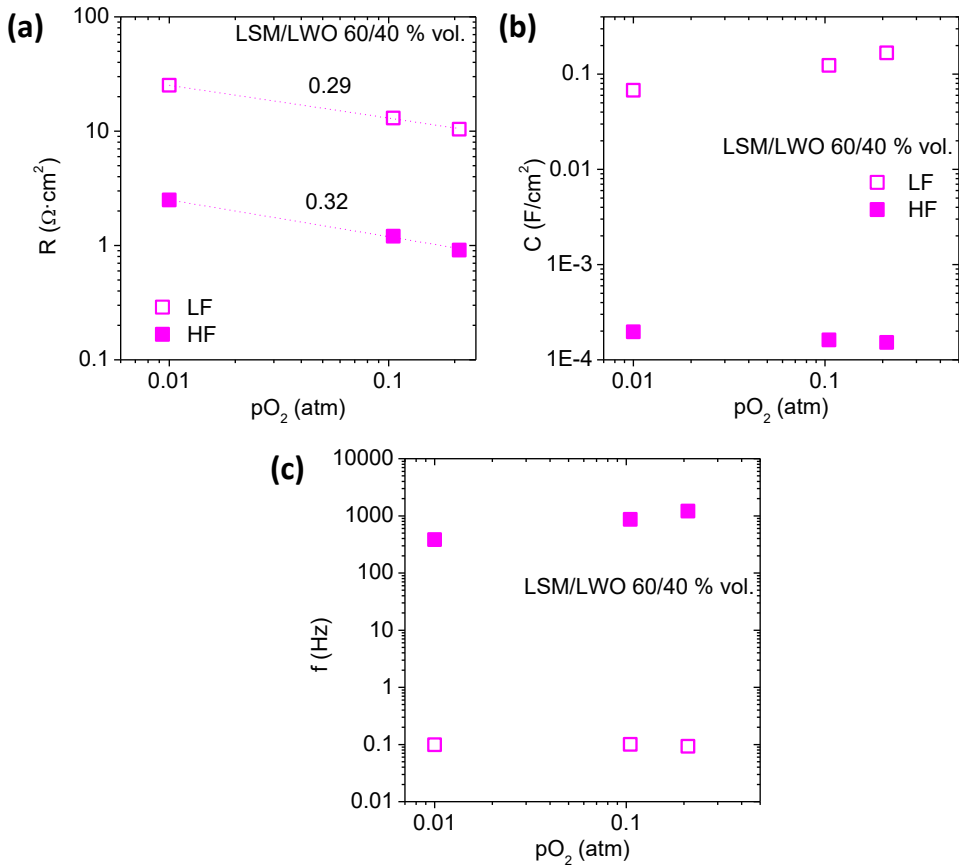
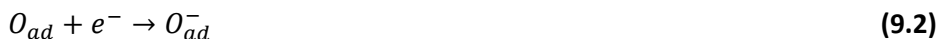


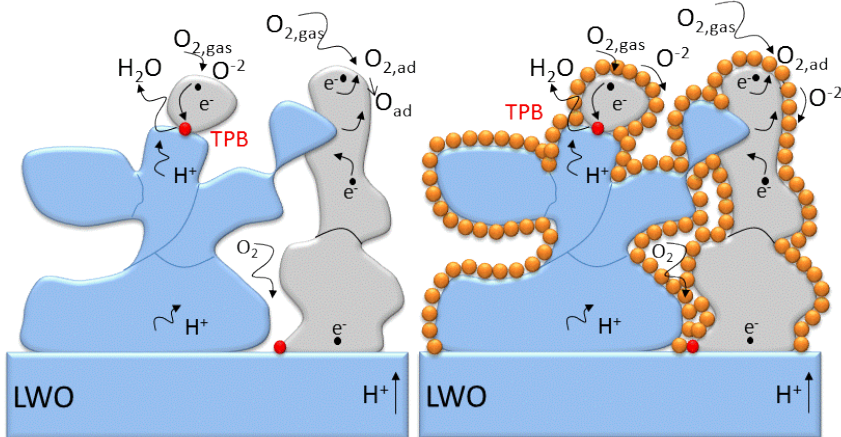
Figure 9.13: Results of the equivalent electrical circuit fitting of LSM/LWO 60/40 electrode as function of oxygen partial pressure in wet conditions; (a) resistances, (b) capacitances and (c) associated frequencies.

9.2.2.4. Infiltration of the electrode composite

As demonstrated in this section, the main limiting steps in the electrode performance are the surface processes. These surface processes take place at low frequencies. As was investigated in this thesis for LSM/GDC composite cathode on GDC the infiltration of different oxides precursor can enhance the cell performance, by reducing the low frequency resistance. The introduction of different nanocatalyst can help the dissociative adsorption of oxygen to O^- :



or/and the diffusion of species to the TPB:



LSM: e conductor LWO: protonic conductor ●nanoparticles

Figure 9.14: Scheme of the cathode composite and cathode composite infiltrated by nanoparticles.

Then, the composite can be used as backbone and be infiltrated with different oxide precursors. The main reason of infiltration is to obtain small particles on the surface of the cathode composite (Figure 9.14). The nanoparticles are infiltrated by dropping the solution on the surface of the calcined electrode. By capillarity, the solution fills all porous and after calcination, the nanoparticles are formed. Since the electrode is calcined before, the temperature of the precursor calcination can be as lower as the maximum operation temperature. By firing the nanoparticles at lower temperatures, the particles are smaller and it can achieve higher active surface area.

Then, the LSM/LWO 60/40 composite cathode calcined at 1150 °C was infiltrated with a solution of 20% samarium doped ceria (SDC). Indeed, ceria sites are known to be active for oxygen reduction reaction and to boost molecular oxygen adsorption/desorption process [19, 26]. Two different firing temperatures were used in order to compare how the surface area of the nanocatalyst affects the cell performance. The two temperatures selected were 900 °C and 750 °C.

9.2.2.4.1. XRD and FESEM characterization

XRD of SDC powder sintered up to 900 °C and 750 °C was measured and it is shown in Figure 9.15. The SDC was produced by dipping and drying a solid solution of Ce and Sm nitrates on silicon single crystal and subsequent thermal treatment in air. XRD peaks can be assigned to the cubic fluorite and grain size calculation reveals the powder sintered at 750 °C are around 21 ± 4 nm while those heated up to 900 °C reach particles sizes of 75 ± 15 nm

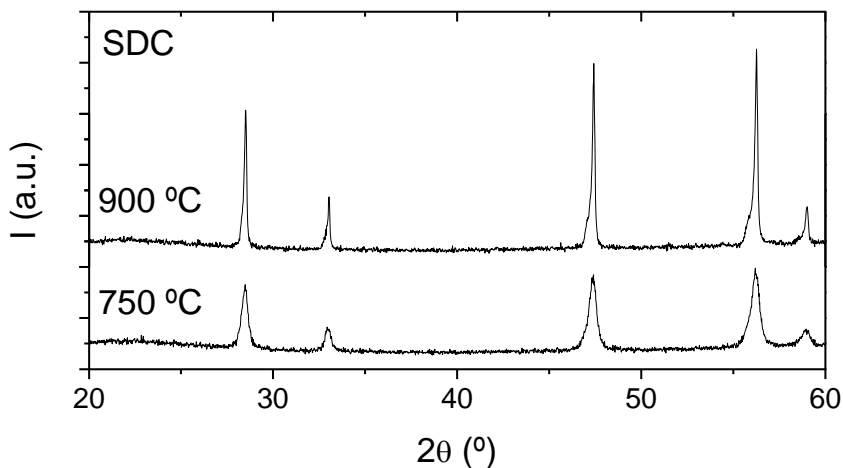


Figure 9.15: XRD patterns of SDC powders sintered up to 900 and 750 °C.

After EIS measurements the samples were analyzed by field emission scanning electron microscopy. The cross-section micrographs of the symmetrical cell are shown in Figure 9.16. As can be observed from the image, the electrode is well attached to the electrolyte. Furthermore, the nanoparticles were covering the entire backbone surface with a good distribution around the whole electrode. In the right side of the picture, two TEM micrographs of the nanoparticles fired at two different temperatures are presented. It can be observed the big difference in the particle size when the oxide is fired a two different temperatures. At 900 °C the average of the particle size is around 75 nm whereas the same material calcined at lower temperature has a particle size around 21 nm.

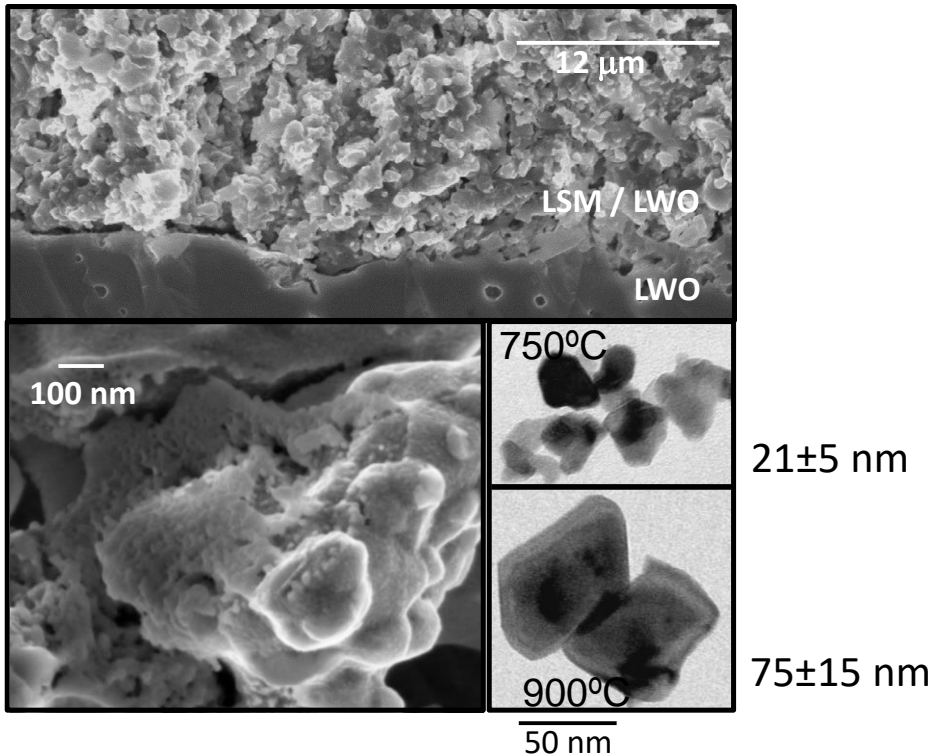


Figure 9.16: FESEM images of the electrode infiltrated with SDC and TEM images of the nanoparticles fired at two temperatures.

9.2.2.4.2. Electrochemical characterization

The polarization resistance of the different cathodes, the pure electronic conductor electrode, the pristine sample (LSM/LWO 60/40) and the two infiltrated electrodes (nanoparticles treated at 900 °C and 750 °C) is plotted in Figure 9.17 as a function of temperature in wet air (2.5 vol. % H₂O).

As can be ascribed from the graph, the different strategies followed in the present chapter can improve the cathode performance in proton conductor cells, *i.e.*, the addition of proton conductor phase in the electrode, and the addition of nanocatalyst reduces the R_p . The worst performance is obtained with LSM electrode, but R_p decreases with the introduction of the protonic phase. The performance is further improved through the SDC nanoparticles infiltration, in all range of the tested temperatures. Since the nanoparticles were fired at two different temperatures (900 °C and 750 °C), the tested

temperatures were different. Furthermore, as the firing temperature of nanocatalyst is reduced the efficiency of the cell increases, *i.e.*, lower R_p is obtained. In figure Figure 9.17, it can be appreciated the high influence of the nanocatalyst active area in the processes at low temperature, indicating a higher activity as lower particle size.

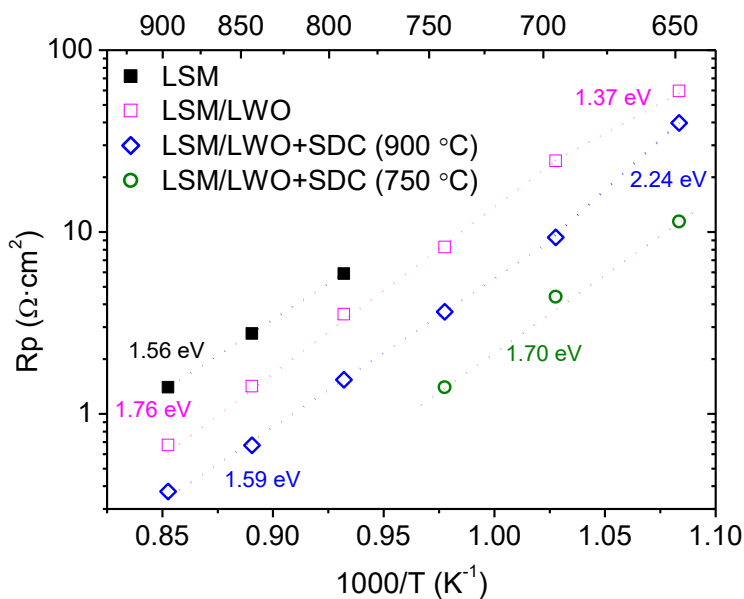


Figure 9.17: Polarization resistance as function of the temperature in wet air (2.5% vol. H₂O).

In this point, it is important to study more in detail the effect in the cell performance of the samarium doped ceria nanoparticles. For that purpose, the EIS spectra of the backbone and the infiltrated electrodes are shown in Figure 9.18. From these graphs at least two different contributions (two separated arcs) can be distinguished. One corresponds to LF and the other one appears at HF. The non-infiltrated composite is strongly limited by LF processes, since the LF arc is much larger than the one shown at HF. It is clear that the addition of the samarium doped ceria in the LSM/LWO composite can improve mainly the resistance at low frequency. The infiltrated cathode treated at 750 °C presents a very important improvement of LF processes with respect to the cathode sintered at 900 °C. It should be emphasized again, that regardless of post-sintering temperature, HF contributions remain constant, as for the non-

infiltrated composite, indicating that HF processes are not directly related to the electrode surface.

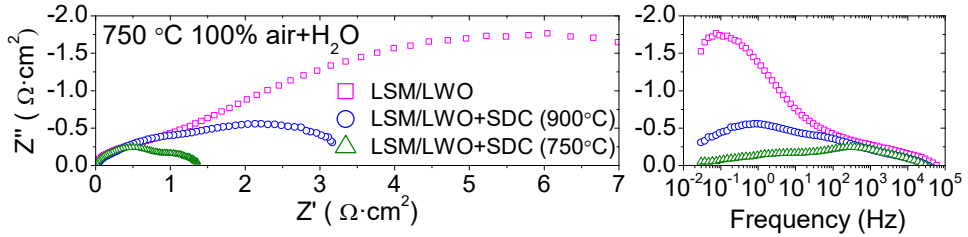


Figure 9.18: Nyquist and bode plot, left and right, respectively, of LSM/LWO 60/40 composite cathode blank and infiltrated with SDC fired a two temperatures (750 °C and 900 °C).

The best electrode (LSM/LWO+SDC 750 °C) and the parent backbone electrode will be studied by equivalent electrical circuit modelling, two R||CPE in series were used. The results of fitting as function of the temperature and oxygen partial pressure are presented in Figure 9.19 and Figure 9.20.

In general, the resistance related with HF processes for both composites are essentially identical irrespective of the temperature and the pO_2 , whereas the LF resistance values are drastically reduced thanks to the nanoparticle infiltration. The similar HF resistances for both samples, indicates that the transport properties of the backbone are maintained whereas the nanoparticles only affect the surface processes. Furthermore, when SDC is infiltrated in the sample the cathode limiting contribution changes from LF to HF. The LF resistance for the sample infiltrated has lower activation energy. Additionally, the capacitance of the different processes is almost maintained in all range of temperature, indicating the same limiting elementary reactions in the electrode. Associated capacitances are around $1 \cdot 10^{-3}$ to $1 \cdot 10^{-4}$ $F \cdot cm^{-2}$ for HF processes and 0.1 to 1 $F \cdot cm^{-2}$ for LF processes.

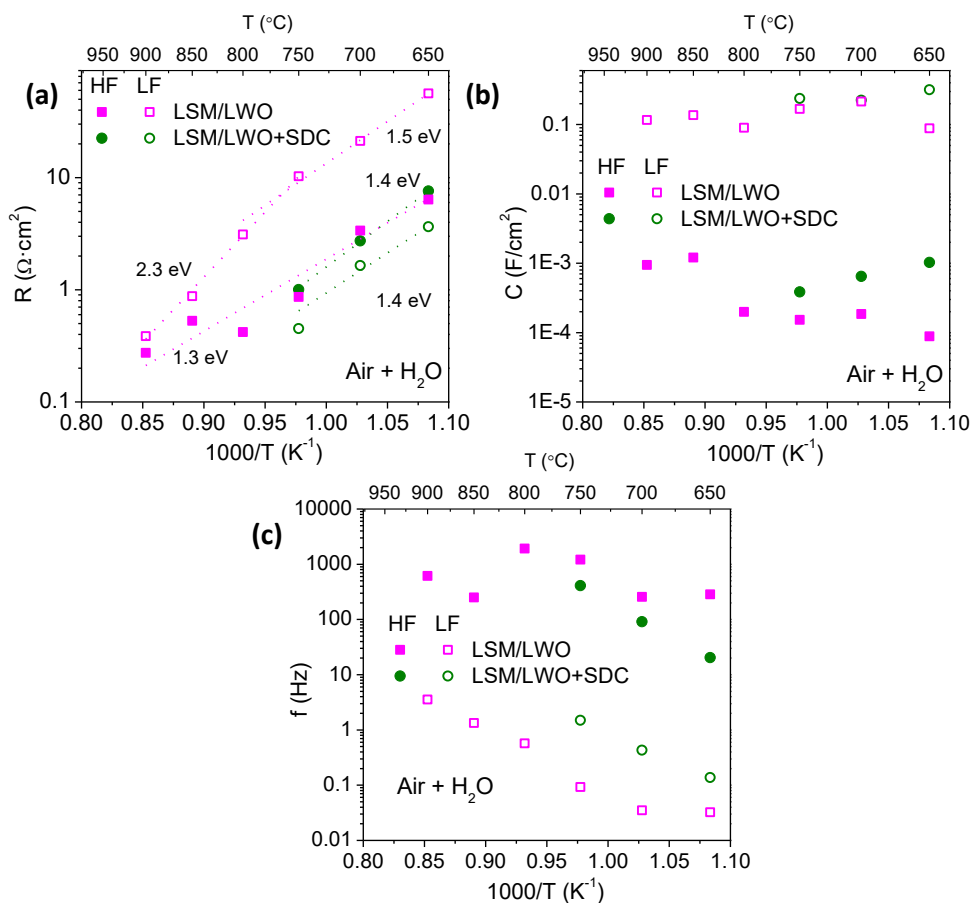


Figure 9.19: Results of the equivalent electrical circuit fitting of LSM/LWO 60/40 and LSM/LWO 60/40 infiltrated with SDC (750 °C) electrode as function of temperature in wet conditions; (a) resistances, (b) capacitances and (c) associated frequencies.

The isothermal analysis of the resistance at HF and LF as a function of the pO_2 at 750 °C is shown in Figure 9.20. The pO_2 dependence of the resistance ($R_i \propto pO_2^{-m_i}$) sheds further light on the nature of the limiting mechanisms in the electrode operation. The values inside the Figure 9.20 (a) are the m parameter calculated. At HF the m value is maintained for the pristine and the infiltrated sample, indicating that the bulk properties are maintained and only the low frequency processes change with the nanoparticles infiltration. Additionally, the HF cannot be related with the ionic transport from the electrode to electrolyte since not dependence of pO_2 should be expected in the resistance (Figure 9.19 a) and the associated capacitances should be smaller (10^{-5} - 10^{-7}

$\text{F}\cdot\text{cm}^{-2}$). Thus, the m value at HF could be associated with the charge transfer limitation ($\text{O}_{ad} + e^- \rightarrow \text{O}_{ad}^-$, $m=3/8$). The $p\text{O}_2$ dependence of pristine composite electrode is $m=0.29$ at LF, whereas the sample with SDC particles has a value of $m=0.41$. m values at LF with an associated capacitances of $\sim 10^{-1} \text{F}\cdot\text{cm}^{-2}$ can be assigned to surface dissociative adsorption and surface diffusion of oxygen [8, 24].

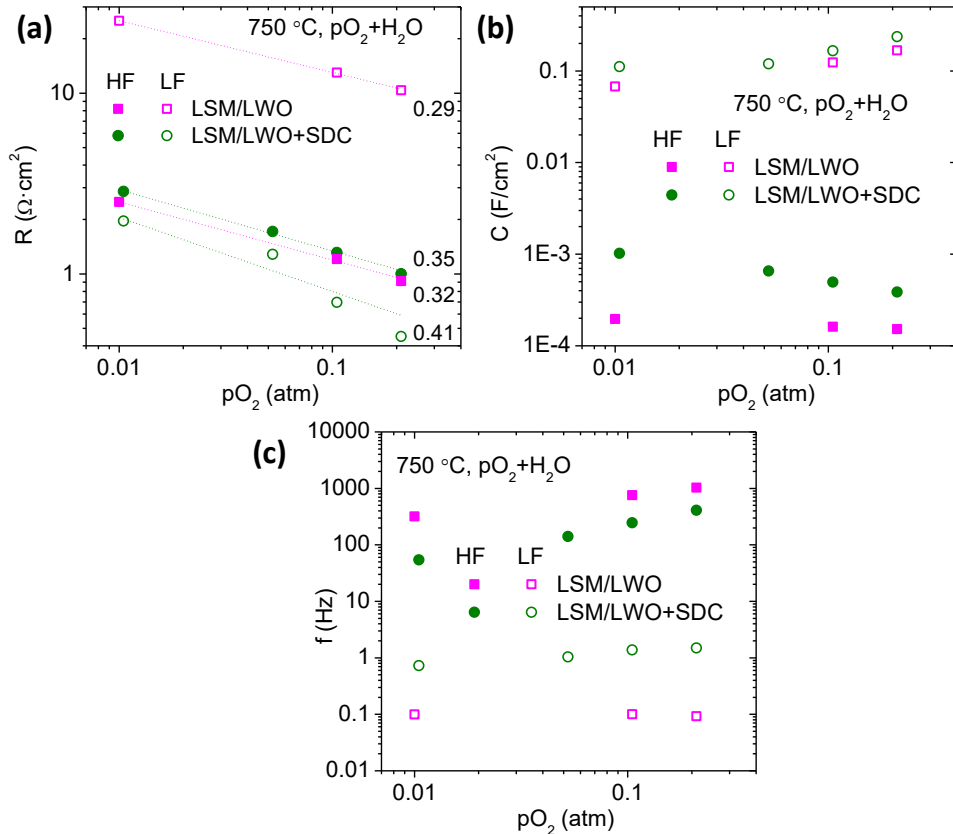


Figure 9.20: Results of the equivalent electrical circuit fitting of LSM/LWO 60/40 and LSM/LWO 60/40 infiltrated with SDC ($750\text{ }^\circ\text{C}$) electrode as function of oxygen partial pressure in wet conditions; (a) resistances, (b) capacitances and (c) associated frequencies.

9.2.2.4.3. Stability of SDC infiltrated sample

One of the most important parameters in real operation conditions is the cell performance stability. Thus, the stability of the polarization resistance of the cathode infiltrated was checked as function of time. For that purpose EIS measurements were carried out during more than 1200 minutes. As can be

ascribed from the graph, the cathode polarization resistance increases with time. Even there is an increase from $0.75 \Omega \cdot \text{cm}^2$ to $1 \Omega \cdot \text{cm}^2$ at the beginning of the cell operation, after 1000 minutes the cathode performance is getting stable. The same behavior was observed for the LSM/GDC cathodes infiltrated (*LSM electrode improvement strategies chapter*). There is a small degradation or equilibration of the sample until it reaches its final state under the operation conditions. After that the R_p value remains constant.

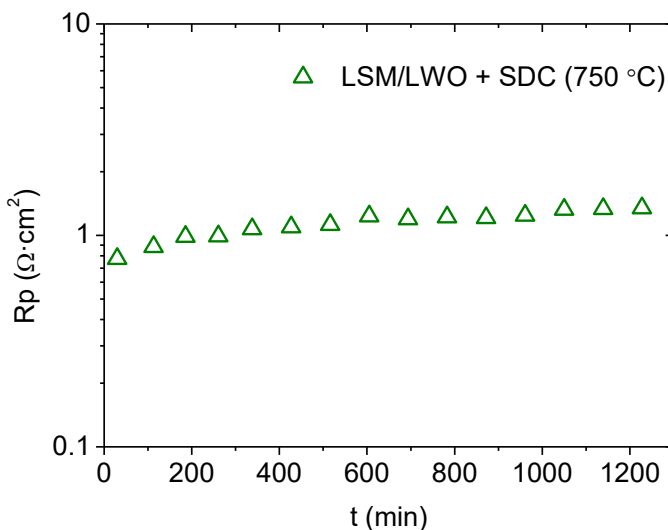


Figure 9.21: R_p of the LSM/LWO 60/40 infiltrated with SDC fired at $750 \text{ }^\circ\text{C}$ as function of time.

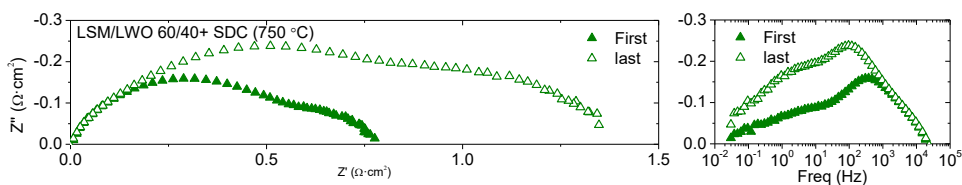


Figure 9.22: Nyquist and bode plot, left and right, respectively, of LSM/LWO 60/40 composite infiltrated with SDC fired at $750 \text{ }^\circ\text{C}$ for the first measurement and after the stability test.

The fitting of the EIS spectra (Figure 9.22) was performed in order to clarify how the resistance changes and results are presented in the Table 9.1. Both, HF and LF resistances increase with operation time ($t=1200 \text{ min}$). Moreover, the frequency range associated with these surface processes is shifted towards lower values, whereas the capacitances associated increase with time. Thus, there is an initial equilibration of the nanoparticles in the operation conditions.

Finally, after 1200 minutes the dominant mechanism is still associated with HF processes.

t min	R_{LF} $\Omega \cdot \text{cm}^2$	C_{LF} F/cm^2	f_{LF} Hz	R_{HF} $\Omega \cdot \text{cm}^2$	C_{HF} F/cm^2	f_{HF} Hz
30	0,26	0,24	3	0,56	6,58E-04	432
1228	0,54	0,28	1	0,91	0,00131	135

Table 9.1: Results of the equivalent electrical circuit fitting of LSM/LWO 60/40 infiltrated with SDC (750 °C) electrode, for the first measurement (t= 30 min) and after the stability test (t= 1228 min).

The LF resistance change could be associated with small particle enlargement, reducing the active area. However, the HF resistance worsening could be results of lower dissociative adsorption involved in the oxygen reduction reaction ($O_{ad} + e^- \rightarrow O_{ad}^-$).

9.2.2.5. Fully-assembled fuel cell

Finally, in order to check the influence of the SDC infiltrated on the cathode in real operation conditions, two samples supported on the electrolyte were tested as fully-assembled fuel cells. LWO was used as electrolyte material and support of the cell, thus the electrolyte was thick. The studied LSM/LWO composite electrode was used as cathode, whereas the anode selected was $\text{La}_{0.85}\text{Sr}_{0.15}\text{Cr}_{0.8}\text{Ni}_{0.2}\text{O}_{3-\delta}$ (LSCNi) [27], a highly active anode material for LWO-based proton conducting fuel cells. The surface catalytic properties of the anode can be also improved by Ni metallic precursor infiltration. Both electrodes, anode (LSCNi) and cathode (LSM/LWO 60/40), were screenpainted on the surface of the electrolyte. After sintering, a gold screenpainted layer was used on top of electrodes to ensure the proper current collection. One of the samples was measured as a parent and any catalyst was infiltrated. The other sample was infiltrated with Ni in the anode electrode (LSCNi), whereas SDC was introduced in the cathode composite (LSM/LWO), as it is shown in Figure 9.23.

The samples were tested in wet air (2.5 % vol.) and wet hydrogen (2.5 % vol.) as fuel cells and the i - V and i - P results are shown in Figure 9.24. The cell is dominated for the ohmic resistance, as can be inferred from the i - V curves, since a straight line is obtained, being not possible to observe the polarization for activation or polarization for concentration. One of the most limiting parameters in the cells performance is the electrolyte thickness, and dramatic improvements in power density can be achieved in SOFCs systems through reduction of the electrolyte thickness [28]. Anyway, by the infiltration of SDC and Ni on the sintered cathode and anode, respectively, the cell performance can be improved by doubling the power density in the same cell conditions. In order to check if the infiltrated particles are the main reason of the enhancement of the infiltrated cell performance, EIS measurements near the OCV were carried out for both samples. The Nyquist and Bode plots are shown in Figure 9.25.

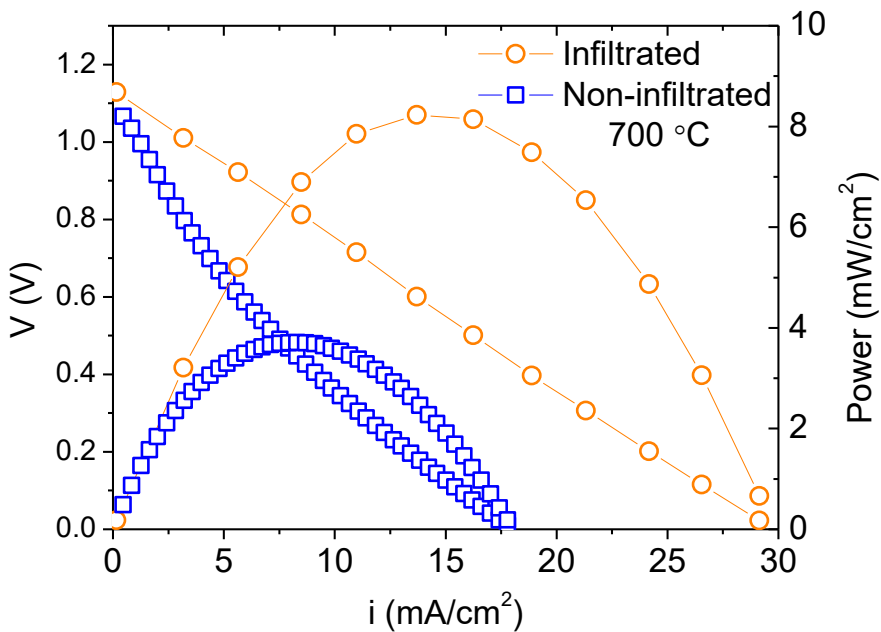


Figure 9.24: i - V and i - P curves of fully-assembled fuel cells supported on the electrolyte; anode LSCNi, electrolyte LWO and cathode LSM/LWO. The infiltrated sample was infiltrated with Ni in the anode and SDC in the cathode.

In order to compare directly the polarization resistance of the electrodes, the real resistance, associated mainly to the electrolyte, was subtracted in the

Nyquist plot. The values of the real resistance related with the thickness of the electrolytes and extracted from the plot were 20 and 29 $\Omega\cdot\text{cm}^2$ for the non-infiltrated and infiltrated sample, respectively. While the resistance of the non-infiltrated sample is dominated by the LF arc, the infiltrated sample shows a small arc at medium frequency. That fact confirms the hypothesis of the catalytic promotion of the infiltrated particles in the fuel cell performance. Additionally, as can be inferred from the graph, the sample infiltrated with SDC and Ni is limited by the electrolyte, since the resistance of the electrolyte is three times bigger than the electrodes contribution. However, in the case of the non-infiltrated sample the electrodes contribution remains bigger than the electrolyte contribution.

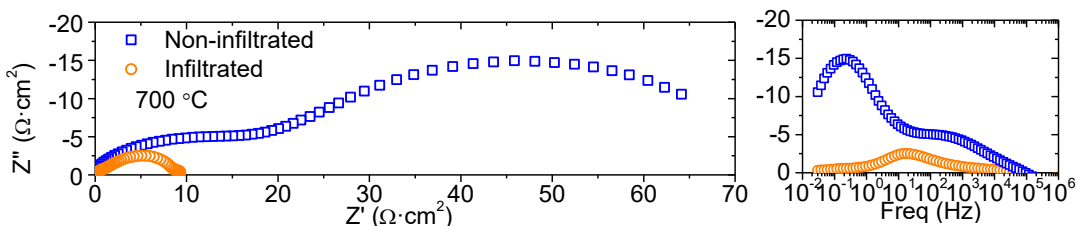


Figure 9.25: EIS spectra of the full assembled fuel cells.

9.3. Conclusions

$\text{La}_{5.5}\text{WO}_{12-\delta}$ (LWO) material presents the necessary properties to consider it as a cathode component and exhibits a good compatibility with $\text{La}_{0.8}\text{Sr}_{0.2}\text{MnO}_{3-\delta}$ (LSM). Different cer–cer composites based on LSM and LWO have been studied and analyzed as cathodes for LWO PC-SOFCs. The improvement of the cathode performance was obtained by the addition of the LWO protonic phase to the pure electronic LSM cathode material. When the amount of LWO was 40 vol.%, the polarization resistance was halved with respect to LSM for the whole temperature range. The electrochemical results showed that the limiting resistances at LF and LLF processes, associated with surface and TPB area, were reduced due to the addition of the LWO protonic phase. This fact is ascribed to the increase of TPB area into a certain cathode thickness with the introduction of the LWO protonic pathways.

Additionally, the surface processes associated with LF were tailored by the incorporation of catalytic active particles. An outstanding improvement of the

electrochemical performance was reached by coating the electrode backbone structure with nanosized catalytic SDC particles. This enhancement was originated from the promotion of surface processes (LF) by the catalyst incorporation. While high frequency resistive contributions were not altered by the nanocatalyst infiltration. Furthermore, the cathode optimized for LWO PC-SOFCs was tested in a fully-assembled fuel cell. The cell infiltrated with SDC and Ni nanoparticles (in cathode and anode, respectively) doubled the power density of the pristine sample. This fact was ascribed to the enhancement of the surface processes in the cell operation conditions. However, the operation performance was limited by the thickness of the electrolyte, indicating that new cell configurations should be taken into account.

9.4. References

- [1] R. Haugsrud, T. Norby, *Nature Materials*, 5 (2006) 193-196.
- [2] P. Babilo, S.M. Haile, *J. Am. Ceram. Soc.*, 88 (2005) 2362-2368.
- [3] J.M. Serra, W.A. Meulenbergh, *J. Am. Ceram. Soc.*, 90 (2007) 2082-2089.
- [4] J.M. Serra, O. Büchler, W.A. Meulenbergh, H.P. Buchkremer, *J. Electrochem. Soc.*, 154 (2007) B334-B340.
- [5] E. Perry Murray, S.A. Barnett, *Solid State Ion.*, 143 (2001) 265-273.
- [6] A. Mai, V.A.C. Haanappel, S. Uhlenbruck, F. Tietz, D. Stöver, *Solid State Ion.*, 176 (2005) 1341-1350.
- [7] C. Huang, D. Chen, Y. Lin, R. Ran, Z. Shao, *J. Power Sources*, 195 (2010) 5176-5184.
- [8] F. He, T. Wu, R. Peng, C. Xia, *J. Power Sources*, 194 (2009) 263-268.
- [9] V.B. Vert, C. Solís, J.M. Serra, *Fuel Cells*, 11 (2011) 81-90.
- [10] E. Fabbri, S. Licocchia, E. Traversa, E.D. Wachsman, *Fuel Cells*, 9 (2009) 128-138.
- [11] C. Solís, V.B. Vert, M. Fabuel, J.M. Serra, *J. Power Sources*, 196 (2011) 9220-9227.
- [12] E. Fabbri, L. Bi, D. Pergolesi, E. Traversa, *Energy & Environmental Science*, 4 (2011) 4984-4993.
- [13] S.P. Jiang, Y.J. Leng, S.H. Chan, K.A. Khor, *Electrochem. Solid State Lett.*, 6 (2003) A67-A70.
- [14] Y. Liu, S. Hashimoto, K. Yasumoto, K. Takeji, M. Mori, Y. Funahashi, Y. Fijishiro, A. Hirano, Y. Takeda, *Curr. Appl. Phys.*, 9 (2009) S51-S53.
- [15] S. Lee, N. Miller, M. Staruch, K. Gerdes, M. Jain, A. Manivannan, *Electrochim. Acta*, 56 (2011) 9904-9909.

- [16] T.Z. Sholklipper, H. Kurokawa, C.P. Jacobson, S.J. Visco, L.C. De Jonghe, *Nano Letters*, 7 (2007) 2136-2141.
- [17] N. Imanishi, R. Ohno, K. Murata, A. Hirano, Y. Takeda, O. Yamamoto, K. Yamahara, *Fuel Cells*, 9 (2009) 215-221.
- [18] F. Zhao, Q. Liu, S. Wang, F. Chen, *J. Power Sources*, 196 (2011) 8544-8548.
- [19] B. Wei, Z. Lü, T. Wei, D. Jia, X. Huang, Y. Zhang, J. Miao, W. Su, *Int. J. Hydrog. Energy*, 36 (2011) 6151-6159.
- [20] Y. Takeda, R. Kanno, M. Noda, Y. Tomida, O. Yamamoto, *J. Electrochem. Soc.*, 134 (1987) 2656-2661.
- [21] M.J. Jorgensen, M. Mogensen, *J. Electrochem. Soc.*, 148 (2001) A433-A442.
- [22] S. Sunde, *Electrochim. Acta*, 42 (1997) 2637-2648.
- [23] S. Sunde, *J. Electrochem. Soc.*, 143 (1996) 1930-1939.
- [24] R. Peng, T. Wu, W. Liu, X. Liu, G. Meng, *J. Mater. Chem.*, 20 (2010) 6218-6225.
- [25] R.R. Peng, T.Z. Wu, W. Liu, X.Q. Liu, G.Y. Meng, *J. Mater. Chem.*, 20 (2010) 6218-6225.
- [26] A. Samson, M. Sjøgaard, R. Knibbe, N. Bonanos, *J. Electrochem. Soc.*, 158 (2011) B650-B659.
- [27] M. Balaguer, C. Solís, F. Bozza, N. Bonanos, J.M. Serra, *Journal of Materials Chemistry A*, 1 (2013) 3004-3007.
- [28] S.M. Haile, *Acta Materialia*, 51 (2003) 5981-6000.

10

**CsH₂PO₄-based
electrochemical cells**

10. CsH₂PO₄-based electrochemical cell

10.1. Introduction

Solid acid proton conductors, based on tetrahedral oxyanions, have attracted interest in the last years because of their potential applications as electrolytes in fuel cells [1], hydrogen pumping [2] or electrochemically promoted water gas shift reactions [3]. Solids acids of interest are those whose chemistry is based on oxyanions groups, linked together by hydrogens bonds and charge balanced by large cations as K⁺, Cs⁺, Rb⁺ and NH₄⁺. Cesium dihydrogen phosphate, CsH₂PO₄ (CDP), is one of the compounds more studied that belong to this group, since has a good compatibility with catalysts and stability [2, 4-6]. Furthermore, H₂-air cells based on CDP electrolytes are able to process streams containing 20 % of CO [7].

CDP exhibits three different crystallographic phases depending on the surrounding temperature. At temperatures below -120 °C, it exhibits a ferroelectric phase with a monoclinic structure in space group of $P2_1$. At temperatures above -120 °C the phase changes to paraelectric with a space group $P2_1/m$. CDP undergoes superprotonic conductivity due to a phase transition to cubic phase with a space group of $Pm\bar{3}m$ at high-temperature (above 230 ± 2 °C). This structure presents cesium cations located at every corner of the cubic cell (Figure 10.1) and the PO₄ group is orientationally disordered about the center of the cell [1]. The dynamically disordered hydrogen bonds and the PO₄ disordered groups are the responsible for the high proton conductivity.

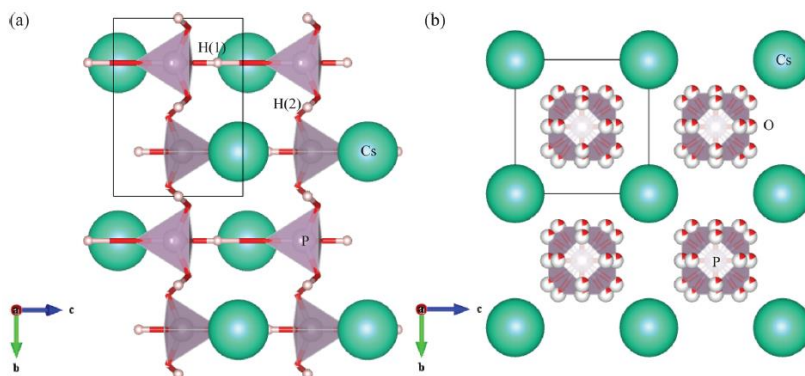


Figure 10.1: Crystal structure of CDP (a) the monoclinic paraelectric and (b) the cubic phases [8].

This solid acid compound facilitates anhydrous proton transport with high proton conductivity. The phase transition (Figure 10.1, Figure 10.2 and Figure 10.3) gives rise to an outstanding protonic conductivity increase by several orders of magnitude.

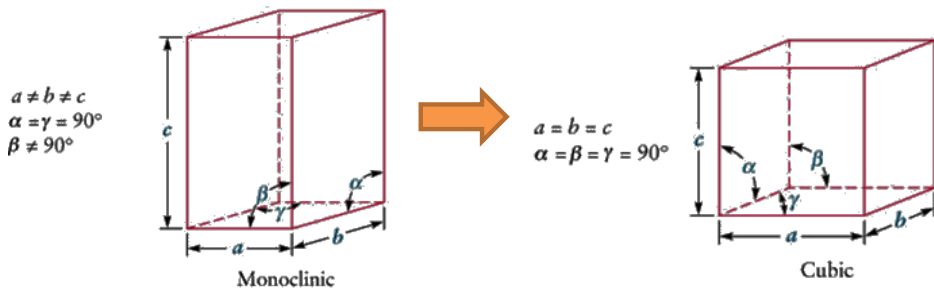


Figure 10.2: Phase transition of the CDP material.

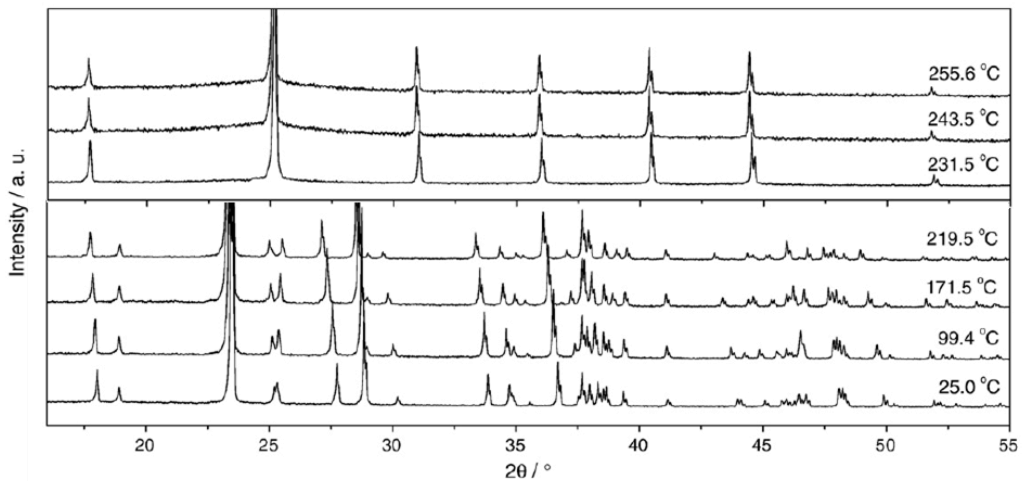


Figure 10.3: XRD patterns of the CDP as function of temperature [9].

The operation temperature of the CDP allows improving some problems obtained in PEMFC operation, as the water humidification control, or the poisoning of the Pt for the presence of CO in the fuel stream. Furthermore, the reduction of precious metal catalyst load or even the entirely elimination of precious metals can be achieved due to the CDP operation temperature.

Haile *et al.*, [1] obtained a power density peak of 415 mW/cm² at 240 °C with hydrogen and oxygen humidified, demonstrating the applicability of CDP as electrolyte for low-medium temperatures.

In this chapter, CDP is studied as electrolyte for operation as fuel cell and electrolyzer at different pressures. The main objective was to tailor the electrodes and electrolyte properties, conferring high stability to the electrolyte and avoiding precious metals for the electrodes catalyst, with the purpose to achieve high performance.

10.2. Results and discussion

10.2.1. Structural characterization

10.2.1.1. XRD characterization

The CDP material was synthesized by precipitation method as was explained in the (4. *Methodology chapter*) and after that, a XRD measurements was carried out at room temperature. As can be ascribed from Figure 10.2, CDP material exhibits a monoclinic structure at room temperature, as described by Louie *et al.*, [9] and no extra peaks were observed in the limits detection of the XRD equipment.

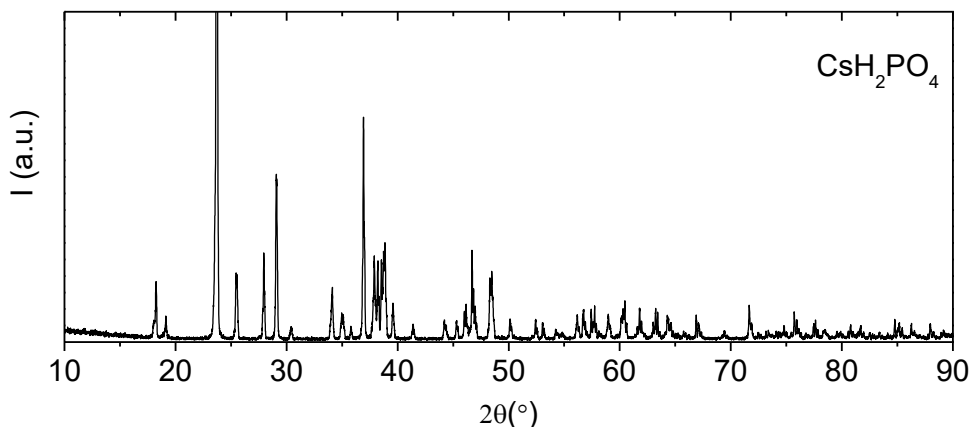


Figure 10.4: XRD pattern of CDP sintered at room temperature.

10.2.1.2. Conductivity characterization

10.2.1.2.1. Influence of temperature

The total conductivity of CDP salt was measured as function of temperature in a mixture of N_2 and water in a 30% of content. As shown in Figure 10.5, there are three different regimes in the total DC conductivity. The first with a low conductivity ($\sim 2 \cdot 10^{-6} \text{ S}\cdot\text{cm}^{-1}$) related with the monoclinic phase, the second one with a huge increase in terms of conductivity values, that can be ascribed to the phase transition (from monoclinic to cubic) and the third one where the conductivity is kept around $\sim 3 \cdot 10^{-2} \text{ S}\cdot\text{cm}^{-1}$. An increase of four orders of magnitude in the conductivity of polycrystalline CDP is observed and ascribed to the phase transition from low conductivity phase to a high conductivity phase (superionic conduction phase) in agreement with the results observed by Otomo *et al.*, [10]. Furthermore, the conductivity suffers a hysteresis behavior, revealing a reverse transformation by cooling the sample, but lower temperatures should be achieved (200 °C) [1].

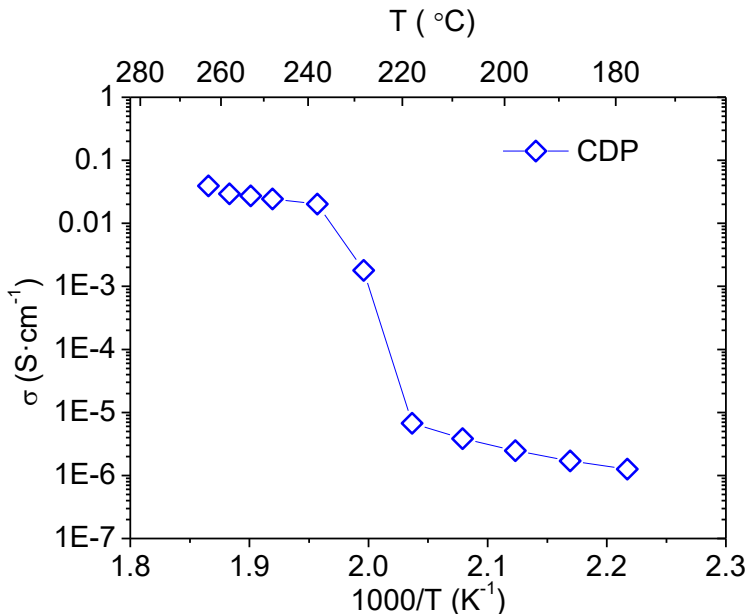
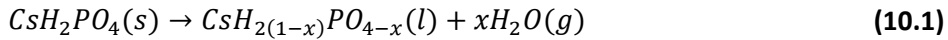


Figure 10.5: DC conductivity measurements of CDP as function of temperature, with a content of 30% of water in N_2 .

10.2.1.2.2. Influence of water partial pressure

As described in the introduction, this type of salt suffers a superprotonic phase transition at temperatures above 232 °C. However, in this type of materials where protons are incorporated in the structure, high temperatures promote the dehydration [11, 12] and CDP can suffer the reaction as follows:



Since the high temperatures force the dehydration of the material, and taking into account that high temperatures (>232 °C) are required to reach superprotonic phase, the optimum operation conditions should be selected. In that way, a complete study of temperature and water partial pressure was performed by Chisholm *et al.*, [7], and it is shown below.

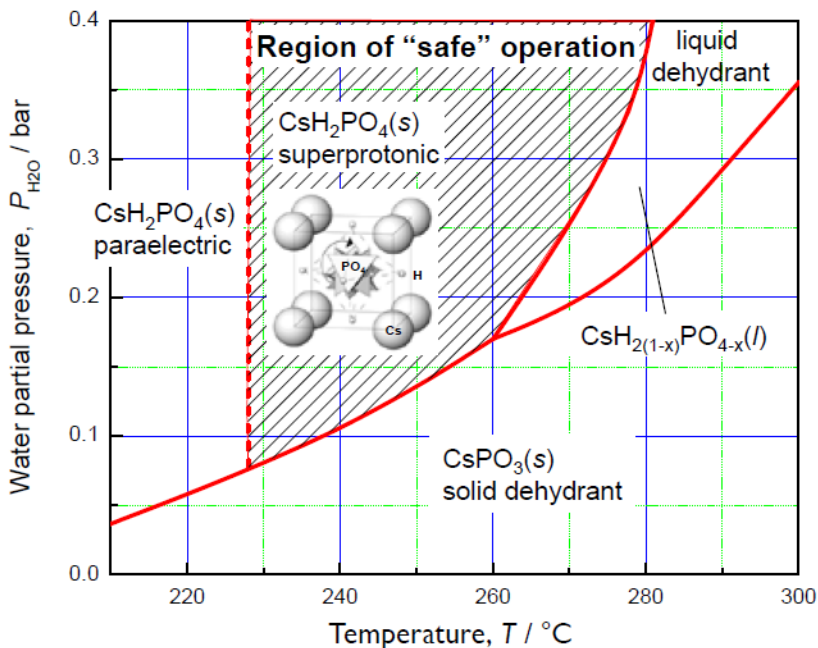


Figure 10.6: Phase stability diagram for solid acid fuel cells based on CDP [7].

Therefore, the operation conditions are limited for the stability of CDP, fixing the range of water content and temperature operation. That range of temperature (230 °C- 280 °C) and water content (of 30 % and 40 % of volume) will be employed for all measurements in the present chapter.

Additionally, the conductivity of the CDP was investigated as function of the water partial pressure. For that purpose a CDP pellet was measured by using two carbon papers as electrodes. The sample was heated up to 242 °C, above the phase transition, then, the conductivity was measured as function of the water partial pressure. The sample was heated up with steam in the Ar flow, in order to avoid the sample dehydration.

As can be ascribed from Figure 10.7, the conductivity of CDP with a partial pressure of 0.04 atm exhibits a value of $1.1 \cdot 10^{-3} \text{ S} \cdot \text{cm}^{-1}$. When the water partial pressure is increased up to 0.31 atm, the conductivity augments in almost one order of magnitude. After the water partial pressure reaches the value of 0.3 atm the conductivity is almost maintained with small improvement with higher $p_{\text{H}_2\text{O}}$.

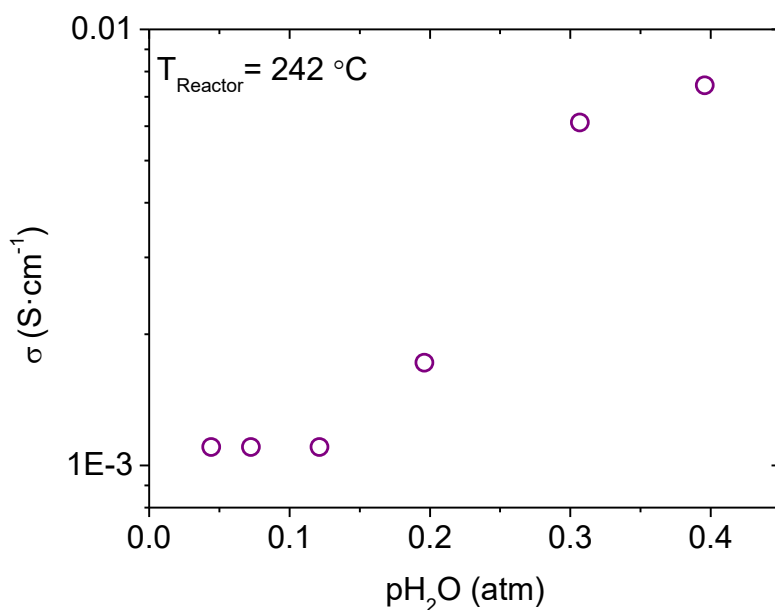


Figure 10.7: DC conductivity measurements of CDP as function of water partial pressure with a mixture of argon.

10.2.2. Electrochemical characterization of symmetrical cells

10.2.2.1. Symmetrical cell configuration

CDP material was tested in a fully-assembled fuel cell as electrolyte. The same material was used for both electrodes, cathode and anode, and the cell was supported on the electrolyte (Figure 10.9 (a)). A commercial gas diffusion layer (GDL), employed for PEMFC to facilitate the diffusion of reactants across the catalyst layered membrane [13], was used as electrode. That GDL (Figure 10.8), composed of carbon fibers, was chosen as backbone for the catalyst infiltration. Usually, platinum is employed as catalyst for electrodes that work at low temperature, but due to its high cost some alternatives should be selected. The range of operation temperature of the CDP allows the utilization of different metals as catalyst. A combination of Cu and Zn was selected as alternative catalyst for the electrodes infiltration. In addition, Pt was used also used for comparison purposes.

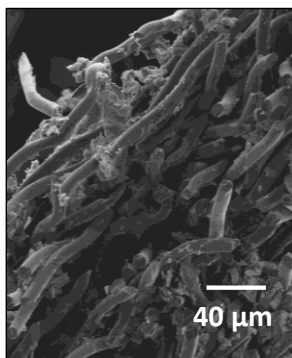


Figure 10.8: GDL SEM image.

SEM micrographs of the different electrodes employed are presented in Figure 10.9 (b) and (c). Cu and Zn oxide particles have a particle size in the range of nanometers, whereas Pt shows a bigger size, both catalysts are supported on $\approx 10 \mu\text{m}$ diameter carbon fibers. Furthermore, the porosity for the gas diffusion in both electrodes is enough and the catalysts are well dispersed around the whole electrode, but in the case of Pt, the content is lower with higher particle size, reducing the active area.

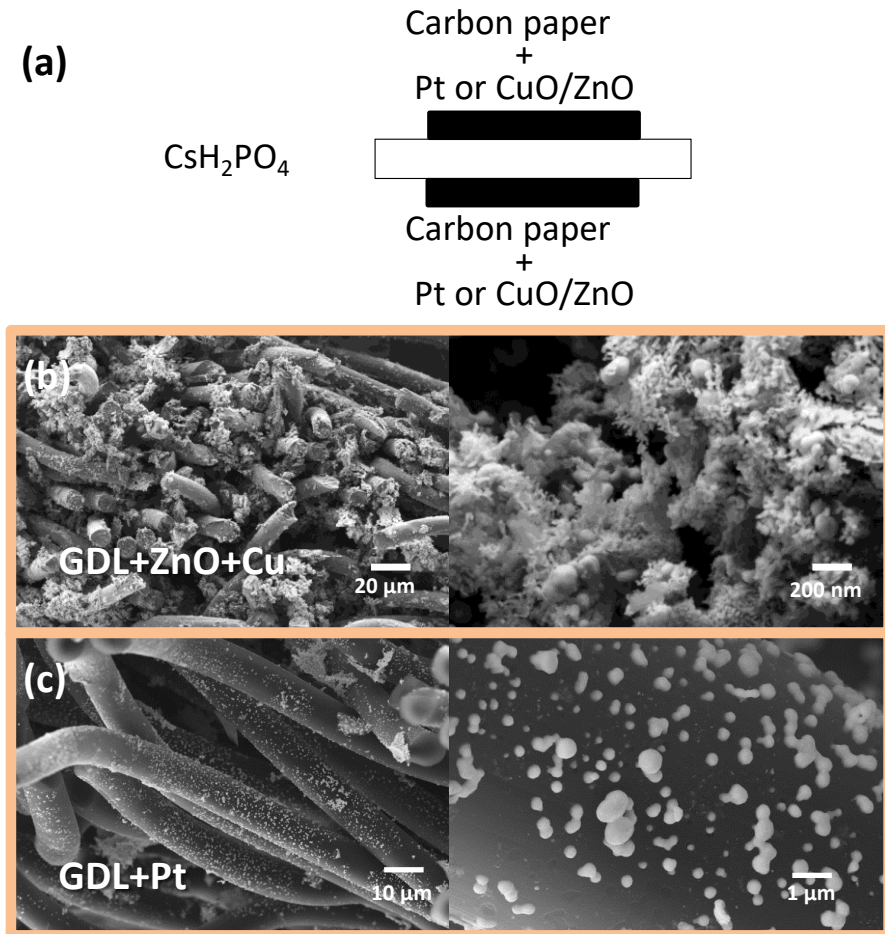


Figure 10.9: (a) symmetrical cell configuration, FESEM micrographs of both electrodes (b) GDL+ZnO+Cu and (c) GDL+Pt.

10.2.2.1.1. Influence of system pressure on the cell operation

Firstly, a sample composed of a thick electrolyte and two electrodes infiltrated with CuO and ZnO (Figure 10.9 (a)) was measured in wet hydrogen and air in a fully-assembled fuel cell mode. The water partial pressure on both chambers was maintained in 0.4 bar during the measurements time. Furthermore, the whole setup was heat-up in order to avoid the water condensation in any part of system, any drop of liquid water could damage the electrolyte.

The influence of the total pressure in the fuel cell was studied (Figure 10.10), and higher pressure lead to improve electrochemical performance. Furthermore, working with a total pressure of 4.5 bar in the cell, the power density peak reaches values around 1.15 mW/cm², four times higher than the same sample at atmospheric pressure. This improvement can be attributed to the higher activity of the Cu-ZnO electrodes under higher pressures. As has been reported previously, Cu and Zn catalysts improve the rate of several reactions by increasing the operation pressures [14, 15]. Furthermore, the same effect was observed for a similar cell by Hallinder *et al.*, working up to 40 bar [16].

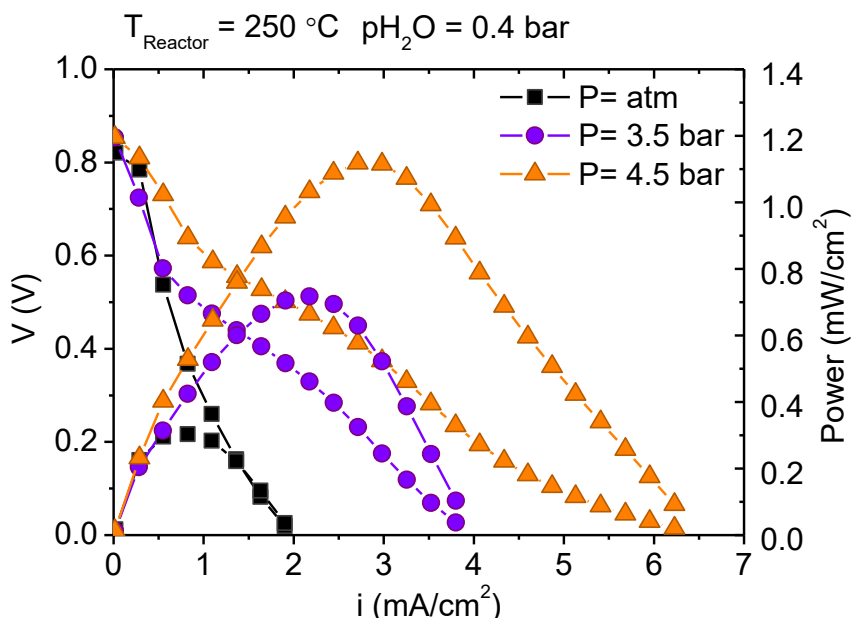


Figure 10.10: i - V and i - P curves of the Cu-ZnO on GDL/CDP/Cu-ZnO on GDL in wet H₂ and air as function of the total pressure of the system.

In addition, as can be inferred from the graph, when the pressure of the system is increased the OCV is not reduced, indicating that there is not leakage between both reaction chambers. That fact confirms the density of the sample, and allows the cell to work at higher pressures. As to confirm how the OCV changes as function of the total pressure in the operation conditions, the equilibrium potential (OCV) was calculated for the range of the tested conditions. The Nernst equation (3.6) was employed and the results are shown in Figure 10.11. The OCV increases by decreasing temperature or/and by increasing the pressure in the system. That behavior can be observed for the fuel cell tested in this thesis, *i.e.*, higher pressures produce higher OCV. However, the difference between the real and the theoretical values should be explained according to the cell performance. As the cell performance decreases, the OCV decreases as well. In the OCV data collection the Solartron equipment applies a small current density, but that current density is enough to reduce the OCV, and the same current density has higher effect in the low performance conditions.

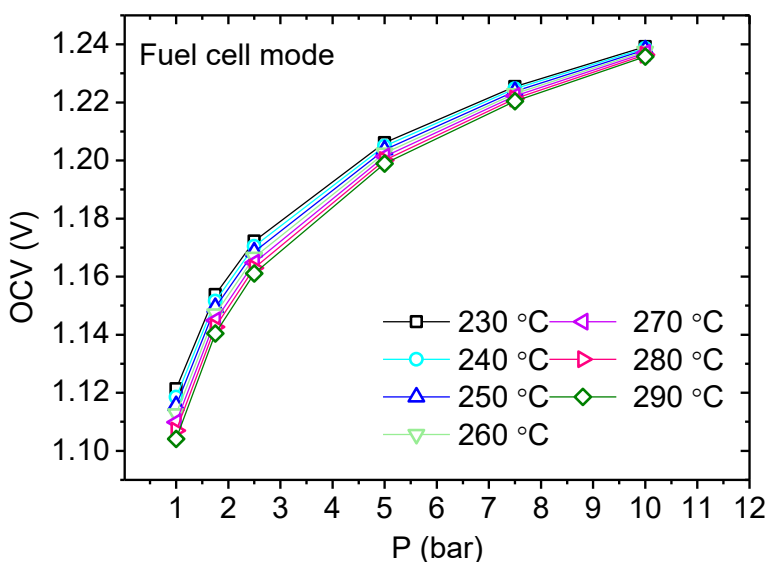


Figure 10.11: Theoretical results of OCV as function of the total pressure determined by equation (3.6) for the fuel cell working with a p_{H_2O} of 0.4 bar in both chambers and pure hydrogen and air in the anode and cathode, respectively.

The same cell configuration was selected to test the influence of Pt as catalyst in the fuel cell. For that purpose, the GDL was submerged in a solution of chloroplatinic acid, and after calcination and reduction, the electrodes were attached to the electrolyte by co-pressing the electrodes and electrolyte powder material. Results of the cell working under different pressures are shown in Figure 10.12. When Pt is employed as catalyst, the cell performance is also improved by using higher pressures in the system. However, the increase is not as high as the one observed for the electrode infiltrated with Cu and Zn oxides. Thus, Pt seems to be activated at low p_{H_2} . Furthermore, the effect of the pressure in the OCV is also observed in the i -V curves, higher OCV is obtained at higher pressures.

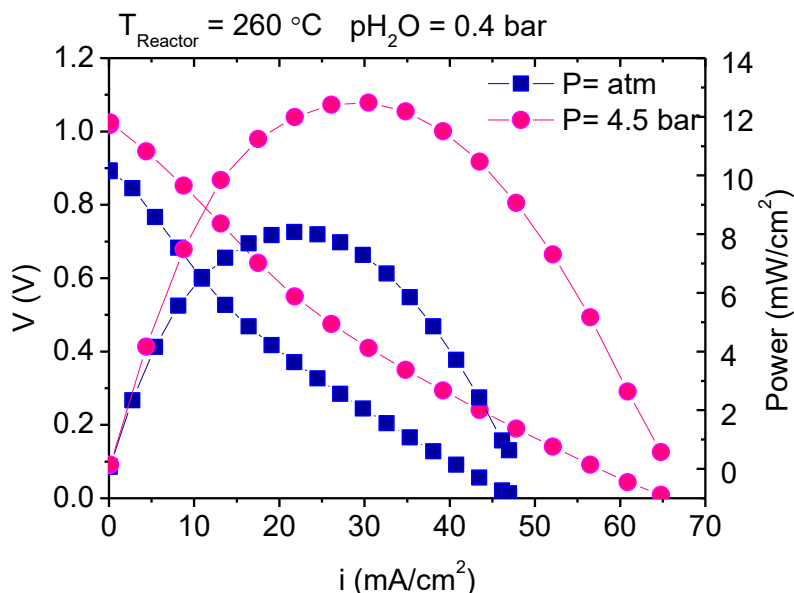


Figure 10.12: i -V and i -P curves of the Pt on GDL/CDP/Pt on GDL in wet H_2 and air as function of the total pressure of the system.

10.2.2.1.2. Influence of steam content on the cell operation

As was mentioned above, the material selected as electrolyte for that type of cells needs high contents of water. As shown in Figure 10.7, higher contents of water, more than 0.3 bar, can improve significantly the conductivity of the material. Thus, the electrolyte performance should be improved. However, the same behavior cannot be expected for the rest of cell components. For that

reason, a variation in the water partial pressure was studied for both symmetrical cells; *i.e.*, CuO+ZnO and Pt as catalysts.

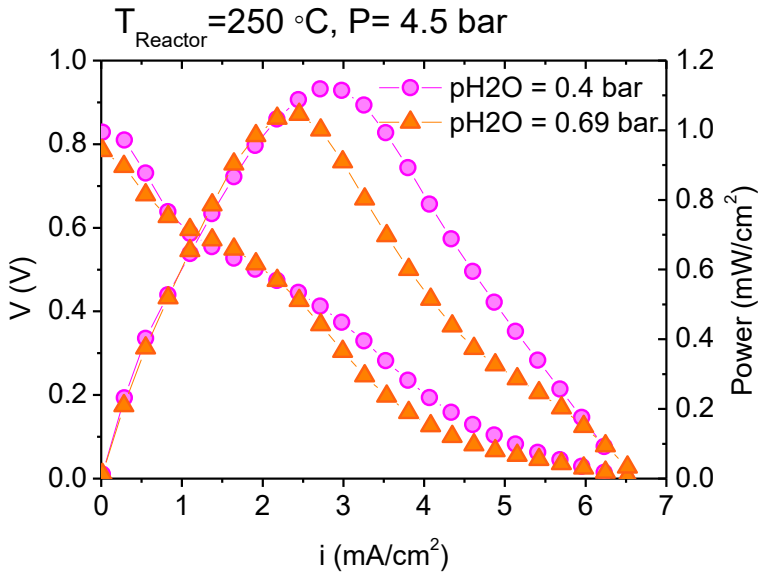


Figure 10.13: *i*-*V* and *i*-*P* curves of the Cu-ZnO on GDL/CsH₂PO₄/Cu-ZnO on GDL in wet H₂ and air as function of water partial pressure.

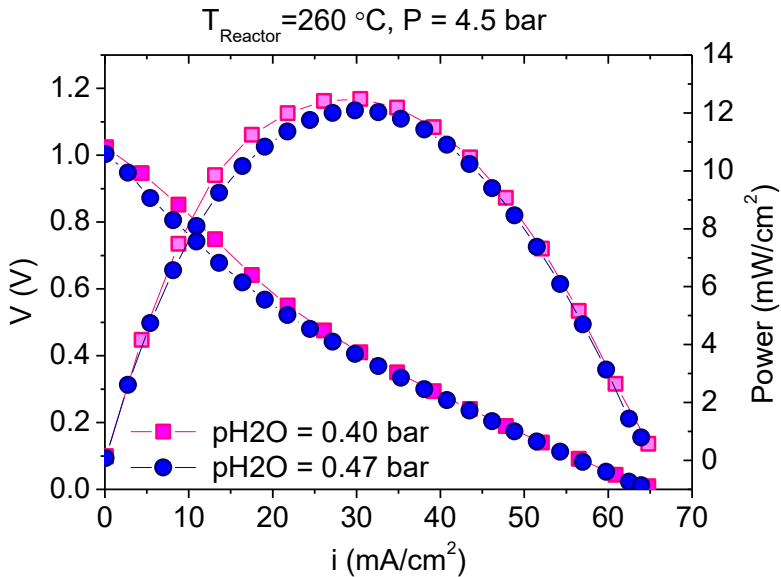


Figure 10.14: *i*-*V* and *i*-*P* curves of the Pt on GDL/CDP/Pt on GDL in wet H₂ and air as function of water partial pressure.

The i-V and i-P curves are shown in Figure 10.13 and Figure 10.14, for both cells working in hydrogen and air with different steam contents. As can be inferred from the graphs, the improvement of the CDP conductivity, associated with higher contents of water (Figure 10.7), is not enough for improving the cell performance. Thus, those results suggest that the cell performance is limited by electrode processes and the same behavior is observed for both catalysts (Pt and Cu-ZnO).

10.2.2.1.3. Influence of temperature on the cell operation

Additionally, the influence of the operation temperature was tested for both symmetrical cells (Figure 10.15 and Figure 10.16). Both samples show a rise in the power density by increasing temperature. But the effect of temperature is different in both cases. For instance, the sample working with Cu and Zn oxide shows an improvement of 43% with 10 °C, whereas the platinum sample increases only the power density in 32% with 20 °C. It seems that this improvement in terms of the power density can be ascribed to the activation of the electrode catalysts with temperature rather than the electrolyte. The results of the CDP conductivity (Figure 10.5) shown a significant increase of conductivity above 235 °C, but after that change, the conductivity increases a little. In order to confirm this hypothesis, electrochemical impedance spectroscopy measurements were performed near the OCV for the sample working with Pt and are shown in Figure 10.17.

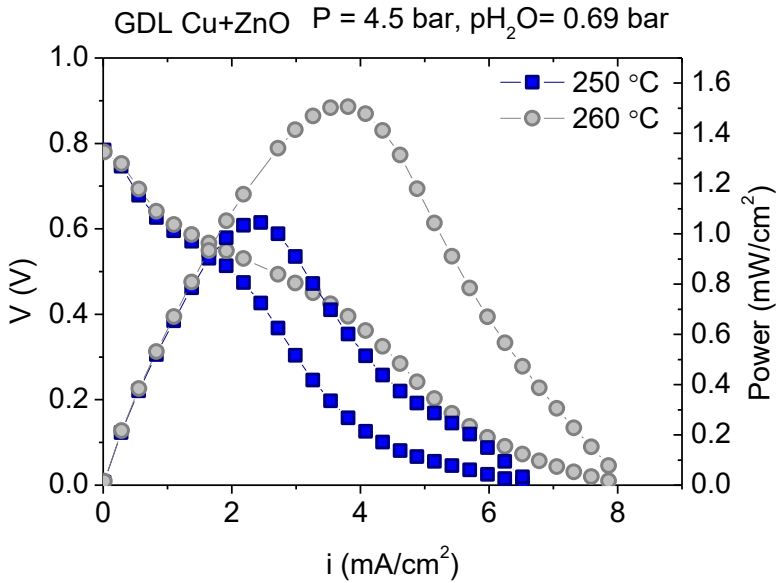


Figure 10.15: i - V and i - P curves of the Cu+ZnO on GDL/CDP/Cu+ZnO on GDL in wet H_2 and air as function of operation temperature.

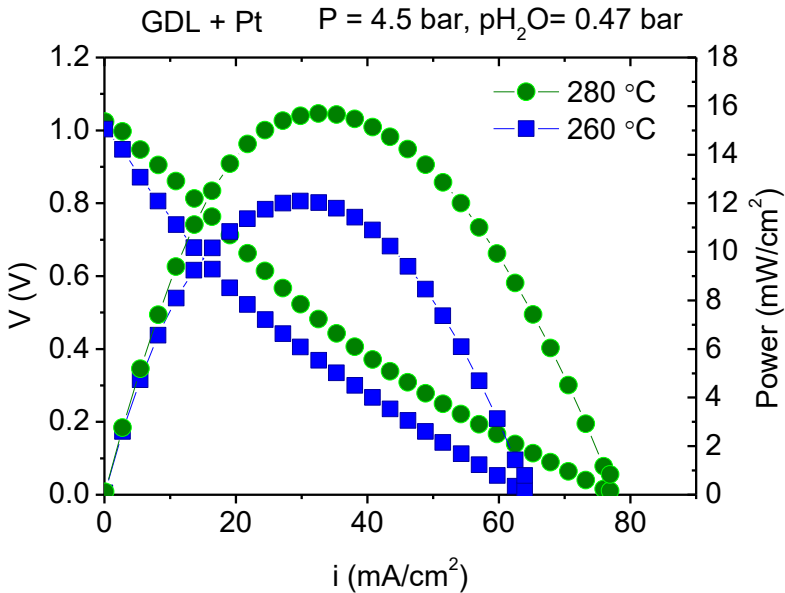


Figure 10.16: i - V and i - P curves of the Pt on GDL/CDP/Pt on GDL in wet H_2 and air as function of operation temperature.

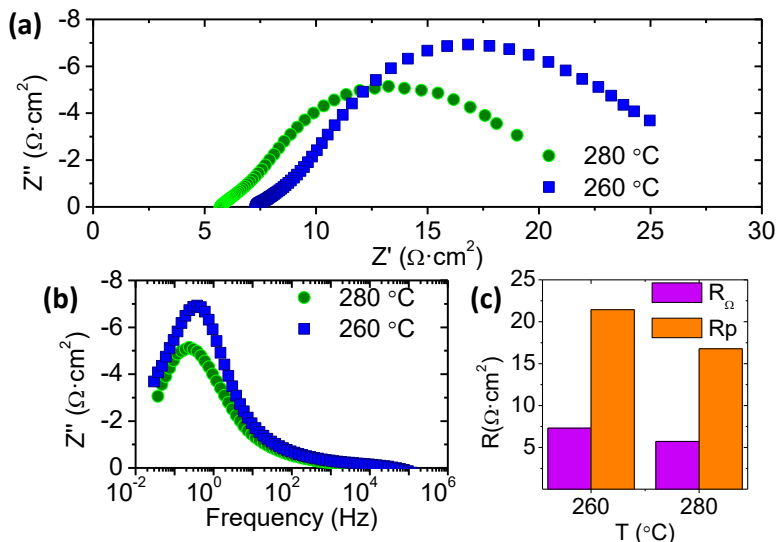


Figure 10.17: (a) Nyquist plot, (b) Bode plot and (c) summary of the EIS contributions of Pt on GDL/CDP/Pt on GDL sample near OCV at 4.5 bar and 0.47 bar of pH₂O function of temperature.

As can be inferred from the graph (Figure 10.17), the temperature can reduce both resistances: the one related with the real resistance (conductivity of the electrolyte) and the polarization resistance of the electrodes. The resistance obtained from the electrolyte with a thickness of 1.8 mm fits with the previous conductivity results (Figure 10.5). The main improvement in the cell performance is attributed to the electrodes enhancement (R_p in Figure 10.17 (c)). In addition, the main limiting processes in the electrodes performance take place at low frequencies (Figure 10.17 (b)). In order to clarify the nature of the limiting processes, the EIS results have been fitted with an equivalent circuit. The equivalent electrical circuit employed consisted of three constant phase in parallel with three resistances (LR_Ω -(RLF1-CPELF1)-(RLF2-CPELF2)-(RLF3-CPELF3)). Results of the fitting are shown in Figure 10.18. As can be observed from Figure 10.18, there are three limiting resistances associated with low frequencies (0.01-0.4 Hz). Those frequencies are usually related with material surface processes, dissociation and oxidation and/or reduction of hydrogen in the cell and morphology of electrodes [17-19]. In addition, the capacitances of those processes are in the range of 0.01 to 0.4 F/cm². The resistances at low frequencies can be associated with a low activity of Pt, and different are the hypothesis proposed: (i) presence of impurities in the Pt/C interface from the Pt precursor, blocking the adsorption/desorption of

hydrogen, (ii) low hydrogen desorption rate due to the high particles size (Figure 10.9 (c)) with low edges and corners sites in the crystal (with a specific crystal orientation) and (iii) Pt area blocked due to the anchoring of particles into the carbon backbone [20]. The high particle size observed in Figure 10.9 can be attributed to the synthesis method and reduction temperature, since high reduction temperatures produce bigger Pt particles [21] and can affect the catalytic activity of Pt in the electrode. Furthermore, the poor distribution of Pt reduces the number of active sites for the hydrogen reduction and oxidation reaction.

RLF1 and RLF2 are almost maintained when temperature is increased, but RLF3 is reduced in $12 \Omega \cdot \text{cm}^2$. Thus, the reduction of the RLF3 with temperature can be associated with the improvement of the catalytic activity. According to results obtained in the EIS measurements, the cell performance is limited by the electrodes having the highest resistance at both temperatures (Figure 10.17 (c)). Usually, cathode reactions are more limiting than the hydrogen oxidation reactions, and are responsible for the cell limitation performance.

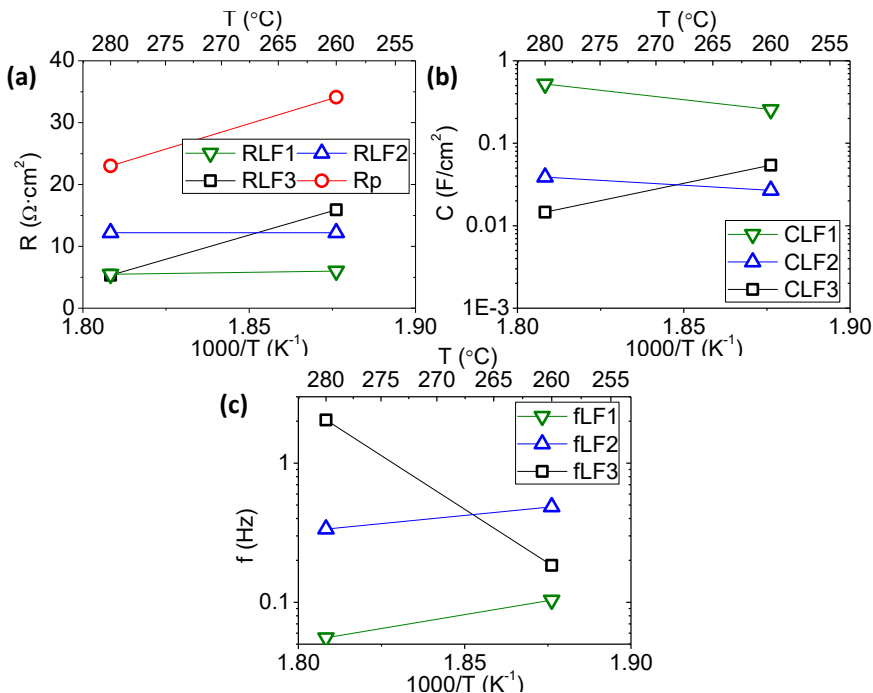


Figure 10.18: Equivalent electrical circuit fitting results; (a) resistance, (b) capacitance and (c) frequency of Pt on GDL/CDP/Pt on GDL near OCV at different temperatures.

10.2.3. Electrochemical characterization in asymmetrical cells

10.2.3.1. Electrolyte supported cell

In order to improve the cell performance, different strategies were followed. The voltage losses ascribed to the electrolyte can be easily diminished by reducing the electrolyte thickness [22]. Thus, the thickness of the electrolyte was reduced and the final thickness of electrolyte was halved to handle the sample in order to use the electrolyte as cell support. Furthermore, Pt was selected as catalyst in the air side to prevent the oxidation of Cu in the air side. One of the problems presented above was the poor distribution of Pt on the GDL surface, producing a low TPB length in the electrode. Ag paste and a Pt solution was mixed and applied on top of the GDL as alternative. After calcination and reduction of both electrodes (GDL+Cu+ZnO and GDL+Pt) at 300 °C in H₂, infiltrated GDL were pressed with CDP in a sandwich configuration.

The cell obtained was characterized electrochemically in a fuel cell and electrolyzer mode and results obtained are shown below.

10.2.3.1.1. Fuel cell mode

Firstly, the sample was tested in a fuel cell mode, for that purpose, the cell was measured with air in the Pt and Ag electrode, whereas the GDL infiltrated with Cu and ZnO was feed with H₂. In order to achieve a high proton conductivity of the electrolyte material, both sides were humidified with a 0.4 bar of water partial pressure. Atmospheric pressure was selected for the measurements in fuel cell mode.

The fuel cell performance as function of temperature is shown in Figure 10.19. As can be inferred from the graph, higher temperatures increase the power density. The fuel cell improvement can be assigned to the thermal activation of the electrodes catalysts. Furthermore, the same behavior as was described above is observed for the OCV, *i.e.*, the OCV is higher at higher temperatures. It seems that there is a big slope in the i-V curves in the activation regime and small current densities produces huge reduction in the cell potential.

If the power density is compared with the value obtained for the symmetrical fuel cell with only Cu and ZnO as catalyst (Cu and ZnO on GDL/CDP/Cu and ZnO

on GDL, Figure 10.10) similar value is obtained. Thus, the electrode with Pt and silver paste does not achieve the performance expected.

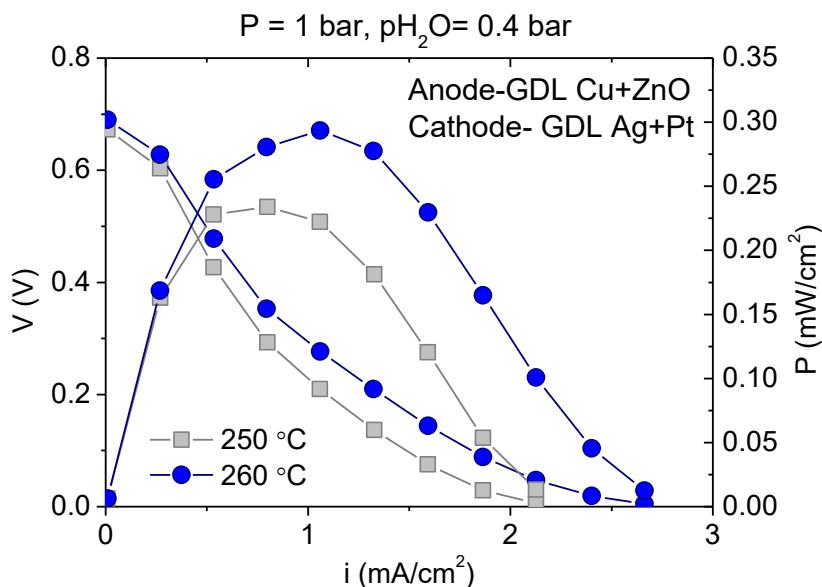


Figure 10.19: i - V and i - P curves of the Ag+Pt on GDL/CDP/Cu and ZnO on GDL in wet H_2 and air as function of operation temperature.

Finally, EIS measurements at both temperatures were performed in order to check the different contributions. For that purpose, EIS measurements were carried out near the OCV, and results are shown in Figure 10.20. The real resistance assigned to the electrolyte contribution has been subtracted in the graph in order to compare directly the electrodes performance. In addition, the EIS spectra were analyzed by equivalent electrical circuit fitting. The equivalent electrical circuit employed consisted of two CPE in parallel with two resistances, and can be written as follows; $LR_{\Omega}-(RLF1-CPELF1)-(RLF2-CPELF2)$, where L is the inductance and R_{Ω} is the real resistance of the electrolyte and set-up connections. The polarization resistance associated with electrodes shows two big contributions at low frequencies (0.1-1 Hz) for both temperatures, indicating the limitation of surface processes, related with the hydrogen evolution reaction accompanied by the adsorption and diffusion processes. The frequencies obtained for both processes (RL1 and RL2) fit perfectly with the values obtained for the symmetrical sample with Pt as catalyst (Pt on GDL/CDP/Pt on GDL, Figure 10.18). However, the capacitances

(Figure 10.21 (b)) are smaller ($2 \cdot 10^{-5}$ - $2 \cdot 10^{-4}$ F/cm²) and that difference may be due to the lower operation pressure in comparison with the 4.5 bar employed for the Pt symmetrical cell. Furthermore, in the Nyquist plot it can observe a second contribution at lower frequencies (<0.01 Hz). This second arc can be associated with gas diffusion, due to the range of frequencies.

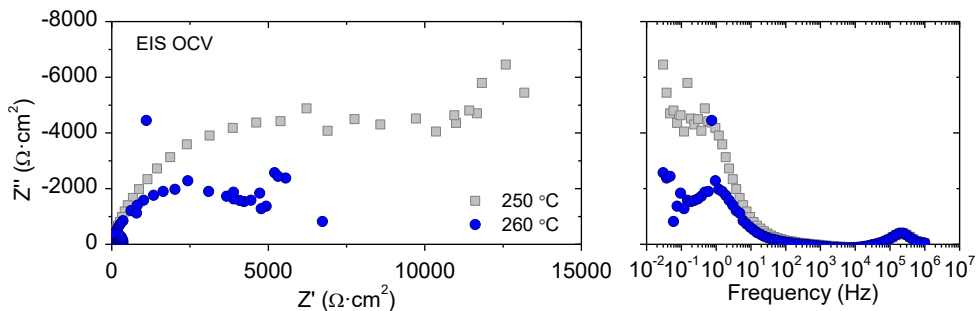


Figure 10.20: EIS results (Nyquist and Bode plots, left and right, respectively) of Pt +Ag on GDL/CDP/Cu-ZnO on GDL near OCV at 1 bar and water partial pressure of 0.4 bar as function of temperature.

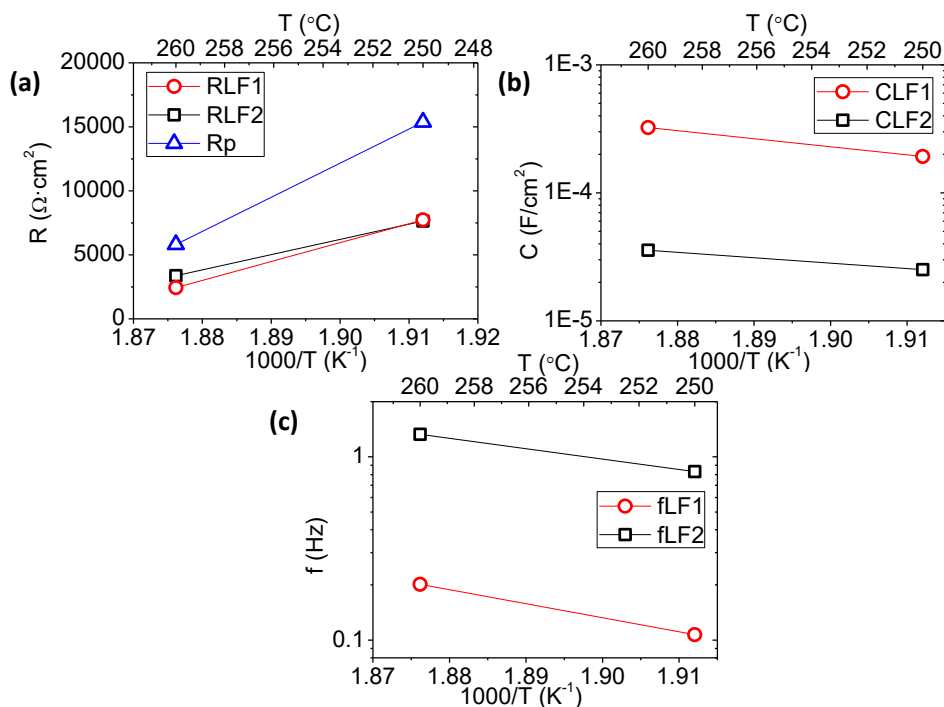


Figure 10.21: Equivalent electrical circuit fitting results; (a) resistance, (b) capacitance and (c) frequency of Pt on Pt +Ag on GDL/CDP/Cu-ZnO on GDL near OCV at different temperatures.

10.2.3.1.2. Electrolysis mode

To go a step further with this type of electrolyte material, the sample tested as fuel cell, was tested in electrolyzer conditions. The cell configuration and the test conditions are shown in Figure 10.22. In that case, N_2 was used in the Pt electrode, whereas Ar was selected for the Cu and ZnO electrode. Before the test of the cell as electrolyzer, the sample was fed during one night only with the inert gases in order to eliminate the residual hydrogen in the bubbler and in the reactor. The current was applied during stages of 30 minutes as it is shown in Figure 10.23. The composition of the outlet gas of the cathode was monitored by using a mass spectrometer.

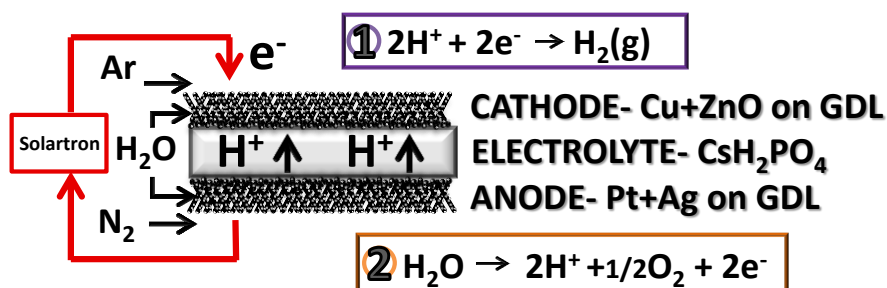


Figure 10.22: Electrolysis cell configuration.

The cell was tested at 260 °C and atmospheric pressure. As can be inferred from Figure 10.23, H_2 production is stable during the 30 minutes when the current is applied to the cell. Thus, those results demonstrate the use of this type of material for the hydrogen production.

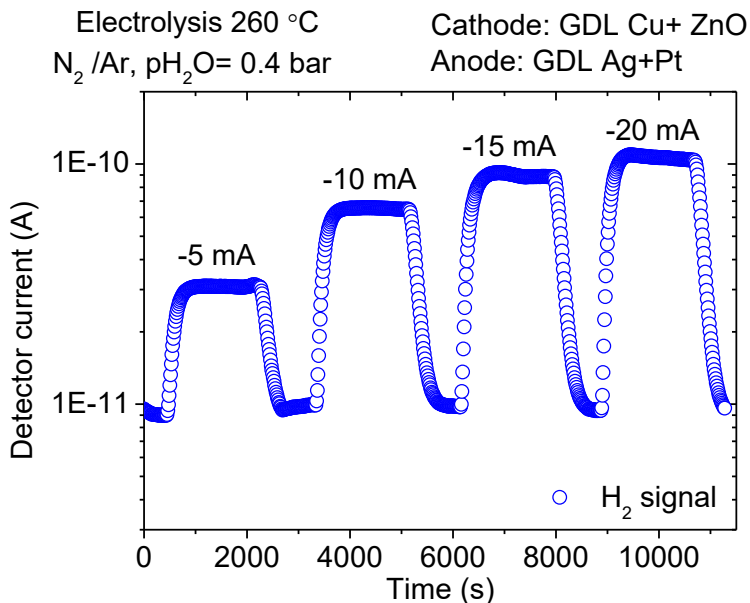


Figure 10.23: H₂ signal of the cathode outlet gas during electrolysis mode.

After that test, the influence of operation conditions were studied, *i.e.*, the system total pressure influence or co-electrolysis mode. The values achieved for the cell overpotential in the different conditions are shown in Figure 10.24. Comparing the three conditions, the water electrolysis test at atmospheric pressure reaches the lowest overpotential value and by increasing the pressure the cell voltage increases. Additionally, the voltage in electrolysis conditions was calculated from the Nernst equation for different pressures (Figure 10.25). As the pressure increases, the OCV of the cell raises as well. As might be expected, the same trend is followed by the electrolysis potential for the tested cell. Additionally, the presence of CO₂ in the inlet gas produces a voltage increase with regard to the atmospheric pressure measurements, but behaves as the system with pressure and without CO₂. However, the last point collected has an unusual performance, since leakage between the chambers was detected and the measurement was stopped.

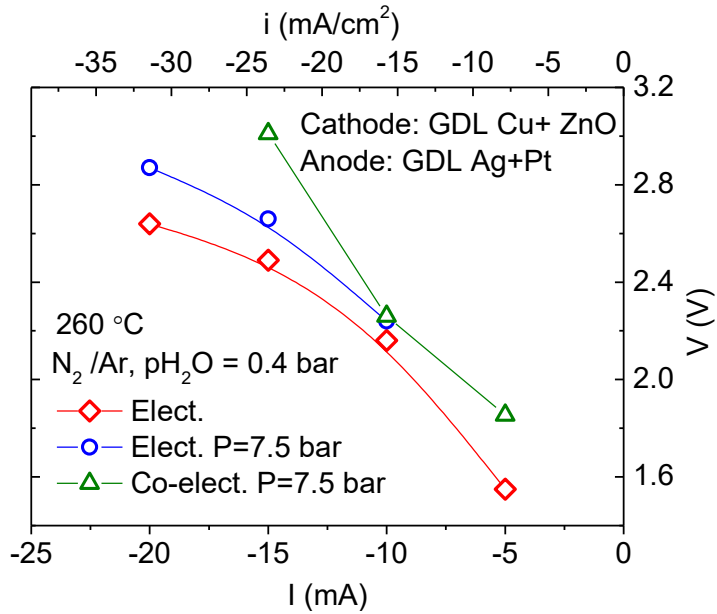


Figure 10.24: Cell overpotential in different conditions: atmospheric pressure (Elect.), system pressure of 7.5 bar (Elect. P=7.5 bar) and coelectrolysis with 3 ml/min of CO_2 (Co-elect. P=7.5 bar).

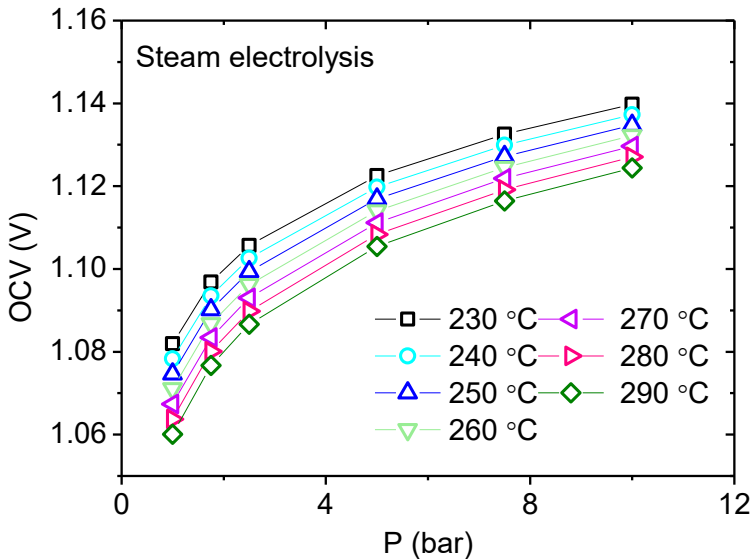


Figure 10.25: Theoretical results of OCV as function of the total pressure determined by Nernst equation for the electrolyzer working with a pH_2O of 0.4 bar in both chambers and Ar and N_2 fed in the cathode and anode, respectively.

The cathode outlet stream was monitored using a gas chromatograph. The measurements were carried out during the time that the current was applied to the cell, consecutive analyses were performed and the average of them (in each current condition) is presented in Figure 10.26. Since CO could not be detected in the co-electrolysis test, the Faraday's efficiency should be assigned to the steam electrolysis at 7.5 bar. The lower efficiency at 7.5 bar might be the result of a small leakage in the reactor and that leakage would cause the lower H₂ production during the electrolysis tests.

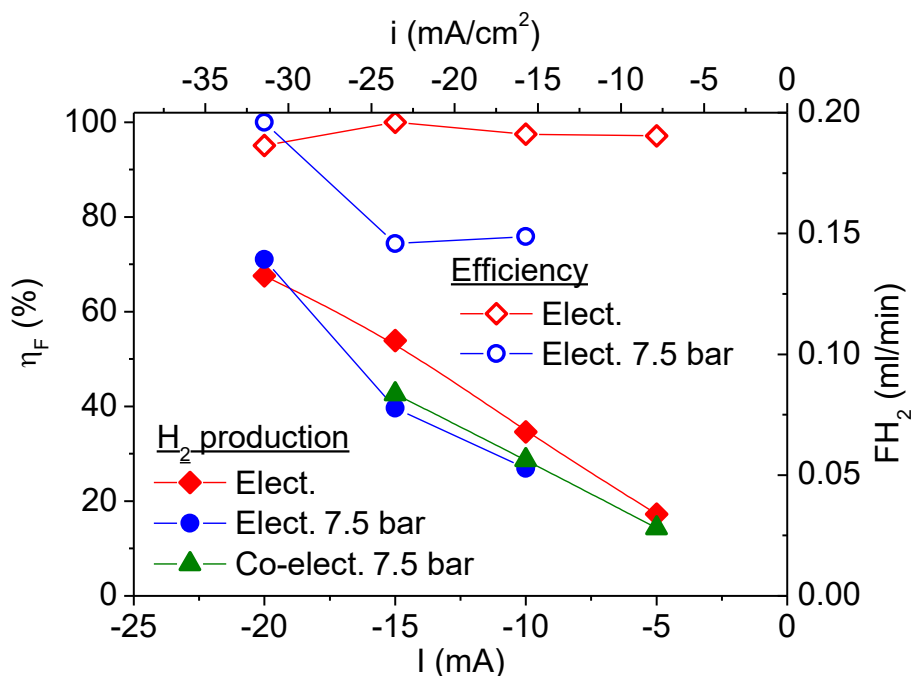


Figure 10.26: Hydrogen production and Faraday's efficiency of the three conditions, working with a water partial pressure of 0.4 bar. Gas chromatograph 1% error.

As was observed for the samples tested so far, the main limiting resistance in the cell is ascribed to the electrodes performance. Probably, the catalytic activity or electrodes configuration are the responsible of the low power density of the fuel cell and high overpotential in the electrolyzer, for that fact different improvements were performed in the cell manufacture.

10.2.3.2. Steel supported cell

The previous samples exhibited some limitations and these should be resolved in order to improve the cell performance. On the one hand, the thickness of the electrolyte should be reduced to achieve lower ohmic resistance in the cell operation, though this is not the limiting resistance in the cell performance. Then, a stainless steel (AISI 316) from GKN support was selected for the cell support to minimize the electrolyte thickness. On the other hand, since the CDP and GDL+Pt or Cu+ZnO can only transport protons and electrons, respectively, it can be assumed that the hydrogen oxidation (HOR) and reduction (HRR) reactions are limited to the triple phase boundary where electrons, protons and gas are in contact (electrode-electrolyte interface). Thus, the incorporation of a second phase in the electrode could increase the length of the TPB along the electrode thickness. For that purpose, the electrode should consist of two phase with a good percolation and well mixed, in order to provide paths for electrons and protons. In addition, high surface areas of both phases will enlarge the active sites [23] for the HOR and HRR. Thus, a proton conductor material (CDP) was introduced in the electrode to enlarge the length of the TPB. The new cell configuration allowed tailoring the characteristic of the electrode nearest to the steel. Additionally, the porosity of the electrodes should be maintained to ensure the proper gas diffusion. With this premise, solid naphthalene was added in the composite electrode for the manufacturing of the cell. After removal of the naphthalene (by sublimation) presented in the sample, the asymmetric cell was tested as fuel cell. The cell configuration is presented in Figure 10.27.

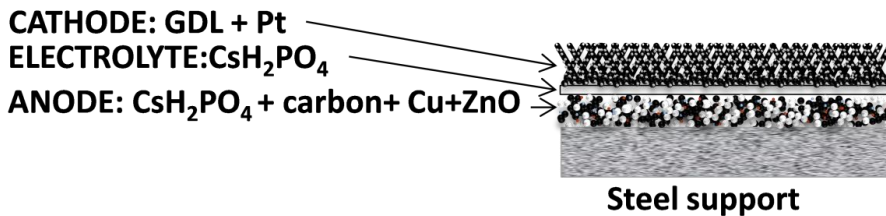


Figure 10.27: Asymmetrical cell configuration: Pt on GDL/CDP/CDP and Cu+ZnO on Carbon supported on porous steel disc.

10.2.3.2.1. Fuel cell mode

This asymmetrical cell was firstly tested as fuel cell: wet H₂ and air were feed in anode and cathode, respectively. The measurements were carried out in atmospheric pressure with 0.4 bar of water partial pressure.

As was observed for the samples tested so far, the operation temperature is a critical parameter for the cell performance. Only 10 °C can increase the power density in more than 38 %, as can be observed in this asymmetric cell (Figure 10.28).

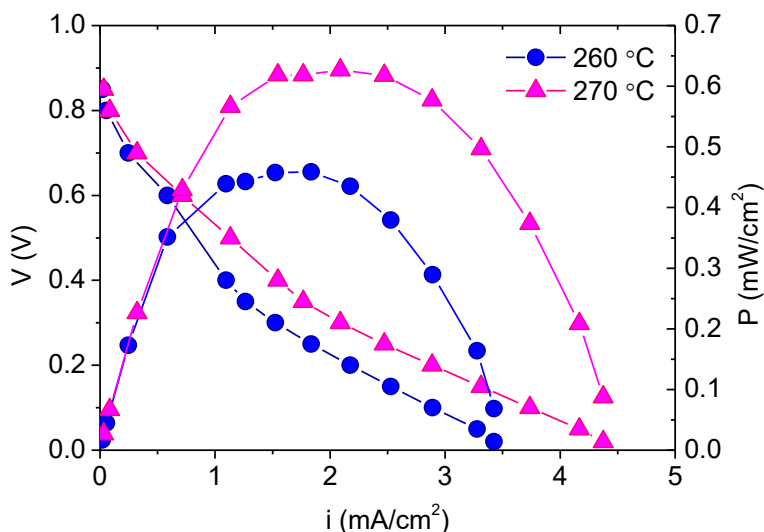


Figure 10.28: i-V and i-P curves of Pt on GDL/CDP/CDP and Cu+ZnO on carbon supported on porous steel disc working in fuel cell conditions as function of temperature. Air supplied in the cathode and hydrogen in anode, both chambers with a water partial pressure of 0.4 bar.

Comparing the results obtained with the asymmetric cell supported on the electrolyte (Figure 10.19) in the same conditions (260 °C), the cell performance is improved in more than 58%. That improvement can be ascribed mainly to the composite anode developed. Thus, the composite anode enables the enlargement of the TPB sites for the hydrogen oxidation along the electrode surface. Furthermore, the reduction of the electrolyte thickness can also improve the cell performance, but taking into account the previous results, the cell is limited by electrodes performance and the electrolyte thickness reduction plays an almost negligible role. In order to clarify the nature of the limiting resistances, EIS measurements were conducted near to OCV and these

results are displayed in Figure 10.29. The real resistance associated to the electrolyte ($8 \Omega \cdot \text{cm}^2$) was subtracted to compare directly the electrodes resistances.

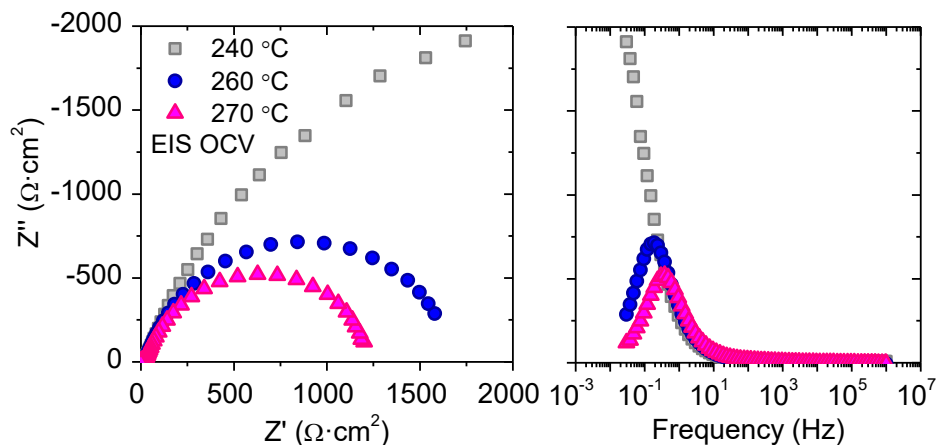


Figure 10.29: Nyquist and Bode plots, left and right, respectively of Pt on GDL/CDP/CDP and Cu+ZnO on Carbon supported on porous steel disc working in fuel cell conditions as function of temperature near OCV.

The EIS spectrum were fitted with an equivalent electrical circuit with three CPE in parallel with three resistances, LR_{Ω} -(RLF1-CPELF1)-(RLF2-CPELF2)-(RLMF-CPEMF) and results are shown in Figure 10.30. Where R_{Ω} is the electrolyte resistance. The biggest resistances take place at low frequencies (RLF1 and RLF2), being RLF1 the most limiting contribution. Furthermore, the resistances at low frequency follow the frequency range observed for the CDP-based fuel cells tested before in this thesis. In addition, the associated capacitances are also maintained (Figure 10.30 (b) and Figure 10.21 (b)). It would be expected that the limiting stages in the HOR and HRR are kept in that sample. However, the sample supported on the porous steel disc reduces the RLF1 and RLF2 with respect to the electrolyte supported cell (Figure 10.21). One of the main improvements can be ascribed to the enlargement of the TPB along the anode electrode reducing the resistance at LF.

Furthermore, as happened before for the rest of the samples, there is a big influence of operation temperature on the electrode performance (Figure 10.29). For instance at 240 °C the electrodes resistance takes place at very low

frequencies, with a big contribution, not allowing to close the complete arc (due to the range of frequencies). However, by rising the temperature 20 °C, electrodes are activated for the oxidation/reduction of hydrogen and a resistance reduction of up to 1250 $\Omega\cdot\text{cm}^2$ is achieved. If the results of both asymmetrical cells are taken into account, it can clarify that the limiting processes associated with LF1 and LF2 are the length of the TPB and the activity of the catalyst in the operation temperature range.

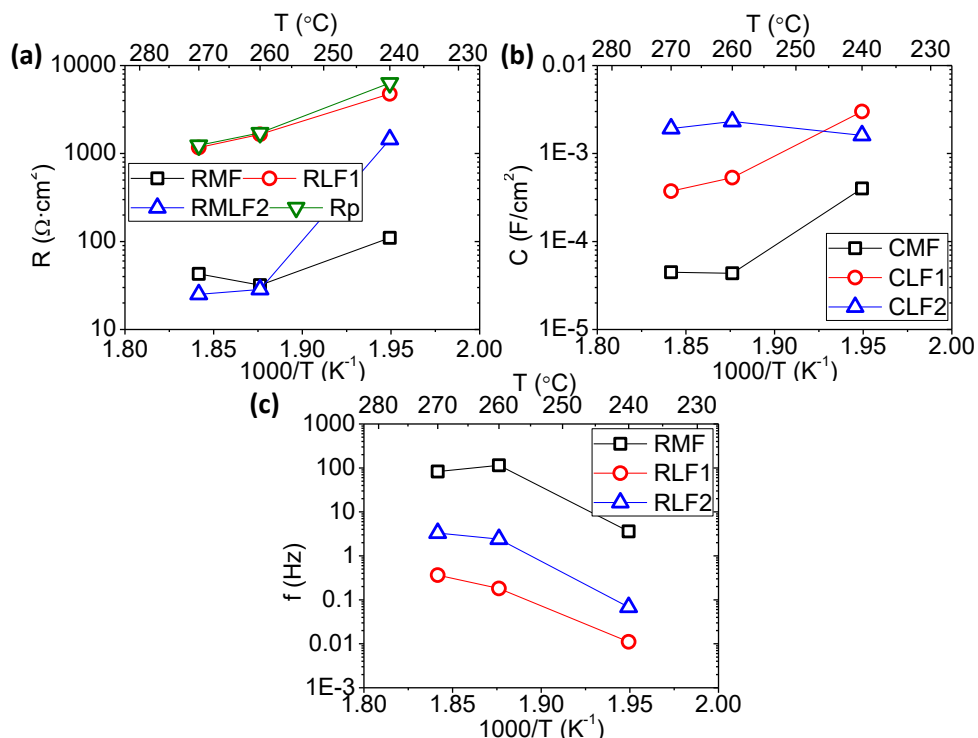


Figure 10.30: Equivalent electrical circuit fitting results; (a) resistance, (b) capacitance and (c) frequency of Pt on GDL/CDP/CDP and Cu+ZnO on Carbon supported on porous steel disc near OCV at different temperatures.

10.2.3.2.2. Electrolysis mode

Finally, the sample was also tested in electrolysis mode, as was explained before; the sample was flushed overnight with wet Ar and N₂ in order to eliminate the residual H₂ in the water. All electrolysis stages were followed by a mass spectrometer and gas chromatograph (Figure 10.32 and Figure 10.33).

In that case, the current was applied only during 15 minutes (Figure 10.32). Thus, the stabilization time was not enough to see a good signal as the obtained for the electrolyte supported electrolyzer (Figure 10.23), the production of H_2 is constant as observed by the mass spectrometer signal.

During the electrolysis mode, only three points were possible to be recorded since a problem occurred in the cell, which can be related with the high overpotential in the sample at -10 mA. Despite that, this second sample was measured as electrolyzer, achieving high Faraday's efficiency in the current range of operation (Figure 10.33).

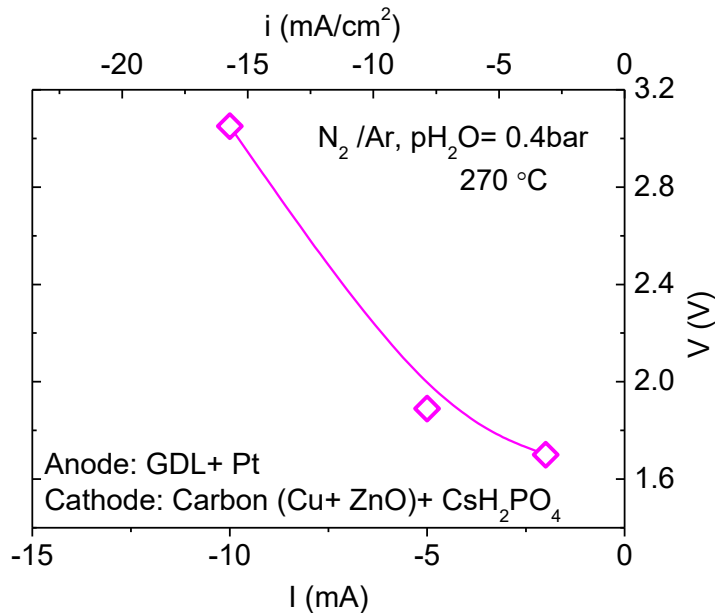


Figure 10.31: Cell overpotential of Pt on GDL/CDP/CDP and Cu+ZnO on Carbon supported on porous steel disc.

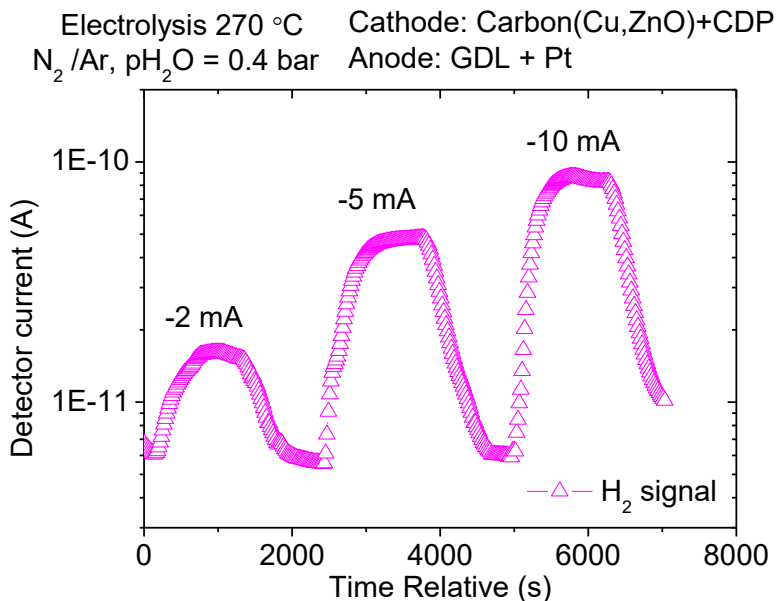


Figure 10.32: Hydrogen signal of the cathode outlet gas during electrolysis mode.

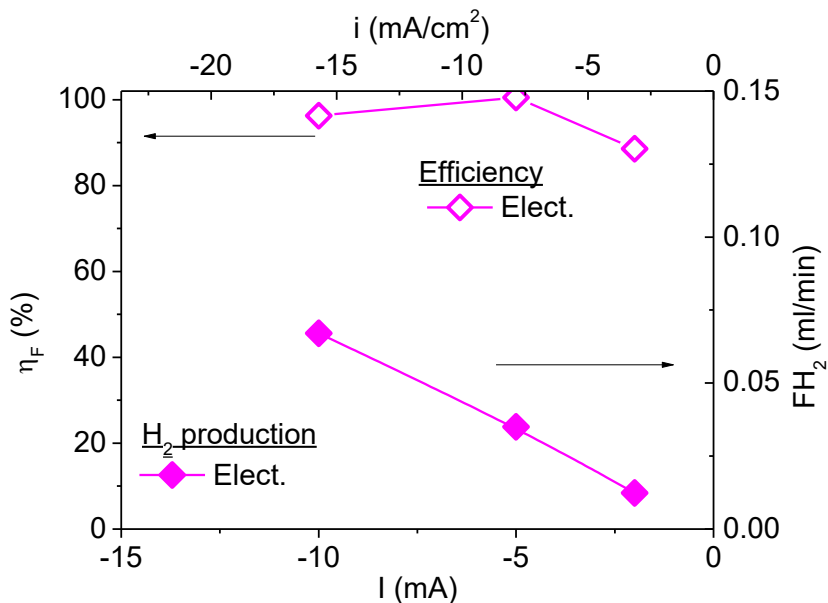


Figure 10.33: Hydrogen production and Faraday's efficiency, working with a 40 % vol. of steam.

10.2.3.2.3. FIB-SEM characterization

After test, the sample was characterized by Focused Ion Beam Scanning Electron Microscopy (FIB-SEM) with an Auriga Compact model in Zeiss equipment. Images of the different cells components and with different magnifications are presented in Figure 10.34.

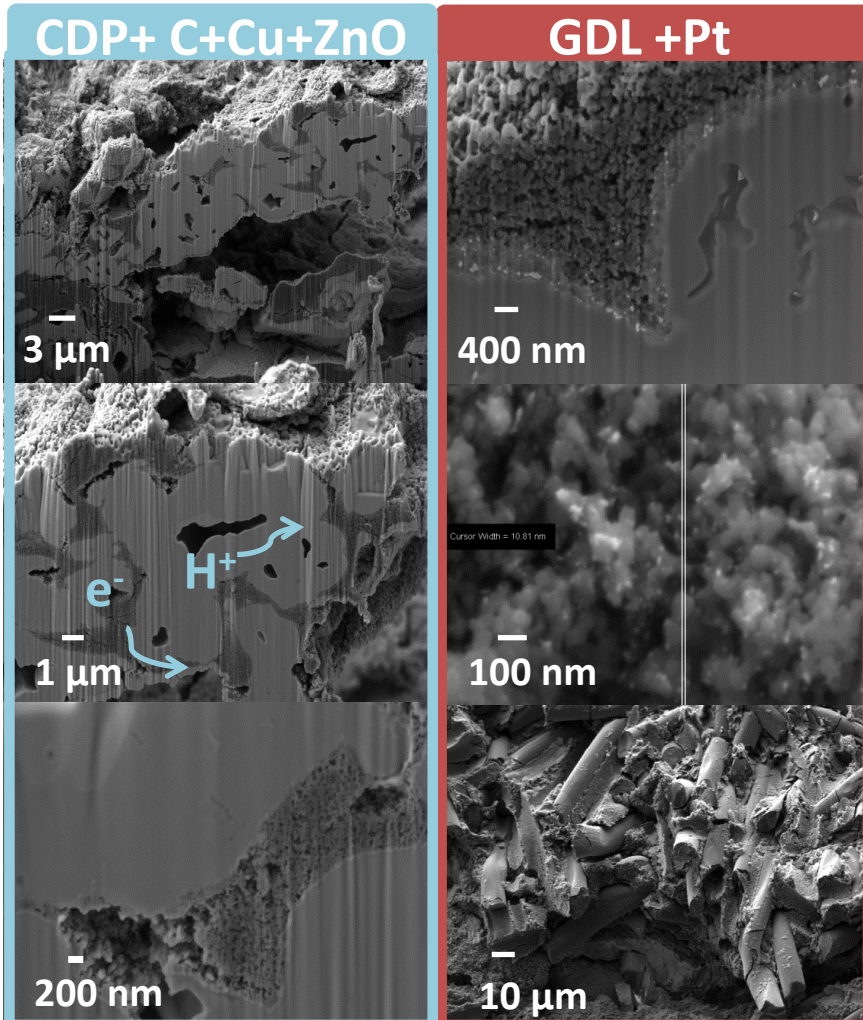


Figure 10.34: FIB-SEM images of the different electrodes with secondary electrons.

The left-hand image, shows that the electrode composed of a mixture of CDP and carbon impregnated with Cu and Zn oxide precursors. As can be inferred from the images, both phases are intimately mixed and there is enough porosity for gas diffusion. Additionally, paths for electrons and protons are created. Furthermore, the whole CDP surface covered by carbon and the Cu and Zn oxide nanoparticles (magnification on the last image in the first column) become active for the H₂ evolution reaction.

In the left-hand image (Figure 10.34) three pictures of the GDL electrode are shown. In the first one, the good attachment between electrode and electrolyte can be observed. Furthermore, the high density of the electrolyte can be ascertained. The image in the middle shows the Pt particles, having sizes ranging from 20 to 10 nm. This particle size range is comparable with the Pt used before in other studies [24]. Pt particles can also be distinguished in the first image since appear with higher brightness. Finally, the carbon fibers that are located at the far end of the electrolyte are shown in the image and have 10 μm of diameter. The thickness of the electrolyte, extracted from SEM images determined a CDP electrolyte of ~300μm.

10.2.4. Tailoring the mechanical properties of CDP electrolyte

The present results are still a long way from real applications, and much more can be done in order to improve the cell performance. Since that type of cell can work at high pressures obtaining higher efficiency, the mechanical stability of the electrolyte should be enhanced. Another challenge of CDP is the high plasticity or ductility that is product of the superprotonic phase [7]. Thus, the addition of another phase can improve the mechanical stability, for instance the addition of 10 % wt. of SiO₂ can improve the mechanical properties, *i.e.*, reduce deformation rates (Figure 10.35):

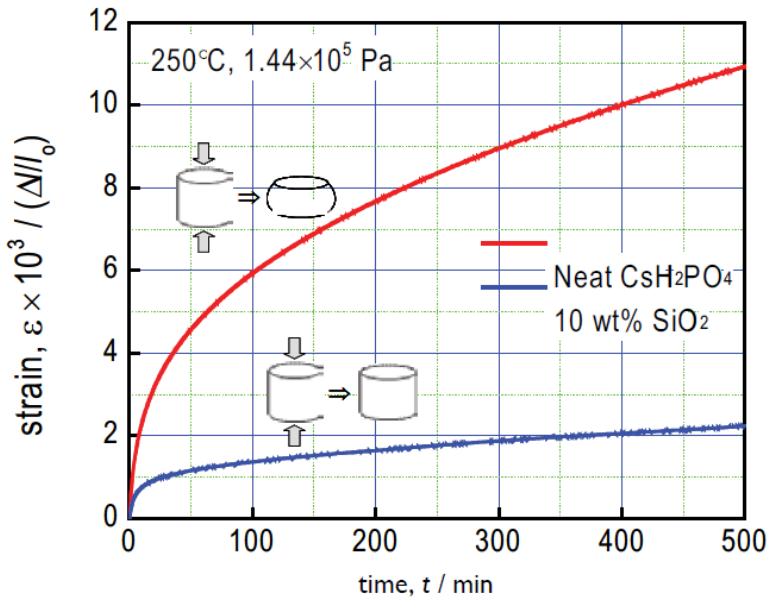


Figure 10.35: Mechanical deformation under constant stress of CsH_2PO_4 and mixture with 10wt% of SiO_2 [7].

Qing *et al.*, [25] studied the influence of working with composite electrolytes, composed of CDP and an epoxy. They found how the flexural strength is reduced by the epoxy incorporation (Figure 10.36).

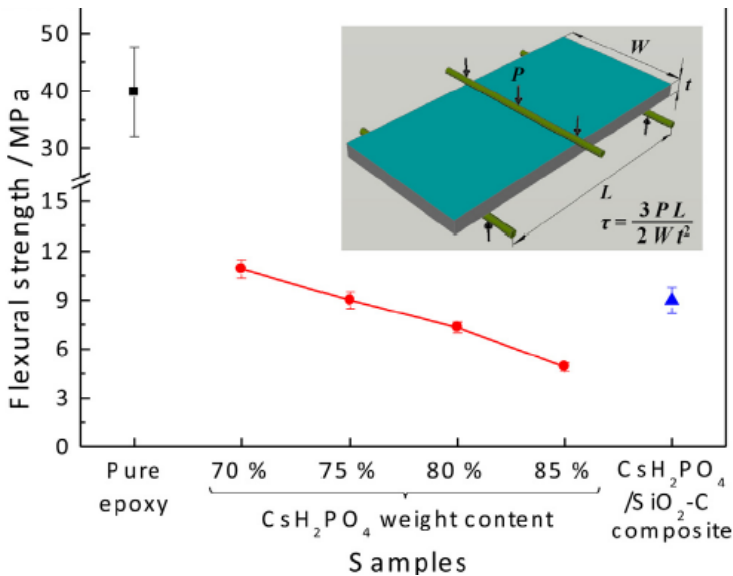


Figure 10.36: Flexural strength of composite electrolyte [25].

10.2.4.1. SEM and XRD electrolyte characterization

In order to improve the mechanical stability, the same method based on epoxy blending [25] was followed in this thesis. Firstly, and after CDP synthesis, the powder was milled for four days in dimethylformamide (DMF) medium. Powder was characterized before and after milling by X-Ray diffraction and SEM. The monoclinic structure of the material is maintained after milling and no extra peaks are observed in the XRD patterns (Figure 10.37), and no amorphization is visible. In addition, the average particle size is reduced at least three times (Figure 10.38). That size reduction allows a good homogenization of the powder and the epoxy. The composite was prepared by mixing in a mortar both materials with different percentages of weight.

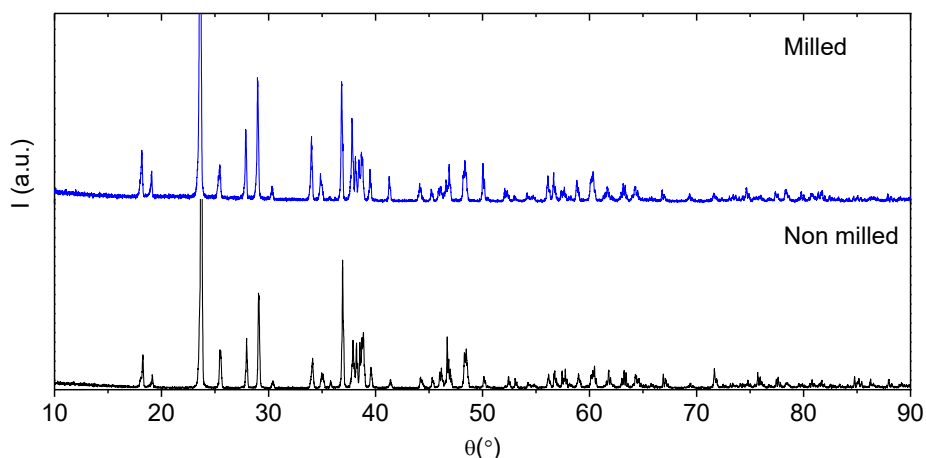


Figure 10.37: X-Ray diffraction of CDP before and after milling 4 days.

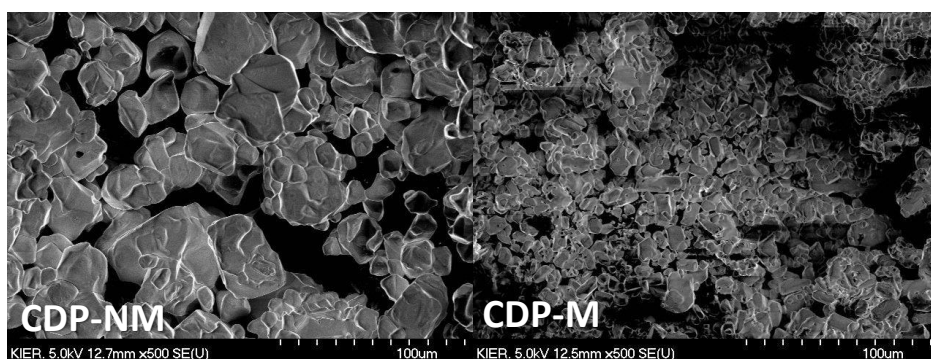


Figure 10.38: SEM micrographs of CDP after synthesis (CDP_NM) and after milling (CDP-M).

10.2.4.2. Electrochemical characterization of the electrolyte

Samples were characterized by electrochemical impedance spectroscopy and for that purpose, electrodes were applied by a silver paste. Argon with a 0.3 bar of water partial pressure was used for the EIS measurements. For all samples, a stabilization period was observed at the beginning during few days. The conductivity increased with time until achieving a steady state. After that, the conductivity results were maintained and by changing the temperature during the cell operation did not affect the stability of the sample conductivity (Figure 10.39). For long periods of time, cells with composite electrolyte were more stable than CDP working alone as electrolyte.

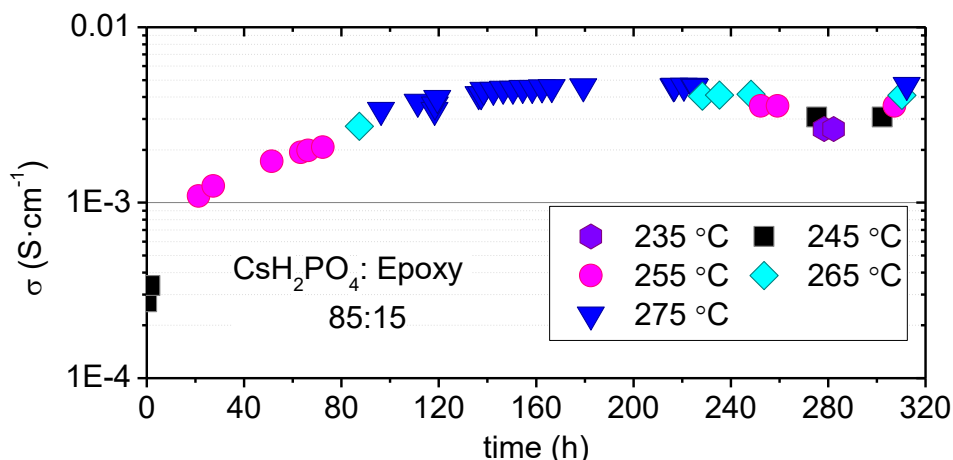


Figure 10.39: CDP: Epoxy 85:15 material conductivity measured as function of time for different temperatures with p_{H_2O} 0.3 bar in Ar.

Results of the conductivity obtained by EIS measurements are shown in Figure 10.40. On top of the graph it is shown the conductivity of the single CDP as electrolyte. As can be inferred from the graph, when the electrolyte is mixed with the epoxy the conductivity is reduced. High contents of epoxy reduce the conductivity in more than two orders of magnitude, whereas a high content of CDP also has the same effect. In the first case, the quantity of epoxy is too high limiting the proton pathways and the big contribution in the resistance is attributed to the negligible conductivity of the epoxy. However, in the second case the homogenization of the sample was very difficult (Figure 10.40), due to

the low content of liquid phase in the mortar. However the samples with 80 and 85 % percentage of CDP show the best results.

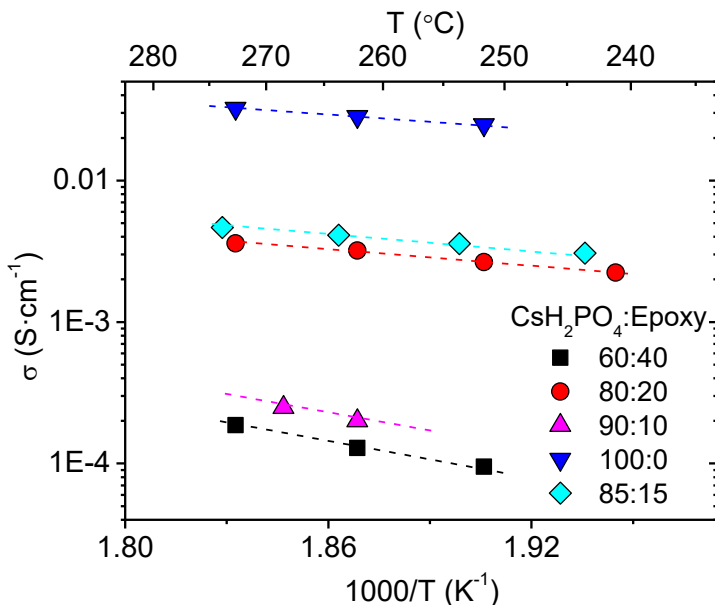


Figure 10.40: Conductivity of CDP: Epoxy composite electrolytes measured in Argon with a 30 % vol. of steam.

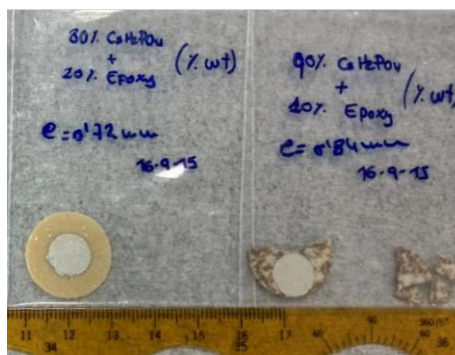


Figure 10.41: CDP: Epoxy samples after electrochemical test.

10.2.5. Active electrode support –Ni sponge

10.2.5.1. SEM and XRD electrode characterization

Finally, for the purpose of designing a cell with an active support electrode, a Ni sponge was selected. Ni electrodes designed for alkaline water electrolysis were studied in this section as support and active electrode for CDP-based

cells. These types of electrodes were developed by Kim *et al.*, [26]. Electrodes show an asymmetrical distribution in size, small pores near one surface ($\sim 5\mu\text{m}$) and the other surface with open structure with pore size between 100-200 μm . That asymmetry allows having one layer that plays the role of electro-catalytic layer whereas the open structure allows the easy gases diffusion. Nickel is well-known for hydrogen evolution reaction in aqueous acids and in alkaline systems [27, 28] and for the same type of cells [29].

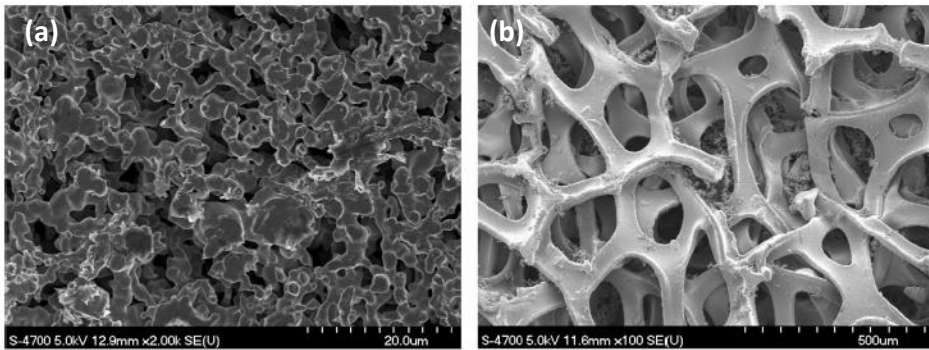


Figure 10.42: SEM images of (a) of the surface with smaller particles and (b) the gas diffusion part [26].

Furthermore, that type of structure allows the possibility to introduce different catalysts on the nickel surface. The catalysts can be introduced by immersing the nickel substrate in different solutions with the final catalyst precursors. Two different catalysts were studied, nickel and Co_3O_4 . Nickel was selected since it is a good catalyst for hydrogen oxidation, but the main objective was to check the influence of the particle size. In order to achieve lower particle size than Ni support, lower firing temperature was selected. However, Co_3O_4 was selected since it has been employed with nickel in different types of devices with good results, as in solar technologies for hydrogen production [30] or cells for water electrolysis which operate in a KOH, showing a high performance of Ni- Co_3O_4 for hydrogen evolution reaction [31]. Furthermore, Ni- Co_3O_4 is widely used for supercapacitor applications [32]. After immersing the different nickel supports in the nickel and cobalt solutions, samples were fired at 450 $^\circ\text{C}$. In order to check, the presence of the different nanocatalysts and phases, electrodes were characterized by XRD (Figure 10.43). As can be ascribed from the graph, cobalt sample shows three different phases, metallic nickel, NiO and

Co₃O₄. The metallic nickel exhibits the highest intensities whereas small peaks of NiO are observed, those peaks can be ascribed to a small oxidation of the sample in the infiltration or calcination process. Additionally, it can differentiate the peaks related with Co₃O₄, obtained after nitrates removal. Moreover, in the nickel oxide sample it can distinguish only two phases, one ascribed with the nickel support and the second one that is the sum of nickel infiltrated and nickel oxide from the support.

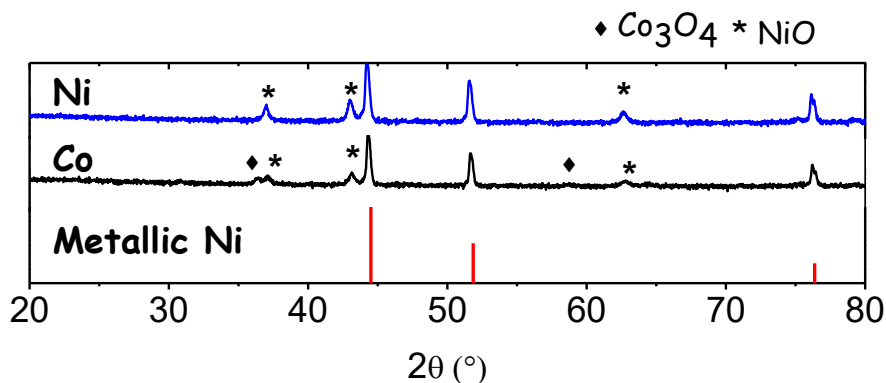


Figure 10.43: XRD of nickel support infiltrated with nickel and cobalt oxides.

The nanoparticles oxides obtained in the Ni support after precursor infiltration were studied by FE-SEM technique. FE-SEM images of NiO and Co₃O₄ nanoparticles are shown in Figure 10.44. Co₃O₄ is composed of sphere-like particles and irregular particles [33] with a size below 30 nm. However, NiO presents octahedral particles [34] with a size ≈ 90 nm. All nickel support was covered with the different nanoparticles.

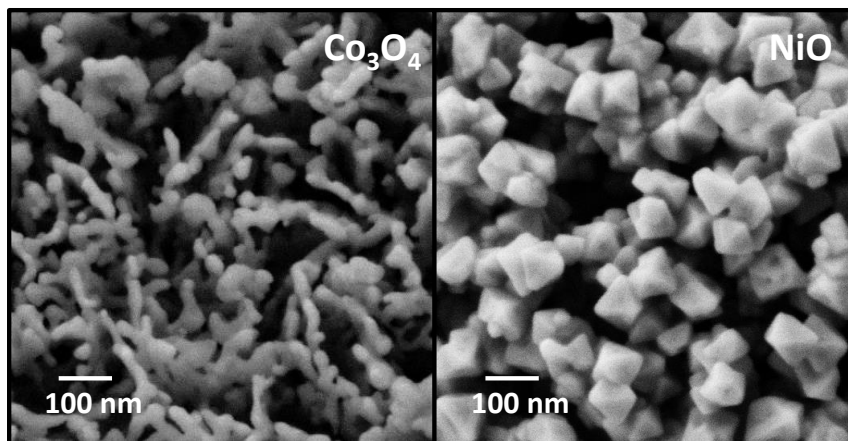


Figure 10.44: FE-SEM images of the nanoparticles infiltrated in the Ni support.

10.2.5.2. Electrochemical characterization

10.2.5.2.1. Electrodes characterization by symmetrical cell configuration

The electrodes obtained by the immersing method were characterized by electrochemical impedance spectroscopy by using symmetrical cells. Furthermore a commercial carbon paper with a 30% of Pt loading was also measured as electrode with a symmetrical cell configuration. The cell configuration consisted of a sandwich of two electrodes (with the same composition) with a CDP electrolyte in between (Figure 10.45). For the cell fabrication, the three parts were co-pressed.

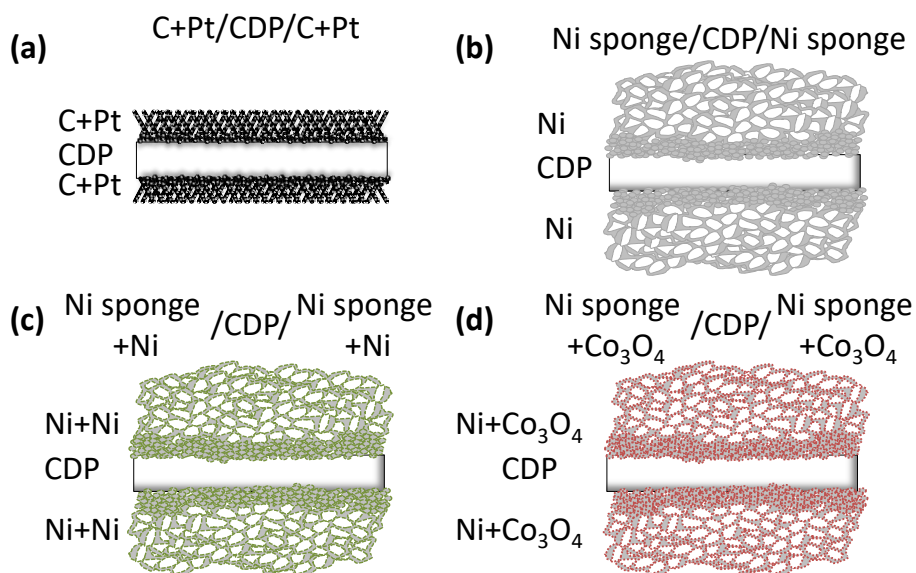


Figure 10.45: Symmetrical cells supported on the electrolyte (CDP) configuration; (a) commercial carbon paper infiltrated with Pt, (b) Ni sponge, (c) Ni sponge infiltrated with Ni and (d) Ni sponge infiltrated with Co_3O_4 as electrodes.

The carbon paper infiltrated with Pt selected for the EIS characterization was a commercial paper, 30 % of Pt on XC-72 with a loading of 0.5 mg/cm^2 supported on TGP-H-120 carbon paper from Naracelltech. FE-SEM images of the commercial electrode are presented in Figure 10.46. The first image shows the carbon fibers of paper, with $10 \mu\text{m}$ of diameter. At the bottom of the figure, two images of the same part of the electrode are shown but one was done with back scattered electrons detector (Figure 10.46 (b)) whereas the other one was done with secondary electrons detector (Figure 10.46 (c)). The first image, shows bright Pt nanoparticles well distributed, with a particle size around 2 nm. That small size of the Pt particles can allow high catalytic activity [21]. On the right side it can appreciate the 50 nm XC-72 particles

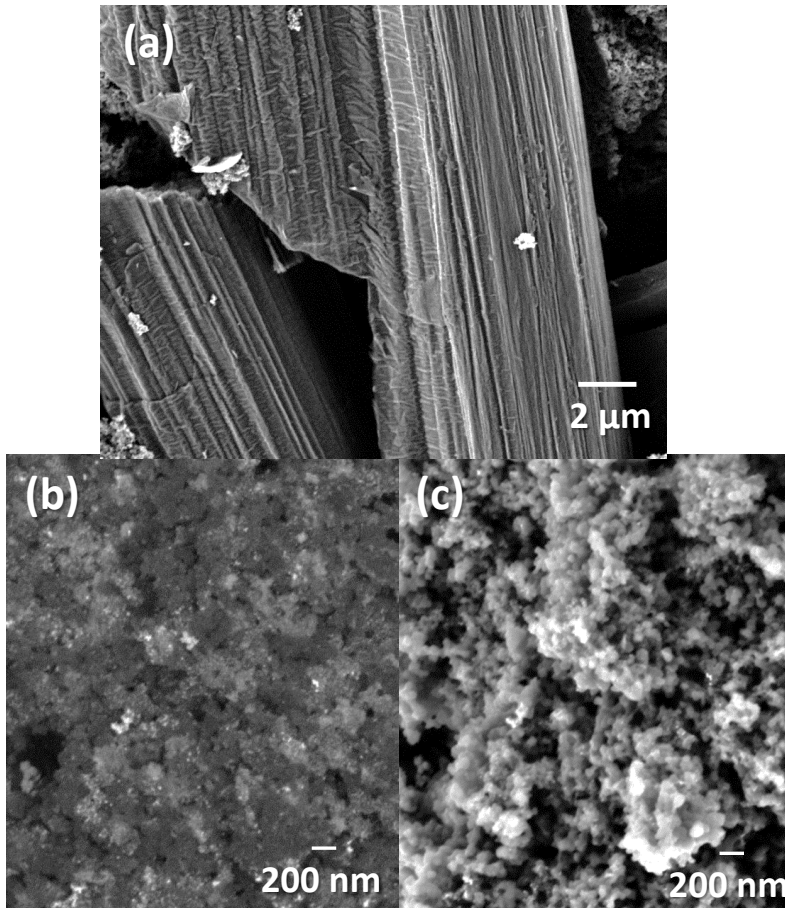


Figure 10.46: FE-SEM images of (a) carbon fibers and (b) BSE (c) SE FE-SEM images of XC-72 with Pt nanoparticles.

Electrochemical impedance spectroscopy measurements of the symmetrical cell with Pt commercial paper as function of time with a reducing atmosphere (3% H₂ in argon with 0.3 bar of water partial pressure) are presented in Figure 10.47. As was expected, Pt is very active for the hydrogen oxidation/ reduction reaction, with relatively low resistance. However, the Pt electrode is very unstable with time, since it was not possible to maintain any value of polarization resistance along the sample test. Additionally, when the temperature is increased the activity of the catalyst is practically not enhanced while the damage of the electrode is still taking place on the EIS results (Figure 10.49). As can be ascribed from both figures (Figure 10.47 and Figure 10.49),

the biggest resistance takes place at medium frequencies (MF 10-1000 Hz) and is shifted to lower frequencies with time. To enable the possibility to check the electrodes limitation, the EIS spectrum as function of time were fitted with an equivalent electrical circuit (LR_Ω-(RLF-CPELF)-(RMF-CPEMF) and results are shown in Figure 10.48. RLF increases with time, whereas the MF resistance remains almost constant with time (Figure 10.48 (a)). For short periods of time the limiting resistance takes places at MF, but after 1000 minutes the RLF becomes the limiting contribution, lowering the associated capacitances (Figure 10.48 (b)). Ciureanu *et al.*, [35] studied the different contributions that appear in the EIS spectrum for Pt electrodes in PEMFC working with H₂ atmospheres in both chambers. They found two arcs, one at high frequency and another at low frequency. The HF arc was related with the charge transfer process ($\text{Pt-H}_{\text{adsorbed}} \rightarrow \text{Pt} + \text{H}^+ + \text{e}^-$) and LF with chemiadsorption of H₂ ($\text{H}_2 + 2\text{Pt} \rightarrow 2\text{Pt-H}_{\text{adsorbed}}$) or due to the low gas flow. Since RMF is maintained with time can be associated with the charge transfer, whereas for LF the chemiadsorption would be the suitable explanation, since the flow was maintained in all tests. The RLF behavior can be related with the poisoning of the Pt in contact with the CDP. The Pt poisoning reduces the activity and sites for the hydrogen chemiadsorption. A strong adsorption of phosphate anions has been reported for phosphoric acid based cells, poisoning the platinum particles [36, 37] and reducing the activity. Other degradation pathways were also observed in Pt nanoparticles by Meier *et al.*, [38] that can be also the explanation of the electrode behavior: (i) dissolution of Pt nanoparticles in the electrolyte material, (ii) agglomeration of Pt particles and (iii) particle detachment. Additionally, the real resistance associated with the electrolyte is kept in all measurements done at 235 °C (Figure 10.47). Despite the fact that there is degradation in the electrode performance with time and higher temperature does not have any effect in the activation of the electrode performance, the electrolyte decreases the resistance (Figure 10.49). As could be expected from the previous results of CDP conductivity, by increasing temperature the proton conductivity increases. Thus, there is not degradation of the electrolyte material with the electrode deterioration.

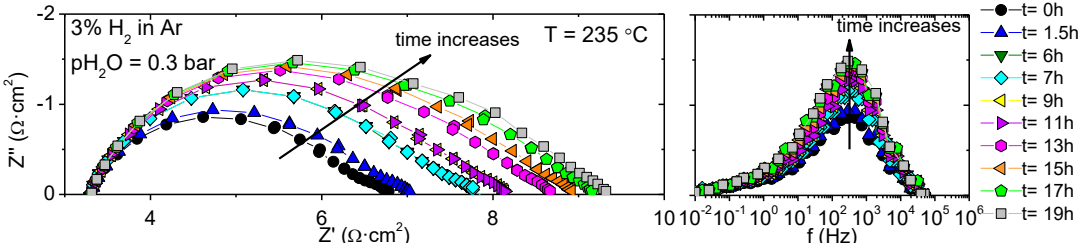


Figure 10.47: Nyquist a Bode plot, left and right, respectively, of carbon paper with Pt at 235 °C as function of time.

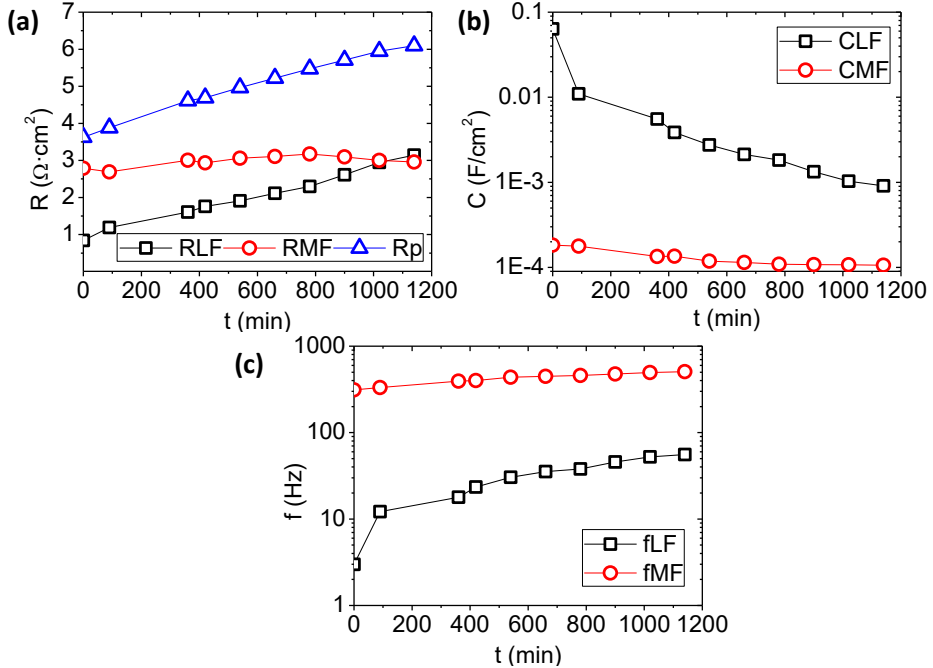


Figure 10.48: Equivalent electrical circuit fitting results; (a) resistance, (b) capacitance and (c) frequency of Pt on C paper/CDP/ Pt on C paper as function of time.

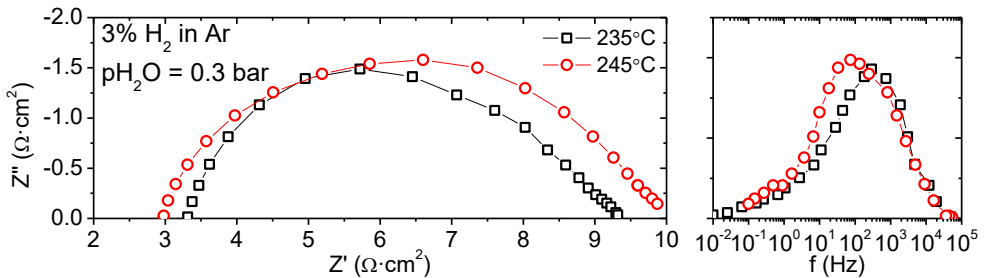


Figure 10.49: Nyquist a Bode plot, left and right, respectively, of carbon paper with Pt as function of temperature.

After the EIS measurements in H₂ atmospheres, the electrode composed of the commercial carbon paper with Pt were tested in air atmospheres with 0.3 bar of water partial pressure at different temperatures (Figure 10.50). In contrast to the H₂ measurements, in air there is activation of the electrode with temperature in spite of the non-stability of the electrode. However, the electrode is not as active as for the hydrogen oxidation, usually the main limiting reactions in proton cells working with Pt as catalyst in PEMFC occur in the cathode [39]. The oxygen reduction reaction that is involved in the cathode can be described by three main stages: (1) O₂ adsorption, (2) electrochemical and chemical reaction with intermediate species and (3) intermediates or O₂ protonation for the water formation [40].

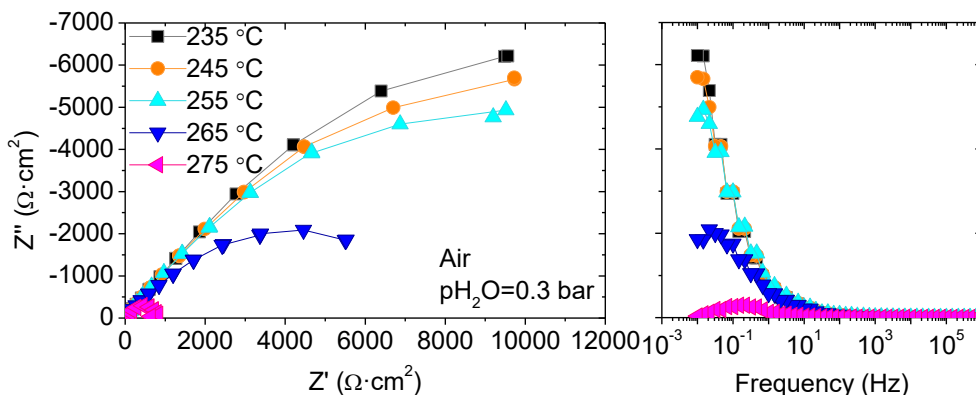


Figure 10.50: Nyquist a Bode plot, left and right, respectively, of carbon paper with Pt at different temperatures in air.

The different contributions in the EIS spectra were distinguished by fitting with an equivalent electrical circuit (LR₀-(RLF1-CPELF1)-(RLF2-CPELF2)). Two resistances limit the electrode performance, and both of them take place at low frequencies with low associated capacitances (Figure 10.51). RLF1 has the highest resistance contribution and reduces its resistance in more than one order of magnitude when the cell works at 275 °C. Thus RLF1 could be associated with the thermal activation of the Pt in the operation conditions. RLF2 has a lowest contribution in all range of temperatures except for 275 °C. At 275°C RL2 becomes the limiting contribution. The associated capacitances are almost constant but increases for both resistances. Parthasarathy *et al.*, [41] showed one big process in OCV conditions (for a PEMFC) that takes place with a relaxation frequency of ≈ 0.15 Hz and can be ascribed to the oxygen-

reduction charge-transfer process. This frequency range fits with the results obtained here for the RLF2 to the mass transport limitation [39], and higher fluxes or pure oxygen could improve the cell performance.

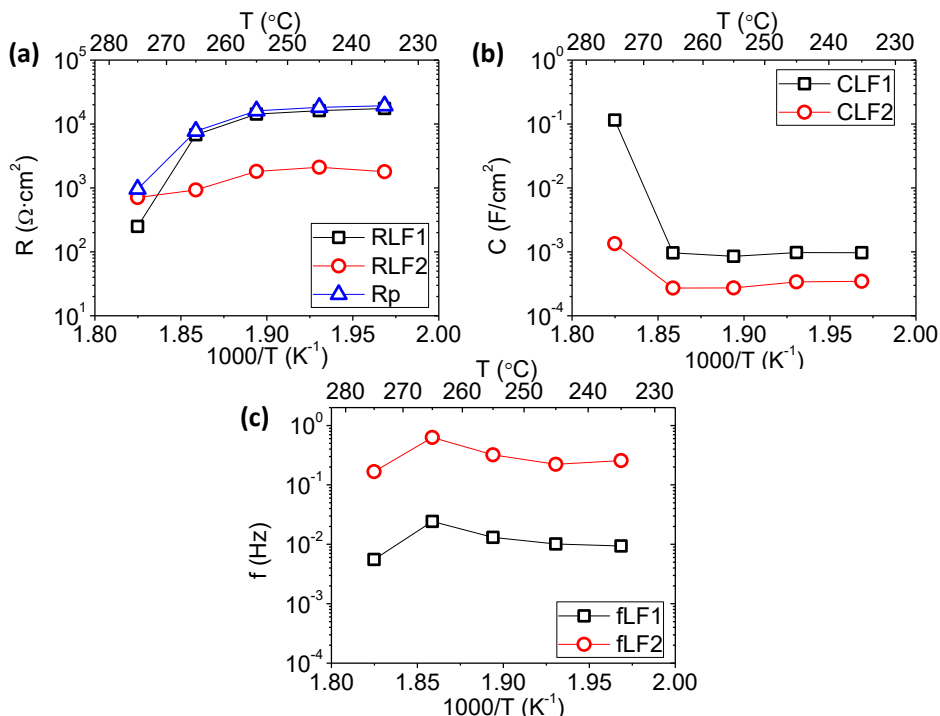


Figure 10.51: Equivalent electrical circuit fitting results; (a) resistance, (b) capacitance and (c) frequency of Pt on C paper/CDP/ Pt on C paper as function of temperature in air conditions with $p_{H_2O} = 0.3$ bar.

Then, the Ni sponge was tested without any catalyst infiltration as electrode in the same conditions selected for the Pt electrodes (3 % H_2 in argon with $p_{H_2O} = 0.3$ bar). EIS spectra of the symmetrical cell as function of temperature are shown in Figure 10.52. As the temperature is increased a big reduction of the polarization resistance is produced, that improvement is result of the catalyst activation with temperature. In addition, it seems that the reduction of the resistance is steeper when the temperature increases above $255^{\circ}C$. Further discussion about this point will be done in detail below. Furthermore, a big stability was obtained for this type of electrode, with a first stabilization accompanied by a reduction of polarization resistance, by finally achieving a constant value (Figure 10.53).

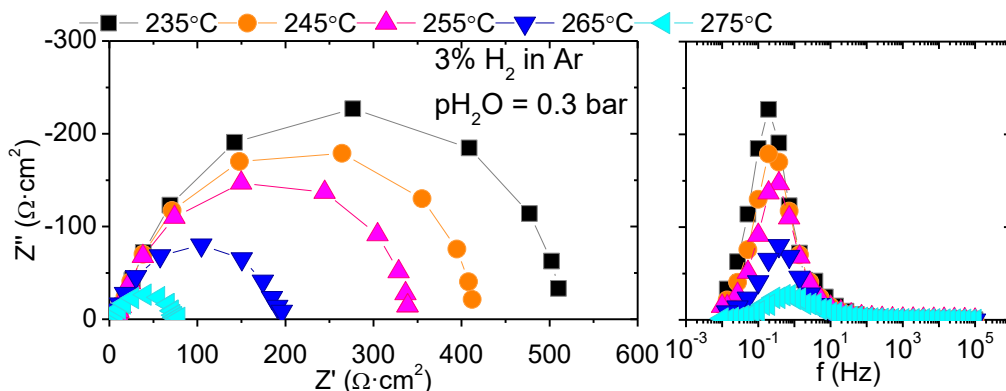


Figure 10.52: Nyquist a Bode plot, left and right, respectively, of Ni sponge/CDP/Ni sponge cell as function of the temperature.

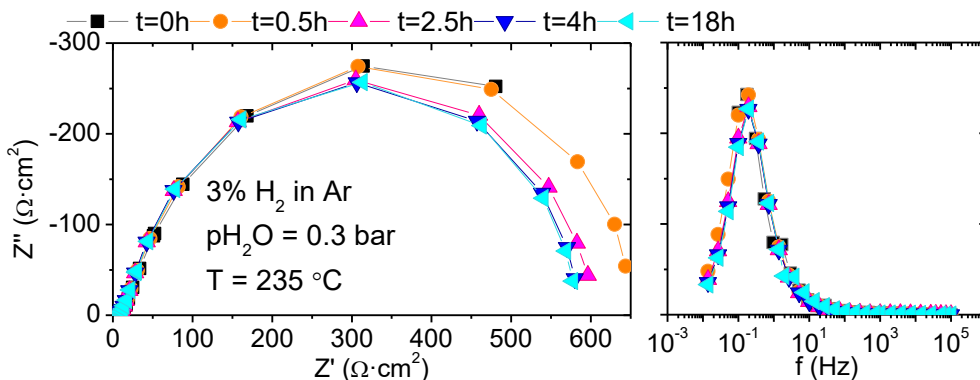


Figure 10.53: Nyquist a Bode plot, left and right, respectively, of Ni sponge/CDP/Ni sponge cell as function of time.

In the same way, the samples infiltrated with Ni and Co_3O_4 precursors were measured as symmetrical cells in the same conditions and the polarization resistance results as function of temperature are shown in Figure 10.54 and Figure 10.55. In order to compare directly the electrode performance, the real resistance ascribed to the electrolyte was subtracted in all Nyquist plots. The real resistance was temperature dependent showing values of $7 \Omega \cdot \text{cm}^2$ at 275°C or $15 \Omega \cdot \text{cm}^2$ at 245°C .

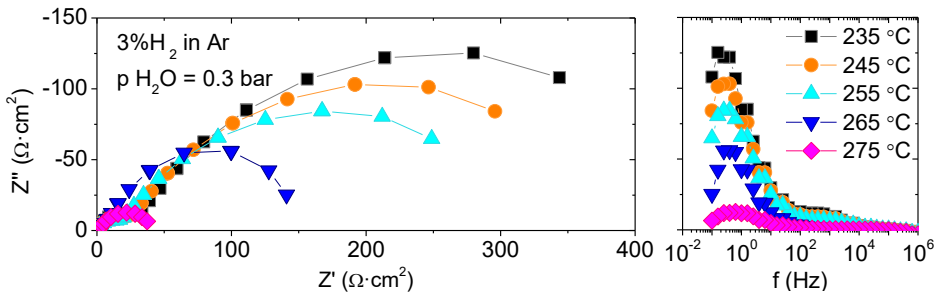


Figure 10.54: Nyquist a Bode plot, left and right, respectively, of Ni sponge+Ni/CDP/Ni sponge+Ni cell as function of the temperature.

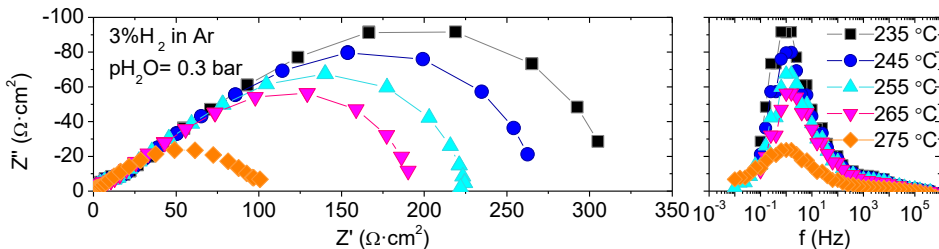


Figure 10.55: Nyquist a Bode plot, left and right, respectively, of Ni sponge+ Co_3O_4 /CDP/Ni sponge+ Co_3O_4 cell as function of the temperature.

Both samples exhibit the same trend with temperature, reducing the polarization resistance when temperature is increased. The activation of the catalyst is obtained by heating the sample. It should be point out that the operation conditions are limited by the stability of CDP being not possible to increase the temperature in the cell above 280 °C (Figure 10.6). Furthermore, the stability at the highest temperature measured for Co_3O_4 infiltrated was checked and results are shown in Figure 10.56. The polarization resistance remains stable after more than 20 hours of measurements, even reducing the polarization resistance. It seems that there is no catalyst contamination or microstructure degradation.

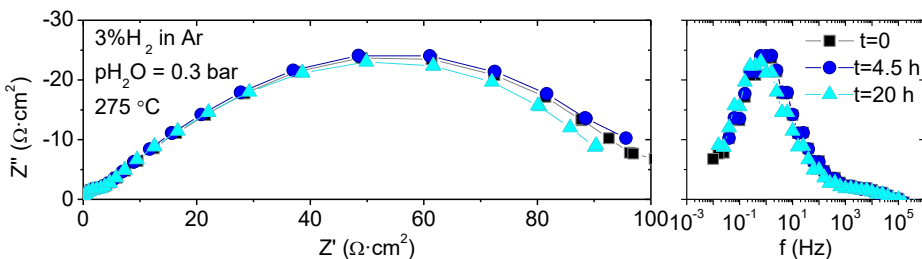


Figure 10.56: Nyquist a Bode plot, left and right, respectively, of Ni sponge+ Co_3O_4 /CDP/Ni sponge+ Co_3O_4 cell as function of time.

In order to compare directly the behavior of the three different electrodes, an Arrhenius type plot of R_p is presented below (Figure 10.57). The three electrodes have two different activation energies, one below 265 °C and the other one at higher temperatures. All samples present a huge reduction of R_p when the temperature is increased above 265 °C. In addition, both infiltrations can reduce the polarization resistance of the pristine sample. However, the behavior of Ni and Co₃O₄ nanoparticles is not the same. At low temperatures the Ni nanoparticles have only a small effect in the R_p improvement, whereas Co₃O₄ can reduce in more than 100 $\Omega\cdot\text{cm}^2$ the blank sample resistance. However, above 275 °C, Ni precursor infiltrated sample exhibits an outstanding improvement achieving a value of 44 $\Omega\cdot\text{cm}^2$, showing that good activity commented above.

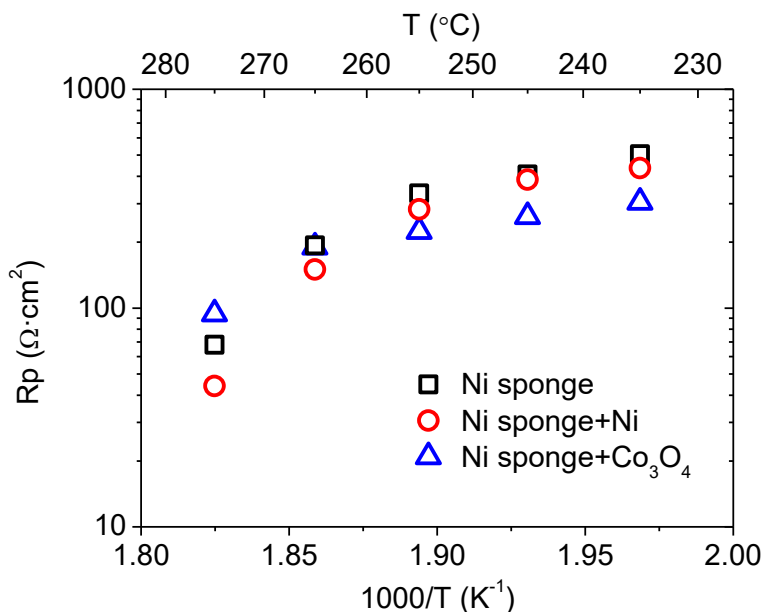


Figure 10.57: Polarization resistance of the three different electrodes: Ni sponge, Ni sponge+Ni infiltrated and Ni sponge and Co₃O₄ infiltrated electrodes as function of temperature.

In order to go one step further the EIS spectra at different temperatures for all Ni sponge electrodes (Figure 10.52, Figure 10.54 and Figure 10.55) were characterized by an equivalent circuit. For the electrodes infiltrated the equivalent electrical circuit consisted of three resistances in parallel with three CPE; LR_Ω-(RLF1-CPELF1)-(RLF2-CPELF2)-(RHF-CPEHF). However, for the parent Ni electrode the equivalent electrical circuit employed is different and is

presented in the Figure 10.58. Results of the fitting are shown in Figure 10.59. As to be able to compare between the different electrodes, the three processes of each electrode have been split depending on the frequency range. LF1, is the lowest resistance, LF2 is low resistance and HF is high frequency. In the case of parent Ni electrode, the RLF2 refers to the R_{chem} .

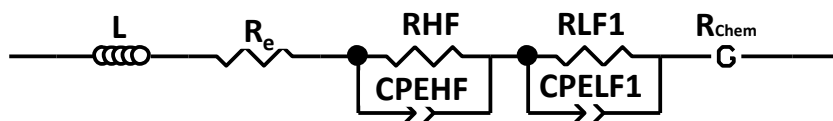


Figure 10.58: Equivalent electrical circuit for the Ni sponge electrode.

The lowest contribution takes place at high frequencies ($2 \cdot 10^3$ to $1 \cdot 10^4$ Hz) with a low associated capacitance for all samples ($3 \cdot 10^{-6}$ to $2 \cdot 10^{-5}$ F/cm²). The resistances for all range of temperature goes from $0.5 \text{ } \Omega \cdot \text{cm}^2$ for the Ni infiltrated sample at the highest tested temperature to $20 \text{ } \Omega \cdot \text{cm}^2$ for the Co_3O_4 at the lowest temperature. The HF resistance can be associated with the charge transfer for the HOR in the interface electrode-electrolyte [39, 42]. Since electrodes are pure electronic conductors, the HOR will take place on the active sites located in the electrode-electrolyte surface (TPB). Co_3O_4 exhibits the highest resistance, whereas nickel support has the lowest ones. The higher electrical conductivity of Ni in contrast with Co_3O_4 could be the explanation of the lower resistance of Ni backbone electrode. In addition, there is a thermal activation in both catalyst infiltrated, improving the charge transfer in the HOR.

RLF1 process has a characteristic frequency in the range of 0.1 to 1 Hz for the three electrodes in all range of temperature. The associated capacitance values vary from $1 \cdot 10^{-3}$ to $8 \cdot 10^{-3}$ F/cm². These resistances have the highest contribution in the R_p for all samples, limiting the cell performance. For all samples there is a thermal activation in all range of temperatures. While Co_3O_4 shows only one activation energy in the RLF2 as function of $1000/T$ (Figure 10.59 (d)), both Ni catalysts exhibit two activation energies. The frequency range for RLF2 is in between 0.5 Hz and 20 Hz. In this case, all samples have similar resistance values until $255 \text{ } ^\circ\text{C}$, where there are different catalytic activations.

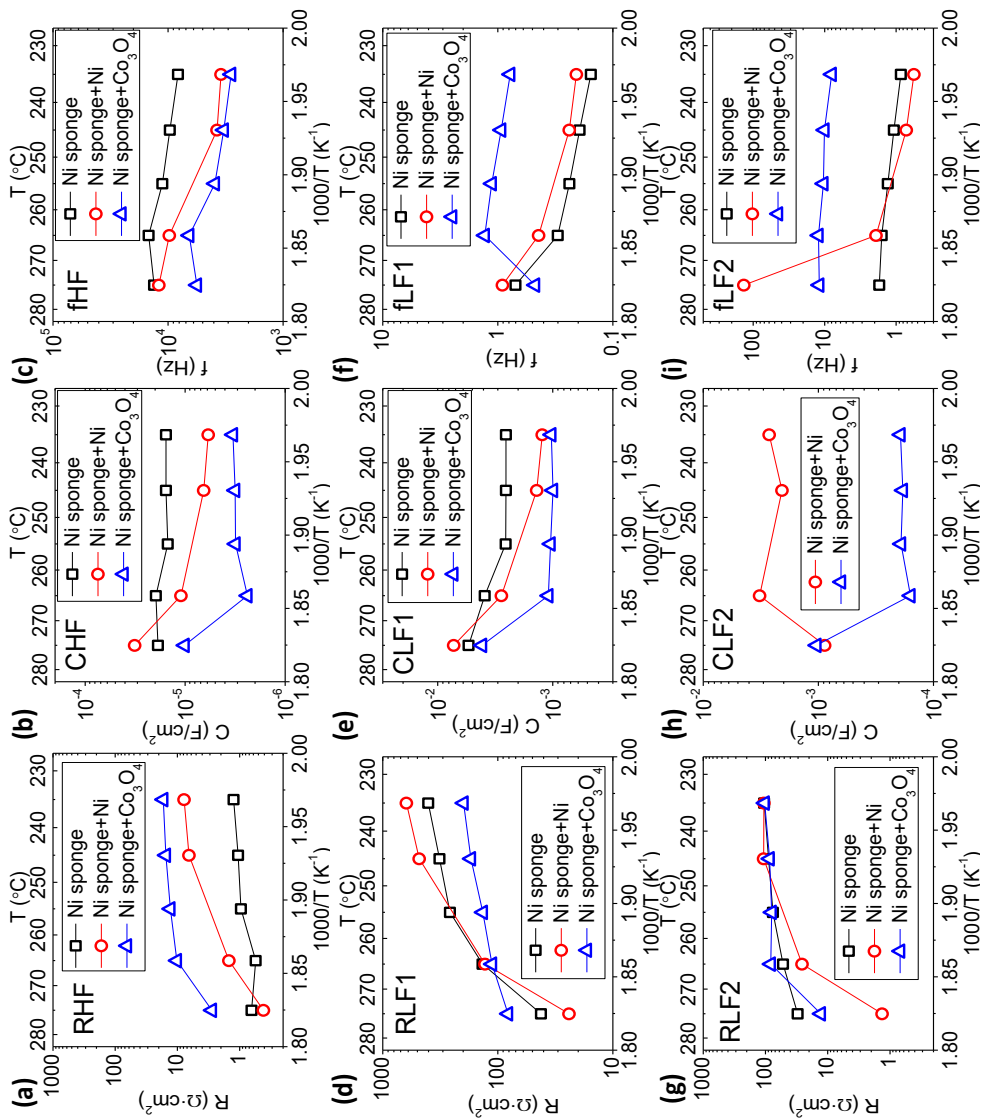


Figure 10.59: Equivalent electrical circuit fitting results; (a) resistance and (c) capacitance and (e) frequency at HF, (d) resistance, (e) capacitance and (f) frequency of LF1, (g) resistance, (h) capacitance and (i) frequency at LF2 of Ni sponge, Ni sponge +Ni and Ni sponge + Co₃O₄ at different temperatures.

Different processes has been suggested for the low frequency resistances, slow gas diffusion due to the low gas flow, gas conversion or dissociative chemisorption of hydrogen at the electrode ($H_2 \rightarrow 2H_{\text{adsorbed}}$) [16, 35, 42]. Since the hydrogen percentage was maintained in 3% due to the limitations in the set-up (all these measurements were performed in Korea Institute of Energy Research in Korea in a different set-up), the lowest frequency resistance could be associated with that fact. Nevertheless, the RLF2 could be interpreted as hydrogen chemisorption and electrochemical reaction coupled, due to the frequency range and the use of Gerischer element in the Ni sponge EIS fitting. Finally, the lower resistance of Ni infiltrated catalyst at high temperatures can be assigned to the higher surface area of the smaller particles, allowing higher active area for the hydrogen oxidation reduction reaction.

10.2.5.2.2. Fuel cell characterization

Finally, the electrolyte composed of Epoxy and CDP with a weight percentage of 20:80 was tested as electrolyte in real operation conditions in a fuel cell mode. For that purpose, Ni-sponge was selected as anode and the commercial carbon paper with 30% of Pt loading as cathode (Figure 10.61).

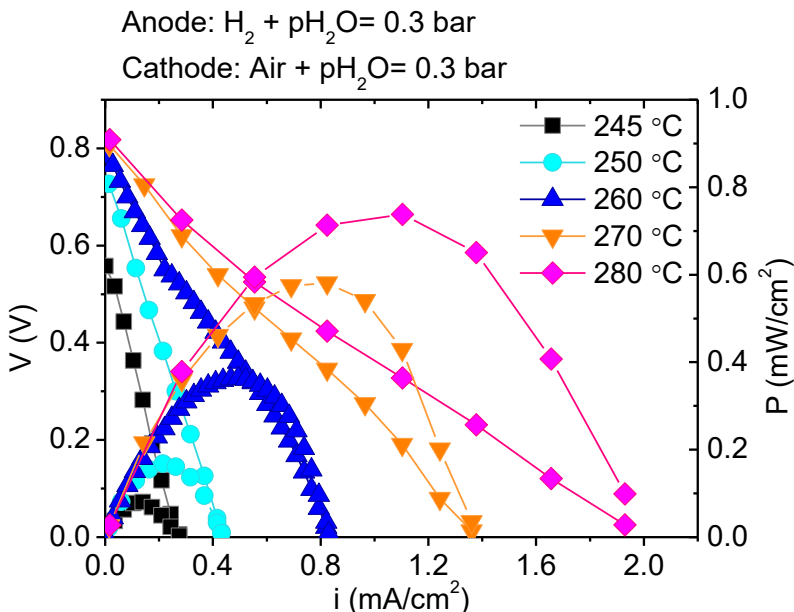


Figure 10.60: i - V and i - P curves of Ni sponge/CDP:Epoxy (80:20)/carbon+Pt as function of temperature.

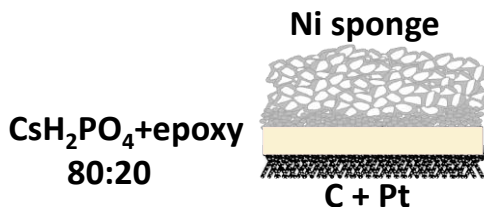


Figure 10.61: Ni sponge/CDP:Epoxy (80:20)/carbon+Pt configuration cell.

Firstly, the sample was tested in a fuel cell mode as function of temperature, and the discharge curves are shown in Figure 10.60. As can be ascribed from Figure 10.60, there is a big influence of the operation temperature on the power density. Furthermore, as the temperature is increased, the OCV of the sample increases. During all measurements, the same behavior was obtained for all samples, indicating that the OCV is dependent on the cell performance and increases when the power density is improved. As the temperature is increased the activity of the electrodes is enhanced, implying higher power densities. As was observed in Figure 10.50 and Figure 10.52, the polarization resistance of electrodes is improved with temperature. Furthermore, the main limitations in the fuel cell efficiency are expected to be ascribed to the electrodes performance. In addition, the cathode reactions limit the fuel cell performance as was previously reported [39] and was observed on the EIS results for the symmetrical cell working in air with Pt catalyst (Figure 10.50), due to the high R_p . Additionally, the composite electrolyte has higher resistance than the pure CDP, producing another contribution to the total cell performance.

Since the electrolyte was developed in order to use it in a system with high pressures, the cell was tested with high pressures. H₂ and air were also used for the anode and cathode, respectively, and the water partial pressure was maintained in 0.3 bar. The OCV also increases with pressure, this behavior fits with the results obtained before. However, at the highest temperature, there is a small reduction of the OCV. A possible leakage in the cell from one chamber to the other would be the explanation of the OCV reduction. Higher pressures can increase the cell performance and the power density reaches values of $\sim 2\text{mW}/\text{cm}^2$ by increasing the system pressure to 5.5 bar, indicating again the catalytic improvement of the electrodes.

Electrochemical impedance spectroscopy was not possible for the cell, since some problems in the wires produced an extremely noisy signal.

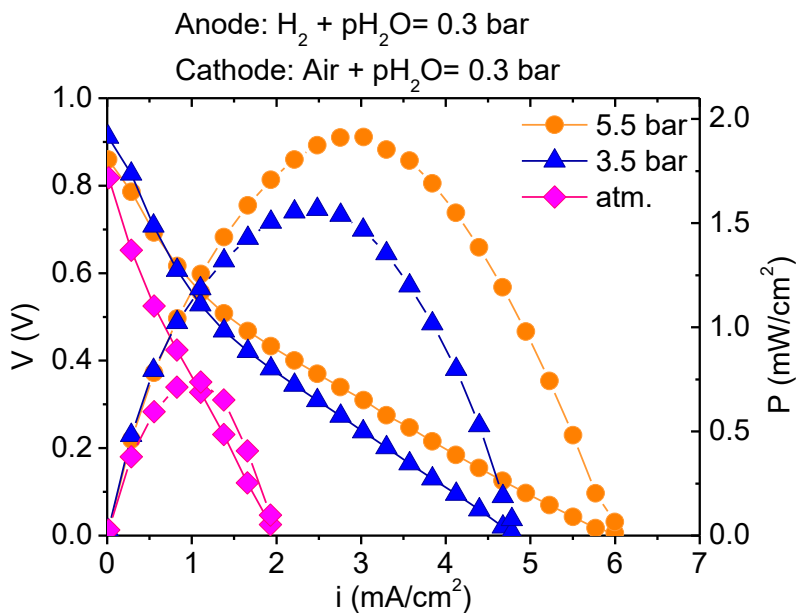


Figure 10.62: i - V and i - P curves of Ni sponge/CDP:Epoxy (80:20)/carbon+Pt as function of the system pressure.

10.3. Conclusions

Firstly, a set-up for measure cells at low temperatures with high contents of water and high pressures was developed in this thesis. After that, CsH_2PO_4 was studied for working as electrolyte in fuel cell and electrolysis conditions.

CsH_2PO_4 (CDP) was characterized by DC conductivity and XRD, showing a phase transition above 232 °C followed by an outstanding conductivity improvement.

Different catalysts were studied in order to replace the expensive Pt used for the common low operation fuel cells. Cu and Zn were used as alternative catalysts for the HOR and ORR, in the fuel cell and electrolysis mode. The influence of different parameters as temperature or pressure was studied. There was an important thermal activation and cell improvement with the system pressure. For instance, the electrode composed of Cu and ZnO could increase the power density four times by increasing the system pressure in 4.5

bar. Two different cell configurations were tested as electrolyzer. In the first one, the electrolyte was used as cell support and two different electrodes were employed, Ag and Pt in the anode and Cu and ZnO in the cathode. After that, the cell performance was improved by reducing the electrolyte thickness and tailoring the electrodes characteristics. An important improvement was obtained by preparing a composite electrode. CDP was selected as the protonic phase, whereas carbon impregnated with Cu and ZnO was used as electronic conductor. That strategy allowed enlarging the TPB along the electrode area.

As to increase the mechanical stability of the electrolyte, composite electrolytes were prepared by mixing CDP an Epoxy.

In addition, Ni sponge was studied as alternative for the hydrogen oxidation reaction catalyst and as support for the cell manufacture. The nickel support performance could be boosted infiltrating different catalysts inside the scaffold as Co₃O₄ and Ni. The higher surface area of the smaller Ni particles infiltrated could reduce the polarization resistance of the electrode. Furthermore, the commercial carbon paper with 30 % of Platinum showed degradation with time, increasing the resistance of the electrode at LF.

The low power densities and the high voltages in the electrolysis mode are still far for real applications but it has been demonstrated the use of these types of cells as fuel cell and electrolyzer and the high influence of pressure, allowing using high pressures in the system and non-precious metals as catalysts.

Further work should be done in order to improve the electrodes performance, but the preliminary results shown here permit to know which characteristics have to be tailor in the cell performance.

10.4. References

- [1] S.M. Haile, C.R.I. Chisholm, K. Sasaki, D.A. Boysen, T. Uda, *Faraday Discuss.*, 134 (2007) 17-39.
- [2] A.B. Papandrew, D.L. Wilson, N.M. Cantillo, S. Hawks, R.W. Atkinson, G.A. Goenaga, T.A. Zawodzinski Jr, *J. Electrochem. Soc.*, 161 (2014) F679-F685.
- [3] H. Muroyama, T. Matsui, R. Kikuchi, K. Eguchi, *J. Electrochem. Soc.*, 156 (2009) B1389-B1393.

- [4] A.B. Papandrew, C.R.I. Chisholm, R.A. Elgammal, M.M. Özer, S.K. Zecevic, *Chem. Mat.*, 23 (2011) 1659-1667.
- [5] S.M. Haile, *Acta Materialia*, 51 (2003) 5981-6000.
- [6] K.A. Sasaki, Y. Hao, S.M. Haile, *Physical Chemistry Chemical Physics*, 11 (2009) 8349-8357.
- [7] C.R.I. Chisholm, D.A. Boysen, A.B. Papandrew, S. Zecevic, S. Cha, K.A. Sasaki, A. Varga, K.P. Giapis, S.M. Haile, *Electrochemical Society Interface*, 18 (2009) 53-59.
- [8] G. Kim, F. Blanc, Y.Y. Hu, C.P. Grey, *J. Phys. Chem. C*, 117 (2013) 6504-6515.
- [9] M.W. Louie, M. Kislitsyn, K. Bhattacharya, S.M. Haile, *Solid State Ion.*, 181 (2010) 173-179.
- [10] J. Otomo, N. Minagawa, C.-j. Wen, K. Eguchi, H. Takahashi, *Solid State Ion.*, 156 (2003) 357-369.
- [11] Y.K. Taninouchi, T. Uda, Y. Awakura, A. Ikeda, S.M. Haile, *J. Mater. Chem.*, 17 (2007) 3182-3189.
- [12] Y.k. Taninouchi, T. Uda, Y. Awakura, *Solid State Ion.*, 178 (2008) 1648-1653.
- [13] H. Li, Y. Tang, Z. Wang, Z. Shi, S. Wu, D. Song, J. Zhang, K. Fatih, J. Zhang, H. Wang, Z. Liu, R. Abouatallah, A. Mazza, *J. Power Sources*, 178 (2008) 103-117.
- [14] G.J.J. Bartley, R. Burch, *Applied Catalysis*, 43 (1988) 141-153.
- [15] A. Bansode, B. Tidona, P.R. von Rohr, A. Urakawa, *Catalysis Science & Technology*, 3 (2013) 767-778.
- [16] J. Hallinder, *Electrolytes and Electrodes for Electrochemical Cells Operating at 200 - 300 °C*, Technical University of Denmark, 2013.
- [17] T.P. Holme, R. Pornprasertsuk, F.B. Prinz, *J. Electrochem. Soc.*, 157 (2010) B64-B70.
- [18] M.W. Louie, K. Sasaki, S.M. Haile, *ECS Transactions*, 2008, pp. 57-62.
- [19] M.W. Louie, S.M. Haile, *Energy and Environmental Science*, 4 (2011) 4230-4238.
- [20] J. Perez, E.R. Gonzalez, E.A. Ticianelli, *Electrochim. Acta*, 44 (1998) 1329-1339.
- [21] R. Chetty, W. Xia, S. Kundu, M. Bron, T. Reinecke, W. Schuhmann, M. Muhler, *Langmuir*, 25 (2009) 3853-3860.
- [22] A. Varga, N.A. Brunelli, M.W. Louie, K.P. Giapis, S.M. Haile, *J. Mater. Chem.*, 20 (2010) 6309-6315.
- [23] R.C. Suryaprakash, F.P. Lohmann, M. Wagner, B. Abel, A. Varga, *RSC Advances*, 4 (2014) 60429-60436.
- [24] V.S. Thoi, R.E. Usiskin, S.M. Haile, *Chemical Science*, 6 (2015) 1570-1577.
- [25] G. Qing, R. Kikuchi, A. Takagaki, T. Sugawara, S.T. Oyama, *Electrochim. Acta*, 169 (2015) 219-226.

- [26] J.H. Kim, J.N. Lee, C.Y. Yoo, K.B. Lee, W.M. Lee, *Int. J. Hydrog. Energy*, 40 (2015) 10720-10725.
- [27] S. Trasatti, *Journal of Electroanalytical Chemistry and Interfacial Electrochemistry*, 39 (1972) 163-184.
- [28] R. Subbaraman, D. Tripkovic, D. Strmcnik, K.-C. Chang, M. Uchimura, A.P. Paulikas, V. Stamenkovic, N.M. Markovic, *Science*, 334 (2011) 1256-1260.
- [29] A.B. Papandrew, T.A. Zawodzinski Jr, *J. Power Sources*, 245 (2014) 171-174.
- [30] S.N. Lvov, *Electrochemical Technologies for Hydrogen Production*, Electrochemical Society, 2010.
- [31] L. Mirkova, V.P. Pashova, M.H. Monev, *ECS Transactions*, 35 (2011) 77-84.
- [32] C.-Y. Yoo, J. Park, D.S. Yun, J.H. Yu, H. Yoon, J.-N. Kim, H.C. Yoon, M. Kwak, Y.-C. Kang, *Journal of Alloys and Compounds*, 676 (2016) 407-413.
- [33] Y. Zhang, Y. Liu, S. Fu, F. Guo, Y. Qian, *Materials Chemistry and Physics*, 104 (2007) 166-171.
- [34] J. Estellé, P. Salagre, Y. Cesteros, M. Serra, F. Medina, J.E. Sueiras, *Solid State Ion.*, 156 (2003) 233-243.
- [35] M. Ciureanu, H. Wang, *J. Electrochem. Soc.*, 146 (1999) 4031-4040.
- [36] R. Kumar, S. Pasupathi, B.G. Pollet, K. Scott, *Electrochim. Acta*, 109 (2013) 365-369.
- [37] Q. He, X. Yang, W. Chen, S. Mukerjee, B. Koel, S. Chen, *Physical Chemistry Chemical Physics*, 12 (2010) 12544-12555.
- [38] J.C. Meier, C. Galeano, I. Katsounaros, A.A. Topalov, A. Kostka, F. Schüth, K.J.J. Mayrhofer, *ACS Catalysis*, 2 (2012) 832-843.
- [39] J. Zhang, *PEM Fuel Cell Electrocatalysts and Catalyst Layers: Fundamentals and Applications*, Springer London, 2008.
- [40] O. Antoine, Y. Bultel, R. Durand, *J. Electroanal. Chem.*, 499 (2001) 85-94.
- [41] A. Parthasarathy, B. Davé, S. Srinivasan, A.J. Appleby, C.R. Martin, *J. Electrochem. Soc.*, 139 (1992) 1634-1641.
- [42] C.B. Prag, *Intermediate Temperature Steam Electrolysis with Phosphate-Based Electrolytes*, DTU Energy Conversion, 2014.

11. General remarks

Different strategies were followed in the present thesis in order to improve the electrode performance and the stability of the different material synthesized.

BSCF performance by B position dopants

- The stability of $\text{Ba}_{0.5}\text{Sr}_{0.5}\text{Co}_{0.8}\text{Fe}_{0.2}\text{O}_{3-\delta}$ (BSCF) perovskite was improved by adding a 3% of Sc, Zr or Y in B position of the perovskite lattice.
- Regarding the materials tested, $\text{Ba}_{0.5}\text{Sr}_{0.5}(\text{Co}_{0.8}\text{Fe}_{0.2})_{0.97}\text{Sc}_{0.03}\text{O}_{3-\delta}$ (BSCF_Sc) shown the best results. The Rp changed from $0.045 \Omega\cdot\text{cm}^2$ for BSCF to $0.0078 \Omega\cdot\text{cm}^2$ for BSCF_Sc in air at $900 \text{ }^\circ\text{C}$.
- A fully-assembled fuel cell with BSCF_Sc as cathode achieved a power density value of $882 \text{ mW}/\text{cm}^2$ at $700 \text{ }^\circ\text{C}$.
- Stable H_2 production in steam electrolysis was carried out using BSCF_Sc as electrode with high current densities applied.
- CO and H_2 were simultaneously produced in the co-electrolysis mode with BSCF_Sc as anode. At low temperatures CH_4 was also produced.

$\text{La}_{2-x}\text{A}_x\text{Ni}_{1-y}\text{B}_y\text{O}_{4+\delta}$ electrodes for ionic electrolytes

- The cell performance of the $\text{La}_2\text{NiO}_{4-\delta}$ was improved by doping in La position with Nd and Pr, whereas Ni position was doped with Co.
- The different dopants produced diverse structural changes, oxygen hyperstoichiometry and different electrochemical behaviors.
- The lowest polarization resistance was obtained for the double substituted sample, $\text{La}_{1.5}\text{Pr}_{0.5}\text{Ni}_{0.8}\text{Co}_{0.2}\text{O}_{4+\delta}$ (LPNCO).
- The maximum power density for the fully-assembled anode supported fuel cell using LPNCO was $385 \text{ mW}/\text{cm}^2$ at $700 \text{ }^\circ\text{C}$.
- Co-electrolysis of CO_2 and H_2O was also performed for the cell using LPNCO as anode with high Faraday's efficiencies.

LSM electrode improvement strategies

- $\text{La}_{0.8}\text{Sr}_{0.2}\text{MnO}_{3-\delta}$ (LSM) performance was enhanced by using a second phase, with a mainly ionic conductivity, $\text{Ce}_{0.8}\text{Gd}_{0.2}\text{O}_{2-\delta}$ (GDC).

- Further improvement was done by tailoring the catalytic activity of the electrode by infiltrating different oxides.
- Adding a second phase, the R_p decreased in almost one order of magnitude, whereas the addition of praseodymium oxide could reduce in more than three orders of magnitude the polarization resistance of the pure LSM.
- Stability of the different oxides infiltrated was checked and a stabilization time was observed for all samples. After that, the R_p was maintained with time.
- LSM-GDC and LSM-GDC +Pr were tested in a fuel cell and electrolyzer mode. The sample infiltrated increased the performance in both modes.

As shown in Figure 11.1, the strategies followed in each chapter, as to improve the parent electrode performance, were successful reducing the polarization resistance. The most relevant results of polarization resistance are summarized in Figure 11.1. The worst electrode in all temperature range was the pure electronic conductor. By using a mixed ionic and electronic conductor (MIEC) material or a cer-cer electrode the R_p was reduced in one order of magnitude (LNO and LSM-GDC). Finally, the BSCF-Sc and LSM-GDC + Pr showed the best results, the first one due to the outstanding electrochemical properties of the material and the second one due to the extraordinary catalytic activity of the praseodymium oxide for the oxygen reduction reaction.

Moreover, the performance of cathode materials for $\text{La}_{5.5}\text{WO}_{12.8}$ -based PC-SOFC was optimized. Different approaches were taken and the most relevant results are presented below.

Cer-cer cathodes for PC-SOFC

- LSM electrode performance was improved by introducing a second phase, $\text{La}_{5.5}\text{WO}_{12.8}$ (LWO) was selected due to its protonic conductivity.
- The best ratio of LSM/LWO electrodes tested was 60/40 % v/v and the sintering temperature was 1150 °C.
- Further improvement was performed by introducing a catalyst. Samarium doped ceria (SDC) was selected and infiltrated into the LSM/LWO

backbone. That catalyst reduced the resistance ascribed to surface processes (low frequency resistances).

- The polarization resistance of the electrode was reduced from $3.67 \Omega \cdot \text{cm}^2$ (at $900 \text{ }^\circ\text{C}$ of SDC) to $1.4 \Omega \cdot \text{cm}^2$ at $750 \text{ }^\circ\text{C}$ in operation conditions by calcining at lower temperature the SDC catalyst ($750 \text{ }^\circ\text{C}$).
- Fully-assembled fuel cells were tested by using LWO as electrolyte. The catalytic properties were tailored by infiltrating SDC and Ni into cathode and anode, respectively. The catalyst could increase the power density of the cell but in both cases the fuel cell performance was limited by the resistance of the electrolyte.

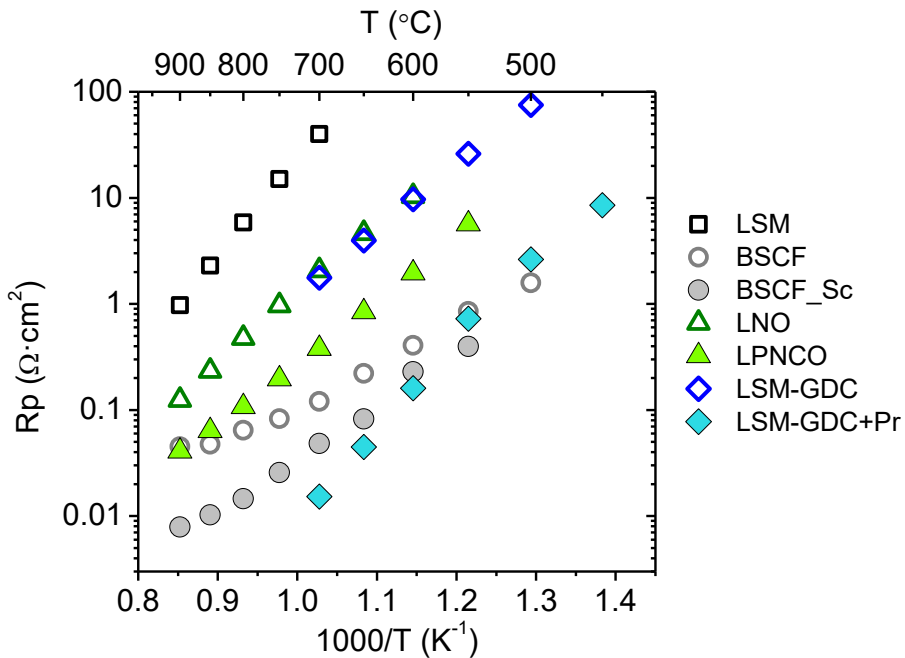


Figure 11.1: Polarization resistance of the most representative cathodes working in air for SOFC.

La_{2-x}A_xNi_{1-y}B_yO_{4+δ} electrodes for proton conductor electrolytes

- LNO series materials were compatible with LWO and were tested as cathode in proton conductor solid oxide fuel cell.
- Improvement of the electrode performance was done by changing the electrode sintering temperature.

- The best electrode was the LNO doped with Pr in La position and Co in Ni position achieving values of $0.62 \Omega \cdot \text{cm}^2$ at 750°C .

A brief summary of the electrodes studied as cathodes in PC-SOFC are shown in Figure 11.2. The efforts focused on improving the performance by boosting the electrochemical properties of the different materials. This was achieved by changing the sintering temperatures, doping the electrode materials, making composite materials or introducing nanocatalysts. As happened before, the pure electronic material showed the worst result, but the addition of a second phase (LWO) or using a MIEC material (LNO) could reduce the polarization resistance. The best cathode tested for PC-SOFC was LPNCO, reducing in more than one order of magnitude the polarization resistance.

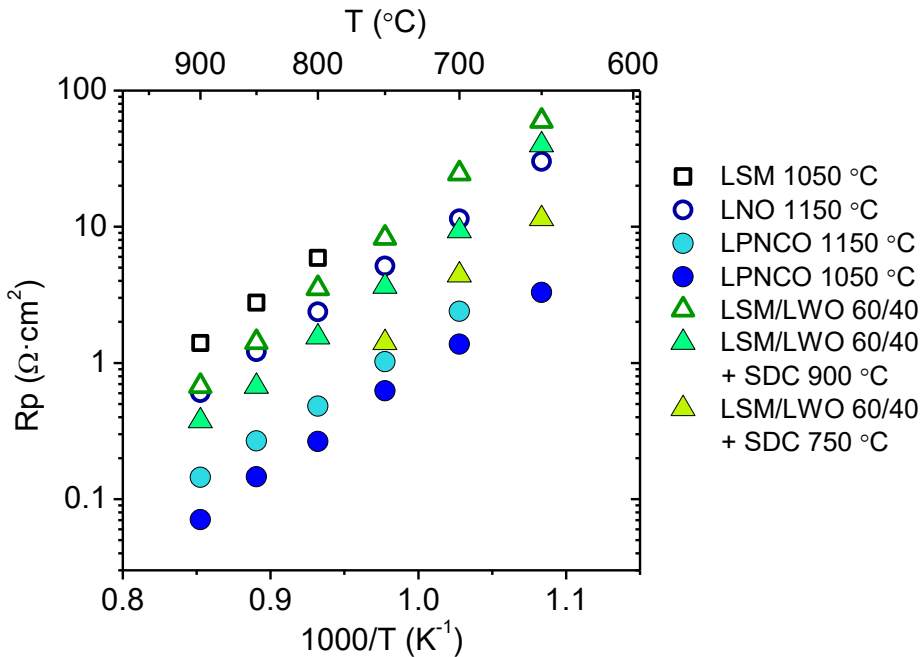


Figure 11.2: Polarization resistance of the most representatives' cathodes working in air (2.5 % vol. H₂O) for PC-SOFC.

CsH₂PO₄-based electrochemical cells

Regarding the cells based on acid salts, different conclusions can be drawn:

- A set-up for the characterization of cells, for different water partial pressures and system pressures, was developed.
- CsH_2PO_4 (CDP) was used as electrolyte in symmetrical cells with high water contents and high pressures.
- Pressure (4.5 bar) could increase more than four times the power density of the cell with Cu and ZnO as catalysts in the electrodes.
- Different cells configuration were studied. The cell was supported in a steel and Ni support allowing the reduction of the electrolyte thickness but keeping its high density (as to avoid gas leakages).
- Steam electrolysis was done with asymmetrical cells, obtaining stable H_2 production and high Faradic efficiencies.
- The mechanical stability of the electrolyte was achieved by mixing Epoxy and CsH_2PO_4 with a ratio of 20/80 % w/w.

12. Acronyms

Acronyms	Definition
a	Width of the bare of DC conductivity
a, b and c	Cell parameter
A	Acceptor
AC	Alternating current
A	cross-sectional area of sample
AFC	Alkaline Fuel cell
A_M	Material constant
b	Thickness of the bare of DC conductivity
BIAS	Direct current applied
BSE	Back scattering electrons
C	Capacitor
C	Cubic phase
C	Catalyst
CDP-M	CsH_2PO_4 milled
CDP-NM	CsH_2PO_4 no milled
CE	Counter electrode
CHF/CMF/CLF	Capacitance at different frequencies
CHP	Combined heat and power
c^i	Partial concentrations
CNG	Compress natural gas
CPE	Constant phase element
d	Spacing of atoms
DC	Direct current
D_{chem}	Chemical diffusion coefficient
D	Donor
DMFC	Direct methanol fuel cell
DOS	Density of states
DP	Double perovskite
E	Potential in no standard conditions
E^0	Potential in standard conditions
E_a	Activation energy
EDX	Energy Disperse X-Ray Spectroscopy
EC	Electronic conductors
E_F	Fermi level
EIS	Electrochemical impedance spectroscopy
E_t	Voltage at time t
Ext.	External
F	Faraday's constant
f	Linear frequency

FE-SEM	Field emissions scanning electron microscopy.
F	Fluorite
FH ₂	Flow rate of hydrogen introduced in a fuel cell
FH ₂	Flow rate produced in electrolysis or coelectrolysis mode
FH ₂ ^o	Flow rate of hydrogen used in the cell
fHF/fMF/fLF	Different frequencies, high, medium and low
FIB	Focused ion beam
FO ₂	Flow rate of oxygen introduced
FO ₂ ^o	Flow rate of oxygen used in the cell
GDL	Gas diffusion layer
GE	Gerischer element
HF	High frequency
<i>H</i>	Hexagonal phase
<i>i</i>	Current density
<i>I</i>	Current
IC	Ionic conductors
<i>I</i> _{H₂/CO}	Current used for H ₂ or CO production
<i>k</i>	Boltzmann's constant
<i>K</i> _A	Acceptor equilibrium constant
<i>K</i> _{chem}	Oxygen exchange coefficient
<i>K</i> _D	Donor equilibrium constant
<i>K</i> _e	Electronic equilibrium constant
<i>K</i> _F	Frenkel equilibrium constant
<i>K</i> _R	Oxygen reduction equilibrium constant
<i>L</i>	Inductor
<i>l</i>	Length
LF	Low frequency
LLF	Low-low frequency
MCFC	Molten carbonate fuel cell
MF	Medium frequency
<i>m</i> _{<i>i</i>}	Exponent related with the limiting species respect to the oxygen partial pressure
MIEC	Mixed ionic and electronic conductors
<i>M</i>	Metal
<i>n</i>	Electrons
<i>n</i> _{<i>i</i>}	exponent related with the limiting species respect to the water partial pressure
<i>n</i> _T	Slope value of log (σ) vs. log (pO ₂)
OCV	Open circuit voltage
Op.	Operation
ORR	Oxygen reduction reaction
<i>P</i>	Power density

PAFC	Phosphoric acid fuel cell
PC-SOEC	Proton conductor solid oxide electrolyzer cell
PC-SOFC	Proton conductor solid oxide fuel cell
p	Electron holes
PEMFC	Polymer electrolyte membrane fuel cell
p_{H_2}	Hydrogen partial pressure
p_{H_2O}	Water partial pressure
p^i	Partial pressure
p_{O_2}	Oxygen partial pressure
P	Perovskite
PV	Photovoltaic
R	Resistance
RE	Reference electrode
RHF/RMF/RLF	Resistance at different frequencies
R	Ideal gases coefficient
R_p	Polarization resistance
RP	Ruddlesden Popper
RT	Room temperature
RWGSR	Reversible water gas shift reaction
R_Ω	Ohmic resistance
S	Active area of the cell
SE	Secondary electrons
SEM	Scanning electron microscopy
SOEC	Solid oxide electrolyzer cell
SOFC	Solid oxide fuel cell
SSR	Solid state reaction
TEC	Thermal expansion coefficient
TEM	Transmission electron microscopy
TGA	Thermogravimetric analysis
t_i	Transport number
TEM	Transmission electron microscopy
TPB	Triple phase boundary
T	Temperature
t	Time
U_{H_2}	Hydrogen utilization
U_{O_2}	Oxygen utilization
V	Voltage
V	Volume cell
V_{exp}	Volume of product obtained in electrolysis and determined experimentally
Vol.-	Volumetric
V_{theor}	Volume of product obtained in electrolysis and determined theoretically

V_{Tn}	Thermoneutral voltage
WE	Working electrode
W_{el}	Maximum electrical work
WGSR	Water gas shift reaction
W_s	Finite length Warburg
XRD	X-ray diffraction
YSZ	Yttria stabilized zirconia
Z	Impedance
Z'	Imaginary impedance
Z''	Real impedance

Greek symbols	Definition
α, β and γ	Cell angles
α_j	Activity
γ_j	Activity coefficient of a j substance
ΔG	Gibbs free energy
ΔG_f	Formation free energy
ΔH	Enthalpy
ΔH_f	Formation enthalpy
ΔS	Entropy
ΔS_f	Formation entropy
η_A	Activation polarization
η_C	concentration polarization
η_{ener}	Energetic efficiency of the co-electrolysis process.
$\eta_{Faraday}$	Faraday's efficiency.
η_{Ω}	Ohmic polarization
θ	Angle
λ	Wavelength
ρ	Resistivity
σ	Conductivity (subscript a, anions, c, cations, n, electrons and p, electron holes)
φ	Phase
ω	Radial frequency

Abbreviation	Compound
BSCF	$\text{Ba}_{0.5}\text{Sr}_{0.5}\text{Co}_{0.8}\text{Fe}_{0.2}\text{O}_{3-6}$
BSCF_Sc	$\text{Ba}_{0.5}\text{Sr}_{0.5}(\text{Co}_{0.8}\text{Fe}_{0.2})_{0.97}\text{Sc}_{0.03}\text{O}_{3-6}$
BSCF_Y	$\text{Ba}_{0.5}\text{Sr}_{0.5}(\text{Co}_{0.8}\text{Fe}_{0.2})_{0.97}\text{Y}_{0.03}\text{O}_{3-6}$
BSCF_Zr	$\text{Ba}_{0.5}\text{Sr}_{0.5}(\text{Co}_{0.8}\text{Fe}_{0.2})_{0.97}\text{Zr}_{0.03}\text{O}_{3-6}$
CDP	CsH_2PO_4
EDTA	Ethylenediaminetetra acetic acid
EG	Ethylene glycol
GDC	$\text{Ce}_{0.8}\text{Gd}_{0.2}\text{O}_{4+6}$
LNCO	$\text{La}_2\text{Ni}_{0.8}\text{Co}_{0.2}\text{O}_{4+6}$
LNO	$\text{La}_2\text{NiO}_{4+6}$
LPNCO	$\text{La}_{1.5}\text{Pr}_{0.5}\text{Ni}_{0.8}\text{Co}_{0.2}\text{O}_{4+6}$
LPNO11	LaPrNiO_{4+6}
LPNO	$\text{La}_{1.5}\text{Pr}_{0.5}\text{NiO}_{4+6}$
LSCF	$\text{La}_{0.58}\text{Sr}_{0.4}\text{Fe}_{0.8}\text{Co}_{0.2}\text{O}_{3-6}$
LSCNi	$\text{La}_{0.85}\text{Sr}_{0.15}\text{Cr}_{0.8}\text{Ni}_{0.2}\text{O}_{3-6}$
LSM	$\text{La}_{0.8}\text{Sr}_{0.2}\text{MnO}_{3-6}$
LSGM	Strontium magnesium doped lanthanum gallate
LWO	$\text{La}_{5.5}\text{WO}_{12-6}$
NdNO	$\text{Nd}_2\text{NiO}_{4+6}$
SCF	$\text{SrCo}_{0.8}\text{Fe}_{0.2}\text{O}_{3-6}$
SDC	Samarium doped ceria

13. Figures list

Figure 1.1: Hydrogen layout of green energy, gas, transport and industrial sector applications [2]..... 13

Figure 3.1: Schematic diagram of fuel cell operation. 29

Figure 3.2: Schematic diagram of reactions in SOFCs based on oxygen ion conductors. 32

Figure 3.3: Schematic diagram of reactions in PC-SOFCs based on proton conductors. 33

Figure 3.4: Schematic diagram of reactions in SOEC based on oxygen ion conductors. 36

Figure 3.5: Schematic diagram of reactions in PC-SOEC based on proton conductors. 36

Figure 3.6: Thermodynamics of H₂O and CO₂ electrolysis at 10 bar [7]. 38

Figure 3.7: Conductivity as function of the metallic state. 41

Figure 3.8: Point defects (a) self-interstitial; (b) vacancy; (c) substitutional impurity atom; and (d) interstitial impurity..... 43

Figure 3.9: (a) Schottky and (b) Frenkel defect..... 44

Figure 3.10: Materials conductivity: (a) metal; (b) semimetal; and (c) insulator/semiconductor. 44

Figure 3.11: Crystal lattice of a (a) p-type and (b) n-type semiconductor..... 45

Figure 3.12: Diagrams of the oxygen and electronic defects concentration as function of the oxygen partial pressure for (a) $K_F > K_e$ and (b) $K_e > K_F$ 51

Figure 3.13: Diffusion mechanisms: (a) vacancy; (b) interstitial and (c) interstitialcy. 52

Figure 3.14: Schematic proton diffusion mechanism (a) steps of the Grotthus mechanism and (b) vehicle mechanism; 1 oxygen vacancy and 2 interstitial hydroxide ion mechanisms. 53

Figure 3.15: (a) Fluorite crystal structure of AO₂, big spheres are O²⁻ and the small are Ce⁺⁴ in CeO₂ or Zr⁺⁴ in ZrO₂. (b) Cubic perovskite structure of LaGaO₃, La⁺³ is the sphere in the center, and the big spheres are O²⁻ and the small are Ga⁺³. 54

Figure 3.16: Conductivity of different electrolytes as function of the reciprocal temperature [25]. 56

Figure 3.17: Proton conductivities of various oxides calculated from data proton concentrations and mobilities according to [36], [26].....	57
Figure 3.18: Crystal structure for $\text{La}_{5.5}\text{WO}_{11.25-\delta}$ with split oxygen and lanthanum sites in space group $Fm\bar{3}m$ [41].	58
Figure 3.19: Crystal structure of CsH_2PO_4 (a) at room and (b) at high temperature.....	59
Figure 3.20: ABO_3 perovskite structure with the origin centered at the B-site ion [44]......	61
Figure 3.21: Ruddlesden–Popper phases, $\text{A}_{n+1}\text{B}_n\text{O}_{3n+1}$, where A and B are cations, and O an oxygen anion [45].	62
Figure 3.22: Solid oxide cells electrodes materials and microstructures [57]. Explanation of the figure is explained in the text.	64
Figure 3.23: (a) Three phase boundary representation. Three phases are involved: electronic phase α , ionic phase γ and gas phase β [58]. Electrode configuration (b) electronic conductor (c) composite and (d) MIEC electrode.	66
Figure 3.24: Elementary kinetic scenarios at a Ni/YSZ TPB. The different stages will be explained below [59]......	67
Figure 4.1: Solid State Reaction for pure multicomponent phase formation ...	76
Figure 4.2: Pechini route for pure multicomponent phase formation.	77
Figure 4.3: Co-precipitation route for pure solid oxide phase formation.	78
Figure 4.4: Precipitation route for pure solid acid phase formation.	79
Figure 4.5: X-ray diffractometer and X-ray pattern for the crystal structure determination.	82
Figure 4.6: The 14 Bravais lattices	83
Figure 4.7: SEM device description.....	84
Figure 4.8: Interaction volume and emitted signals from beam/specimen interaction [11].	85
Figure 4.9: TEM device description.....	87
Figure 4.10: Schematic representation of the TGA equipment.	88
Figure 4.11: Main steps for rectangular probes and electrolytes densification.	90
Figure 4.12: Main steps for high temperature electrodes fabrication.	92
Figure 4.13: Main steps for low temperature electrode fabrication.....	93
Figure 4.14: Rectangular bar configuration for DC total electrical conductivity.	94

Figure 4.15: (a) Multisample DC conductivity measurement set-up, (b) chamber of the DC conductivity set-up and (c) furnace controller, programmable current source (Keithley 2601) and sixteen channel multimeter (Keithley 3706), from top to bottom.95

Figure 4.16: (a) Characteristic signal applied and response in an EIS measurement and (b) impedance results as function of the imaginary and real impedance. Inset represents the equivalent electrical circuit fitting for the EIS measurement response.98

Figure 4.17: Connections between the Solartron equipment 1470E and 1455A module, with the electrochemical cell.....100

Figure 4.18: (a) Description of the i-V curves of a fuel cell with the different losses and (b) combined fuel cell i-V and power density curves.101

Figure 4.19: Description of the i-V curves of an electrochemical cell with the different losses in the electrolyzer and fuel cell mode.....103

Figure 4.20: Set-up for high temperature cells characterization.....106

Figure 4.21: Detail of the reactor for high temperature.....107

Figure 4.22: Set-up for low temperature cells characterization.108

Figure 4.23: Schematic representation of the GC equipment [24].....109

Figure 4.24: Schematic representation of the MS equipment [26].....110

Figure 5.1: XRD pattern of $Ba_{0.5}Sr_{0.5}(Co_{0.8}Fe_{0.2})_{0.97}B_{0.03}O_{3-\delta}$ (B= Sc, Zr and Y) after calcination at 1150 °C.117

Figure 5.2: XRD pattern of $Ba_{0.5}Sr_{0.5}(Co_{0.8}Fe_{0.2})_{0.97}B_{0.03}O_{3-\delta}$ (B= Sc, Zr and Y) after stability test at 750 °C during two weeks.118

Figure 5.3: TG analysis of $Ba_{0.5}Sr_{0.5}(Co_{0.8}Fe_{0.2})_{0.97}B_{0.03}O_{3-\delta}$ (B= Sc, Zr and Y) in presence of CO₂.119

Figure 5.4: Total DC conductivity (a) as function of temperature in dry air and (b) as function of oxygen partial pressure.121

Figure 5.5: SEM micrographs of $Ba_{0.5}Sr_{0.5}(Co_{0.8}Fe_{0.2})_{0.97}B_{0.03}O_{3-\delta}$ /GDC electrodes after calcination at 950 °C. All composites were supported on GDC+CoO_x electrolytes.122

Figure 5.6: Nyquist and Bode plot obtained by means of the EIS measurements, left and right, respectively.123

Figure 5.7: Polarization resistance of $Ba_{0.5}Sr_{0.5}(Co_{0.8}Fe_{0.2})_{0.97}B_{0.03}O_{3-\delta}$ /GDC electrodes in air as function of temperature.124

Figure 5.8: EIS spectrums of $\text{Ba}_{0.5}\text{Sr}_{0.5}(\text{Co}_{0.8}\text{Fe}_{0.2})_{0.97}\text{B}_{0.03}\text{O}_{3-\delta}/\text{GDC}$ electrodes in synthetic air. (a) Nyquist and (b) Bode plot at 800 °C. (c) Nyquist and (d) Bode plot at 650 °C.	126
Figure 5.9: Equivalent electrical circuit used for the fitting at high temperature (a) and low temperature (b).	127
Figure 5.10: Results from the fitting with an equivalent electrical circuit for GDC/BSCF composite as function of temperature. (a) Resistance, (b) capacitance and (c) associated frequency.	127
Figure 5.11: Equivalent electrical circuit fitting results; (a) resistance, (b) capacitance and (c) frequency of different processes at 800 °C in air.	129
Figure 5.12: Equivalent electrical circuit fitting results; (a) resistance, (b) capacitance and (c) frequency of different processes at 650 °C in air.	129
Figure 5.13: Equivalent electrical circuit fitting results for BSCF composite electrode; (a) resistance, (b) capacitance and (c) frequency of different processes at 900 °C in air and (d) resistance, (e) capacitance and (f) frequency of different processes at 650 °C in air.	133
Figure 5.14: Equivalent electrical circuit fitting results for BSCF_Sc composite electrode; (a) resistance, (b) capacitance and (c) frequency of different processes at 900 °C in air and (d) resistance, (e) capacitance and (f) frequency of different processes at 650 °C in air.	134
Figure 5.15: Influence of CO_2 containing atmosphere in the cell performance on BSCF ; (a) polarization resistance as function of time, (b) Nyquist plot and (b) Bode plot in CO_2 presence and free atmosphere.	135
Figure 5.16: Influence of CO_2 containing atmosphere in the cell performance on BSCF_Sc ; (a) polarization resistance as function of time, (b) Nyquist plot and (b) Bode plot in CO_2 presence and free atmosphere.	136
Figure 5.17: Fuel cell mode system configuration.	137
Figure 5.18: i-P and i-V curves of the Ni-YSZ/YSZ/GDC/(BSFC_Sc/GDC) at different temperatures working with wet H_2 (2.5 % vol. H_2O) and pure air.	138
Figure 5.19: Nyquist and Bode plot obtained from the results of the EIS spectra in fuel cell mode near to the OCV.	138
Figure 5.20: i-P and i-V curves of the Ni-YSZ/YSZ/GDC/(BSFC_Sc/GDC) at different oxygen partial pressure working with wet H_2 (2.5 % vol. H_2O) (a) at 700 °C and (b) 600 °C.	139

Figure 5.21: i-P and i-V curves of the Ni-YSZ/YSZ/GDC/(BSFC_Sc/GDC) at different wet hydrogen partial pressure (2.5 % vol. H₂O) working with air(a) at 700 °C and (b) 600 °C. 141

Figure 5.22: i-P and i-V curves of the Ni-YSZ/YSZ/GDC/(BSFC_Sc/GDC) at different water partial pressure working with wet H₂ and pure air. 142

Figure 5.23: i-P and i-V curves of the Ni-YSZ/YSZ/GDC/(BSFC_Sc/GDC) at different total inlet flows working with wet H₂ (2.5 % vol. H₂O) and pure air (a) at 700 °C and (b) 550 °C. 143

Figure 5.24: Stability of the fully-assembled fuel cell Ni-YSZ/YSZ/GDC/(BSFC_Sc-GDC) working with wet H₂ (2.5 % vol. H₂O) at 600 °C and pure air at a constant current density of 0.78 A/cm². 144

Figure 5.25: Nyquist and Bode plot obtained from the results of the EIS spectra in fuel cell mode near to (a) the OCV and (b) with a BIAS of 0.2 A at the beginning and the end of the stability test at 600 °C. 145

Figure 5.26: Electrolysis mode system. 146

Figure 5.27: i-P and i-V curves of the Ni-YSZ/YSZ/GDC/BSFC_Sc-GDC at different temperatures working with wet H₂ (2.5 % vol. H₂O) and pure air. 146

Figure 5.28: Mass spectrometer results of the steam electrolysis at different temperatures; (a) 700 °C (b) 600 °C and (c) 500 °C. Values in the graph are the current densities applied. 147

Figure 5.29: i-V curves for the steam electrolysis. 148

Figure 5.30: (a) Hydrogen production and (b) Faradic efficiency (η_F) for the steam electrolysis working at 700°C, 600°C and 500 °C. 149

Figure 5.31: Co-electrolysis mode system. 150

Figure 5.32: i-V curves for the cell working in a co-electrolysis mode. 151

Figure 5.33: Mass spectrometer results of the co-electrolysis at different temperatures; (a) 700 °C (b) 600 °C and (c) 500 °C. 152

Figure 5.34: (a) Thermodynamics of the CO₂ and H₂ reduction reactions and (b) water-gas shift [49]. 153

Figure 5.35: Mass spectrometer results of the co-electrolysis at 450 °C with a total flow of (a) 100 ml/min and (b) 50 ml/min. The percentage of each reactant is maintained. 154

Figure 5.36: (a) Hydrogen (b) carbon monoxide and (c) methane production working at 700, 600°C, 500 °C and 450 °C. 155

Figure 5.37: Results of the flow rate obtained during the Co-electrolysis mode at 450 °C and the corresponding values in the equilibrium.	156
Figure 5.38: Co-electrolysis efficiency.	157
Figure 5.39: Comparison between i-V curves of electrolysis and co-electrolysis.	157
Figure 6.1: Ruddlesden-Popper structure for $\text{La}_2\text{NiO}_{4+\delta}$ [21].	166
Figure 6.2: XRD patterns of $\text{La}_{2-x}\text{A}_x\text{Ni}_{1-y}\text{B}_y\text{O}_{4+\delta}$ after sintering recorded at room temperature. It is presented the logarithmic intensity of each compound. Impurities are marked on the graph (*).	168
Figure 6.3: Rietveld refinements (lines) of $\text{La}_2\text{NiO}_{4+\delta}$ data (circles), shown above the corresponding difference patterns. Vertical bar indicate the Bragg positions.....	169
Figure 6.4: From top to bottom: oxygen hyperstoichiometry, cell parameters and bond distance obtained by the Rietveld refinement.	170
Figure 6.5: Oxygen hyperstoichiometry as function of temperature in air. Results obtained by TGA.	173
Figure 6.6: Total conductivity results in air for the different $\text{La}_{2-x}\text{A}_x\text{Ni}_{1-y}\text{B}_y\text{O}_{4+\delta}$ synthesized compounds.	174
Figure 6.7: SEM micrographs of the different electrodes measured as symmetrical cells.....	176
Figure 6.8: Polarization resistance values in an Arrhenius plot of the different MIEC electrodes in a temperature range from 900 °C to 600 °C. The numbers in parentheses are the activation energies (E_a) of each compound.	177
Figure 6.9: (a) Nyquist and (b) Bode plots at 750 °C for the different electrodes in air(c) Results of the equivalent electrical circuit fitting at 750 °C (d). Schematic representation of the equivalent electrical circuit used for the EIS fitting.	179
Figure 6.10: LPNCO electrode polarization resistance values as function of time in air at 900 °C.....	181
Figure 6.11: (a) Overall polarization resistance (R_p) and the different contributions, (b) capacitances associated and (c) frequencies after equivalent electrical circuit fitting of LPNCO as function of temperature in air.	182
Figure 6.12: Equivalent electrical circuit fittings results: (a) resistance at low frequencies (LF) and medium frequencies (MF), (b) capacitance and (c)	

frequency at 750 °C and 900 °C at different pO_2 . (d) EIS measurements at 900 °C with different pO_2 for LPNCO. 183

Figure 6.13: SEM micrographs of the fully-assembled fuel cell; Ni-YSZ/YSZ/GDC/LPNCO. 186

Figure 6.14: i-V and i-P curves for the fully assembled fuel cell at different temperatures, working with air in the cathode and wet hydrogen in the anode. 187

Figure 6.15: (a) i-V curves and (b) measured and theoretical hydrogen production in steam electrolysis mode. 188

Figure 6.16: a) i-V curves for steam electrolysis and co-electrolysis and (b) measured hydrogen and carbon monoxide production in co-electrolysis mode. 190

Figure 6.17: Thermodynamic results for the co-electrolysis simulation at 700 °C. 191

Figure 7.1: Improvement strategy for electrodes; (a) electronic conductor electrode, (b) composite electrode and (c) composite electrode and catalyst nanoparticles. 200

Figure 7.2: LSM and GDC compatibility test at 1150 °C (2h). * XRD holder. ... 201

Figure 7.3: From left to right; back SEM backscattering electrons of the LSM-GDC backbone, Co backbone infiltrated. Infiltrated oxide SEM magnification; Pr, Zr, Co, Ce, Ba and Sm. 202

Figure 7.4: LSM-GDC infiltrated by Pr, calcined at 700 °C 2h (a) 100K X (c) 10 K X, LSM-GDC infiltrated by Pr, after EIS measurements (b) 100K X (d) 10 K X. 203

Figure 7.5: XRD of the electrodes after infiltration and calcination. Peaks of different oxides infiltrated are marked by symbols. 204

Figure 7.6: Arrhenius plot of the R_p obtained from the EIS measurements for the symmetrical cells in air. The composites infiltrated are labeled by the nanocatalyst infiltrated. Blank is the LSM-GDC composite and LSM is the parent electrode. 205

Figure 7.7: Reproducibility of the LSM-GDC electrodes infiltrated with Pr measured by symmetrical cells configuration. 206

Figure 7.8: Equivalent circuits used for impedance spectra results fitting. 207

Figure 7.9: Electrochemical impedance spectra for LSM and LSM-GDC electrodes. 208

Figure 7.10: Polarization resistance of LSM-GDC infiltrated in the stability test.	209
Figure 7.11: Electrochemical impedance spectra from the symmetrical cell analysis.	210
Figure 7.12: Fitting results of the (a) resistances (b) capacitances and (c) frequencies for High (HF), Medium (MF), Medium-Low (M-LF) and Low frequencies (LF) at 600°C for different pO_2 and m value for the different frequencies.	213
Figure 7.13: i-V and i-P curves for LSM-GDC/YSZ/Ni-YSZ and LSM-GDC+Pr/YSZ/Ni-YSZ.	214
Figure 7.14: i-V curves of the steam electrolysis for the pristine and the Pr infiltrated anode.	215
Figure 7.15: Mass spectrometer results of the steam electrolysis at 700 °C (a) for the LSM-GDC composite and (b) LSM-GDC infiltrated by praseodymium oxide.	216
Figure 7.16: Faradic efficiency and hydrogen production in the steam electrolysis for LSM-GDC/YSZ/Ni-YSZ and LSM-GDC+Pr/YSZ/Ni-YSZ.	217
Figure 8.1: Schematic diagram of MIEC cathode reaction mechanisms for a LWO proton conducting electrolyte.	224
Figure 8.2: XRD patterns of LWO, La_2NiO_{4+6} and a 50% mixture of both phases at room temperature and after being calcined at 1150 °C for 5 h.	225
Figure 8.3: SEM analysis of the fracture cross-section of a cell (after electrochemical testing) consisting of a LWO dense electrolyte coated with LPNCO cathode at 1150 °C.	226
Figure 8.4: Polarization resistance as a function of 1000/T in wet synthetic air for LNO, LPNO, LPNCO and NdNO. Electrodes sintered at 1150 °C (2h).	227
Figure 8.5: Impedance spectra, (a) Nyquist and (b) Bode plots, of LNO, LPNO, LPNCO and NdNO measured at 750 °C in wet synthetic air.	228
Figure 8.6: Modeled results of LNO, LPNO, LPNCO and NdNO (a) resistances, (b)capacitances (c) and frequencies as a function of the 1000/T in humidified air.	229
Figure 8.7: Modeled results of LNO, LPNO, LPNCO and NdNO electrodes sintered at 1150 °C; (a) resistances, (b) capacitances (c) and frequencies as a function of the pO_2 in humidified conditions.	232

Figure 8.8: R_p as a function of $1000/T$ of $\text{La}_{1.5}\text{Pr}_{0.5}\text{Ni}_{0.8}\text{Co}_{0.2}\text{O}_{4+\delta}$ sintered at 1050 °C, 1100 °C and 1150°C.234

Figure 8.9: Modeled results of LPNCO electrode sintered at 1050, 1100 and 1150 °; (a) capacitances and (b) frequencies as a function of the $1000/T$ in humidified air.234

Figure 8.10: R_p as a function of $1000/T$ of $\text{Nd}_2\text{NiO}_{4+\delta}$ sintered at 1100°C and 1150 °C.....235

Figure 8.11: Schematic diagram of mechanisms in a MIEC/proton conductor composite cathode on a LWO proton conducting electrolyte.236

Figure 8.12: R_p as a function of $1000/T$ of LPNO sintered at 1150 and LPNO:LWO composite electrodes sintered at 1150 °C and 1050 °C.....236

Figure 8.13: Polarization resistance of LNO as function of $p\text{O}_2$ in different humidified (H_2O and D_2O) and dry conditions.238

Figure 8.14: Impedance spectra, (a) Nyquist and (b) Bode plots, of $\text{La}_2\text{NiO}_{4+\delta}$ measured at 750°C in air in different humidified (H_2O and D_2O) and dry conditions.....238

Figure 8.15: Modeled results of LNO electrode sintered at 1150 °C; (a) resistances, (b)capacitances (c) and frequencies as a function of the $p\text{O}_2$ in different humidified (H_2O and D_2O) and dry conditions.....240

Figure 8.16: Impedance spectra, Nyquist (a) and bode (b) plots, of LPNCO measured at 750 °C in air in different humidified (H_2O and D_2O) and dry conditions.....241

Figure 8.17: Modeled results of LPNCO electrode sintered at 1150 °C; (a) resistances, (b)capacitances (c) and frequencies as a function of the $p\text{O}_2$ in different humidified (H_2O and D_2O) and dry conditions.242

Figure 8.18: Impedance spectra, (a) Nyquist and (b) Bode plots, of LPNO electrode sintered at 1150 °C and measured at 750 °C in air in different humidified (H_2O and D_2O).243

Figure 8.19: Impedance spectra, (a) Nyquist and (b) Bode plots, of NdNO electrode sintered at 1150 °C and measured at 750 °C in air in different humidified (H_2O and D_2O).243

Figure 8.20: Equivalent electrical circuit used for the fitting of the NdNO EIS spectra.244

Figure 8.21: Modeled results of NdNO sintered at 1150 °C measured in humidified air (H_2O and D_2O) at 750 °C.244

Figure 8.22: Summary of Rp in different humidified conditions at 750 °C in air.	244
Figure 8.23: TGA results recorded in dry air when the samples were heated up, with the fresh samples (1 st time) and heated again after cooled down the samples in dry conditions (2 nd time).	246
Figure 8.24: Total DC conductivity of (a) LPNO (c) LPNCO and (e) NdNO and zoom of conductivity at lower temperatures (b) LPNO (d) LPNCO and (f) NdNO in dry and wet (2.5 vol.% of H ₂ O) conditions.	247
Figure 9.1: Scheme of the electrode mechanisms in (a) a pure electronic electrode and (b) in an electronic and protonic conductor cer-cer electrode.	254
Figure 9.2: XRD pattern of LWO and LSM phases, mixture of LSM and LWO at room temperature and after calcination at 1150 °C for 5h.	256
Figure 9.3: SEM images of LSM and LWO powders (top of the image) and LSM/LWO cer-cer cathode 50/50 vol. % (bottom of the image) sintered at 1050 °C and 1150 °C.	257
Figure 9.4: TEM images and EDX spectra of a FIB-lamella showing the cross section of a LSM cathode on the electrolyte calcined at 1150 °C.	259
Figure 9.5: Polarization resistance as function of the temperature in wet air (2.5% vol. H ₂ O). Activation energy values are written on the right.	260
Figure 9.6: Equivalent electrical circuit used for the fitting of the EIS spectra.	260
Figure 9.7: Results of the equivalent electrical circuit (a) resistances, (b) capacitances and (c) the related frequencies of the LSM and LSM/LWO composite in wet air as function of the temperature.	261
Figure 9.8: Type of clusters that can be originated in a composite electrode.	263
Figure 9.9: Polarization resistance as function of the LSM and LWO ratio in wet air (a) as function of the temperature and (b) as function of the phase's ratio.	264
Figure 9.10: Nyquist and bode plot, left and right, respectively, of the different composites electrodes tested at (a) 900 °C and (b) 750 °C in wet air.	265
Figure 9.11: Nyquist and bode plot, left and right, respectively of LSM/LWO 60/40 composite cathode as function of the temperature in wet air.	266

Figure 9.12: Results of the equivalent electrical circuit fitting of LSM/LWO 60/40 electrode as function of the temperature in wet air; (a) resistances, (b) capacitances and (c) associated frequencies.267

Figure 9.13: Results of the equivalent electrical circuit fitting of LSM/LWO 60/40 electrode as function of oxygen partial pressure in wet conditions; (a) resistances, (b) capacitances and (c) associated frequencies.....269

Figure 9.14: Scheme of the cathode composite and cathode composite infiltrated by nanoparticles.....270

Figure 9.15: XRD patterns of SDC powders sintered up to 900 and 750 °C.....271

Figure 9.16: FESEM images of the electrode infiltrated with SDC and TEM images of the nanoparticles fired at two temperatures.....272

Figure 9.17: Polarization resistance as function of the temperature in wet air (2.5% vol. H₂O).273

Figure 9.18: Nyquist and bode plot, left and right, respectively, of LSM/LWO 60/40 composite cathode blank and infiltrated with SDC fired a two temperatures (750 °C and 900 °C).274

Figure 9.19: Results of the equivalent electrical circuit fitting of LSM/LWO 60/40 and LSM/LWO 60/40 infiltrated with SDC (750 °C) electrode as function of temperature in wet conditions; (a) resistances, (b) capacitances and (c) associated frequencies.275

Figure 9.20: Results of the equivalent electrical circuit fitting of LSM/LWO 60/40 and LSM/LWO 60/40 infiltrated with SDC (750 °C) electrode as function of oxygen partial pressure in wet conditions; (a) resistances, (b) capacitances and (c) associated frequencies.276

Figure 9.21: R_p of the LSM/LWO 60/40 infiltrated with SDC fired at 750 °C as function of time.277

Figure 9.22: Nyquist and bode plot, left and right, respectively, of LSM/LWO 60/40 composite infiltrated with SDC fired at 750 °C for the first measurement and after the stability test.277

Figure 9.23: Scheme of the protonic fully-assembled fuel cells, and FE-SEM micrographs of the different electrodes: LSM/LWO 60/40, LSCNi, LSM/LWO 60/40 +SDC and LSCNi+Ni (from top to bottom).279

Figure 9.24: i-V and i-P curves of fully-assembled fuel cells supported on the electrolyte; anode LSCNi, electrolyte LWO and cathode LSM/LWO. The

infiltrated sample was infiltrated with Ni in the anode and SDC in the cathode.	280
Figure 9.25: EIS spectra of the full assembled fuel cells.	281
Figure 10.1: Crystal structure of CDP (a) the monoclinic paraelectric and (b) the cubic phases [8].	287
Figure 10.2: Phase transition of the CDP material.	288
Figure 10.3: XRD patterns of the CDP as function of temperature [9].	288
Figure 10.4: XRD pattern of CDP sintered at room temperature.	289
Figure 10.5: DC conductivity measurements of CDP as function of temperature, with a content of 30% of water in N ₂	290
Figure 10.6: Phase stability diagram for solid acid fuel cells based on CDP [7].	291
Figure 10.7: DC conductivity measurements of CDP as function of water partial pressure with a mixture of argon.	292
Figure 10.8: GDL SEM image.	293
Figure 10.9: (a) symmetrical cell configuration, FESEM micrographs of both electrodes (b) GDL+ZnO+Cu and (c) GDL+Pt.	294
Figure 10.10: i-V and i-P curves of the Cu-ZnO on GDL/CDP/Cu-ZnO on GDL in wet H ₂ and air as function of the total pressure of the system.	295
Figure 10.11: Theoretical results of OCV as function of the total pressure determined by equation (3.6) for the fuel cell working with a p _{H₂O} of 0.4 bar in both chambers and pure hydrogen and air in the anode and cathode, respectively.	296
Figure 10.12: i-V and i-P curves of the Pt on GDL/CDP/Pt on GDL in wet H ₂ and air as function of the total pressure of the system.	297
Figure 10.13: i-V and i-P curves of the Cu-ZnO on GDL/CsH ₂ PO ₄ /Cu-ZnO on GDL in wet H ₂ and air as function of water partial pressure.	298
Figure 10.14: i-V and i-P curves of the Pt on GDL/CDP/Pt on GDL in wet H ₂ and air as function of water partial pressure.	298
Figure 10.15: i-V and i-P curves of the Cu+ZnO on GDL/CDP/Cu+ZnO on GDL in wet H ₂ and air as function of operation temperature.	300
Figure 10.16: i-V and i-P curves of the Pt on GDL/CDP/Pt on GDL in wet H ₂ and air as function of operation temperature.	300

Figure 10.17: (a) Nyquist plot, (b) Bode plot and (c) summary of the EIS contributions of Pt on GDL/CDP/Pt on GDL sample near OCV at 4.5 bar and 0.47 bar of p_{H_2O} function of temperature.301

Figure 10.18: Equivalent electrical circuit fitting results; (a) resistance, (b) capacitance and (c) frequency of Pt on GDL/CDP/Pt on GDL near OCV at different temperatures.302

Figure 10.19: i-V and i-P curves of the Ag+Pt on GDL/CDP/Cu and ZnO on GDL in wet H_2 and air as function of operation temperature.304

Figure 10.20: EIS results (Nyquist and Bode plots, left and right, respectively) of Pt +Ag on GDL/CDP/Cu-ZnO on GDL near OCV at 1 bar and water partial pressure of 0.4 bar as function of temperature.305

Figure 10.21: Equivalent electrical circuit fitting results; (a) resistance, (b) capacitance and (c) frequency of Pt on Pt +Ag on GDL/CDP/Cu-ZnO on GDL near OCV at different temperatures.305

Figure 10.22: Electrolysis cell configuration.306

Figure 10.23: H_2 signal of the cathode outlet gas during electrolysis mode. ...307

Figure 10.24: Cell overpotential in different conditions: atmospheric pressure (Elect.), system pressure of 7.5 bar (Elect. P=7.5 bar) and coelectrolysis with 3 ml/min of CO_2 (Co-elect. P=7.5 bar).308

Figure 10.25: Theoretical results of OCV as function of the total pressure determined by Nernst equation for the electrolyzer working with a p_{H_2O} of 0.4 bar in both chambers and Ar and N_2 fed in the cathode and anode, respectively.308

Figure 10.26: Hydrogen production and Faraday’s efficiency of the three conditions, working with a water partial pressure of 0.4 bar. Gas chromatograph 1% error.309

Figure 10.27: Asymmetrical cell configuration: Pt on GDL/CDP/CDP and Cu+ZnO on Carbon supported on porous steel disc.310

Figure 10.28: i-V and i-P curves of Pt on GDL/CDP/CDP and Cu+ZnO on carbon supported on porous steel disc working in fuel cell conditions as function of temperature. Air supplied in the cathode and hydrogen in anode, both chambers with a water partial pressure of 0.4 bar.311

Figure 10.29: Nyquist and Bode plots, left and right, respectively of Pt on GDL/CDP/CDP and Cu+ZnO on Carbon supported on porous steel disc working in fuel cell conditions as function of temperature near OCV.312

Figure 10.30: Equivalent electrical circuit fitting results; (a) resistance, (b) capacitance and (c) frequency of Pt on GDL/CDP/CDP and Cu+ZnO on Carbon supported on porous steel disc near OCV at different temperatures.	313
Figure 10.31: Cell overpotential of Pt on GDL/CDP/CDP and Cu+ZnO on Carbon supported on porous steel disc.	314
Figure 10.32: Hydrogen signal of the cathode outlet gas during electrolysis mode.	315
Figure 10.33: Hydrogen production and Faraday's efficiency, working with a 40 % vol. of steam.	315
Figure 10.34: FIB-SEM images of the different electrodes with secondary electrons.	316
Figure 10.35: Mechanical deformation under constant stress of CsH_2PO_4 and mixture with 10wt% of SiO_2 [7].	318
Figure 10.36: Flexural strength of composite electrolyte [25].	318
Figure 10.37: X-Ray diffraction of CDP before and after milling 4 days.	319
Figure 10.38: SEM micrographs of CDP after synthesis (CDP_NM) and after milling (CDP-M).	319
Figure 10.39: CDP: Epoxy 85:15 material conductivity measured as function of time for different temperatures with pH_2O 0.3 bar in Ar.	320
Figure 10.40: Conductivity of CDP: Epoxy composite electrolytes measured in Argon with a 30 % vol. of steam.	321
Figure 10.41: CDP: Epoxy samples after electrochemical test.	321
Figure 10.42: SEM images of (a) of the surface with smaller particles and (b) the gas diffusion part [26].	322
Figure 10.43: XRD of nickel support infiltrated with nickel and cobalt oxides.	323
Figure 10.44: FE-SEM images of the nanoparticles infiltrated in the Ni support.	324
Figure 10.45: Symmetrical cells supported on the electrolyte (CDP) configuration; (a) commercial carbon paper infiltrated with Pt, (b) Ni sponge , (c) Ni sponge infiltrated with Ni and (d) Ni sponge infiltrated with CO_3O_4 as electrodes.	325
Figure 10.46: FE-SEM images of (a) carbon fibers and (b) BSE (c) SE FE-SEM images of XC-72 with Pt nanoparticles.	326

Figure 10.47: Nyquist a Bode plot, left and right, respectively, of carbon paper with Pt at 235 °C as function of time.328

Figure 10.48: Equivalent electrical circuit fitting results; (a) resistance, (b) capacitance and (c) frequency of Pt on C paper/CDP/ Pt on C paper as function of time.....328

Figure 10.49: Nyquist a Bode plot, left and right, respectively, of carbon paper with Pt as function of temperature.328

Figure 10.50: Nyquist a Bode plot, left and right, respectively, of carbon paper with Pt at different temperatures in air.329

Figure 10.51: Equivalent electrical circuit fitting results; (a) resistance, (b) capacitance and (c) frequency of Pt on C paper/CDP/ Pt on C paper as function of temperature in air conditions with $p_{H_2O} = 0.3$ bar.330

Figure 10.52: Nyquist a Bode plot, left and right, respectively, of Ni sponge/CDP/Ni sponge cell as function of the temperature.....331

Figure 10.53: Nyquist a Bode plot, left and right, respectively, of Ni sponge/CDP/Ni sponge cell as function of time.331

Figure 10.54: Nyquist a Bode plot, left and right, respectively, of Ni sponge+Ni/CDP/Ni sponge+Ni cell as function of the temperature.....332

Figure 10.55: Nyquist a Bode plot, left and right, respectively, of Ni sponge+Co₃O₄/CDP/Ni sponge+ Co₃O₄ cell as function of the temperature...332

Figure 10.56: Nyquist a Bode plot, left and right, respectively, of Ni sponge+Co₃O₄/CDP/Ni sponge+ Co₃O₄ cell as function of time.332

Figure 10.57: Polarization resistance of the three different electrodes: Ni sponge, Ni sponge+ Ni infiltrated and Ni sponge and Co₃O₄ infiltrated electrodes as function of temperature.333

Figure 10.58: Equivalent electrical circuit for the Ni sponge electrode.334

Figure 10.59: Equivalent electrical circuit fitting results; (a) resistance, (b) capacitance and (c) frequency at HF, (d) resistance, (e) capacitance and (f) frequency of LF1, (g) resistance, (h) capacitance and (i) frequency at LF2 of Ni sponge, Ni sponge +Ni and Ni sponge + Co₃O₄ at different temperatures.....335

Figure 10.60: i-V and i-P curves of Ni sponge/CDP:Epoxy (80:20)/carbon+Pt as function of temperature.336

Figure 10.61: Ni sponge/CDP:Epoxy (80:20)/carbon+Pt configuration cell.....337

Figure 10.62: i-V and i-P curves of Ni sponge/CDP:Epoxy (80:20)/carbon+Pt as function of the system pressure.338

Figure 11.1: Polarization resistance of the most representative cathodes working in air for SOFC.	345
Figure 11.2: Polarization resistance of the most representatives' cathodes working in air (2.5 % vol. H ₂ O) for PC-SOFC.....	346

14. Tables list

Table 3.1: Comparison of different fuel cells [1-4].	28
Table 3.2: Half-cell reactions of the different electrolysis cells.	34
Table 3.3: Region dependent equations for defect species concentration in Frenkel disorder oxides.	50
Table 3.4: Kröger–Vink notation for defect chemistry.	68
Table 4.1: Synthesis conditions of the different compounds used.	80
Table 4.2: Parameters for discs densification.	91
Table 4.3: The most common circuit elements used for the equivalent electrical circuit fittings. Where l is the square root (-1) and ω the angular frequency of the AC signal.	99
Table 5.1: Ion radii in BSCF [5].	116
Table 5.2: n values of $\log(\sigma)$ vs. $\log(pO_2)$.	120
Table 5.3: Activation energy of $Ba_{0.5}Sr_{0.5}(Co_{0.8}Fe_{0.2})_{0.97}B_{0.03}O_{3-\delta}$ /GDC electrodes in synthetic air. E_{a1} related with high operation temperature and E_{a2} with low temperature.	125
Table 5.4: Equivalent electrical circuit fitting results for BSCF in air and air and CO_2 .	135
Table 5.5: Oxygen utilization at 700 °C.	140
Table 5.6: Oxygen utilization at 600 °C.	140
Table 5.7: Hydrogen utilization at 700 °C.	142
Table 5.8: Hydrogen utilization at 600 °C.	142
Table 5.9: Hydrogen utilization at 700 °C with different flow rates.	144
Table 5.10: Hydrogen utilization at 550 °C with different flow rates.	144
Table 6.1: List of the different synthesized and its abbreviation name used in the text.	167
Table 6.2: Refined structural parameters for $La_{2-x}A_xNi_{1-y}B_yO_{4+\delta}$. The data are refined in F/mmm orthorhombic space group. Numbers in parentheses are the standard deviations of the significant digits.	171
Table 7.1: E_a (eV) of the cathodes in air.	206
Table 7.2: Fitting results for the EIS spectrums for the symmetrical cells; LSM and LSM-GDC.	208
Table 7.3: Degradation rate of electrodes ($\Omega \cdot cm^{-2} \cdot h^{-1}$).	208

Table 7.4: Fitting results at $t_1 = 30$ min and t_2 after 1200 min for the pristine and infiltrated samples.	211
Table 7.5: Fitting results for the EIS spectrums recorded at the OCV in fully-assembled fuel cell at 700 °C.	215
Table 8.1: Elementary reaction steps in the cathode working with a protonic electrolyte [22].....	230
Table 8.2: Elementary reactions in the cathode and their order reaction respect to oxygen partial pressure (m_i) and water partial pressure(n_i).	231
Table 8.3: m_i values from the fitting of $R_i \propto pO_2^{-m_i}$	233
Table 8.4: Modeled results of LPNO sintered at 1150 and LPNO:LWO composite electrode sintered at 1150 °C at 750 °C in humidified air.	237
Table 8.5: Modeled results of LPNO sintered at 1150 °C measured in humidified air (H ₂ O and D ₂ O) at 750 °C.....	243
Table 9.1: Results of the equivalent electrical circuit fitting of LSM/LWO 60/40 infiltrated with SDC (750 °C) electrode, for the first measurement ($t = 30$ min) and after the stability test ($t = 1228$ min).....	278

15. Scientific contribution

Publications

- **L. Navarrete**, M. Balaguer, V. B. Vert and J.M. Serra. Optimization of SOFC composite cathodes based on LSM and doped cerias $\text{Ce}_{0.8}\text{Ln}_{0.2}\text{O}_{2-\delta}$ (Ln=Gd, Er, Tb and Pr). Journal of The Electrochemical Society, 163, issue 13, F1440-F1443 (2016).
- S. Somacescu, **L. Navarrete**; M. Florea; J.M. Calderon-Moreno and J.M. Serra. Self-assembled (Ni/Cu, Ti)-YSZ with potential applications for IT-SOFCs: catalytic and electrochemical assessment. Journal of Alloys and Compounds. 690, 873–883 (2017).
- C. Gaudillere, **L. Navarrete** and J.M. Serra. CO_2 hydrogenation on Ru/Ce based catalysts dispersed on highly ordered micro-channeled 3YSZ monoliths fabricated by freeze-casting. International Journal of Hydrogen Energy.
- C. Solís, **L. Navarrete**, F. Bozza, N. Bonanos and J. M. Serra. Surface Promotion of Composite Cathodes in Protonic Ceramic Fuel Cells. ChemElectroChem 2, 1106-1110 (2015).
- **L. Navarrete**, C. Solis and J. M. Serra. Boosting the oxygen reduction reaction mechanisms in IT-SOFC cathodes by catalytic functionalization. Journal of Materials Chemistry A 3, (2015). 16440-16444.
- **L. Navarrete**, F. Toldra-Reig, J. M. Serra and S. Somacescu. SnO_2 and Ce modified SnO_2 mesostructured for selective ethanol detection. Proceedings of IEEE Sensors 39, vol. 2014-December, (2014) pp. 297-300.
- C. Gaudillere, **L. Navarrete** and J. M. Serra. Syngas production at intermediate temperature through H_2O and CO_2 electrolysis with a Cu-based solid oxide electrolyzer cell Journal of hydrogen energy 39, (2014) 3047-3054.
- C. Soils, **L. Navarrete**, M. Balaguer and J. M. Serra. Development and understanding of $\text{La}_{0.85}\text{Sr}_{0.15}\text{Cr}_{1-x}\text{Ni}_x\text{O}_{3-\delta}$; anodes for $\text{La}_{5.6}\text{WO}_{11.4-\delta}$ -based Proton Conducting Solid Oxide Fuel Cells. Journal of power sources. 258 (2014) 98-107.
- C. Solis, **L. Navarrete** and J. M. Serra. Study of Pr and Pr and Co doped $\text{La}_2\text{NiO}_{4+\delta}$; as cathodes for $\text{La}_{5.5}\text{WO}_{11.25-\delta}$; based protonic conducting fuel cells. Journal of Power Sources 240 (2013) 691-697.

- S. Somacescu, P. Osiceanu, J. M. Calderon-Moreno, **L. Navarrete** and J.M. Serra. Mesoporous nanocomposite sensors based on $\text{Sn}_{1-x}\text{Ce}_x\text{O}_{2-\delta}$; metastable solid solution with high percentage of Ce^{3+} valence state for selective detection of H_2 and CO . *Microporous and Mesoporous Materials* 179 (2013) 78–88.
- M. Balaguer, V. B. Vert, **L. Navarrete** and J. M. Serra. SOFC composite cathodes based on LSM and co-doped cerias ($\text{Ce}_{0.8}\text{Gd}_{0.1}\text{X}_{0.1}\text{O}_{2-\delta}$, X = Gd, Cr, Mg, Bi, Ce). *Journal of Power of Sources* 223 (2013) 214-220.
- C. Solís, **L. Navarrete**, S. Roitsch and J. M. Serra. Electrochemical properties of composite fuel cell cathodes for $\text{La}_{5.5}\text{WO}_{12-\delta}$; proton conducting electrolytes. *J. Mater. Chem.* (2012), 22, 16051–16059.
- V.B. Vert, F.V. Melo, **L. Navarrete** and José M. Serra. Redox stability and electrochemical study of nickel doped chromites as anodes for H_2/CH_4 -fueled solid oxide fuel cells. *Applied Catalysis B: Environmental* 115–116 (2012) 346–356.

Patent

- J.M. Serra, J. Garcia-Fayos, L. Navarrete y V.B. Vert. Catalytic layer and use thereof in oxygen-permeable membranes. WO2016001465 A1. 2016.

Congress participation

- **L. Navarrete**, M. Balaguer and J. M. Serra. Tailoring the performance of LSM-based electrodes on oxide-ion conducting electrolytes. Poster. 14th International Conference on Inorganic membranes. Atlanta (USA). 2016.
- J. Garcia-Fayos, R. Ruhl, M. Balaguer, H. Bouwmeester, J.M. Serra and **L. Navarrete**. Oxygen permeation optimization of CO_2 & SO_2 stable dual-phase membranes by means of surface catalytic activation under oxyfuel-like conditions. Oral presentation. 14th International Conference on Inorganic membranes. Atlanta (USA). 2016.
- C. Gaudillere, **L. Navarrete**, D. Catalán and J.M. Serra. Freeze-Casting for the fabrication of highly ordered and porous microstructured reactor and its implementation as catalyst support for CO_2 methanation catalytic reaction. Poster. 5th International Conference on Structural Catalysts and Reactors. Donostia-San Sebastián. 2016.

- **L. Navarrete**, C. Solís, M. Fabuel and J. M. Serra. Boosting the electrode performance by nanocatalyst infiltration for IT-SOFC and IT-SOEC applications. Poster. International YWS Camp and Smart Sister Workshop. Daejeon (South Korea). 2015.
- **L. Navarrete** and J. M. Serra. IT-SOFC and IT-SOEC Electrochemical Performance Enhancement by Boosting the Oxygen Reduction Reaction with Nanocatalyst Infiltration. Poster. The 11th Pacific Rim Conference of Ceramic Societies. Jeju (South Korea). 2015.
- **L. Navarrete** y J. M. Serra. CsH₂PO₄-Based Fuel Cells and Electrolyzers. Oral presentation. 20th International Conference on Solid State Ionics. Colorado (USA). 2015.
- F. Toldra-Reig, **L. Navarrete**, J. M. Serra and S. Somacescu. SnO₂ and Ce modified SnO₂ mesostructure for selective ethanol detection. Poster. Summer School: Ionic and protonic conducting ceramic membranes for Green energy applications. Valencia. 2015.
- **L. Navarrete** and J. M. Serra. New generation of proton fuel cells and electrolyzers based on CsH₂PO₄ electrolytes. Oral presentation. 14th International Conference of European Ceramic Society. Toledo. 2015.
- **L. Navarrete**, N. Bausá, C. Solís, and J.M. Serra. High temperature electrolyzers based on protonic and ionic conducting ceramics, differences in operation conditions and cell materials. Poster. 14th International Conference of European Ceramic Society. Toledo. 2015.
- **L. Navarrete**, C. Solís, and J.M. Serra. SOFC and SOEC electrochemical performance enhancement by nanocatalyst infiltration in LSM-GDC composite electrode. Poster. 14th International Conference of European Ceramic Society. Toledo. 2015.
- J.M. Serra, N. Bausá, C. Solís and **L. Navarrete**. Conversión de CO₂ a hidrocarburos en electrolizadores de alta temperatura basados en cerámicas protónicas (ELECTRA). Poster. Aportando valor al CO₂. Madrid. 2015.
- **L. Navarrete**, F. Toldra-Reig, J. M. Serra and S. Somacescu. SnO₂ and Ce modified SnO₂ mesostructure for selective ethanol detection. Poster. IEEE sensors 2014. Valencia. 2014.
- **L. Navarrete**, C. Solis and J. M. Serra. LSM-GDC cathode improvement through nanocatalyst infiltration. Poster. 11th European SOFC & SOE Forum. Lucerne (Switzerland). 2014.

- **L. Navarrete**, S. Escolástico, A. Andrio, V. Compañ and J.M. Serra. Electrochemical Reactors based on Solid CsH_2PO_4 Electrolyte Membranes. Oral presentation. 9th Ibero-American Congress on Membrane Science and Technology. Santander 2014.
- C. Gaudillere, **L. Navarrete** and J. M. Serra. Syngas production at intermediate temperature through H_2O and CO_2 electrolysis with Cu-based solid oxide electrolyzer. Poster. Summer School: Inorganic membranes for green chemical production and clean power generation. Valencia. 2013.
- C. Gaudillere, **L. Navarrete** and J. M. Serra. Syngas production at intermediate temperature through H_2O and CO_2 electrolysis with Cu-based solid oxide electrolyzer. Poster. 13th Conference of European Ceramic Society. Limoges (France). 2013.
- C. Solís, S. Escolástico, F. Bozza, M. Balaguer, **L. Navarrete**, N. Bonanos and J.M. Serra. Enhanced catalytic properties of high performance electrodes for LWO based PC-SOFC. Oral presentation. 19th International Conference of Solid State Ionics. Kyoto (Japan). 2013.
- C. Solís, S. Escolástico, F. Bozza, M. Balaguer, **L. Navarrete**, N. Bonanos and J.M. Serra. Tailor-made electrodes for LWO based PC-SOFC. Oral presentation. Prospects Protonic Ceramic Cells 2013 International Workshop. Montpellier, (France). 2013.
- **L. Navarrete**, M. Fabuel, C. Solís and J. M. Serra. Doped $\text{La}_{2-x}\text{A}_x\text{Ni}_{1-y}\text{B}_y\text{O}_{4+\delta}$ (A=Pr, Nd, B=Co, Zr, Y) as IT-SOFC cathode. Oral presentation. 10th European SOFC Forum. Lucerne (Switzerland).2012.
- C. Solís, V. B. Vert, M. Fabuel, **L. Navarrete**, J. M. Serra, F. Bozza and N. Bonanos. New Cercer Cathodes of Electronic and Protonic Conducting Ceramic Composites for Proton Conducting Solid Oxide Fuel Cells. Oral presentation. 10th European SOFC Forum. Lucerne (Switzerland). 2012.
- M. Balaguer, C. Solis, V.B. Vert, **L. Navarrete** and J. M. Serra. Tailoring SOFC cathodes conduction properties by Mixed Ln-doped ceria/LSM. Poster. 10th European SOFC Forum. Lucerne (Switzerland). 2012.
- J. M. Serra, M. Balaguer, C. Solís, S. Escolástico, **L. Navarrete** and V. B. Vert. Ln-doped ceria (Ln = Gd, La, Tb, Pr, Eu, Er, Yb) materials and its applicability as SOFC cathodes and oxygen. Oral presentation. International Symposium on Ceramic Materials and Components for

Energy and Environmental Applications (10th CMC). Dresden (Alemania). 2012.

- M. Balaguer, V. B. Vert, M. Fabuel, **L. Navarrete** and J. M. Serra. SOFC cathodes based on mixtures of LSM and doped-cerias with tailored conduction properties. Oral presentation. Symposium X: "Fuel cells energy conversion". Nice (France). 2011.
- C. Solís, V. B. Vert, M. Fabuel, **L. Navarrete** and J. M. Serra. New cathodes for proton conducting solid oxide fuel cells based in mixed ionic-electronic and protonic ceramic composites. International Conference on Solid State Ionics. Warsaw (Poland).2011.

Agradecimientos/Acknowledgements

Pensaba que lo más difícil sería escribir la tesis, pero al abrir el archivo en blanco para escribir los agradecimientos, me he dado cuenta que estaba bastante equivocada. Ya son seis años desde que pisé por primera vez el ITQ, y durante este tiempo son muchas las cosas que han pasado. Estos seis años han sido un viaje en montaña rusa, buenos momentos, con algún que otro buen resultado, pero también algunos no tan buenos, acompañados de alguna que otra lágrima. Seis años que me han ensañado que la “ciencia es paciencia” y que los logros en grupo saben mucho mejor y que las derrotas son menos dolorosas.

En primer lugar, me gustaría agradecerle a José la posibilidad que me brindó al dejarme hacer el doctorado en el ITQ. Y agradecerle especialmente la confianza que ha depositado en mi desde el primer momento, confiando mucho más en mi de lo que yo realmente podría haber llegado a confiar. Y gracias por ayudarme a avanzar y poder terminar esta tesis.

I would like to thank Chung-Yul for one of the best experiences of my life. Thank you for your support during my four months abroad, helping me with all the formalities and work, and also showing me your culture. 감사합니다!!!

Seis años, y se dice pronto, recuerdo mi primer día, cuando Vicente me estuvo explicando en qué iba a consistir mi trabajo, hablando de cosas como la impedancia o conductividades, no sé cuánto rato estuvimos en la sala de reuniones, pero me di cuenta que había otra persona que podía llegar a hablar igual o incluso más rápido que yo. Coincidimos poco tiempo en mis inicios, pero años después pude tener el gusto de trabajar más tiempo con él.

Las serranas creo que nos llamaban, después de que Vicente se fuera, sólo quedábamos chicas en el laboratorio. Sandra con la que pude disfrutar de momentazos, como el de cantar a dúo Camela. También estaba Cecilia, la Asturiana y física del laboratorio, con la que pude compartir mi primera salida del ITQ. El destino era el sincrotrón de Suiza, y el desplazamiento fue en furgoneta, dos días de viaje y noches en vela midiendo, todo un planazo. Me gustaría agradecerle su apoyo y las charlas que hemos tenido en estos años. Las de Villar también formaban parte del grupo de las Serranas. Un café

mañanero o un cigarrito, suyo claro, siempre iba bien para poder tomar un poco de aire fresco. Un gran apoyo en estos años de tesis, gracias María F. Muchas también son las risas que he podido compartir con María B., sé que mis bocadillos de aire no se le van a olvidar. Y por último estaba Sonia, la moledora oficial de aire, y con la que he compartido también buenos momentos y alguno faroleando (¡me encanta este verbo!). Un laboratorio femenino, pero creo que a “bruticas” no nos ganaba nadie.

En septiembre hubo dos nuevas incorporaciones, Raquel y Julio. Raquel una de las persona con más paciencia que conozco para explicarte las cosas, y la que al principio no decía ni un taco, pero un doctorado es lo que tiene. Y Julio, mi vecino de pH, muchas horas juntos tratando datos y muchos momentos de risas y algún que otro momento Superman. Y con el que aún tengo pendiente un baile.

Y el laboratorio fue creciendo, y llegó Cyril, el francés con el que me tocó lidiar al principio, pero que con los años se convirtió en un gran apoyo. David, el que siempre abre el laboratorio y siempre está dispuesto a echar una mano. Mateusz, el que se fue para volver, supertrabajador y con ganas de ayudar en lo que haga falta. Muchos son los que han pasado por ITQ, por tesis de master, estancias, etc. pero Mischa, un alemán nada alemán, es uno de los que recuerdo con más cariño, ¿puede que sea por los momentos de striptease?.

El laboratorio fue creciendo, y con la incorporación de Fidel y Nuria el grupo de los de la Universidad de Valencia también se fue haciendo más grande. Fidel creo nunca olvidará los momentos que pasamos dentro de la campana cambiando los caudalímetros. Y Nuria, por la que pasé de tener un adosado en el laboratorio a un pisito, pero con la que he compartido muchas risas. Y el grupo siguió aumentando, y llegó Sara, la cantarina del grupo. Pero esto no terminó aquí: Álvaro, Juan E. (un café mañanero siempre ayuda a empezar bien el día), Sebastián, Juan B y Daniel también se unieron al grupo.

Pero mi paso por el ITQ no habría sido lo mismo sin contar con la compañía de mucha más gente. El laboratorio de combinatoria, mi segunda familia en el ITQ. Francis, Juanjo; el tete, que pese a ser de Sagunto es bastante majo, Eva; la segorbina con la que siempre puedes hablar, y Nuria; ¿qué sería sin esas llamadas mediante golpes en la pared o esas tertulias tipo Sálvame?. Mis

sirenos; Ángel y Belén, porque un buen desayuno después del madrugón y de unos largos siempre sienta bien, y más, si es en buena compañía. A la gente de reacción, en especial a Tere, Amada y Elena, por ser cada una como es y acogerme desde el minuto cero. Gracias también a taller, gases e informáticos, mucho del trabajo de la tesis no hubiera sido posible sin ellos. A Saray, porque la beca nos ha dado muchos quebraderos de cabeza, pero entre las dos lo hemos conseguido. A Marta, por compartir esas comidas en el césped y alguna que otra fiesta. A Manolo, Alberto, Pedro y Eli por ser tan grandes, y compartir muchas risas conmigo. Y como no, al trío; Isabel, Cristina y Carmen, por su apoyo, ánimo y por esos abrazos de Cris, que siempre sientan tan bien. En especial a Isabel, por ser como es, por escucharme, por aguantarme en estos meses, y por ser uno de mis pilares en el ITQ.

Este doctorado no hubiera sido lo mismo sin dos de las personas con las que llevo más años; Raquel y Borja. Qué decirle a Raquel que no sepa ya, más de 10 años avalan nuestra amistad. Otro de mis pilares en el ITQ y fuera de este, un hombro en el que llorar, pero también una persona con la que reír. ¿Y a Borja?, que es un gran amigo y una gran persona, con el que las cosas son más fáciles de lo que parecen (gracias por ser así).

Gracias también a mis amigos por soportarme en estos meses tan estresantes para mí, y por ayudarme a desconectar del trabajo.

Creo que me he dejado para el final lo más difícil, gracias a mi familia, el gran pilar de mi vida, GRACIAS por dejar que nunca me caiga. Gracias por aguantar ese mal genio con el que llegaba a casa los días en que las cosas no habían salido como quería, y animarme para que al día siguiente fuera con más fuerza. Gracias por haber hecho lo que soy hoy. Y a mi abuelo, que aunque no entendiera lo que es un doctorado, sé que allí donde esté, estará muy orgulloso de mí.

¡Gracias a todos por compartir conmigo este viaje!

